5-15-2009

Nanoscale Thermal Fluctuation Spectroscopy

Patrick Louis Garrity
University of New Orleans

Nanoscale Thermal Fluctuation Spectroscopy

A Dissertation

Submitted to the Graduate Faculty of the
University of New Orleans
in partial fulfillment of the
requirements for the degree of

Doctor of Philosophy
in
Engineering and Applied Science
Physics

by

Patrick Louis Garrity

Bachelor of Science, Mechanical Engineering, University of New Orleans, 2002
Master of Science, Physics, University of New Orleans, 2003

May, 2009

Table of Contents

List of Figures

Table of Figures

Abstract

The utilization of thermal fluctuations or Johnson/Nyquist noise as a spectroscopic method to determine transport properties in conductors or semiconductors is developed in this paper. The autocorrelation function is obtained from power spectral density measurements thus enabling electronic transport property calculation through the Green-Kubo formalism. This *experimental* approach is distinct from traditional numerical methods such as molecular dynamics simulations, which have been used to extract the autocorrelation function and directly related physics only. This work reports multi-transport property measurements consisting of the electronic relaxation time, resistivity, mobility, diffusion coefficient, electronic contribution to thermal conductivity and Lorenz number from experimental data. Double validation of the experiment was accomplished through the use of a standard reference material and a standard measurement method, i.e. four-probe collinear resistivity technique. The advantages to this new experimental technique include the elimination of any required thermal or potential gradients, multi-transport property measurements within one experiment, very low error and the ability to apply controlled boundary conditions while gathering data. This research has experimentally assessed the gas pressure and flow effects of helium and argon on 30 nm Au and Cu thin films. The results show a reduction in Au and Cu electronic thermal conductivity and electrical resistivity when subjected to helium and argon pressure and flow. The perturbed electronic transport coefficients, attributed to increased electron scattering at the surface, were so dominant that further data was collected through straight-forward resistance measurements. The resistance data confirmed the thermal noise measurements thus lending considerable evidence to the presence of thin film surface scattering due to elastic and inelastic gas particle scattering effects with the electron ensemble.

Keywords: Thermal fluctuations, Nyquist noise, Autocorrelation function, Green-Kubo theory Gas particle scattering, Electronic thermal conductivity, Electrical resistivity

Chapter 1

Introduction to Nanostructures Interfaced with a Gaseous Boundary, Transport Property Perturbations and Quantum Decoherence

1.1 Research Objective

The fundamental research objective embodied in this dissertation can be described by three components that make up the central research problem. Specifically, the central problem is the thermal and electrical transport property effects on a solid state conductor in the nanoscale size regime when interfaced with a gaseous boundary. Furthermore, the research interest lies in nanostructure electron and/or phonon scattering due to gas atoms or molecules (hereafter termed particles to include both atoms and molecules) interactions occurring at the material surface. Unlike the well studied area of chemical and physical adsorption of gas particles at a solid surface,[1-14] the perturbed thermal and electrical transport incurred by the solid conductor due to kinetic gaseous scattering interactions has received virtually no attention. Therefore, the study of energetic surface perturbations of a gaseous environment on a nanostructure is pertinent, especially with the large increase in surface area to volume ratio of materials in the low dimensional regime. This observation allows the first two components of the central problem to be put forth: 1) the theoretical study of gas particle scattering effects on nanostructures and 2) the experimental study of gas particle scattering effects on nanostructures.

The third component of the central problem lies in the fundamental physics of a quantum system and the transition to a classical regime due to environmental interaction. This process known as quantum decoherence, is essential to explaining how quantum systems become effectively classical. The relevance to the study of nanostructures interfaced with a gas particle field should be clear as most reports in the literature treat nanoscale materials in isolation, as if they will never interact with their environment.[15-19] With respect to functional nanodevices or components, this will never be the case. For example, imagine a carbon nanotube unconnected to the external world and isolated from environmental interactions such as gas particles or radiation (normal photon bombardment). How useful will this nanotube be with regards to a real application? Furthermore, how useful are the many published reports on nanoscale transport properties that never considered the environmental interactions and corresponding decoherence process that has now transitioned this foregone quantum system to classical phase space? With respect to thermal and electrical transport properties, the consideration of environmental

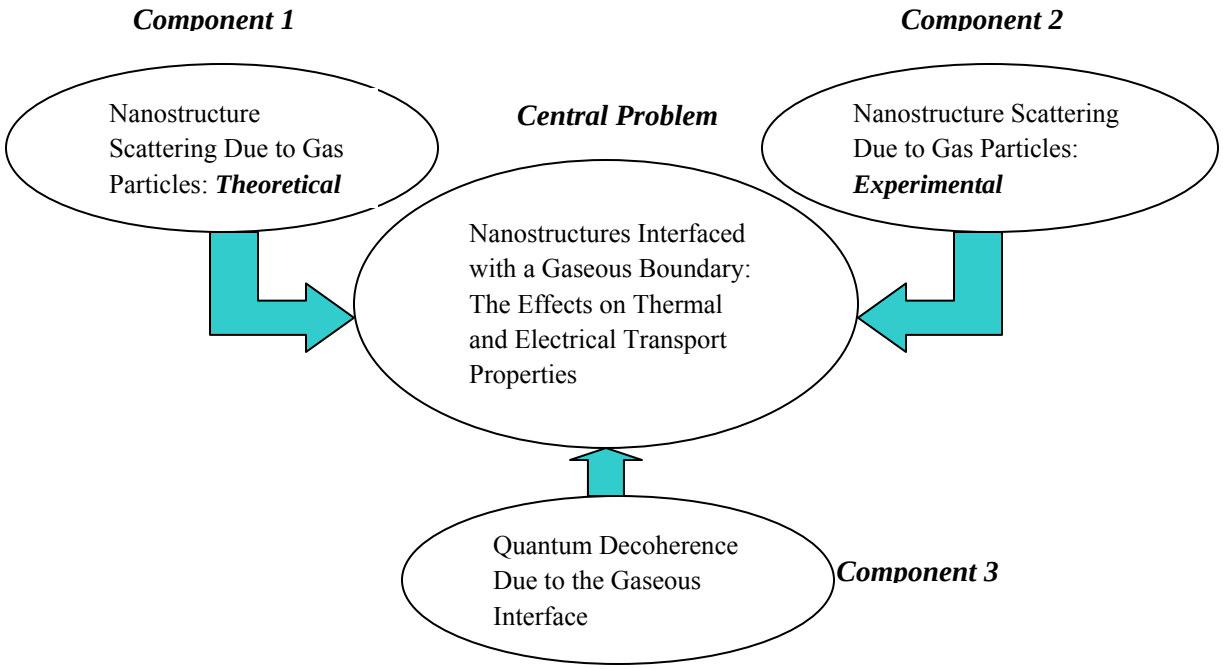

Figure 1.1: The central research problem with the three primary supporting components.

interactions and the knowledge of the appropriate transport regime, whether quantal or classical, is imperative in understanding the flow of heat and charge.

Figure 1.1 above graphically details the central problem of this research with the three core components that serve to support the investigation contained herein. The remaining sections in this introductory chapter build upon the central research problem from the "bottom up." Hence, the closed quantum system with no environmental interactions is introduced first followed by the sequential emergence of classical properties due to environmental correlations. Relevant quantum solid state transport coefficients are then derived and their transition to macroscopic values as a result of multi-body interactions is overviewed. Finally, the utilization of electronic noise to experimentally measure thermal and electrical transport coefficients is brought forth and noted to be one of the major contributions to the central research problem.

1.2 The Transition of a Closed Quantum Solid State System into an Open Quantum System

The theoretical idealization of isolated systems representing materials in the solid phase such as metals, semiconductors and dielectrics permeates the theoretical study of quantum systems. In most quantum textbooks for example, quantum systems are presented in a manner which by and large have satisfied the idealization of being isolated and totally uncoupled to any external environment.[20-21] The particle in a box, the harmonic isolator, the free particle and the hydrogen atom are cases in point. Any such isolated or *closed* system possesses a wave function or superposition of wavefunctions of the coordinates only of that system. Naturally, these wavefunctions determines the state of that system. At this point the quantum density matrix is introduced. Quantum density matrices or reduced density matrices play a vital role within the

scope of research encompassed in this work. Specifically, the study of complex many-body systems falls under *quantum statistical mechanics* and it is in this discipline that the density matrix finds great utility.[22] In an isolated closed system, the quantum density matrix is populated with both diagonal and off-diagonal coherent wavefunctions.[23] Now consider "opening up" this closed quantum system to the environment. Such, for example, is the case of a gas of N particles maintained at a constant temperature through contact with the subject solid phase material. Very simply, if x denotes coordinates of the solid phase material and y coordinates of the gas field or environment, then whereas the closed composite of solid phase material plus environment has a self-contained or "interaction" Hamiltonian and wavefunction $\Psi(x, y)$, this wavefunction does not, in general, fall into a product $\Psi_1(x)\Psi_2(y)$. The key concept conveyed by this statement is *quantum entanglement*, where two systems are described by a quantum state that, loosely speaking, cannot be separated into two separate quantum states.[24] Subsequently, entangled states are the equivalent of quantum correlations between the two systems. Such correlations often result in new physical properties for the composite system that were not present in the two individual systems. Stated in other words and continuing to use the example at hand, the gas particles interactions in the quantum setting no longer amount to a mere perturbation of the solid state material. Instead, the coupling of the gas particle field to the material now defines the observable physical properties of the system. At the same time, quantum coherence, a measure of the "quantumness" of the system, is delocalized into the entangled material-environment state, which effectively removes quantum coherence from our observation.[25] This *decoherence* process is typically irreversible and represents a key component in explaining how the classical world experienced by human senses emerges from the underlying quantum substrate. This statement is loaded with meaning and some explanation is now due on how the emergence of

classical properties fits in with the research embodied in this work. Basically, the classical properties referred to are thermal and electrical transport properties in solid state conductors and semiconductors. Hence, the following statement is put forth: *The energetic perturbation of an isolated Hamiltonian cannot persist in a system previously in a closed quantum state, without the onset of quantum decoherence due to environmental interactions. The resulting system plus environment defines a statistical ensemble that can be described by quantum or classical statistical mechanics.* This profound observation indicates a connection between the loss of quantum coherence and the emergence of observable thermal or electrical transport through statistically fluctuating properties. This is the case indeed as exemplified in Chapter 7 of this report. For the moment, the fundamental transport of heat and electricity is elucidated in the next section.

1.3 The Emergence of Heat and Electrical Transport Properties and Their Transition to the Classical Regime

This section begins by departing from the solid/gas interactions outlined in the example of Section 1.2 yet continues with the notion of opening up a closed quantum system by allowing interactions with the surrounding environment. In particular, the simple case of connecting a low dimensional material to contact reservoirs is put forward. The low dimensional material measures in the nanoscale regime and is assumed to exhibit ballistic carrier transport. Quite simply, this means that the charge carriers (electrons in this example) experience no collisions or energy exchanging interactions during the "ballistic" transversal between the contacts. Figure 1.2 details the conductor so described.

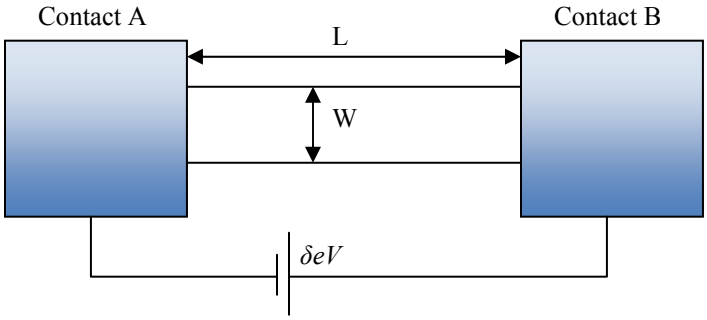

Figure 1.2: A conductor is connected to two contacts which has an external potential voltage applied. Electrons are assumed to be able to exit the conductor with zero probability of reflection. The entire system is at temperature 0 K.

A qualitative description of the conductance exhibited by the subject example parallels that of Datta[26] and proceeds as follows. In the ballistic transport approach, the system is characterized by the transmission and reflection of the incoming waves at contacts A and B. Essentially, this is a scattering matrix approach. If the contacts are described by Fermi levels E_{FA} and E_{FB}, which are under a small applied potential voltage $e\delta V$, then only those electrons flowing from filled states on the left to the empty states on the right contribute to the current. This is prevalent at T = 0 K where electron states are completely filled up to the Fermi level and completely empty for energies *above* the Fermi level. Since the carriers move ballistically, electrons leaving the left contact at the Fermi energy arrive at the right contact with an excess energy $e\delta V$. Furthermore, if there is no barrier to this flow, the current is determined solely by the number per unit time of electrons which can leave the source contact A. Through straightforward analysis of the number density of electrons and the prevalent one dimensional density of states,[26] the quantum of electrical conductance $\sigma_{Quantum}$ is found to be expressed as:

$$\sigma_{Quantum} = \frac{2e^2}{h}, \tag{1.1}$$

where e is the electron charge, h is Planck's constant and a factor of 2 appears to account for electron spin degeneracy. The significance of the quantum electrical conductance is that the conductance exhibits a fundamental value multiplied by the number of waveform modes that are transmitting. Additionally, it is important to note that the system detailed in Figure 1.2 cannot take on zero resistance due to the absence of carrier scattering but must exhibit at least one quanta of conductance equivalent to equation (1.1). As the quantum conductance is driven from the modal domain to the macroscopic regime due to increased degrees of freedom, many-body effects and increased temperatures, the conductance assumes the value typical of the material at hand *yet representative of the underlying scattering processes incurred by the electron ensemble*. It is this regime that falls under the central research problem of this survey.

Pause is taken at this point to view this problem from the quantum standpoint of Section 1.2. The initially closed quantum system of the one dimensional conductor shown in Figure 1.2 has been opened up through wavefunction entanglement with two contacts. This process resulted in the loss of coherent wavefunction states resulting in the onset of decoherence. The once isolated Hamiltonian of the conductor has transformed to an interaction Hamiltonian which contains energetic components of the conductor and both contacts. The resulting "observable" which in this example happens to be quantum conductance, is a causal result of the correlations formed between the conductor and contacts. Here again, the path beginning with quantum decoherence and leading to energy transport is evident and noted to be occurring in causal fashion.

Thermal conductance follows similar behavior to the electrical conductance when submitted to ballistic transport. One dimensional systems under low temperatures exhibit the quantized value of the thermal conductance $k_{quantum}$ equivalent to.[27-28]

$$k_{quantum} = \frac{\pi^2 k_B^2 T}{3h}, \tag{1.2}$$

where k_B is Boltzmann's constant and T is temperature. Interestingly, the quantum thermal conductance does not depend on the statistics of the heat carriers.[29] In other words, the quantum thermal conductance is identical for both bosons and fermions or with regards to solids, phonons and electrons.[29] Similar to the electrical conductance, the thermal conductance takes on macroscopic values due to dimensional and temperature increases again representative of the underlying scattering events experienced by the heat carriers. The central research problem of this work is again noted to lie within many-body scattering effects. Theoretically, the appearance of quantal values in heat transport is also a causal effect manifested by the decoherence process and clearly a macroscopic observable. Indeed, one finds again that the vanishing off-diagonal states in the quantum density matrix must precede the transport of energy between a system and the correlated environment. Here again, the transition from a closed quantum system to an open quantum system exhibiting classical properties is incrementally assembled and directly related to the central research problem.

Now consider an open circuited 1D (x-direction only) conductor, with no electrical current present. Next apply an x-directed temperature gradient. Under the influence of this gradient the charge carriers, electrons or holes, will initially drift in the x-direction. This transient thermal current subsequently redistributes the electric charge in the material, creating

an electric field E_x. During equilibrium conditions, this electric field exerts a force on the charge carriers that exactly offsets the opposite driving force produced by the temperature gradient. The ratio of the resulting electric field E_x to the temperature gradient is known as the *absolute Seebeck* effect and is characterized by the Seebeck coefficient S.[30] When dissimilar conductors are joined together followed by the application of a temperature gradient, the resulting electric field E_x ratio to the temperature gradient is identified as the *relative Seebeck* effect because S is a result of the cumulative absolute Seebeck effects. Interestingly, the opposite physical phenomena exists in the case of an applied electric current density which results in a temperature gradient in the system. Consequently, this phenomena is known as the Peltier effect and is represented by the Peltier coefficient Π. It is imperative to understand the dual nature of energy transport by the electrons or holes. When an electrical current flows, it simultaneously transports heat in the form of a thermal current. The cross-correlation between the two currents is characterized by thermoelectric phenomena, i.e. the Seebeck and Peltier effects. Therefore, we arrive at the equations for the electrical and thermal current densities which clearly show the cross-correlated thermoelectric effects S and Π:[30]

$$J_E = \sigma E_x + \sigma S \nabla T_x, \tag{1.3}$$

$$J_Q = \sigma \Pi E_x + k_e \nabla T_x, \tag{1.4}$$

where σ is the electrical conductivity, k_e is the electronic thermal conductivity and the thermal gradient in the x-direction is represented by ∇T_x.

Considering the thermal, electrical and thermoelectric transport properties developed above and focusing on the scattering processes that limit the flow of heat and/or electricity, Section 1.4 continues the development of the central problem embodied in this research.

1.4 Nanostructures Interfaced with a Gaseous Boundary and the Possible Effects on Solid State Transport Properties

From a heat and electrical transport perspective, gradients of temperature or electric potential create a flux of energy proportional to the magnitude of the gradient. This proportionality is represented by the thermal conductivity or electrical conductivity coefficients introduced in the previous section. Specifically, these coefficients are properties of a material that indicates the ability to conduct heat and/or electricity.[31] As outlined in Section 1.3, transport coefficients such as thermal and electrical conductivity are not simply values determined empirically with no underlying physical basis. Considering transport in the presence of many-body effects, these coefficients can be calculated by well known techniques using transport equations that encompass scattering events by the heat or charge carriers, i.e. phonons and electrons.[32] Naturally, an energy flux is impeded by the presence of excessive scattering and is consequently enhanced by decreased scattering events. Moreover, different scattering mechanisms exist in solids such as interactions with material impurities, crystal lattice defects, photons, and other members of the electron or phonon ensemble. All of these scattering processes are well understood both theoretically and experimentally.[33] However, there is another potential scattering mechanism that is not treated in *any* textbook thus representing the first and second research components (Figure 1.1) that make up the central research problem. This potential scattering mechanism is that caused by gas particles that constantly interact with a solid

surface via collisions. The interest lies specifically with kinetic scattering effects to the electrons and/or phonons of a solid. For example, a 1 mm x 1 mm solid surface receives approximately 2 x 10^{21} gas particle impacts per second in air under normal atmospheric pressure (calculated using the numerical program in Appendix A). This phenomenon is primarily isolated to surface interactions with some adsorption of gas particles that is usually limited to a few angstroms below the material surface.[1,34] Considering an electrically conductive material such as a metal, the gas particles interact with the lattice as well as the jellium which is the electron charge "cloud" whose quantum wave function extends beyond the material surface and decays a few angstroms into the adjacent gas field. Wave function overlap and interactions between the gas particles and solid surface result suggesting the probability of scattering events and subsequent contributions to thermal and electrical transport coefficients.[34] However, it is true that for a macroscopic material, the surface scattering incurred by gas particles is minimal compared to the internal dominant bulk scattering processes. This may explain the lack of theoretical or experimental work in this area. As material dimensions decrease, the surface area to volume ratio follows an exponential increase suggesting the possibility of surface scattering contributions that may dominate the overall scattering landscape in low dimensional materials. Figure 1.3 shows an example of material size reduction and the corresponding surface area to volume ratio A_{Surf}/Vol increase. One can see that by reducing the material thickness only, while keeping the same length and width, results in a dramatic surface area ratio growth. In terms of numbers, reducing the sample material thickness of Figure 1.3 from 3 mm to 3 μm results in a A_{Surf}/Vol increase of 342.

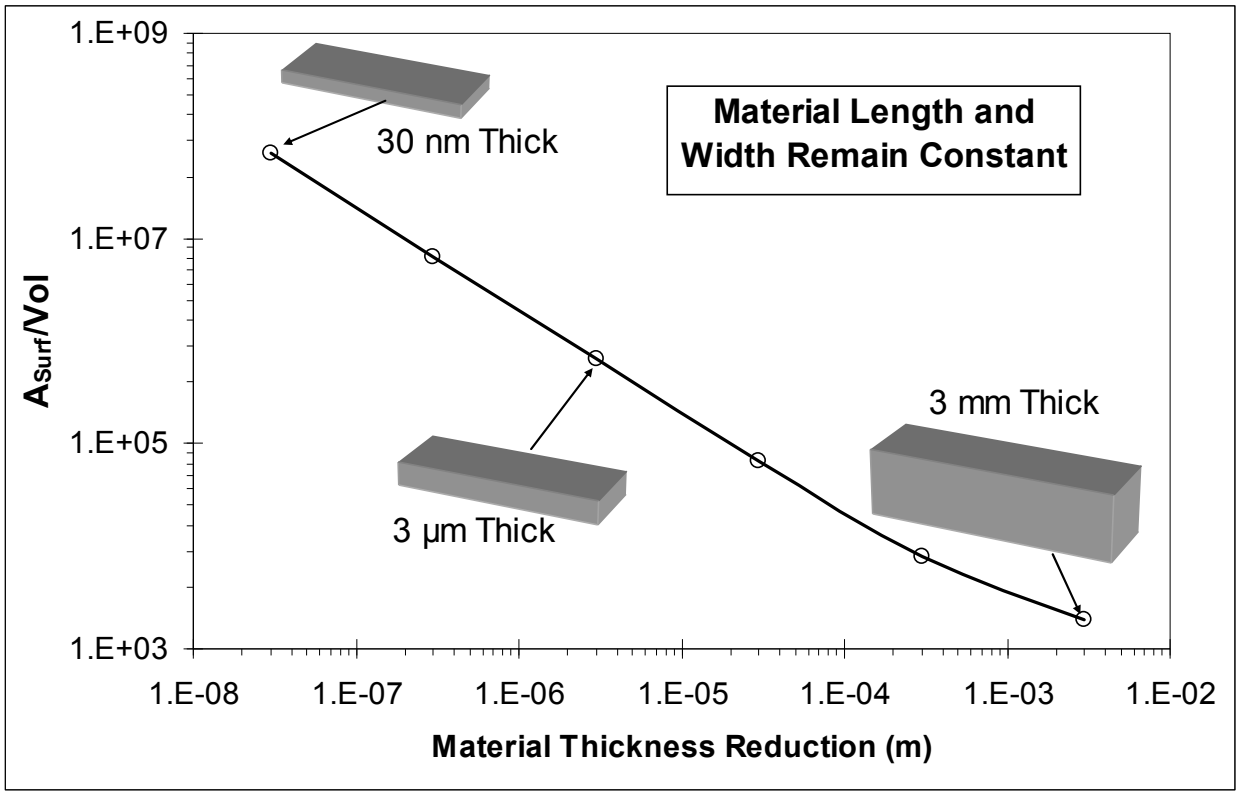

Figure 1.3: Log-log plot of the surface area to volume ratio increase due to material thickness reduction.

With this information in hand, the argument is put forth that perturbations to transport properties due to gaseous scattering effects (in lieu of chemical or physical adsorption) should be observable in nanoscale materials through transport property deviations. The closest relevant work in this area has occurred primarily in the surface science community with regards to helium atom scattering (HAS) spectroscopy.[1] Comprehensive studies have appeared in the literature on helium atom scattering induced by the crystal lattice surface or jellium in an effort to understand the HAS spectroscopic results.[35-36] It should be made clear however, that these reports investigate the scattering effects occurring in the helium gas field and *do not encompass the scattering effects on the solid material.* An isolated group which reported resistivity and thermoelectric coefficient changes in carbon nanotubes under different gaseous environments

attempted to explain the effect by assuming "dents" were formed in the nanotube walls upon each gas particle impact.[37-38] Their macroscopic type treatment encompassed little quantum or classical scattering theory and is completely disconnected from the useful and experimentally validated reports of the HAS community. Another group reported electrical conductance variations of V_2O_5 nanowires submitted to helium and air and even obtained data under helium flow conditions.[39] Unfortunately, their explanation of the phenomena was limited to physical adsorption. Yet another research group has reported voltage and current generation of carbon nanotubes submitted to a gas and liquid flows.[40-41] Their theoretical explanation however was limited to an unusual use of macroscopic fluid flow equations with no discussion of basic fluid-surface scattering effects. It is particularly interesting to overview the direct evidence of nanostructure scattering evidence that has eluded several groups. This research effort shall attempt to theoretically and experimentally quantify the nanostructure kinetic surface scattering through transport property deviations due to gas particle scattering effects.

The theoretical treatment of gaseous energetic perturbations with nanostructure phonons and electrons has been consummated in this research effort and appears in later chapters of this report. The *experimental measurement* of thermal and/or electrical transport perturbations due to a gas field presents problems that have led this investigation to formulate new experimental methods to assess the gaseous boundary. Surprisingly (or not), the new experimental method introduced in the next section is uniquely intertwined with both quantum decoherence as well as multiple scattering environments and the corresponding transport of heat and charge.

1.5 Experimental Measurement of Thermal and Electrical Transport Properties Due to External Scattering Mechanisms

The experimental measurement of perturbations to thermal and electrical transport coefficients due to a gaseous interface is not trivial given the traditional experimental techniques available. Typically, a one dimensional thermal gradient or electrical potential is applied to a material which resides in a vacuum to help eliminate gaseous convective effects.[42] Additionally, radiation exchange with the experimental apparatus is minimized by selective materials that enclose the sample with some setups even heating or cooling the enclosure in order to match the sample temperature.[42] Immediate conflicts arise with the traditional experimental methods just described and the investigation underway in this work. Instead of eliminating gaseous boundaries, this work seeks to assess their effects. Consequently, an alternative experimental technique is desired and the descriptive steps developed in the following paragraphs represents an overview of the new methodology. The focus is concentrated on the electron ensemble however, the generalized application of this new experimental technique shall be explicated in Chapter 6.

Development now begins on how to experimentally measure the scattering effects induced by a gaseous boundary on a conducting material's electron cloud or jellium. The electrons in all conductors and semiconductors are thermally energetic and move randomly through the material, experiencing collisions with the host lattice, imperfections, impurities and with each other. The random motions are responsible for thermal noise or equivalently, Johnson/Nyquist noise in recognition of the discoverers of this phenomena.[43-44] The generalized equation describing thermal noise applies to any conductor whether it be solid, semiconductor or even liquid where

the mean square noise voltage $\overline{V^2}$ and power spectral density $S_V(f_0)$ are theoretically expressed as:[45]

$$\overline{V^2} = 4k_B TR\Delta f \,, \tag{1.5}$$

$$S_V\left(f_0\right) = \overline{V^2} = 4k_B TR \,, \tag{1.6}$$

where R represents the material resistance, Δf is the frequency domain of interest with center frequency f_0 and equation (1.5) is the traditional Johnson/Nyquist noise. Thermal noise is readily measurable with a sensitive voltmeter as the root mean square voltage fluctuations manifested by the fluctuating electron cloud is typically in the nanovolt range. The statistical properties of this stationary white noise holds information that can be investigated through the calculation of the autocorrelation function. The autocorrelation function is the inverse Fourier transform of the power spectral density $S_V(f_0)$, *which can be measured experimentally*.[45] Once the autocorrelation function is calculated, the transport coefficients may be calculated through the methods initiated by Green and Kubo. Basically, Green and Kubo showed that transport coefficients such as thermal and electrical conductivity could be expressed quite generally as integrals over the autocorrelation function.[46-48] The theoretical foundation supporting Green-Kubo transport theory is rigorous given its foundations in quantum mechanics. Furthermore, their theory encompasses all scattering events, regardless of their source, even two-body, three-body or any multiple-body, multi-potential collision process. With regards to the experimental

implementation of Green-Kubo theory, simplicity is an added bonus due to the lack of any thermal or electrical gradient required during the experimental process. In fact, the power of this method from an experimental standpoint lies in the ability to add or remove boundary conditions to the subject material thus enabling direct measurement of transport properties and any perturbations to their fundamental values. The uniqueness of this methodology is evident when compared to the traditional transport property experiments described in the opening of this section. Obviously, this experimental line of attack specifically fits the requirements of the second component of the central problem put forth in the Section 1.1: to experimentally measure the effects of gaseous boundaries on the electron cloud through thermal noise measurements and subsequent perturbations to the thermal and electrical conductivities.

1.5 Summary of Research Scope and Objectives

A general high-level introduction has been given to the subject matter encompassed in this research. Theoretical and experimental details including results are detailed in the remaining chapters of this dissertation. Chapter 2 derives the theoretical scattering to nanostructure phonons and electrons in addition to numerical results. Chapter 3 advances the Green-Kubo theory and develops the spectroscopic method to measure transport properties of the electron ensemble. Chapters 4 and 5 describe the experimental apparatus, calibration, validation and results of gaseous interfaces with both nanostructures and bulk materials. Chapter 6 extends the research beyond electron ensembles and shows the generalized applicability of the spectroscopic measurement of thermal noise for other material phases such as gases, liquids and crystal lattices (phonons). Quantum decoherence and the theoretical connection to the work executed in Chapters 2 through 6 is described in Chapter 7. Finally, Chapter 8 concludes this report with a

final summary, discussion and view of future work. All relevant references and appendices follow Chapter 8.

Chapter 2

Solid Surface Scattering Due to Gas Particle Interactions: Theoretical Assessment

2.1 Primary Objective of the Theoretical Assessment of the Solid Surface Scattering Due to a Gaseous Interface

The primary objective of this chapter is to adopt a theoretical focus on solid surface scattering due to energetic perturbations of a gaseous interface. Therefore, this objective directly supports the first component of the central research problem defined in Chapter 1, Section 1.1. The scattering of gases from solid surfaces has found great utility in the surface science community with regards to surface characterization.[1] The energetic perturbation process on a surface is therefore a central topic when viewed from the *gaseous* side of the interaction. Stated in other words, there has been considerable work done on understanding the scattering effects to the *gas particle field* because the gas particles serve as a probing mechanism subsequently measured by a detector to interpret the surface interaction. For example, elastic interactions can give information about the symmetry and geometric arrangement of atoms near the solid surface. Inelastic scattering on the other hand, yields data about possible excitations of a surface *both phononic and electronic*.[1-2] Obviously, energetic interactions taking place through an interparticle potential energy perturb not only the gas particle, but the lattice ion or electron as

well. This research effort resides firmly on the solid side of the scattering process, hence the interest in the surface science spectroscopic results. Indeed, their results provide robust proof that the possibility of gaseous scattering effects may perturb the transport properties of nanoscale materials.

This chapter is organized as follows. Section 2.2 overviews the relevant research results that support the theoretical interests of this work. Section 2.3 follows with a derivation of the lattice scattering transition rate due to gaseous perturbations. Despite extensive literature searches, the subject derivation followed by numerical analysis results in Section 2.4, appears to be the first assessment of phonon scattering by gas particles. Section 2.5 presents the electron scattering transition rate from a theoretical standpoint, which numerically interfaces with a finite element penalty function solution to the variational Boltzmann transport equation. The Boltzmann transport equation solution method is a major result of this research and constitutes a powerful transport coefficient prediction tool, especially with regards to nanostructures. The full finite element penalty function method applied to the variational Boltzmann transport equation is given in Appendix B.

2.2 Current Research Assessment of Solid Surface Scattering Due to Gas Particles

The surface science community has produced a great deal of experimental data quantifying the interaction of gases with surfaces. Therefore, providing a comprehensive review of gas atom or molecular beam spectroscopic results is beyond the scope of this section. For this reason, the concentration is relegated to results specific to solid surface perturbations. Janda et al.[49] reported a kinetic energy transfer of 213 K (some groups report results in units of temperature) for Ar

atoms impinging on a 393 K Tungsten surface. The incident Ar atoms transferred part of their kinetic energy to the dynamic modes of the surface phonons.[34] Similarly, a gas atom can gain energy via the annihilation of a surface phonon.[1] Coupling of the perturbed surface modes to the bulk lattice then occurs through anharmonic vibrational modes.[1] Surface phonon dispersions (or Rayleigh surface waves) on a Ni (100) surface obtained by High Resolution Electron Energy Loss Spectroscopy (HREELS) data confirm an inward relaxation of the surface atomic layer.[50] Helium Atom Scattering (HAS) groups can easily explore the transition from single phonon to multi-phonon scattering by varying the He impact energy. Undoubtedly, the impact of a gas particle on a surface has been shown to result in lattice perturbations and the comparatively shallow depth of a nanostructure inner lattice indicates propagation of the collision effects to be a potential scattering mechanism. Moreover, the large surface area to volume ratio of nanostructures points to the possibility of gaseous interfaces dominating the overall scattering landscape.

Considering the electron cloud or jellium of a conducting material, the HAS community has recognized both experimentally and theoretically the interaction of He atoms with the electron charge density.[35-36,51-54] In fact, the resolution between the disagreement between experiment and theory (which initially considered lattice interactions only), was possible only through the theoretical inclusion of the dynamical interaction of He atoms with the electron jellium.[35-36] This should come as no surprise as the electron wavefunction decays not at the surface, but several angstroms into the gaseous interface.[34]

The phenomena associated with gas particle scattering in nanostructures has appeared through transport property deviations. Wortman and Canady[55] reported electrical resistance changes in 40 nm thin Au films when exposed to Oxygen. Yu et al.[56] measured a 5% increase in

metal oxide nanobelt conductance upon exposure to nerve agents and attributed the conductance change to gas chemisorption. Romero et al.[38] noted systematic changes in Carbon nanotubes resistance and thermopower as a function of gas species. A fascinating experiment was run by Amirav and co-workers on semiconducting materials.[57-58] They bombarded the semiconductors with Xe atoms and recorded an induced current due to electron-hole pair creation. Their work is apparently the first experimental proof of electronic excitations within a solid due to gas-surface interactions.

A gaseous interface will be present on many nanotechnology applications such as nanosensors, nanoelectromechanical systems and nanocoatings,[56,59-60] yet a formal nanosurface-gas phonon scattering rate quantifying the interaction has never been derived. This is probably due to an insignificant contribution to the carrier mean free time (MFT) in bulk materials because scattering interactions are dominated by the bulk constituents and not by the surface-to-gas interface. Electrons and phonons in nanoscale materials however, can undergo ballistic or quasiballistic transport and the high surface area to volume ratio suggests that carrier lifetimes can be substantially impacted by nanosurface-gas interactions. Considering the experimental evidence and aforementioned surface area to volume ratio of nanostructures, the objective of Section 2.3 is to derive a quantitative expression describing lattice-gas particle scattering.

2.3 Derivation of the Phonon Scattering Rate of a Solid Due to Gas Particle Interactions

The intent of the following derivation is to obtain a generalized expression of the relaxation time describing the crystal lattice response to a perturbation by an impinging gas

particle field. This derivation parallels the work by Garrity.[61] Figure 2.1 provides details of the nanosurface-gas scattering event. The lattice perturbation occurs upon a diffuse interaction with

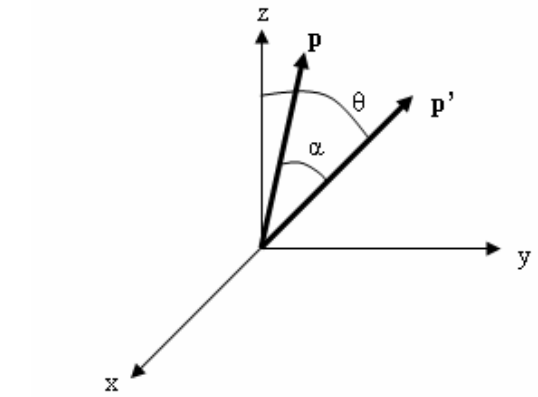

a)

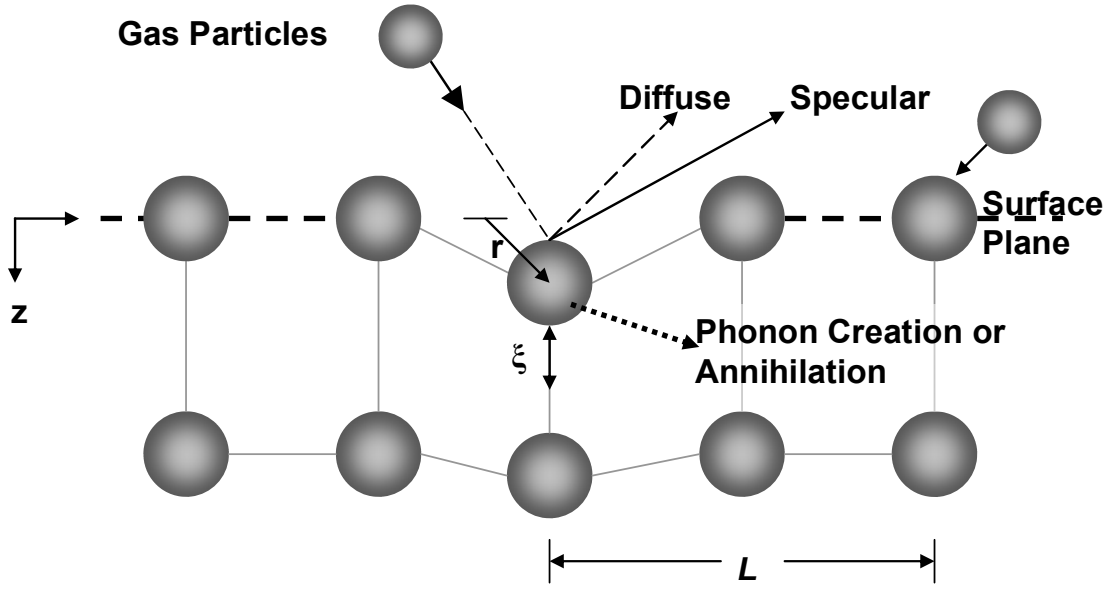

b)

Figure 2.1: The nanosurface-gas particle scattering event: **a)** Coordinate system of the nanosurface-gas scattering process detailing the incident and scattered momenta and the polar angle, α. **b)** Scattering details of the nanosurface-gas collision process. The average distance between lattice atom-gas particle scattering sites is *L* and **r** is a two-dimensional position vector. The rms fluctuation amplitude of the lattice atom due to the collision process is ξ. The diffuse collision density where energy exchange sites occur is defined by the accommodation coefficient, which can range from 0 to 1. Gaseous boundaries represent a scattering mechanism particular to nanostructures and can create or annihilate phonons.

a gas particle and is correlated to the average distance between simultaneous scattering sites. Over a finite time period, these scattering sites move and change locations over the nanosurface in a dynamic manner according to the fluctuating gas collision frequency. A material surface interfaced with a gaseous boundary experiences a perturbing potential energy due the fluctuating collision rate of gas particles:

$$V(z) = V_0(z) + U(z), \tag{2.1}$$

where $V_0(z)$ is the crystal lattice potential and $U(z)$ is the perturbation induced by the stationary or flowing gas interactions. The perturbation $U(z)$ is expressed as:

$$U(z) = V_G(z)\xi(\mathbf{r}), \tag{2.2}$$

where $V_G(z)$ is the potential energy of the gas particle. As shown in Figure 2.1b, r represents a two dimensional position vector in the interface plane and $\xi(r)$ is a random function that measures the atomic displacements of the lattice due to gas particle collisions. Furthermore, the function $\xi(r)$ implicitly encompasses lattice atom physics and is not macroscopic in nature. On a slightly larger scale, the surface roughness and other related surface effects on a gas field are described by the gaseous accommodation coefficient, which shall be incorporated in this derivation later. Evaluating the matrix element for scattering in the Born approximation yields:

$$H_{\mathbf{p}',\mathbf{p}} = \frac{1}{A}\int \Psi^*_{\mathbf{p}'}(z)\left[U_G(z)\right]\Psi_{\mathbf{p}}(z)dz$$

$$= \int_{-\infty}^{\infty} \Psi^*_{\mathbf{p}'}(z)\left[V_G(z)\right]\Psi_{\mathbf{p}}(z)dz \cdot \frac{1}{A}\int_A \xi(\mathbf{r})e^{i(\mathbf{p}_{//}-\mathbf{p}'_{//})\cdot\mathbf{r}_{//}}d^2\mathbf{r} \quad , \tag{2.3}$$

where A is the area and $p_{//}$ and $p'_{//}$ are the momentum of the initial and final phonon states, respectively. Utilizing the scattering coordinate system shown in Figure 2.1a and incorporating the plane wave assumption, the first integral in equation (2.3) can be expressed as:

$$\int_{-\infty}^{\infty} e^{-i\mathbf{p}'\cdot\mathbf{r}/\hbar}\left[V_G(z)\right]e^{i\mathbf{p}'\cdot\mathbf{r}/\hbar}d^3r$$

$$= \int_0^{2\pi} d\varphi \int_0^{\pi} \int_0^{\infty}\left[V_G(z)\right]e^{i(\mathbf{p}-\mathbf{p}')\cdot\mathbf{r}/\hbar}r^2 dr\sin\theta d\theta \tag{2.4}$$

After integration of equation (2.3), the matrix element reduces to:

$$H_{\mathbf{p}',\mathbf{p}} = 2\pi\int_0^{\infty}\left[V_G(z)\right]dr \cdot \frac{1}{A}S(\boldsymbol{\beta}_{//}) \, . \tag{2.5}$$

The power spectrum $S(\beta_{//})$ is the Fourier transform of the autocovariance function $\xi(r)$. Dynamic light scattering by gases has shown experimentally[62] that the fluctuating behavior of position and momenta dependent properties exhibits exponential behavior, which results in the following autocovariance function that is exponential in form:

$$\xi(\mathbf{r}) = \Delta^2 e^{-r/L}, \tag{2.6}$$

where Δ is the root mean square (rms) amplitude of the lattice atom fluctuation due to the nanosurface-gas collision. The length L, displayed in Figure 2.1b and defined in equation (2.6) is the average distance between lattice-gas interaction sites and governs the decay of the autocovariance function. By convolution, the power spectrum is the Fourier transform of the autocovariance function $\xi(r)$ and is expressed as:

$$S(\beta) = \pi\Delta^2 L^2 \frac{1}{\left[1 + (L^2\beta^2/2)\right]}. \tag{2.7}$$

Using these results, determination of the transition rate is straightforward:

$$W(\mathbf{p}_{//},\mathbf{p}'_{//}) = \frac{2\pi}{\hbar}\left|H_{\mathbf{p}',\mathbf{p}}\right|^2 \delta(\Delta E)$$

$$= \frac{8\pi^4\Delta^2 L^2}{\hbar A^2}\cdot\frac{1}{\left[1+(L^2\beta^2/2\right]}\cdot\left|\int_0^\infty\left[V_G(z)\right]dr\right|^2 \delta(\Delta E), \tag{2.8}$$

where the delta function simply defines energy conservation and ΔE is the change in gas particle energy due to scattering. Equation (2.8) is the transition rate due to a single lattice-gas interaction. To determine the total scattering rate due to a gas field, equation (2.8) must be multiplied by the number of gas molecules per unit area $N_G A$, then scaled by the accommodation coefficient α. The accommodation coefficient is the ratio of diffusely scattered gas particles. Specular reflection is defined as $(1 - \alpha)$. As mentioned earlier, the nanosurface-gas interaction is described on two levels. At the macroscopic level, the accommodation coefficient represents diffuse interactions and implicitly conveys surface roughness, defects, etc. At the atomic level, the autocovariance function describes the actual perturbation due to the lattice-gas collision. Incorporating $N_G A\alpha$ into equation (2.8) results in the total transition rate of a surface-gas field:

$$W(\mathbf{p}_{//},\mathbf{p}'_{//}) = \frac{8\pi^4\Delta^2 L^2 N_G\alpha}{\hbar A}\cdot\frac{1}{\left[1+(L^2\beta^2/2\right]}\cdot\left|\int_0^\infty\left[V_G(z)\right]dr\right|^2 \delta(\Delta E)\,. \tag{2.9}$$

The transition rate equation (2.9) is now evaluated in the relaxation time expression:

$$\frac{1}{\tau(\mathbf{p}_{//})} = \int W(\mathbf{p}_{//}, \mathbf{p}'_{//})(1-\cos\theta)d\theta\,. \tag{2.10}$$

Integration of equation (2.10) results in the final relaxation time expression for the nanosurface-gas field interaction:

$$\tau_{GI}(p_{//}) = \frac{\hbar^3}{2\pi^2\Delta^2 L^2 N_G \alpha}\left\{\int_0^\infty [V_G(z)]dr\right\}^{-2}\left[\frac{2}{\gamma} - \frac{1}{\gamma^2}\ln(2\gamma+1)\right]^{-1}(E_f - E_i)^{1/2}, \tag{2.11}$$

where $$\gamma = \left[L^2\left(\frac{p}{\hbar}\right)^2\right]. \tag{2.12}$$

The gas particle momentum is p and the initial and final gas particle energy is E_i and E_f respectively.

2.4 Numerical Analysis and Data Correlation of Phonon Scattering by a Gas Particle Field

2.4.1 Phonon Scattering Rates with Varying Gas Velocity and Accommodation Coefficient

The parametric numerical investigation of the nanosurface-gas scattering rate behavior was motivated by three primary parameters: accommodation coefficient, gas flow velocity and gas particle mass. Additionally, a nanostructure geometry that matched experimental studies was desired in order to allow correlation of theoretical predictions to actual experimental data. A SiO_2 thin film was selected as the numerical model because it allowed a comparative analysis to thermal conductivity results reported by Yamane et al.[63] The dimensions of the thin film modeled are 30 nm x 30 nm with a thickness of 20 nm. The surrounding gas was chosen to be N_2 at 1 atmosphere pressure and 298 K. A parametric study of gas pressure influence on scattering rates was performed but is not reported in this paper. The number of incident gas particles N_G that collide with the nanosurface for both stationary and moving flow fields was determined by standard rarefied gas dynamic equations.[64] It should be noted that the continuum approach for nanosurface-gas interactions must be abandoned and replaced with a discrete particle approach due to gas mean free paths (MFP) exceeding the thin film characteristic dimensions. The collisional energy transfer (E_f–E_i) is obtained from the Baule formula.[34] The rms amplitude of the lattice ion fluctuations Δ, was determined from a solution in Neumann series form derived by Chambers and Kinzer.[65] The average distance between nanosurface-gas interaction sites L, was assumed to be equal to the gas particle average separation distance defined in standard kinetic theory. The interaction potential energy V_G, was described by a pair-wise summation of Lennard-Jones (L-J) form[66] with a smooth cutoff at 1.0 Å.[67] The thin film was run in all parametric cases with incident gas flow perpendicular to the nanosurface or

equivalently, an angle of attack of 90 degrees. Furthermore, nanosurface-gas interactions were assumed to occur on one side of the thin film only. Table 2.1 summarizes the primary parameters used in this work.

Table 2.1 Numerical data used for the N_2/SiO_2 combination

Δ (Å) (Mach 0)	***L* (nm)**	N_G **(Mach 0)**	N_G **(Mach 0.9)**	**Accom Coef α**	**L-J Constant σ (Å)**	**L-J Constant ε (J)**
0.0683	3.44	1.17E12	3.35E12	0.75	3.681	1.2627E-21

Figure 2.2 shows the relaxation times predicted by equation (2.11) as a function of accommodation coefficient and Mach number, which were varied from 0.1-1.0 and 0-0.9 respectively. Interestingly, the relaxation time shows a greater dependence on the

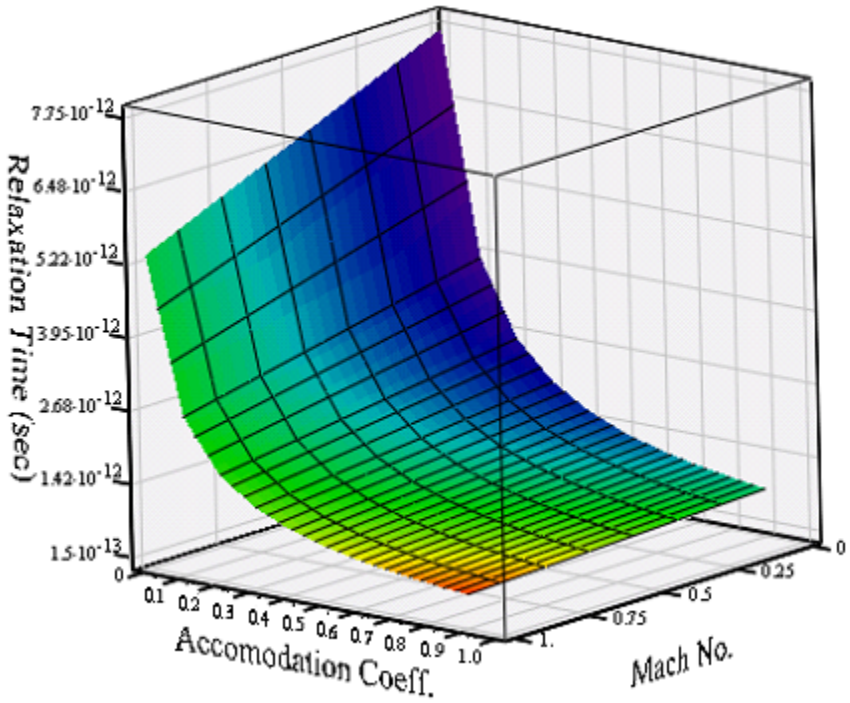

Figure 2.2: Relaxation time behavior as a function of accommodation coefficient and flow velocity for the N_2/SiO_2 combination. Phonon lifetimes are highly dependent on the accommodation coefficient and show weaker dependence on the flow velocity.

accommodation coefficient over the flow velocity for Mach numbers 0-0.9. This phenomenon occurs because N_G is directly factored by the accommodation coefficient. In effect, the accommodation coefficient numerically represents the coupling mechanism between the gas field and nanosurface and gives the magnitude of interfacial diffuse collisions. The weak dependence on flow velocity is attributed to minimal rms lattice amplitude increases of only 0.00536 Å when flow transitions from 0 to Mach 0.9. Additionally, lattice ion relaxation after impact is found to take approximately 20 picoseconds (ps), which is over 15 times longer than the interaction time of about 1.3 ps. A maximum carrier lifetime of 7.6 ps occurs at stationary flow and 0.1 accommodation while the shortest lifetime of 0.69 ps is noted to occur at Mach 0.9 and full

accommodation. For stationary flow, an accommodation coefficient of 0.8 is required to reduce carrier lifetimes below 1.0 ps (0.961 ps).

2.4.2 Phonon Relaxation Rates with Varying Gas Particle Mass

Figure 2.3 conveys the relaxation times as a function of flow speed predicted by equation (2.11) during impingement of inert gas particles of various masses. To institute consistent

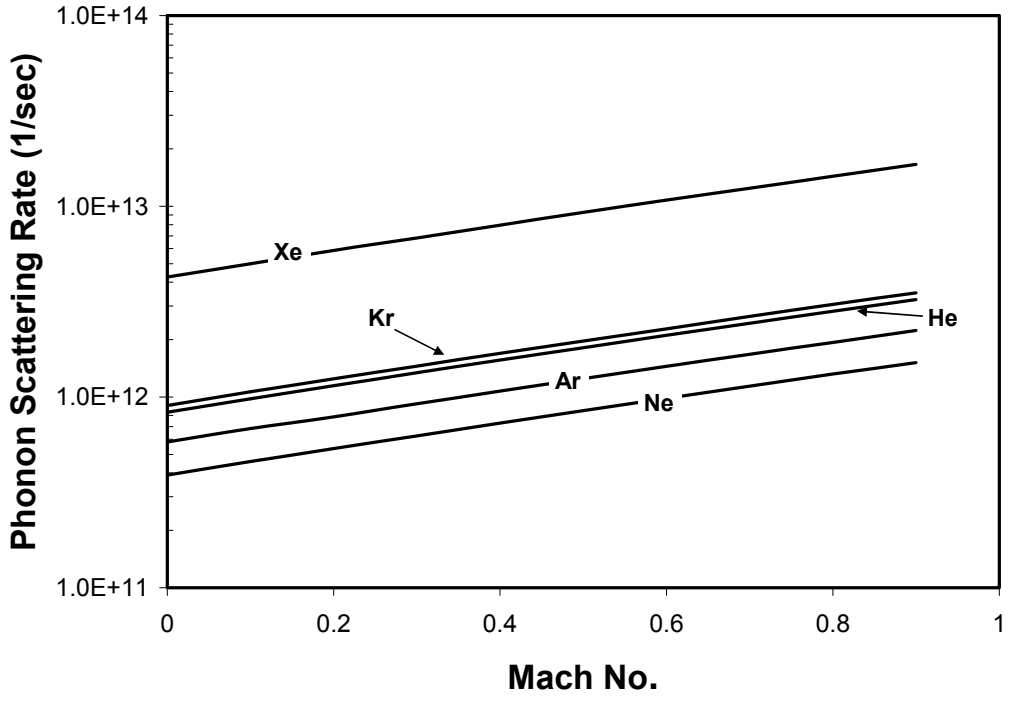

Figure 2.3: Log plot of phonon relaxation rates due to inert gas interactions with varying mass. The flow velocity was varied from Mach 0 (stationary flow) to Mach 0.9 with a constant accommodation coefficient of 0.75. Shorter phonon lifetimes of He over Ar and Ne were found to be induced by a higher collision density particular to the nanostructure/rarefied gas flow regime.

analysis ground rules, the analysis parameters were left unchanged except for those properties associated with each particular gas.[66] For example, the actual accommodation coefficient for He is likely to be different than for Kr.[68] Under stationary flow, the shortest phonon lifetimes of 0.23 ps and 1.1 ps are generated by Xe and Kr respectively due to the atomic mass inducing larger lattice rms amplitudes as shown in Table 2.2. Interestingly, He scattering rates follow closely behind Kr values. Investigation into this phenomena is found to be caused by the large collision density (Table 2.2) of He compared to Ne and Ar, which are heavier elements. Basically, the increased number of dynamic gas particle impingement sites by He is analogous to the behavior of lattice impurities; an increased concentration means shorter carrier lifetimes. Previous numerical work on gas particle energy exchange with surfaces[69-70] found similar gas mass-lattice amplitude responses however neither considered the collision density variations associated with different gas species. Furthermore, it is important to note that the collision density effects on lattice-gas scattering is specific to nanostructures due to the rarefied gas regime and should be considered for each particular nanosurface-gas interface. The dependence on flow velocity is again found to be rather weak with similar trends in the lattice fluctuation amplitude as noted with N_2. Moreover, the efficient scattering capabilities of He may help explain the success of its use in experimental surface science work.

Table 2.2: Gas collision rates and RMS lattice amplitudes for the SiO_2 thin film analysis

	He	Ne	Ar	Kr	Xe	He
Gas Collision Rate at Mach 0 (sec^{-1})	3.09E12	1.38E12	9.79E11	6.76E11	1.8E11	3.09E12
Δ (Å)	0.031	0.039	0.057	0.081	0.54	0.031

2.4.3 Lattice-Gas Scattering Comparison to Adsorbed Gas Particle Scattering

The results of this work suggest the total phonon scattering rate at a nanosurface-gas interface to be comprised of two components: adsorbed gas particles and lattice-gas particle collisions. In order to obtain numerical predictions of the magnitude of the lattice-gas component, equation (2.11) was computed as a ratio with Rayleigh waves which are scattered with adsorbed gas particles:[71]

$$\frac{1}{\tau_{GA}} = \frac{c(\delta m)^2}{8\rho^2 B^2 v^4}\omega^5\left[A_1(kz) + A_2(kz) + A_2(kz)\right], \tag{2.13}$$

where δm is the difference in adsorbed gas mass, c is the concentration of defects per unit surface area, ρ is the solid density, v is the Rayleigh wave velocity, k is the wave vector, z is the adsorbed particle depth as detailed in Figure 2.1b and ω is the wave frequency. A_1, A_2 and A_3 are dimensionless parameters that describe scattering into Rayleigh waves, longitudinal body waves and transverse body waves respectively. These coefficients are highly dependent on the

adsorbed particle depth and define the proportional scattering into surface and body waves. The parameter B is a function of the material Poisson ratio. Numerical values of $B = 3.1$, $A_1 = 5$, $A_2 = 0.625$ and $A_3 = 0.625$ were used to simulate an adsorbed N_2 molecule at a depth of 0.5 Å below the surface. Stationary flow conditions for the thin film N_2/SiO_2 model were obtained and the resulting relaxation time ratio was plotted as a function of adsorbed gas particle defect concentration. The results shown in Figure 2.4 indicate that with an adsorbate concentration percentage of 10%, the lattice-gas scattering term is 2.25 times larger than the adsorbate value. The scattering rates of the two components become equivalent at 23% adsorbate concentration and at 90% adsorbate concentration, the lattice gas scattering component represented approximately 24% of the total scattering rate. The adsorbate concentration is a material

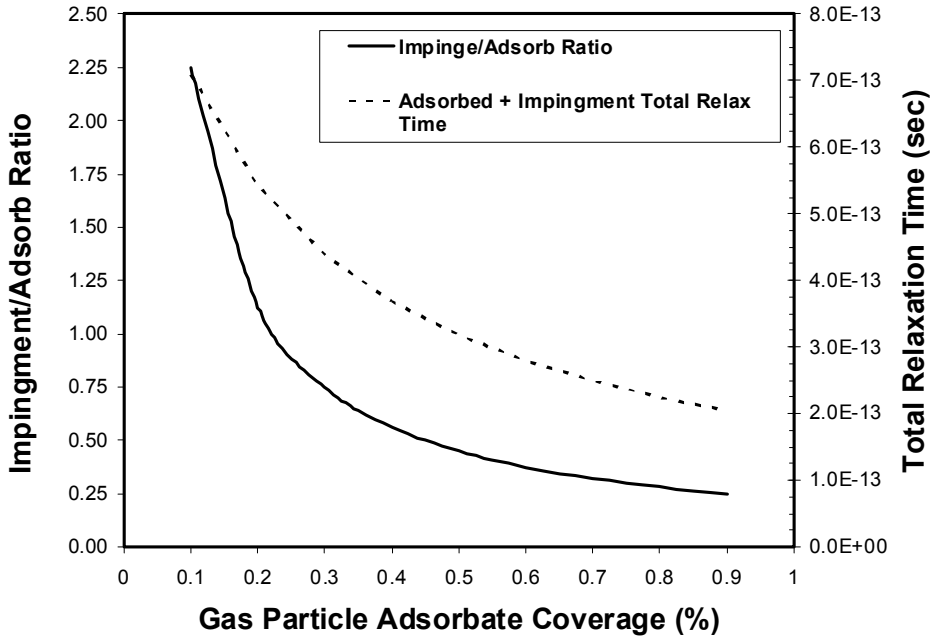

Figure 2.4: Computed phonon relaxation rate ratio due to impinging N_2 gas particles at Mach 0 to adsorbed gas particles $\left(\tau_{GI}^{-1} / \tau_{GA}^{-1}\right)$ plotted against the adsorbate coverage percentage. The combined total phonon lifetimes of both lattice-gas and adsorbed particles is also shown as a function of adsorbate coverage.

dependent transient process and takes varying amounts of time to reach steady state conditions.[34] To gain some understanding of the total scattering rate transient behavior as adsorbate concentrations increase or decrease, the phonon lifetimes were also plotted in Figure 2.4. Although the carrier lifetimes are found to decrease as the adsorbate concentration rises, the drop is not substantial. Furthermore, the total carrier scattering rate displays trends similar to transport property measurements[72] and implies that initial transport property responses to gases are dominated by lattice-gas interactions while final transport values that take some period of time to stabilize may be controlled by the underlying adsorbate approach to steady state conditions.

2.4.4 Lattice-Gas Scattering Effects on Thermal Conductivity

The scattering events of the nanosurface-gas show their effects through transport coefficient deviations that may be a function of gas species, flow velocity, accommodation coefficient, etc. To investigate the nanosurface-gas effects on transport coefficients and due to the dielectric nature of SiO_2, thermal conductivity was chosen as the transport parameter. Yamane et al.[63] reported thermal conductivity measurements for a 20 nm thick sputtered SiO_2 thin film. In order to anchor the numerical calculation, a Debye model[73] was used and the calculated thermal conductivity was correlated to the results of Reference 63 by introducing boundary scattering only. Nanosurface-gas scattering was then added to simulate the introduction of an N_2 environment. Again, all previous numerical parameters were left unchanged (see Table 2.1). An adsorbate concentration of 50% was used and assumed to be at

steady state conditions. The resulting change in thermal conductivity shown in Figure 2.5 is found to decrease as expected due to increased scattering at the nanosurface. Upon introduction

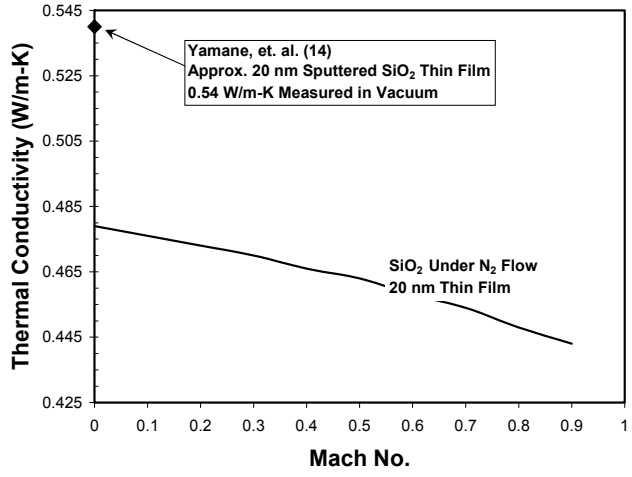

a)

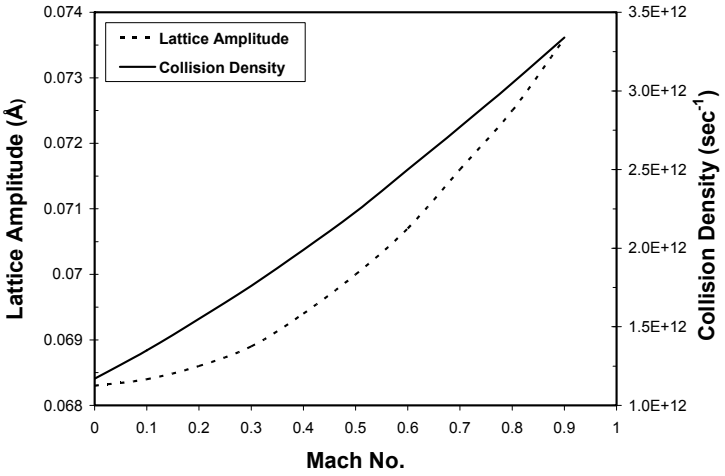

b)

Figure 2.5: a) The SiO_2 thin film model thermal conductivity is correlated to experimental data (solid diamond) then submitted to a N_2 environment (solid line) to characterize the effects on thermal conductivity. The flow velocity is increased to Mach 0.9 to obtain predicted trends to the thermal conductivity behavior. Thermal conductivity is predicted to decrease by 12% when the stationary flow N_2 atmosphere is introduced. **b)** The corresponding SiO_2 thin film lattice rms amplitude and collision density increases with N_2 flow velocity. The predicted decrease in thermal conductivity is a strong function of collision density with a weaker dependence on the lattice amplitude increase.

of the N_2 environment, a decrease of 12% is predicted with thermal conductivity dropping from 0.54 W/m-K in vacuum (matching Reference 63 results) to 0.478 W/m-K. As the flow velocity increases, phonon lifetimes are shortened due to an increased gas collision density and larger rms lattice amplitudes resulting in a predicted value of 0.443 W/m-K at Mach 0.9. The decrease in thermal conductivity is found to be approximately linear as Mach numbers increase.

2.5 The Electron Scattering Rate of a Solid Due to Gas Particle Interactions

The aim of this section is to present the electron scattering probability due to gas particle scattering. This objective seeks to complete the theoretical solid surface scattering assessment that constitutes this chapter. As reviewed in Section 2.2, HAS experimental results showed spectra that indicated the electronic perturbations to be important.[35-36] Therefore, some reports appeared in the literature which proposed energy excitations of the electron ensemble due to gas particle collisions.[74-75] Typically, the incoming gas particle is treated as a classical particle which assumes that the atom or molecule moves along a classical trajectory and simply acts as an external perturbation on the substrate electrons. The most relevant work performed by Gunnarsson and Schoonhammer[76] assembled a quantum mechanical treatment and compared the results to the classical calculation. Their work argued that for small rare-gas energy and momentum transfers a classical treatment is sufficient except for very low initial gas velocities. Later computational work by Billing also showed appreciable energy transfer to a Cu surface by Hydrogen molecules.[34] It should be noted that the theoretical work discussed so far addresses pure scattering only (not chemical or physical adsorption phenomena) which is in direct relation

to the research at hand. The quantum mechanical probability ${}_{QM}P_k^{k'}$ of exciting an electron from wave vector state k to k' is given as:[76]

$$ {}_{QM}P_k^{k'} = c^2 \frac{k^f}{k^i} \left\{ \frac{\hbar \alpha v^i}{\left(\hbar^2\alpha^2/2M\right)^2 + \hbar^2\alpha^2 \frac{1}{2}\left(v^{i^2} + v^{f^2}\right) + \left[\varepsilon - \hbar\mathbf{k}\cdot\frac{1}{2}\left(\mathbf{v}^i + \mathbf{v}^f\right)^2\right]} \right\}^2, \tag{2.14} $$

where

$$ c = \frac{2t_0 k k' e^{-\alpha Z_0}}{\Delta\phi}, \tag{2.15} $$

$$ \alpha = k + k', \tag{2.16} $$

And the gas initial and final velocity v^i and v^f are the perpendicular velocity components. The gas particle turning point is Z_0, the gas particle mass is M, the quantum scattering t matrix for a plane wave with wave vector $k = 0$ is t_0, the gas particle energy is ε and ϕ is the electronic plane wave eigenfunction. The classical scattering probability ${}_{CL}P_k^{k'}$ of exciting an electron from wave vector state k to k' is given as:[76]

$$ {}_{CL}P_k^{k'} = c^2 \left[\frac{\hbar \alpha v^i}{\left(\hbar \alpha v^i\right)^2 + \left(\varepsilon - \hbar \mathbf{k} \cdot \mathbf{v}^f\right)} \right]^2 . \tag{2.17} $$

An interesting theoretical result regarding the quantum mechanical scattering probability equation (2.14) is the gas particle wave function behavior as it nears the solid surface.[76] Basically, the gas particle final-state wave function penetrates deeper into the solid surface if the perpendicular gas particle energy $\hbar^2 k^2 / 2M$ is increased. Therefore, this prediction says that the perturbing interaction with the electronic states becomes stronger. In light of the current research reported in this work, some preview of the experimental results detailed in Chapter 5 is highly relevant. Specifically, this investigation has confirmed the predictions of equation (2.14) by verifying increased scattering and transport perturbations to the electron ensemble with gas particle energy increases. The detailed experimental results can be found in Chapter 5.

The electron scattering probability expressions of equations (2.14) and (2.17) can be used within the Boltzmann transport equation (BTE) to calculate transport coefficients. A variational expression of the BTE specific to transport properties was derived by Ziman.[77] The traditional solution method has always been through the use of a trial function to minimize the functional however this research has developed and derived a finite element formulation using the penalty function solution method. One of the main advantages of the finite element formulation is the ability to discretize a nanostructure with elements that encompass only a few material crystals. The nodal solution matrix then returns transport coefficients at each nodal point thus allowing the prediction of discrete solutions at different locations of a material. Considering the current

research effort and using electrical resistivity as an example, the resulting solution would show resistivity differences at a material surface where gas particles perturb the electron cloud. In the internal nanostructure volume however, relaxation of the higher surface resistivity should result as would be evidenced by an appropriately sized finite element mesh. See Appendix B for the complete derivation of this powerful transport property finite element solution method as well as a sample solution.

Chapter 3

Transport Property Measurement Through Electronic Thermal Noise: Theoretical Formalism of Dynamic Electron Scattering

3.1 Introduction to Thermal Noise and Transport Property Measurements Through Electronic Fluctuation Spectra

The aim of this chapter is to present the theoretical formalism required to obtain electronic transport properties through the measurement of Johnson/Nyquist or equivalently, thermal noise. More precisely, the intention is to demonstrate the development of an experimental spectroscopic technique that utilizes ever-present voltage fluctuations in a conductor or semiconductor to obtain autocorrelation functions. Previous research in this area has been limited to numerical work[78-85] with no reported experimental investigations comparable to the work documented in this report. Emphasis must be placed on the fact that the experimental method developed in this chapter utilizes *equilibrium* thermal noise only. Other electronic noise phenomenon such as 1/f or shot noise is not part of this research effort. This means that there are no thermal or potential gradients placed upon the experimental sample material at any time. Moreover, the assumption of statistically stationary fluctuation spectra, characterized by ergodic properties and displaying a white spectrum with a Gaussian probability density[86] is prevalent to all work in this research. Through the rigorous Green-Kubo theory, which shows that phenomenological transport coefficients can be expressed quite generally as

integrals over the autocorrelation function (ACF),[46-47] multiple transport properties of the electron ensemble can be measured in a single experiment. The experimental implementation of the Green-Kubo formalism explains the reasoning behind the lack of any electrical or thermal gradients applied to the subject material which clarifies the exclusive use of Johnson/Nyquist noise. This is noted to be especially advantageous to materials that may be difficult to obtain measurements on, such as nanostructures. During the course of this research, a better reference to this newly developed spectroscopic technique was desired in lieu of the term "the experiment." Hence, the term *Dynamic Electron Scattering* or DES was adopted due to experimental similarities with dynamic light scattering as well as the realistic accuracy of the term.

The DES theoretical formalism with foundations in Johnson/Nyquist noise power spectral densities is formulated in Section 3.2.1. The autocorrelation function measurements obtained from DES spectra is then coupled to Green-Kubo linear response transport theory in Section 3.2.2. Additional electronic transport property results are derived in Section 3.2.3. Finally, the experimental application of all relevant theoretical foundational formalism is condensed into a summary format in Section 3.3.

3.2 Electronic Transport Property Measurements: DES Theoretical Formalism

3.2.1 Thermal Noise of Conductors and Semiconductors

Beginning with Johnson and Nyquist's original discovery and explanation of electronic noise, the literature base abounds with derivations of stationary white noise phenomenon.[86-93] Therefore, the intent of this section is not to rigorously re-derive existing results. Instead, the

objective of this section is two fold: 1) to qualitatively explain the phenomena from a spectroscopic viewpoint to support the theoretical formalism and 2) to derive existing and *new* theoretical results that are especially relevant to the experimental measurement of electronic transport properties. It should also be noted that although this work has focused on metals, the theoretical and experimental formalism is applicable to any conductor or semiconductor whether solid or liquid. Subsequently, the remainder of this work shall reference conductors however the ideas associated with this term implicitly applies to any material that contains free electrons or holes in a medium that exhibits non-zero resistance at temperatures above 0 K.

Consider a conductor above temperature 0 K with free electrons under thermal motion that exhibits some value of electrical resistance. Fundamentally, contributions to a materials resistivity stem from the electron scattering differential cross section with respect to phonons, lattice imperfections, impurities and other forms of scattering mechanisms.[34] These scattering events, manifested through the imperfect lattice domain, perturb the electron cloud in a manner that can be described by contemporary scattering theory. Subsequently, the electron cloud, though uniform on average, undergoes fluctuations in density due to scattering events thus inducing internal micro-currents, which propagate in a manner similar to Brownian motion thereby creating elementary voltage impulses. An ensemble average of these voltage pulses embodies a considerable amount of underlying physics describing the dynamic evolution of this statistically stationary yet fluctuating landscape. Furthermore, it is possible to speak about a spectrum of these voltage pulses which is the distribution of the power with frequency. This power distribution is known as the power spectral density (PSD) and is typically defined in a frequency band Δf with center frequency f_0.[90] With respect to this work, there are three spectral densities obtained from the voltage fluctuation measurements. These include the *voltage* PSD,

the *thermal* PSD and the *thermoelectric* cross spectral density (CSD). The voltage PSD will be introduced first and carries units of $V^2\ Hz^{-1}$. Specifically, the experimentally measured mean square noise voltage $\overline{V^2}$ and voltage PSD $S_V(f_0)$ correspond to the first set of spectra expressed as:[45]

$$\overline{V^2} = 4k_B TR\Delta f\ , \tag{3.1}$$

$$S_V\left(f_0\right) = \frac{\overline{V^2}}{\Delta f} = 4k_B TR\ , \tag{3.2}$$

where R represents the electrical resistance, T is the temperature, k_B is Boltzmann's constant and the square root of equation (3.1) is the traditional expression of Johnson/Nyquist noise.[43-44] In order to experimentally measure a samples voltage fluctuations however, a low noise amplifier is required in addition to a band pass filter that determines the frequency band of measurement Δf.[45] Furthermore, there is the resistance and capacitance of the interconnecting coaxial cables. Clearly, the addition of an amplifier and other electronic components to the measurement circuit adds an additional impedance and gain that must be accounted for in addition to the sample resistance R. Therefore, modification of equation (3.1) is required:[94]

$$\overline{V^2} = 4k_B TR\int_0^\infty \left|G(f)\right|^2 df\ , \tag{3.3}$$

where $|G(f)|$ is the magnitude of the voltage gain. The additional impedance of the experimental measurement circuitry is accommodated by the modifier *M* resulting in:

$$\overline{V^2} = 4k_B TR \frac{\int_0^\infty |G(f)|^2 \, df}{M}, \tag{3.4}$$

where

$$M = \left(1 + \frac{R}{R_i}\right)^2 + \left(\omega C_i R\right)^2, \tag{3.5}$$

where the additional impedance capacitance is C_i, additional impedance resistance is R_i, and $\omega = 2\pi f$. Notational simplification of the additional impedance and gain expression is attained by introducing $Z(f_0)$:

$$Z(f_0) = \frac{\int_0^\infty |G(f)|^2 \, df}{M}. \tag{3.6}$$

Resulting in the experimental measurement of voltage fluctuations as:

$$\overline{V^2} = 4k_B TR\Delta f Z\left(f_0\right), \tag{3.7}$$

or

$$\frac{\overline{V^2}}{Z\left(f_0\right)} = 4k_B TR\Delta f. \tag{3.8}$$

The determination of $Z(f_0)\Delta f$ is performed during the experimental calibration procedure with a representative example for this research given in Chapter 4, Section 4.3.2.

The autocorrelation function is an important spectroscopic function with respect to the statistically stationary yet fluctuating voltage pulses. Fluctuation spectra of a conductor's physical quantities (such as voltage or current) are characterized by an ACF that provides a direct theoretical link to linear transport theory *and* quantum decoherence. With respect to the spectroscopic methodology developed in this work through DES, the ACF shall be shown to exhibit powerful experimental versatility when used to analyze electronic thermal noise. Basically, the ACF measures how long a given fluctuation persists at time zero and later.[86,95] Let $V(t)$ be a random voltage fluctuation. Further let two instants in time be t and $t + \Delta t$ where Δt is a small increment in time. The autocorrelation function $\Gamma(t)$ is defined as the average with time of the product of the random values $V(t)$ and $V(t + \Delta t)$:[89]

$$\Gamma(t) = \langle V(t) + V(t + \Delta t) \rangle, \tag{3.9}$$

where the angle brackets indicate a time averaging operation. The PSD and the ACF are related by a Fourier transformation pair. This is the Weiner-Khintchine theorem[89] which has direct application to the experimental measurement of thermal noise. Bearing in mind that the ACF and $\cos(2\pi ft)$ are even symmetric functions in time, the PSD is determined from the ACF through the Fourier cosine transform:[89]

$$S_V(f_0) = 4\int_0^\infty \langle \Gamma_V(t) \cdot \Gamma_V(t+\tau) \rangle \cos(2\pi ft)\, df \,, \tag{3.10}$$

where the notation of equation (3.10) is understood to be $\langle \Gamma_V(t) \cdot \Gamma_V(t+\Delta t) \rangle = \langle V(t) \cdot V(t+\Delta t) \rangle$. Furthermore, it should be clear that equation (3.10) is a general result despite the subscript *V* that specifies the voltage PSD and ACF. By the Weiner-Khintchine theorem, the ACF in turn is the inverse Fourier transformation of the PSD:[89]

$$\langle \Gamma_V(t) \cdot \Gamma_V(t+\Delta t \rangle = \frac{1}{2\pi}\int_0^\infty S_V(f_0) \cos(2\pi ft)\, df \,. \tag{3.11}$$

By evaluating the above equations at $t = 0$, an important relation is obtained between the variance σ^2, mean square voltage or energy, spectral density and ACF. Both voltage and thermal relations are shown in equations (3.12) and (3.13):

Voltage spectra:
$$\sigma_V^2 = \overline{V^2} = \int_0^\infty S_V(f_0) df = \Gamma_V^2(0) \,. \tag{3.12}$$

Energy Spectra:
$$\sigma_Q^2 = \overline{J^2} = \int_0^\infty S_Q(f_0) df = \Gamma_Q^2(0) \,, \tag{3.13}$$

where J is Joules and the energetic fluctuations σ_Q equivalence to the thermal spectral density $S_Q(f_0)$ will be shown to exhibit an important relation to the Green-Kubo linear transport theory. From an experimental data analysis standpoint, equations (3.12) and (3.13) are extremely useful because they allow an immediate comparison of the ACF value at time zero and the mean square voltage or energy.

Pause is taken at this point to discuss the experimental data acquisition of voltage fluctuations and subsequent numerical analysis. As one can see from equation (3.2), the measurement of a series of voltage fluctuations squared, followed by taking the mean value results in the equivalent measurement of the PSD. In fact, the use of a band pass filter which determines the frequency measurement band Δf ensures the measurement of the spectral distribution.[96] See Appendix C for a detailed proof of this experimental fact. Therefore, when measuring a series of voltage fluctuations, the *inverse Fourier transform* must be applied to the experimental data set to obtain the autocorrelation function as shown mathematically by equation (3.11).

The second PSD and ACF held within the voltage fluctuation spectra are the *thermal* components which are defined as:

$$S_Q\left(f_0\right) = \frac{\overline{V^2}}{4R\Delta f} = k_B T\,, \tag{3.14}$$

$$\left\langle \Gamma_Q(t)\Gamma_Q(t+\Delta t\right\rangle = \frac{1}{2\pi}\int_0^\infty S_Q\left(f_0\right)\cos(2\pi ft)df\,. \tag{3.15}$$

The power spectral densities $S_V(f_0)$ and $S_Q(f_0)$ stem from the same electronic noise source yet embody two distinct sets of spectra within the noise landscape. The spectral content of $S_V(f_0)$ and $S_Q(f_0)$ contain subtle yet discrete differences that are relevant to the development of DES spectroscopic analysis. Fundamentally, $S_V(f_0)$ carries electron charge deviations from the average value while $S_Q(f_0)$ carries thermodynamic energy deviations from the average value ($S_Q(f_0)$ carries units of W/Hz). The recognition of the thermal PSD supports the spectroscopic methodology developed in this work and represents a major result of this research which shall become evident when utilized within the Green-Kubo theory. Considering electron energy fluctuations or equivalently, the statistical standard deviation, the relationship to the thermal PSD (see equation (3.13)) is developed in the following theorem:

Theorem 1. *The thermal PSD* $S_Q(f_0)$ *is exactly equal to the electron canonical ensemble root-mean-square energy fluctuations,* $\sigma_H \equiv S_Q(f_0)$.

Proof: In a canonical ensemble, the energy fluctuations are expressed by the root-mean-square deviation of the Hamiltonian from its average value $\langle H \rangle$:[97]

$$\sigma_H = \sqrt{\langle H^2 \rangle - \langle H \rangle^2}, \tag{3.16}$$

where H is the energy or Hamiltonian and σ_H is the root-mean-square deviation . The energy fluctuations have a unique thermodynamic relationship which can be expressed in terms of Boltzmann's constant, temperature and heat capacity C_V:[97]

$$\sigma_H = \sqrt{k_B T^2 C_V} \,. \tag{3.17}$$

Subsequently, the thermal energy fluctuations carry units of watts per Hz:

$$\sigma_H = \sqrt{k_B T^2 C_V} = J = W \cdot s = \frac{W}{Hz} = [E][t], \tag{3.18}$$

Where W is watts, J is Joules, s is seconds and the dimensional analysis[98] notation of energy $[E]$ and time $[t]$ are used for the last term on the right of equation (3.18). Similar dimensional expansion[98] shall now be applied to the thermal power spectral density introduced in equation (3.14):

$$S_Q(f_0) = k_B T = \frac{\overline{V^2}}{4R\Delta f} = J = W \cdot s = \frac{W}{Hz} = [E][t], \tag{3.19}$$

Clearly, the electron thermal spectral density of equation (3.19) is the exact dimensional equivalent of the thermal energy fluctuations expressed by equation (3.18). Transitioning back from the dimensional based expansions to symbolic format allows the explicit equivalence of the thermal power spectral density to the root-mean-square thermal energy fluctuations to be elucidated:

$$\sqrt{\left\langle H^2 \right\rangle - \left\langle H \right\rangle^2} = \sigma_H = \sigma_Q = \sqrt{k_B T^2 C_V} = S_Q(f_0) = \frac{\overline{V^2}}{4R\Delta f}. \tag{3.20}$$

The full spectroscopic utility of equation (3.19) shall be fully realized upon derivation of the thermal conductivity coefficient via Green-Kubo formalism in Section 3.2.2. This completes the proof of Theorem 1. An alternative proof of Theorem 1 is given in Appendix D.

The third and final spectral density held within voltage fluctuation spectra is the thermoelectric CSD $S_{VQ}(f_0)$. The thermoelectric CSD is a cross-spectral density related to the quantities $\Gamma_V(t)$ and $\Gamma_Q(t)$[47] and carries units of *VJ*/Hz:

$$S_{VQ}(f_0) = 4\int_0^\infty \left\langle \Gamma_V(t) \cdot \Gamma_Q(t+\Delta t) \right\rangle \cos(2\pi f t) df\,, \tag{3.22}$$

where $\Gamma_V(t)$ and $\Gamma_Q(t)$ are obtained from the experimental voltage data set. The noise spectra can be represented by the PSD matrix:

$$\begin{bmatrix} S_{VV}(f_0) & S_{VQ}(f_0) \\ S_{QV}(f_0) & S_{QQ}(f_0) \end{bmatrix}, \tag{3.23}$$

where the off diagonal terms are each other's complex conjugate. Equation (3.23) shall be developed further in the next section within Green-Kubo theory. Applying the inverse Fourier transform to $S_{VQ}(f_0)$ will of course yield the ACF however there is a more direct method available to analyze DES data. By numerically calculating the voltage and thermal ACF's first, the thermoelectric ACF may be obtained by the product of the complex conjugate of $\Gamma_V(t)$ and $\Gamma_Q(t)$:

$$\left\langle \Gamma_V(t) \cdot \Gamma_Q(t+\Delta t) \right\rangle = \left\langle \Gamma_V^*(t) \cdot \Gamma_Q(t+\Delta t) \right\rangle, \tag{3.24}$$

where the asterisk denotes the complex conjugate.

3.2.2 Electronic Transport Property Measurement Through Green-Kubo Linear Response Transport Theory

The fluctuation-dissipation theorem states that the systematic part of microscopic forces is actually determined by the correlation of the random system forces. Thus, the fluctuation-dissipation theorem states a general relationship between the response of a system to an external perturbation and the internal fluctuation of the system in the absence of the perturbation. Such a response is characterized by a response function or equivalently an *admittance* or *impedance*.[99] The system's internal fluctuation is characterized by a correlation function of relevant physical quantities (voltage with respect to this work) fluctuating in thermal equilibrium. Therefore, fluctuation-dissipation theorem can be applied in two ways. The first application would be to predict fluctuation characteristics of a system from known admittances or impedances while the second application would be to calculate the admittance from the experimental measurement of fluctuation spectra. This research shall apply the second application to experimental data consisting of electronic voltage fluctuations thus resulting in rigorous measurements of transport properties. Green and Kubo made great progress in the area of irreversible thermodynamics and the extension of the fluctuation-dissipation theory to linear response transport theory.[46-48,100-101] In tandem with the previous section, the intent is not to re-derive existing theory that can be readily obtained in the literature. Instead, the theoretical formalism shall focus on details relevant to the DES spectroscopic method developed in this work as well as laying the foundation for theoretical interconnections to quantum decoherence elucidated in Chapter 7.

Consider a system of particles with momenta p and spatial coordinates q of the entire particle set. If the system is perturbed by a small external force $F(t)$, then the Hamiltonian of the system is a function of $F(t)$:[101]

$$\hat{H}(t) = -\hat{A}F(t)\,, \tag{3.25}$$

where

$$\hat{A} = \frac{\partial}{\partial F}\hat{H}(p,q;F) \tag{3.26}$$

is the corresponding displacement and the hat indicates a quantum mechanical operator or classical dynamical value. In general, the force $F(t)$ can be a vector or there can be multiple forces. For example, $F(t)$ could be an electric field. The system response to this perturbation is observed by $\Delta B(t)$ of a physical quantity B. Initially, the system state is specified by the quantum density matrix ρ which satisfies $\left[\hat{H},\rho\right] = 0$. Subsequently, the response $\Delta B(t)$ of the physical quantity B is:

$$\Delta B(t) = \mathrm{Tr}\Delta\rho(t)B\,, \tag{3.27}$$

where

$$\dot{B}(t) = \frac{1}{i\hbar}\left[B(t),\hat{H}\right], \quad B(0) = B\,, \tag{3.28}$$

and Tr denotes the quantum density matrix trace operation, $\hbar$ is Planck's constant divided by 2π and $B(t)$ is the Heisenberg representation of B. The corresponding response to this perturbation is expressed by the response function $\phi_{BA}(t)$:

$$\phi_{BA}(t) = -\frac{1}{i\hbar}\mathrm{Tr}\left[\hat{A},\rho\right]B(t)\,. \tag{3.29}$$

Theoretically, equation (3.29) leads to Kubo's admittance χ_{BA}:[101]

$$\chi_{BA}(\omega) = \lim_{\varepsilon\to 0+}\int_0^\infty \phi_{BA}e^{-i\omega t-\varepsilon t}dt\,, \tag{3.30}$$

then

$$\chi_{BA}(\omega) = \lim_{\varepsilon\to 0+}\int_0^\infty e^{-i\omega t-\varepsilon t}dt\ \frac{1}{i\hbar}\mathrm{Tr}\left[\rho,A\right]B(t) \tag{3.31}$$

Progressing directly to the response function expression gives:

$$\phi_{BA}(t) = \frac{-1}{k_BT}\left\langle \Delta\hat{A},\Delta\dot{\hat{B}}(t)\right\rangle = \frac{-1}{k_BT}\left\langle \Delta A(0)\ \Delta B(t)\right\rangle, \tag{3.32}$$

where the canonical correlation in the classical limit is equivalent to the canonical average of the product of the two quantities. In writing equation (3.32), advantage was taken of the fact that the correlation function for statistically stationary spectra does not depend on the origin of time. The last term in equation (3.32) relates the ensemble average to the time for ergodic systems, thus *connecting the experimental fluctuations to the ensemble statistics*. Furthermore, the theoretical development thus far is based on the existence of an external perturbation. This condition is not

required for the above formalism to remain rigorous. In the limit that $F(t)$ approaches zero ($F(t)$ is zero during DES measurements), the phase space trajectory ($q(t)$,$p(t)$) is unaffected by $F(t)$, and $A(t)$ and $B(t)$ are just phase functions of the system in equilibrium. With regards to electronic fluctuations, the phase functions may exhibit a zero average yet their correlations have a *non-zero* value. This is noted to be the case for Johnson/Nyquist noise. Next consider the case at hand where $\hat{B}$ is the voltage potential fluctuation $\hat{E}$ corresponding to the displacement $\hat{A}$. The fluctuation $\hat{E}$ can be expressed as:

$$\hat{E}(t) = \frac{d}{dt}\hat{A}(t) \equiv \left[\hat{A}(t), \hat{H}\right]\frac{1}{i\hbar}, \tag{3.33}$$

where the equilibrium potential fluctuation clearly vanishes $\left\langle \hat{E} \right\rangle = 0$. Using the so-called Kubo formula,[101] the response function of equation (3.32) now equates to:

$$\phi_{\mu\nu}(t) = \frac{1}{k_B T}\left\langle \hat{E}_\nu \cdot \hat{E}_\mu(t) \right\rangle, \tag{3.34}$$

where the subscripts indicate tensor notation in order to obtain a formally rigorous result. Furthermore, the emergence of the correlation function $\left\langle \hat{E}_\nu \cdot \hat{E}_\mu(t) \right\rangle$ is evident and directly

related to the ACF developed in the previous section. Subsequently, the resulting electrical resistivity is obtained which is useful at any frequency:

$$\rho_{\mu\nu}(\omega) = \frac{1}{k_B T}\int_0^\infty dt e^{i\omega t}\left\langle \hat{E}_\nu \cdot \hat{E}_\mu \right\rangle. \tag{3.35}$$

Equation (3.35) represents a result applicable to this research. Specifically, the experimental measurement of the voltage ACF is found to be exactly equal to equation (3.35) thus allowing the material resistivity to be obtained through integration of the temporally evolving DES voltage ACF:

$$\rho = \frac{1}{k_B T}\underbrace{\int_0^\infty \left\langle E(0)\cdot E(t)\right\rangle dt}_{\text{Green-Kubo Theory}} \equiv \frac{1}{k_B T}\overbrace{\int_0^\infty \left\langle \Gamma_V(0)\cdot \Gamma_V(t)\right\rangle dt}^{\text{Experimental Voltage ACF}}, \tag{3.36}$$

where the assumption of diagonal tensor components and the low frequency limit is applied. Furthermore, the electron velocity diffusion coefficient D_e is expressed as:

$$D_e = \underbrace{\int_0^\infty \left\langle E(0)\cdot E(t)\right\rangle dt}_{\text{Green-Kubo Theory}} \equiv \overbrace{\int_0^\infty \left\langle \Gamma_V(0)\cdot \Gamma_V(t)\right\rangle dt}^{\text{Experimental Voltage ACF}}. \tag{3.37}$$

At this point, the equivalency of the sample voltage fluctuations and electron velocity fluctuations should be clarified. This experimental work focuses upon a conservative electron ensemble characterized by a spatially uniform electron concentration. Therefore, fluctuations of voltage density (or current density) arise merely from the fluctuations of electron velocity.[82] Consequently, the coefficient D_e from equation (3.37) represents a velocity based diffusion coefficient. Equation (3.36) differs from the usual form, which typically expresses the electrical *conductivity* σ as the functional result instead of the resistivity.[97] However, the experimental data of this work is in the form of voltage fluctuations instead of current fluctuations, therefore the derivation above, and the resulting equation (3.36), takes the form of resistivity instead of conductivity. Had the experimental data taken the form of current PSD $S_I(f_0)$, then the transport coefficient of equation (3.36) would be σ. Most importantly, equations (3.36) and (3.37) are theoretically and experimentally exact when measuring voltage fluctuations.[47-48] Implementation of numerical integration of the experimental voltage ACF produces the diffusion coefficient and the electrical resistivity.

Thermal perturbations to a system differ somewhat from the so-called mechanical perturbations typical of electric fields. For thermal transport, the driving forces are temperature gradients which are themselves of statistical nature and are internal to the system.[48,102] Therefore, the treatment of thermal perturbations takes on a slightly different theoretical development. In parallel with McQuarrie,[97] the heat conduction equation is first introduced:

$$\rho C_V \frac{\partial \tilde{E}}{\partial t} = k_e \nabla^2 \tilde{E}\,, \tag{3.38}$$

where ρ is the material density, C_V is specific heat, k_e is the electronic contribution to the thermal conductivity and $\tilde{E}$ is used instead of temperature T. The energy $\tilde{E}(\mathbf{r},t)$ is defined as the excess energy above the *average* energy. This is an important point with regards to the following theoretical development. Stated in other words, $\tilde{E}(\mathbf{r},t)$ is a fluctuation in the average energy of the electron ensemble in thermal equilibrium. Let $L(\mathbf{k},t)$ be the Fourier transform of $\tilde{E}(\mathbf{r},t)$ resulting in the following expression:

$$L(\mathbf{k},t) = L(\mathbf{k},0)e^{-k_e k^2 t/\rho C_V} \tag{3.39}$$

The microscopic expression for $\tilde{E}(\mathbf{r},t)$ is:

$$\tilde{E}(\mathbf{r},t) = \sum_{j=1}^{N} \tilde{E}_j \delta(\mathbf{r} - \mathbf{r}_j), \tag{3.40}$$

Where $\tilde{E}_j$ is the fluctuation in energy of electron j and the delta function δ operates on the positional radius vector $\mathbf{r}_j$. The Fourier transform of equation (3.40) gives:

$$L(\mathbf{k},t) = \sum_{j=1}^{N} \tilde{E}_j e^{i\mathbf{k}\cdot\mathbf{r}_j(t)}. \tag{3.41}$$

Taking **k** in the z direction and noting the same coordinate system used in the experimental work, equation (3.41) can be expressed as:

$$L(\mathbf{k},t)=\sum_{j=1}^{N}\tilde{E}_j e^{ikz_j(t)}\,. \tag{3.42}$$

Multiplication of both sides of equation (3.39) by the complex conjugate of equation (3.42) at time zero, then taking the ensemble average yields:

$$\left\langle \sum_{j=1}^{N}\sum_{l=1}^{N}\tilde{E}_j(0)\tilde{E}_l(0)e^{ik\left[z_l(0)-z_j(0)\right]}\right\rangle \exp\left(\frac{-k_e k^2 t}{\rho C_V}\right), \tag{3.43}$$

where one is again reminded that k_e is the electronic contribution to the thermal conductivity and is not to be confused with the wave vector k. Additionally, ρ in equation (3.43) remains the material density. Progression of this derivation now begins to incorporate the results from Section 3.2.1. The evaluation of the first term in equation (3.43) results in the following equality:

$$\left\langle \sum_{j=1}^{N}\sum_{l=1}^{N}\tilde{E}_j\tilde{E}_l\right\rangle=\sqrt{\left\langle E^2\right\rangle-\left\langle E\right\rangle^2}\,. \tag{3.44}$$

Pause is taken to fully understand equation (3.44). The right side is noted to be the energetic fluctuations of the electron energy probability distribution denoted in equation (3.16). From the

resulting proof of Theorem 1, the associated equations (3.16) through (3.20) can be used within the Green-Kubo formalism to rigorously associate the electron thermal PSD with the right side of equation (3.44):

$$\sqrt{\left\langle E^2\right\rangle-\left\langle E\right\rangle^2}=\sigma_E=\sigma_Q=\sqrt{k_B T^2 C_V}=S_Q(f_0)=\frac{\overline{V^2}}{4R\Delta f}. \tag{3.45}$$

The underlying meaning of equation (3.45) is that the fluctuations carried by the thermal PSD have a direct thermodynamic relationship to the electrons ensemble fluctuation spectra *and* linear transport theory. Equation (3.45) is another major result of this work evidenced by enabling the electronic contribution to the thermal conductivity to be experimentally measured rather easily. Proceeding straight to the final result where the final mathematical steps are easily found[97] gives:

$$k_e=\frac{1}{3\Theta k_B T^2}\underbrace{\int_0^\infty\left\langle J_Q(0)\cdot J_Q(t)\right\rangle dt}_{\text{Green-Kubo Theory}}=\frac{1}{3\Theta k_B T^2}\overbrace{\int_0^\infty\left\langle \Gamma_Q(0)\cdot \Gamma_Q(t)\right\rangle dt}^{\text{Experimental Thermal ACF}}, \tag{3.46}$$

where

$$J_Q(t)=\frac{d}{dt}\sum_{j=1}^{N}\mathbf{r}_j\left(E_j-h\right), \tag{3.47}$$

where k_e represents the electronic thermal conductivity, Θ is the crystal volume, $\mathbf{r}_j$ is the position vector of electron j and h is the enthalpy per electron. The expansion of $J_Q(t)$ shown in equation (3.47) is shown to mathematically illustrate why the voltage ACF $\Gamma_V(t)$ cannot be used within equation (3.46). Quite simply, the ACF of the adjusted flux of internal energy is required,[32] which resides in the inverse Fourier transformed *thermal* PSD. Subsequently, the thermal PSD and ACF is a separate experimental data set apart from the voltage PSD and ACF and is used exclusively to determine the electronic thermal conductivity. Implementation of numerical integration of the experimental thermal ACF results in the electronic contribution to thermal conductivity.

The benchmark paper by Kubo[47] rigorously treated not only thermal transport phenomena but thermoelectric transport phenomena as well. To aid the derivation that follows, we digress for a moment to the electrical and thermal currents as a function of their origins, the electric field E and temperature gradient ∇T :[32]

$$J_E = \sigma E + \sigma S \nabla T \,, \tag{3.48}$$

$$J_Q = \sigma \Pi E + k_e \nabla T \,, \tag{3.49}$$

where J_E is the electric charge current, J_Q is the thermal current, S is the thermoelectric Seebeck coefficient, Π is the Peltier coefficient and σ is the electrical conductivity. In conjunction with the spectral density matrix introduced in equation (3.22), the off-diagonal thermoelectric term in equations (3.48) and (3.49) represent cross-correlations between the thermal *and* electric currents. Using Onsager's hypothesis and irreversible thermodynamics,[103-104] Kubo derived the linear transport theory expression for the Seebeck coefficient:[47]

$$S = \frac{1}{3\Theta k_B T^2}\int_0^\infty \left\langle J_E(0)\cdot J_Q(t)\right\rangle dt\,, \tag{3.50}$$

where the cross-correlation function $\left\langle J_E(0)\cdot J_Q(t)\right\rangle$ is evident and theoretically equates to the electronic voltage fluctuation cross-correlation derived in equations (3.22) and (3.24). Hence, the experimental measurement of the Seebeck coefficient from Johnson/Nyquist noise is possible through the following relation:

$$S = \frac{1}{3\Theta k_B T^2}\underbrace{\int_0^\infty \left\langle J_E(0)\cdot J_Q(t)\right\rangle dt}_{\text{Green-Kubo Theory}} = \frac{1}{3\Theta k_B T^2}\quad \overbrace{\int_0^\infty \left\langle \Gamma_V(0)\cdot \Gamma_Q(t)\right\rangle dt}^{\text{Experimental Thermoelectric ACF}}\quad . \tag{3.51}$$

Equation (3.51) represents another major contribution to this research. Using equation (3.51) to evaluate experimental voltage fluctuations enables a *direct* measurement of the Seebeck coefficient which was experimentally impossible prior to this work.

3.2.3 Additional Electronic Transport Coefficients and Results Obtainable from Thermal Noise Measurements

A directed flux of electrons or equivalently, an electron current, carries both charge and heat. Under specific assumptions such as a spherical Fermi surface and elastic scattering, a ratio of the electronic thermal conductivity and the electrical conductivity may be obtained:[42]

$$\frac{k_e}{\sigma} = \left[\frac{\pi^2}{3} \left(\frac{k_B}{e} \right)^2 \right] T \,. \tag{3.52}$$

This is known as the Wiedemann-Franz law which is unfortunate as it would more accurately be termed a "rule-of-thumb." Spherical Fermi surfaces are a good first assumption for some materials however accurate calculations must take in to account the non-spherical Fermi surface which invalidates equation (3.52).[42] Furthermore, elastic scattering may be a theoretical wish however real materials under varied boundary conditions and suffering from size effects coupled with fabrication anomalies inevitably introduce some inelastic scattering mechanisms to the electron cloud. Nevertheless, equation (3.52) does offer experimental utility through the Lorenz number L which is a factor from equation (3.52):

$$L = \left[\frac{\pi^2}{3} \left(\frac{k_B}{e} \right)^2 \right], \tag{3.53}$$

which takes on the theoretical value of 2.45×10^{-8} $\mathrm{W\Omega K^{-2}}$. From an experimental viewpoint, L can provide information about the presence of inelastic scattering effects as well as different relaxation times between the thermal and electric currents. This fact shall be used to help explain some of the experimental results in later chapters. In line with the theoretical foundation being laid out to support the experimental work, the Lorenz number may be directly measured through transport property coefficients:

$$L = \frac{k_e}{\sigma T}, \tag{3.54}$$

where σ and k_e are obtained experimentally from equations (3.36) and (3.46) (note that $\sigma = 1/\rho$).

The electron relaxation time in a conductor is realistically an average value resulting from a spectrum of relaxation times. In conjunction with the theoretical development thus far, the experimental measurement of the relaxation time τ may be obtained from the voltage ACF. Previous theoretical studies on solids focused on numerical calculation of the ACF by solving the Boltzmann equation.[105-106] Bulashenko and Kochelap[107] derived the ACF expressions for a 2D and 3D electron gas by solving the Boltzmann transport equation. Their results are pertinent to this research and take the form:

$$\Gamma_{2D}(t) = \frac{e^2 n_2}{m}\frac{d}{L}k_B T \exp\left(-t/\tau\right) f(u) \qquad \textit{where} \quad u = \frac{\gamma t}{\tau}$$

$$f(u) = \begin{cases} 1 - \dfrac{4u}{3\pi} & 0 < u < 1 \\ \dfrac{2}{\pi}\left(\arcsin\left(u\right)^{-1} + \dfrac{1}{3}\left(1-u^{-2}\right)^{1/2}\left(2u+u^{-1}\right) - \dfrac{2u}{3}\right) & u > 1, \end{cases} \tag{3.55}$$

$$\Gamma_{3D}(t) = \frac{e^2 n_3}{m}\frac{A}{L}k_B T \exp\left(-t/\tau\right) f(u)$$

$$f(u) = \begin{cases} 1 - \dfrac{3u}{8} & 0 < u < 1 \\ \dfrac{3}{4}u^{-1}\left(1 - \dfrac{1}{6}u^{-2}\right) & u > 1, \end{cases} \tag{3.56}$$

where n is the 2D or 3D electron concentration, d is the material width, L is the material length, A is the material area, τ is the electron relaxation time, t is time, γ is the electron mean free path to material width ratio and m is the electron mass. As explained in the previous section, the sample voltage fluctuation data set was inverse Fourier transformed to obtain the ACF. The theoretical ACF expressed by equation (3.55) or (3.56) was then used with all relevant material parameters. The unknown relaxation time τ was then used as a curve fitting parameter to obtain the experimental value of the electron relaxation time.

Finally, the experimental data also yields the electron mobility μ through the expression:[32]

$$\mu = \frac{\sigma}{ne}. \tag{3.57}$$

3.3: DES Theoretical Formalism: Experimental Application Summary

This chapter is concluded with a condensed summary of the theoretical formalism laid out in successive steps implemented experimentally during the course of this research:

1) Obtain enough voltage fluctuation data from an experimental sample material to be representative of a statistically stationary ensemble average. The DES experimental configuration used a band pass filter followed by squaring the voltage data, time averaged then divided by the measurement frequency bandwidth and equipment impedance $\Delta f Z(f_0)$.

This process results in the measurement of the voltage PSD and is equivalent to equation (3.8) divided by Δf.

2) Compute the thermal PSD by dividing the band pass filtered, squared, time averaged voltage data by $4R\Delta fZ(f_0)$. This results in the measurement of the thermal PSD and is equivalent to equation (3.14) divided by $\Delta fZ(f_0)$.

3) Calculate the Johnson/Nyquist noise through equation (3.8).

4) Take the inverse Fourier transform of the voltage and thermal PSD's obtained in steps 1 and 2 above to obtain the corresponding voltage and thermal ACF's. Compare each ACF value at time $t = 0$ to the respective PSD's. The values should be close due to equations (3.12) and (3.13).

5) Compute the thermoelectric ACF by taking the complex conjugate of the voltage and thermal ACF's as per equation (3.24).

6) Numerically integrate the voltage, thermal and thermoelectric ACF's. This formally gives the voltage, thermal and thermoelectric diffusion coefficients and is the primary entry point to Green-Kubo transport theory.

7) Calculate the resistivity, electronic contribution to thermal conductivity and Seebeck coefficient through equations (3.36), (3.46) and (3.51). The Peltier coefficient is easily calculated by multiplying the Seebeck coefficient by the experimental measurement temperature. Similarly, the electrical conductivity is easily calculated by computing ρ^{-1}.

8) Compute the average electron relaxation time by curve fitting equation (3.55) or (3.56) to the experimental voltage ACF decay.

9) Calculate the Lorenz number and mobility through equations (3.54) and (3.57).

10) Calculate the normalized probability density function from the experimental voltage data. This calculation is implemented numerically and should produce a Gaussian distribution with a zero mean value. The resulting plot is used as an experimental check to ensure statistically stationary data.

Chapter 4

Electronic Transport Property Measurements: Experimental Apparatus, Methodology, Data Acquisition and Analysis

4.1 Introduction to the Experimental Methodology of Transport Property Measurements With Gaseous Boundaries

The objective of this chapter is to show the experimental apparatus, construction and implementation used to obtain electronic transport property measurements of materials interfaced with gaseous boundaries. Furthermore, the data acquisition and analysis techniques required to obtain valid, reliable results are explained as well. The formulation and assembly of the experiment required different design parameters than those typically used in the transport property community due to the intended application of a gaseous interface. In fact, traditional transport property measurements are made exclusively with the intentional elimination of boundary effects. Instead of eliminating gaseous boundaries, this work seeks to assess their effects under two primary regimes: stationary and non-stationary flow. The stationary flow regime incorporated vacuum and pressure environments while the non-stationary or flowing gas field remained at atmospheric pressure. Consequently, alternative experimental apparatus was designed and fabricated as described in Sections 4.2.1 and 4.2.2. Section 4.3 provides details particular to the acquisition, processing and analysis of experimental data.

4.2 Experimental Apparatus and Methodology

4.2.1 Experimental Apparatus for DES Measurements in Vacuum or Pressure Under Stationary Gaseous Conditions

An experimental apparatus was designed and constructed specific to gathering DES data from a conductor under vacuum or pressure spanning 0.1 Pa to 3.44 MPa. As detailed in Figure 4.1, the sample holder was fitted with a vacuum and pressure tight enclosure, which also served to provide additional electromagnetic (EM) shielding from extraneous noise sources. DES

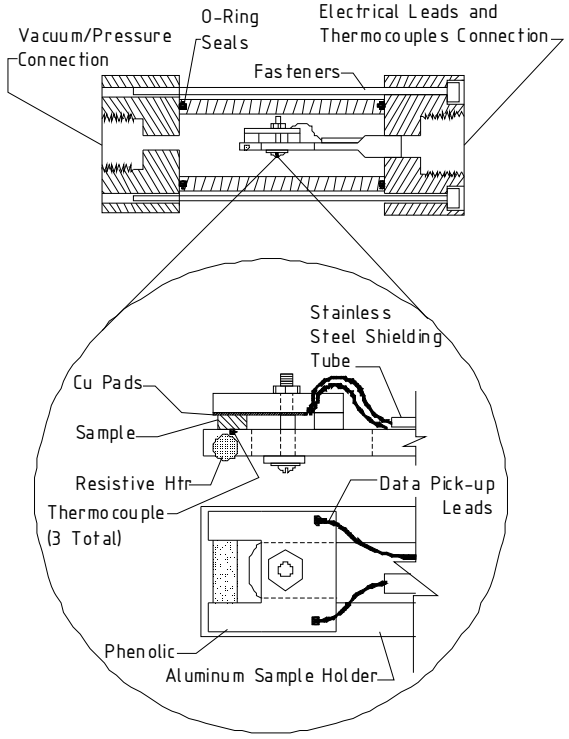

Figure 4.1: Sample holder and vacuum/pressure chamber. Large surface area copper pads interfaced the sample surface to the data collection leads. The design and layout of the sample holder and chamber was centered around the minimization of extraneous unwanted noise sources.

measurements for all samples was accomplished using an aluminum sample holder equipped with resistive heating capability. The sample holder could accommodate samples ranging from

0.5 – 3mm wide by 5 – 7 mm long. The samples were interfaced to the data leads through large surface area copper pads and additional shielding between the leads was obtained by placing one of them in a stainless steel tube. Figure 4.2 shows a mounted sample before insertion into the vacuum/pressure tight enclosure while Figure 4.3 shows the assembled enclosure.

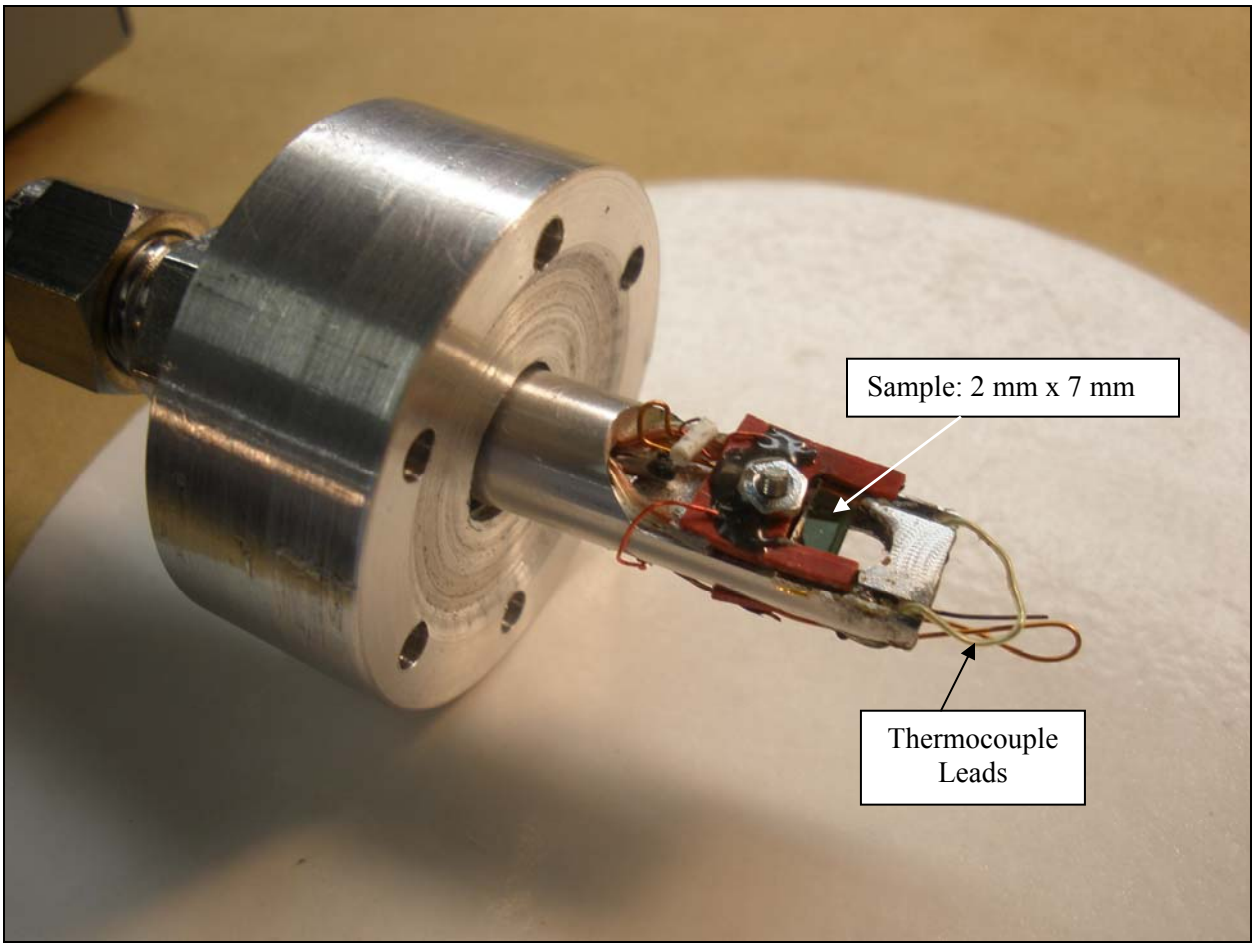

Figure 4.2: Mounted sample prior to insertion into the vacuum/pressure enclosure. The red phenolic equipped with copper interface pads on the underside can slide in either direction to allow sample placement adjustment over the resistive heater.

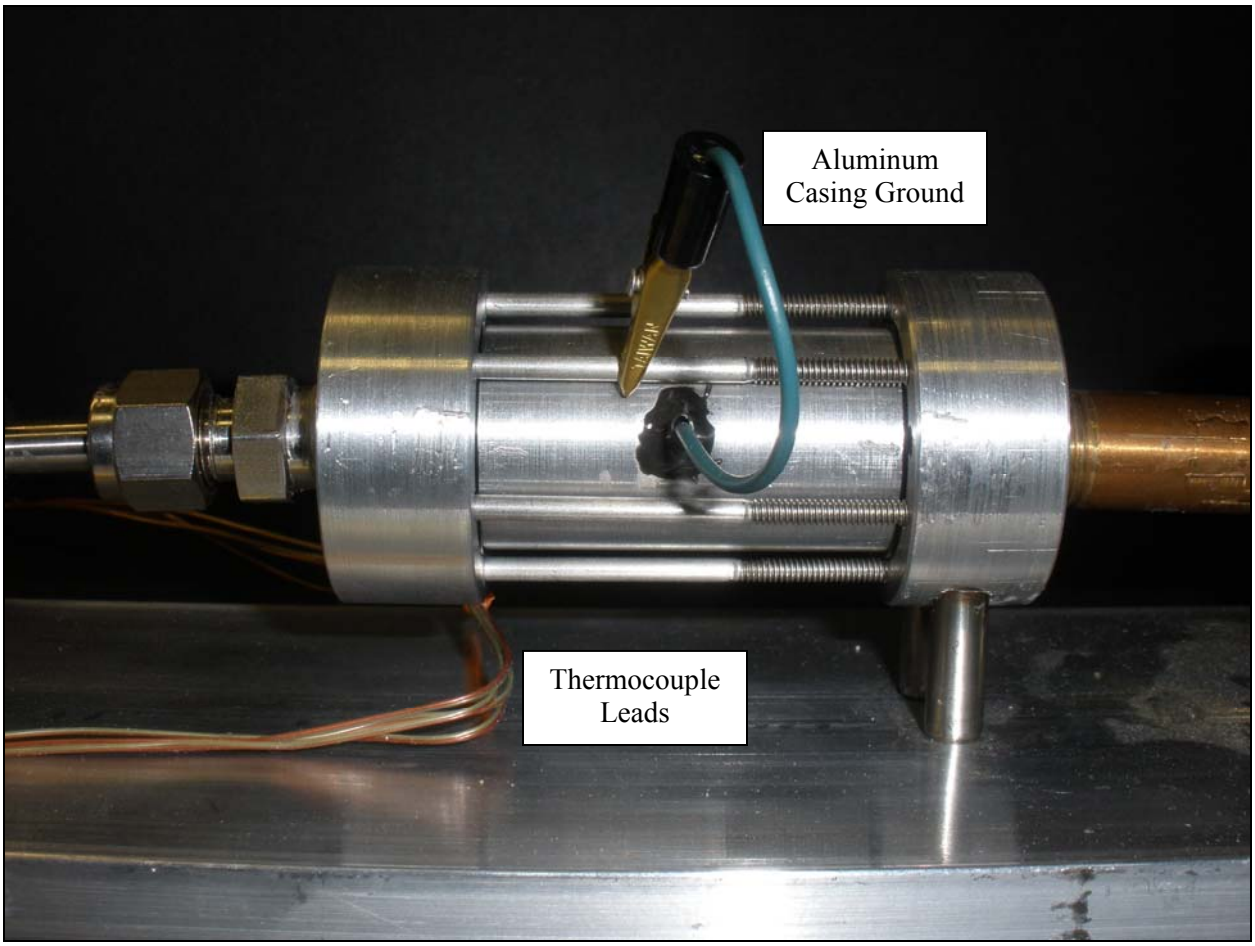

Figure 4.3: Assembled vacuum/pressure enclosure with grounding system in place. A separate casing ground lead was required due to the electrical isolation effect of the O-ring seals (see Figure 4.1 for O-ring location and details).

Both data collection leads and coax leads were twisted together after exiting the vacuum/pressure enclosure to further eliminate spurious environmental EM noise. Carefully routing ground paths helped avoid ground loops and shielding followed the recommendations found in Reference 108. A separate grounding rod was also installed dedicated to this experimental setup only. Temperature measurement was accomplished by using three type K thermocouples. Two thermocouples were placed in a machined slot in the base beneath each side of the sample while a third thermocouple was used in the differential mode to allow any temperature difference between each data collection lead to be recorded (see Figure 4.1). A

separate set of leads were run into the sample mounting area and soldered together. These leads were connected to a by-pass switch to allow noise measurements of the leads only with no sample in the measurement loop. Pressure measurement was obtained by a SSI Technologies digital gauge with 0 – 3.44 MPa range, 0.1 Pa resolution and +/-0.5% accuracy. Vacuum measurement was obtained by a separate Supco digital gauge with 0 – 0.101 kPa range, 0.01 Pa resolution and +/-0.5% accuracy. Figure 4.4 shows the assembled experimental apparatus.

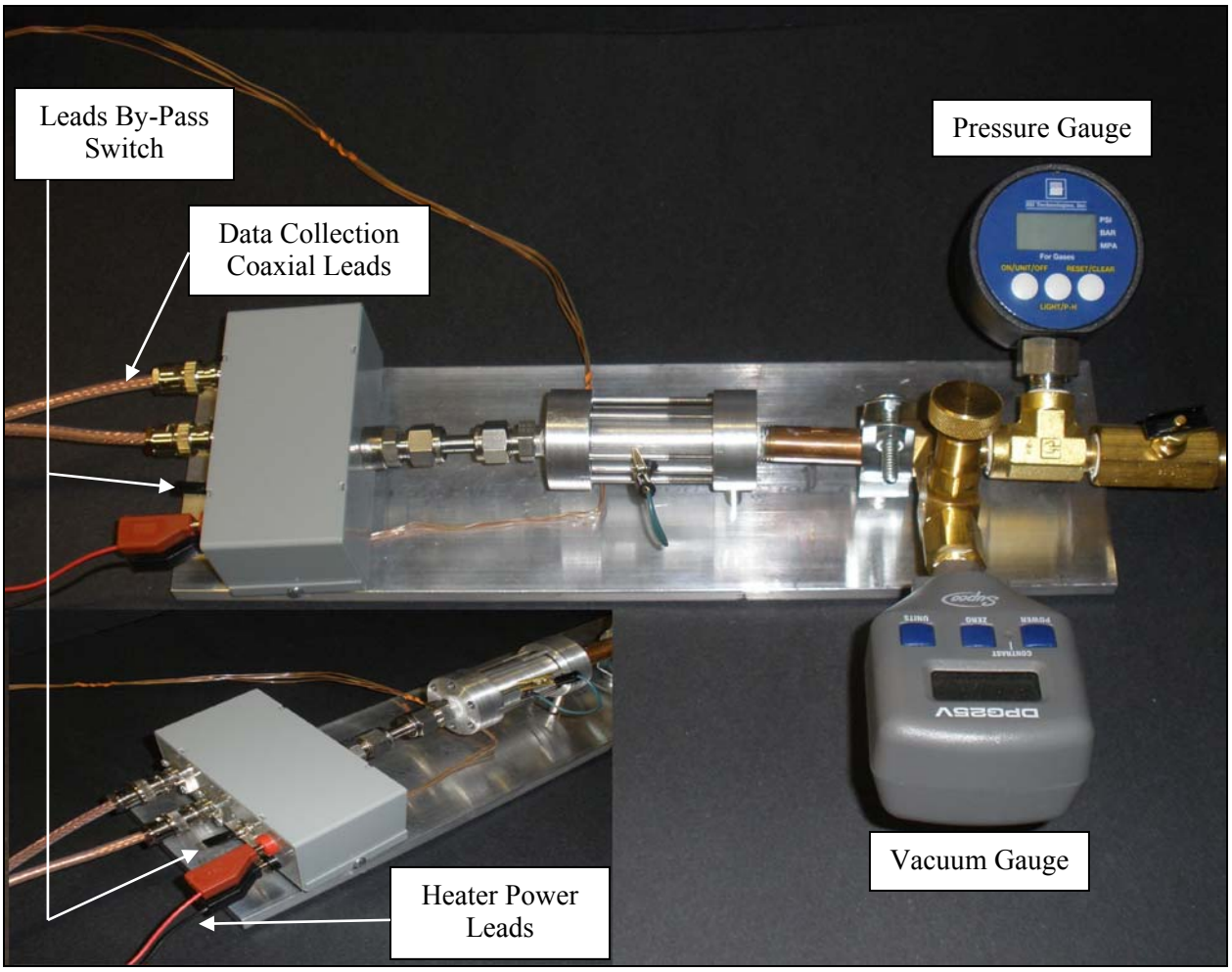

Figure 4.4: Assembled experimental apparatus to obtain DES measurements on a sample in pressure ranges from 0.1 Pa to 3.44 MPa.

As mentioned in the beginning of this section, the aluminum enclosure serves double duty as both a vacuum/pressure barrier as well as providing EM shielding to outside noise sources. Such a shield is typically known as a Faraday shield which is characterized by the shielding skin depth.[109] Basically, a material acting as an EM shield should be thicker than the corresponding shielding skin depth in order to actively deter extraneous EM noise sources. The shielding skin depth δ is expressed as:

$$\delta = \frac{1}{\sqrt{\pi f \mu \sigma}}, \tag{4.1}$$

where f is the desired shielding frequency, μ is the shield material permittivity and σ is the shield material electrical conductivity. The aluminum cylindrical enclosure had a wall thickness of 6.35 mm which provided a minimum low frequency shielding of 120 Hz according to equation (4.1). The bulkheads at each end of the cylindrical enclosure (see Figure 4.1) had a thickness of 12.7 mm which provided a minimum low frequency shielding of approximately 50 Hz. Effective high frequency shielding was provided by the experimental enclosure because the required skin depth decreases with higher ambient EM frequencies as per equation (4.1).

Further consideration of the experimental setup should be given to the capacitances of the probes and leads, which should be as low as possible. This requirement is due to the possibility of building an experimental setup that has a frequency cutoff f_C below the actual experimental measurement frequency. The cutoff frequency is defined as:[94]

$$f_C = \frac{1}{2\pi R_i C_i}, \tag{4.2}$$

where R_i and C_i are the additional equipment resistance and capacitance respectively and are the same variables brought forth in equation (3.5). Coaxial cable length and leads were kept at a minimum length and twisted together whenever possible. Extremely low capacitance coaxial cable was used which was rated at 0.41 pF per cm. Upon calculation of the entire experimental equipment, leads resistances and capacitances, the final approximation to the experimental cutoff frequency was f_C = 376 kHz. The measurement frequency remained at 10 – 30 kHz throughout all experimental runs in this research which is noted to be far below the cutoff frequency of 376 kHz thereby lending confidence to the accurate measurement of sample voltage fluctuation data.

Validation and calibration of the resistive heater system was required to correlate the required heater power to the actual sample surface temperature. The primary motivation for this information stems from the nanoscale samples used in this research, which consist of thin film metals applied to 1 mm thick microscope slides. Furthermore, the time required to approach steady state conditions is needed in order to ensure a samples thermal equilibrium at any measurement temperature. The heater consisted of a 51 ohm resistor embedded into a machined slot on the underside of the aluminum sample holder (see Figure 4.1 for details). High temperature epoxy was applied as an adhesive to keep the resistor in place. A mock sample consisting of a 1 mm thick microscope slide measuring 2 mm x 7 mm was equipped with a surface mounted type K thermocouple in order to accurately assess the actual glass slide surface temperature during heating. The experiment was assembled, then placed in vacuum at 15 mTorr. Incremental supply voltages were then applied while simultaneously measuring the sample

holder temperature as well as the thermocouple equipped mock sample. The calibration results for heater power levels of 0.5 W, 2.1 W, 4.8 W and 5.92 W are shown in Figure 4.5 below. The mock sample surface temperature was found to run between 5 °C and 10 °C lower than the actual aluminum sample holder temperature depending on the heater power. The approach to steady state conditions was found to take approximately 15 – 20 minutes, also depending on the heater power. Therefore, all subsequent experimental work was held at 30 minutes for each power setting before acquiring data in order to ensure complete steady state conditions. These results were used during experimental work detailed in Chapter 5.

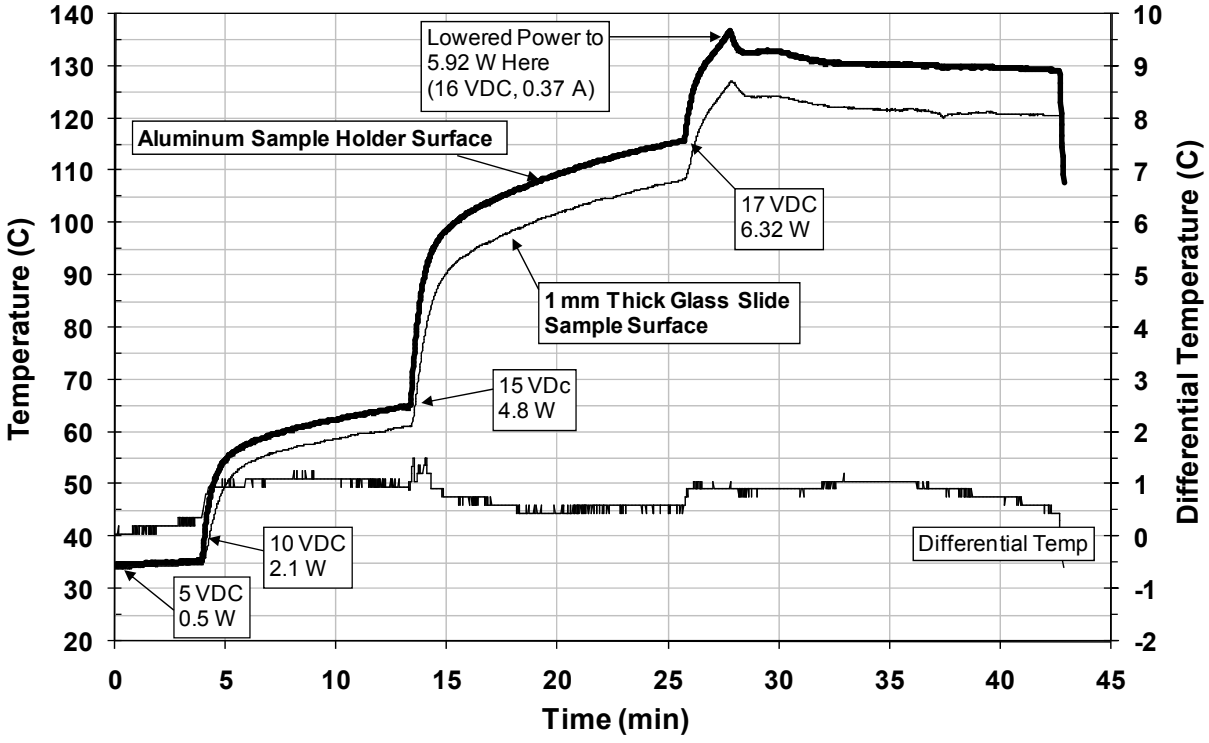

Figure 4.5: Resistive heater calibration/validation data for the stationary flow vacuum and pressure experimental apparatus. A 1 mm thick glass slide equipped with a type K thermocouple was used to characterize the sample surface temperature .

4.2.2 Experimental Apparatus for DES Measurements Under Non-Stationary Gaseous Flow

An experimental apparatus was designed and fabricated specific to gathering DES data from a conductor during gaseous flow conditions. As detailed in Figure 4.6, the subject gas entered a nozzle which increased the gas velocity resulting in a sample impact energy E_i. By varying the inlet gas pressure, the impact energy E_i could be easily controlled. The sample

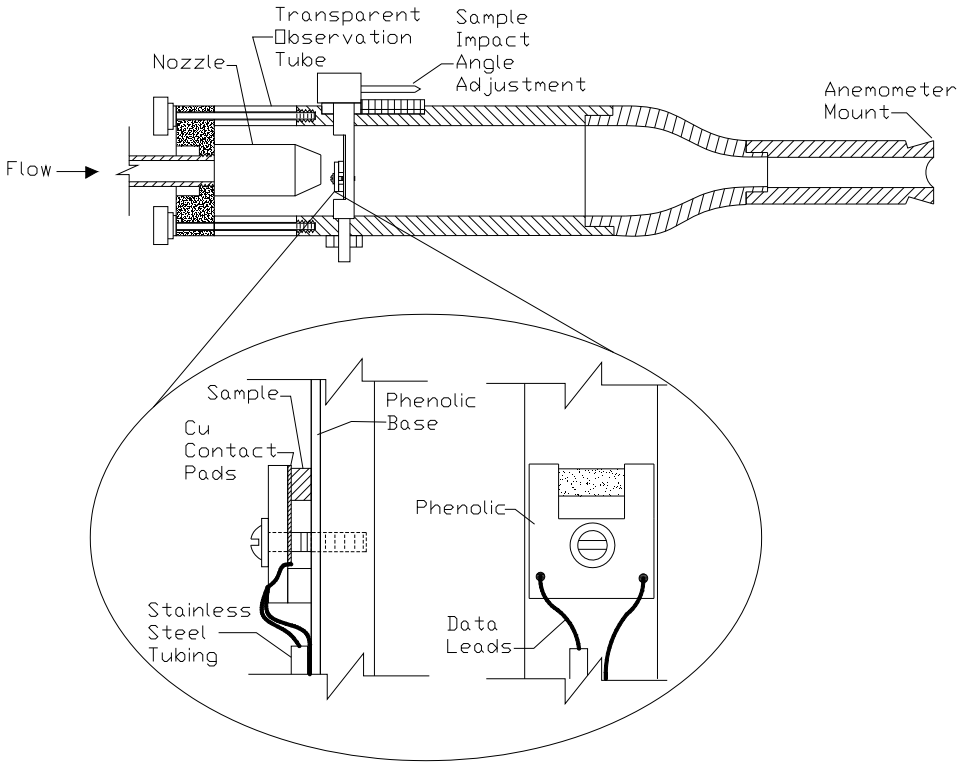

Figure 4.6: Sample holder and gaseous flow chamber. Identical to the vacuum/pressure sample holder, large surface area copper pads interfaced the sample surface to the data collection leads. The design and layout of the sample holder and chamber was again centered around the minimization of extraneous unwanted noise sources, as well as providing an adjustable gas impact angle.

mounting stem was designed to rotate through gas impact angles of 0° θ – 90° θ and could accommodate samples ranging from 0.5 – 3mm wide by 5 – 7 mm long. The samples were

interfaced to the data leads through large surface area copper pads and additional shielding between the leads was obtained by placing one of them in a stainless steel tube. A clear acrylic section was installed at the nozzle location to serve as a sample observation window during experimentation. After sample contact, the gas flow path proceeded through the chamber and exited through the anemometer mounting location (reference Figure 4.6).

To characterize the apparatus gas flow impact energy, thermodynamic states such as temperature, pressure and flow conditions were required at specific locations. Figure 4.7 shows the corresponding locations for each measurement. Temperature *T* and pressure *P* data was

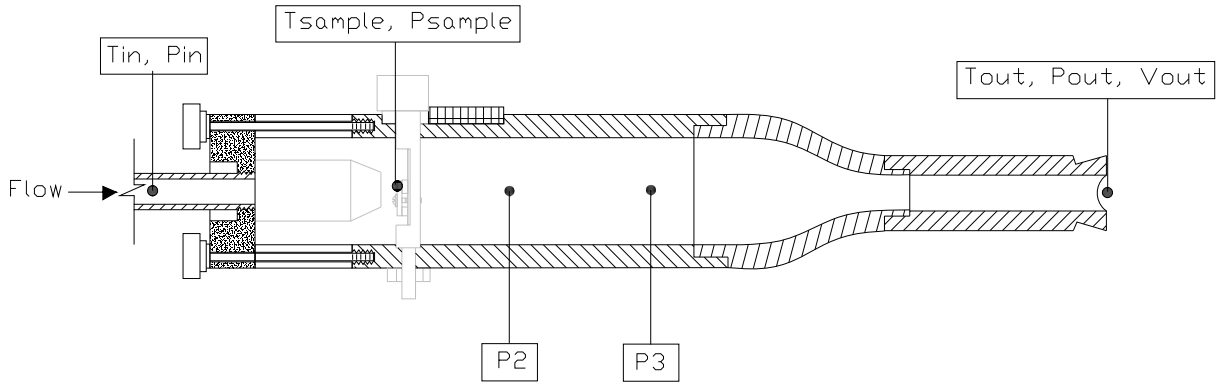

Figure 4.7: Temperature *T*, pressure *P* and velocity *V* measurement locations used to characterize impact energy values for each gas.

obtained at the gas inlet, sample mounting and gas exit locations. The gas exit velocity V_{out} was measured at the chamber outlet only. Temperature data was acquired through type K thermocouples while pressure measurements was obtained by a Dwyer low pressure magnehelic gauge with 0 – 248.8 Pa range, 2.48 Pa resolution and +/-2.0% accuracy. Gas exit velocity was measured with an Omega mini-vane anemometer with 0.8 – 12 m/sec range, 0.01 m/sec resolution and +/-2% accuracy.

Figures 4.8 and 4.9 provide a view of the completed flow chamber assembly, including data collection leads. Both data collection leads and coaxial cables were twisted together after

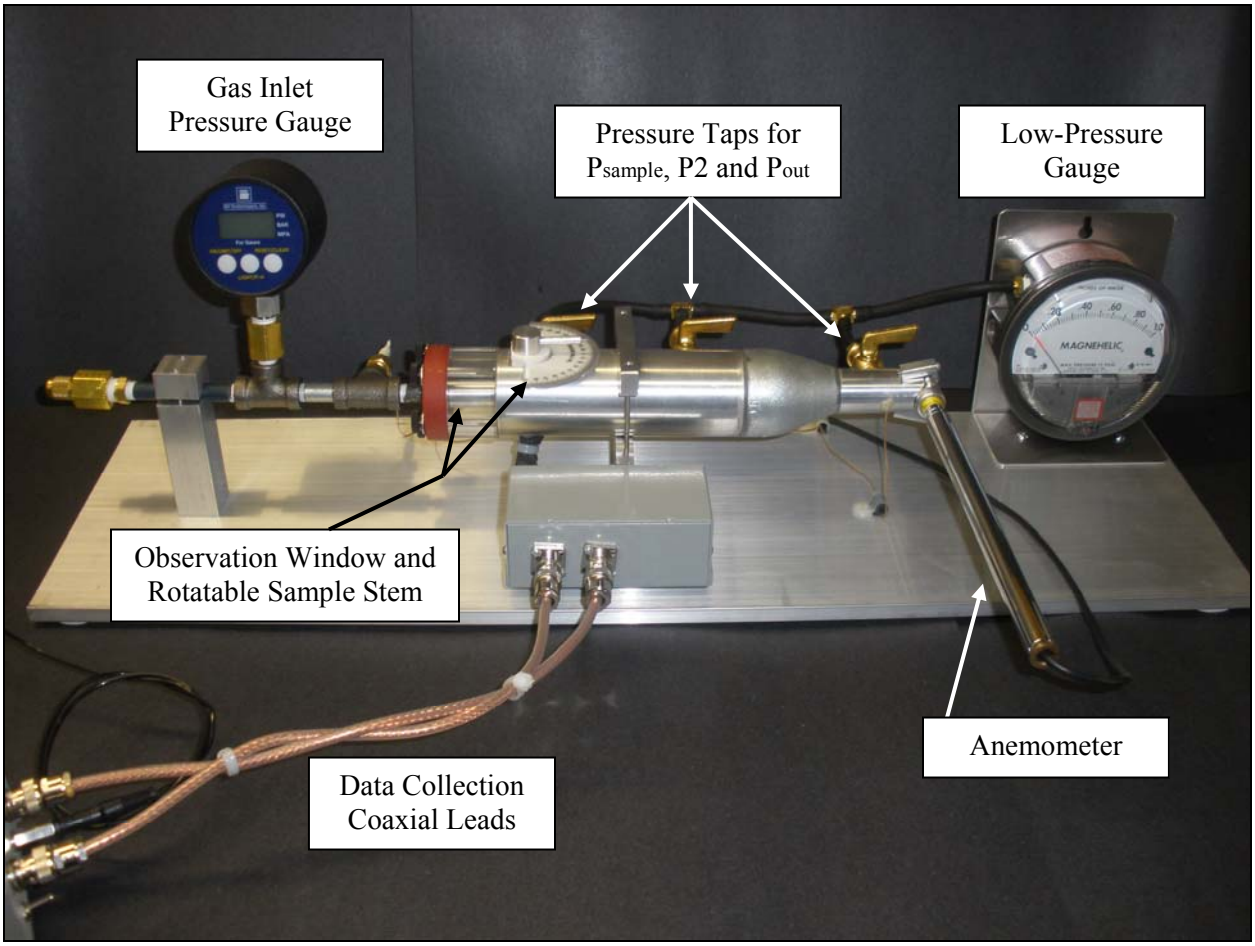

Figure 4.8: Complete flow chamber assembly with all data collection systems in place.

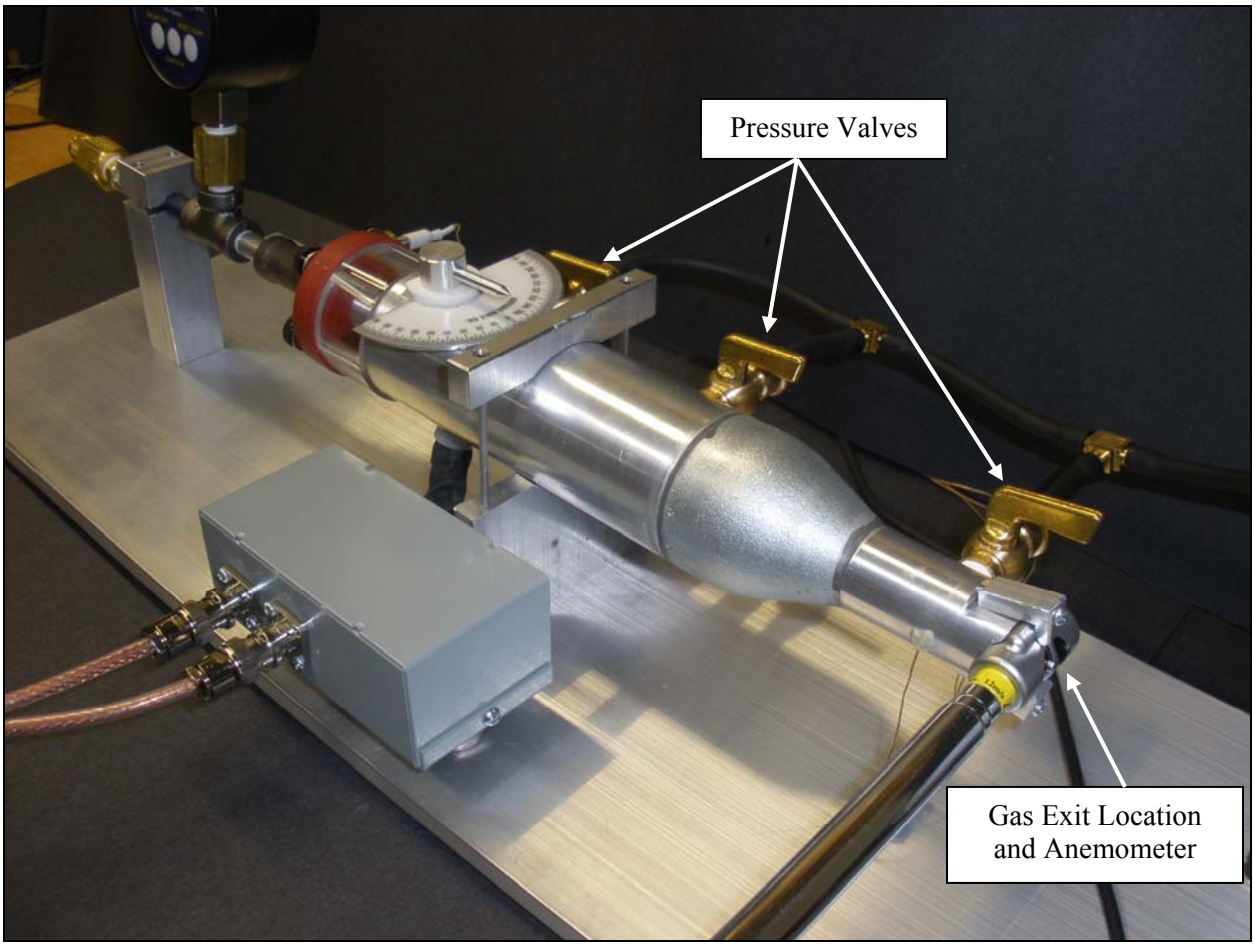

Figure 4.9: Complete flow chamber assembly with a focused view of the pressure tap valves and anemometer mounting location.

exiting the sample mounting section to further eliminate spurious environmental noise. Carefully routing ground paths helped avoid ground loops and shielding followed the recommendations found in Reference 108. Observation of the sample during flow conditions was easily performed as detailed in Figure 4.10. The Figure inset shows a typical thin metal film sample mounted and ready for an experimental run.

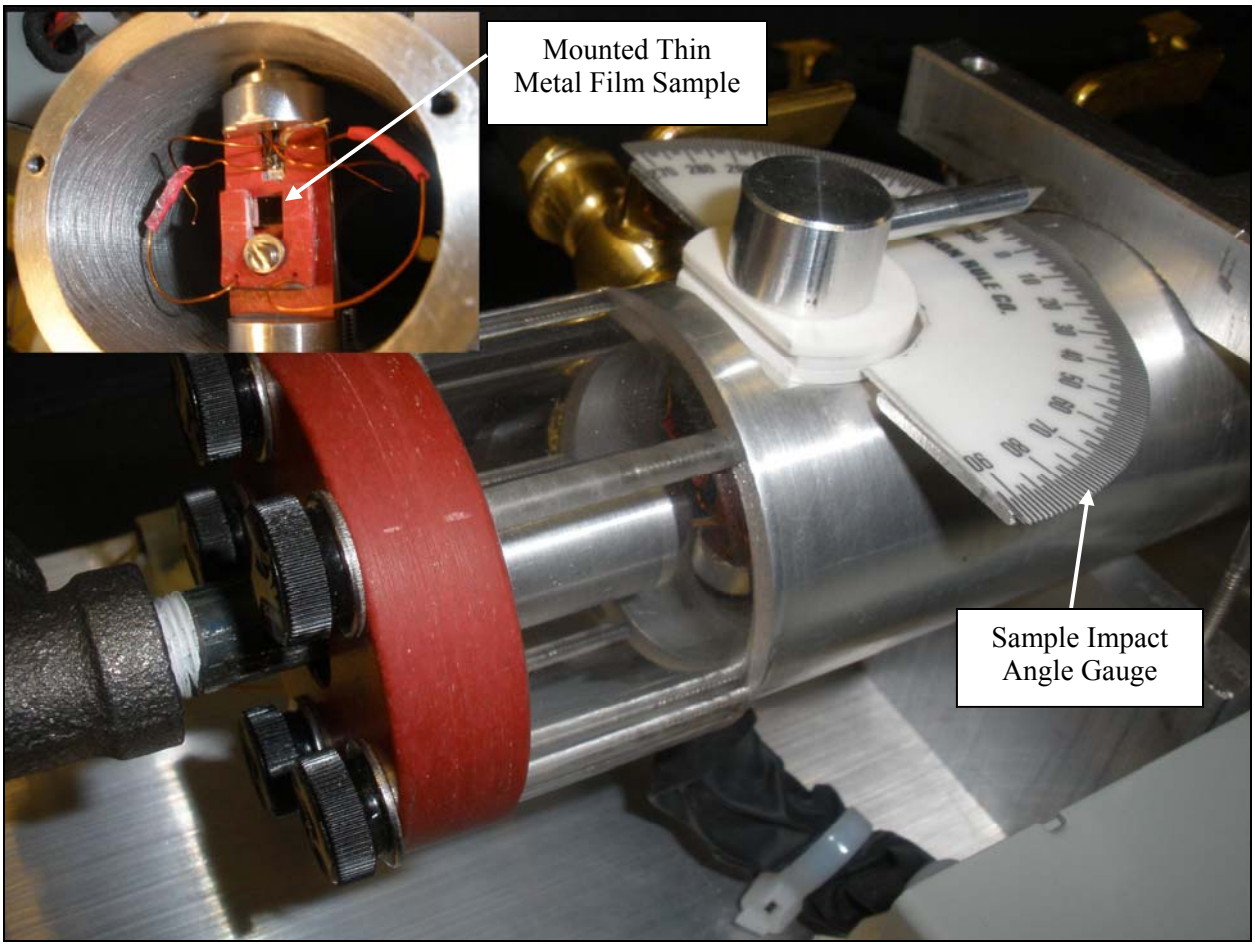

Figure 4.10: Close-up view of the flow chamber observation window section with a clear view of the nozzle. Note the rotatable sample stem with impact angle gauge. The inset shows a typical thin film sample mounted and ready for an experimental run.

From an experimental viewpoint, two primary calibration objectives were required: 1) the gas impact energy E_i on the sample and 2) the corresponding sample temperature during flow conditions. The impact energy is required to characterize scattering effects on the sample and the sample temperature is required due to an expected decrease in gas temperature due to the nozzle Joule-Thomson effect. A mock sample consisting of a 2 mm x 7 mm glass slide was equipped with a type K thermocouple similar to the vacuum/pressure chamber setup and is shown in Figure 4.11. A second thermocouple was mounted adjacent to the mock sample to

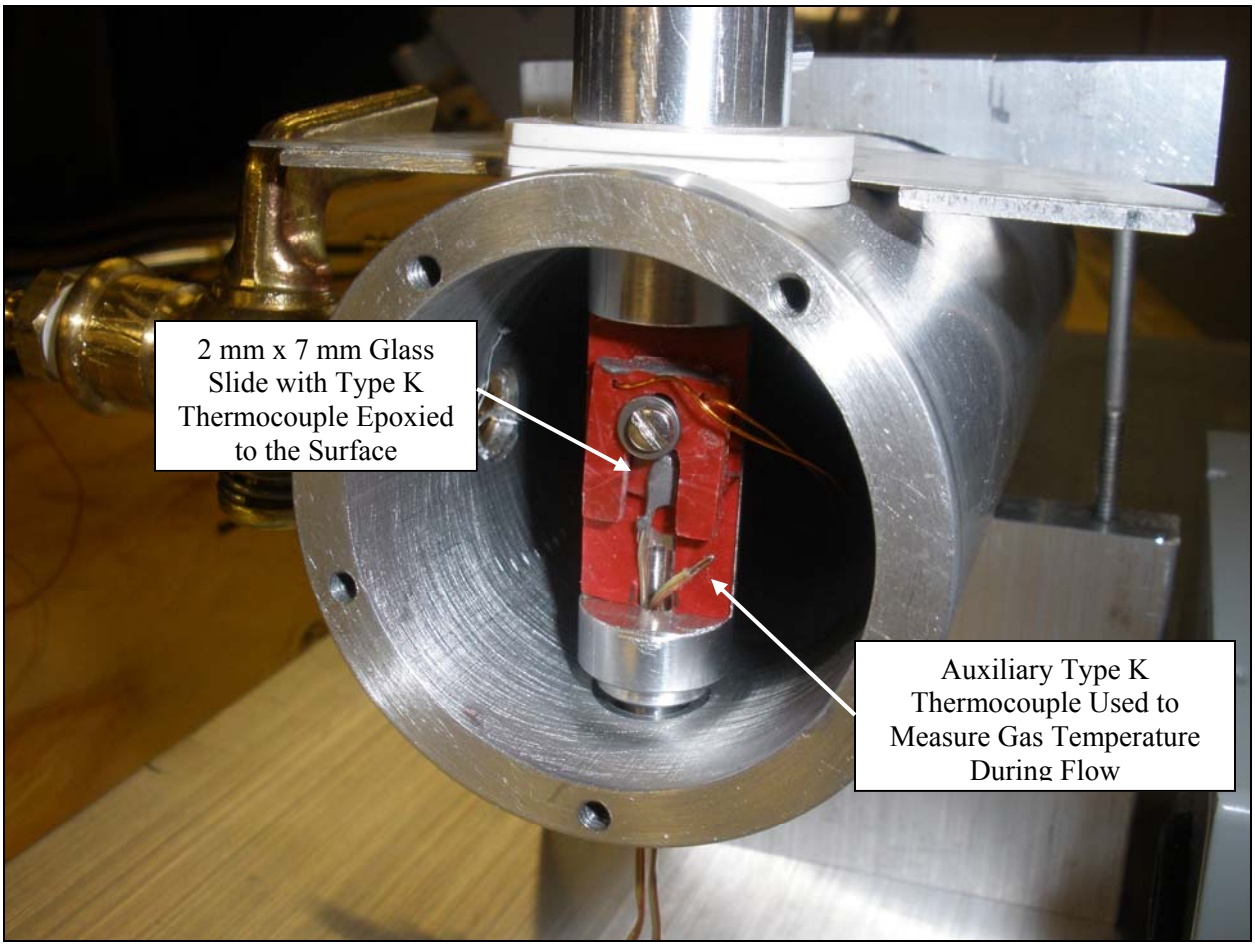

Figure 4.11: Characterization of the sample temperature during gas flow conditions was achieved with a mock sample equipped with a type K thermocouple. An auxiliary thermocouple was used to record general gas temperatures during flow conditions.

obtain nozzle exit gas temperature data. The calibration and characterization of the flow chamber proceeded through a series of test runs using helium and argon, which are the same gases used during the research phase of this work. The inlet pressure to the nozzle was incremented in discrete steps of 172.369 kPa until a maximum gas pressure of 1.412 MPa was reached. At each discrete inlet pressure step increase of 172.369 kPa, all temperature, pressure and flow velocity data was recorded. Using NIST12 thermodynamic properties software, the inlet, nozzle and outlet gas density was obtained from the measured T_{in}, P_{in}, T_{sample}, P_{sample} and

T_{out}, P_{out} data respectively (see Figure 4.7). The mass flow rate of the chamber was then calculated at each discrete inlet gas pressure according to:[110]

$$\dot{m}_{out} = \rho_{out} V_{out} A_{out}, \tag{4.3}$$

where the mass flow rate is $\dot{m}_{out}$, the outlet gas density is ρ_{out}, the exit velocity (obtained from the anemometer measurement) is V_{out} and the outlet upstream tube area is A_{out}. Due to the conservation of mass $\dot{m}_{in} \equiv \dot{m}_{out}$, the nozzle inlet velocity can be calculated by using:

$$V_{in} = \frac{\dot{m}_{out}}{\rho_{in} A_{in}}, \tag{4.4}$$

where the inlet tube area is A_{in}. The nozzle gas velocity V_{sample}, which is incident upon the sample is then determined through the expression:

$$V_{sample} = \frac{\dot{m}_{out}}{\rho_{noz} A_{noz}}, \tag{4.5}$$

where the nozzle orifice area is A_{noz}. Several nozzle orifice diameters were tried during characterization of this experiment. The nozzle orifice design objective was to cover a range of gas impact energies that spanned the inelastic to elastic phonon scattering regime as determined by the HAS community.[111-112] Through a literature survey, this range equated to approximately 23 – 70 meV (inelastic) to 70 meV and up (elastic). This design objective was partly motivated

by the phonon to electron coupling that is prevalent in gas-surface scattering.[36] The best range of impact energies for both helium and argon was found to be provided by an orifice diameter of 0.254 mm. This nozzle diameter was used throughout the remaining experimentation reported in this research. The gas impact energy (carrying units of eV) on the sample was calculated at each discrete inlet pressure step by:

$$E_i = k_B T_{sample}. \tag{4.6}$$

The primary characterization results of E_i, $\dot{m}$ and sample surface temperature for both helium and argon are shown in Figures 4.12 – 4.17.

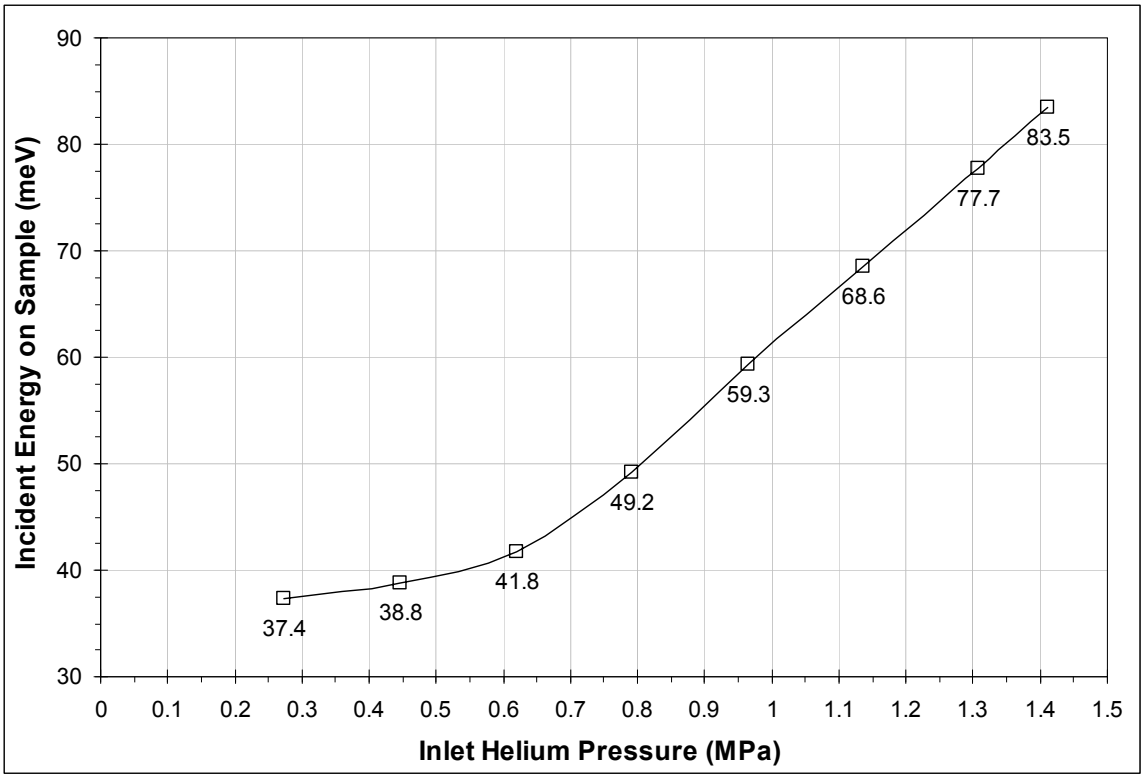

Figure 4.12: Helium incident energy characterization results using a 0.254 mm nozzle orifice diameter.

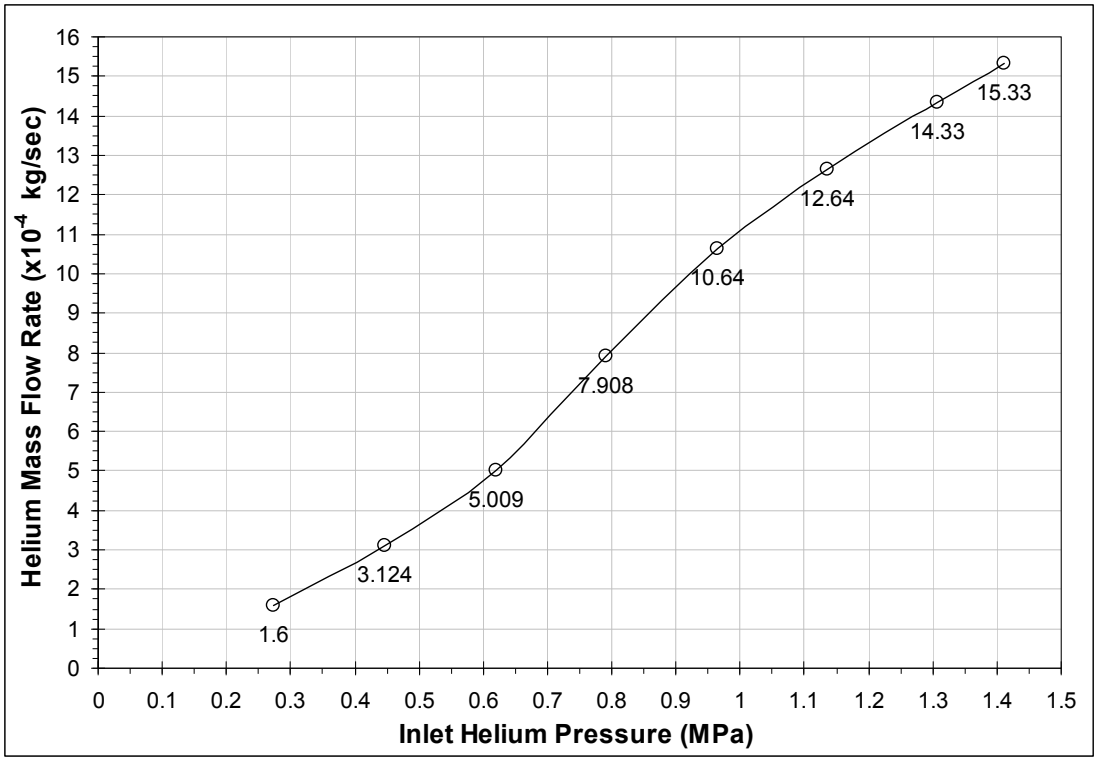

Figure 4.13: Helium mass flow rate results at 8 discrete inlet pressure steps.

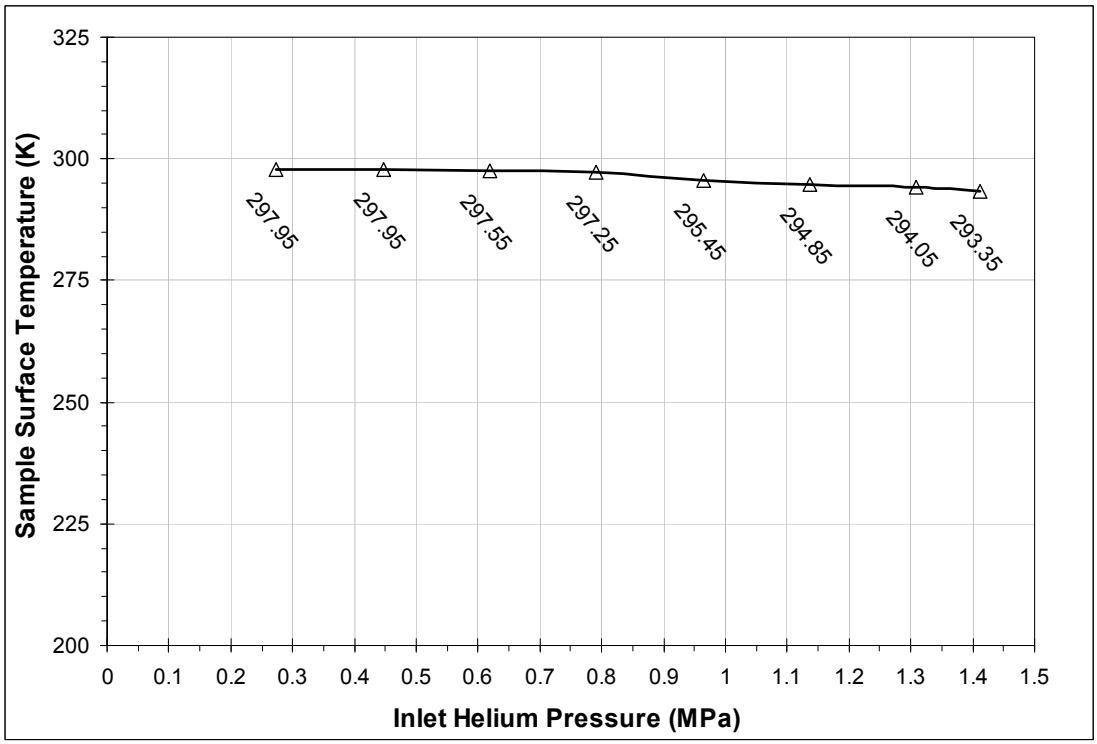

Figure 4.14: Sample surface temperature results at 8 discrete inlet pressure steps.

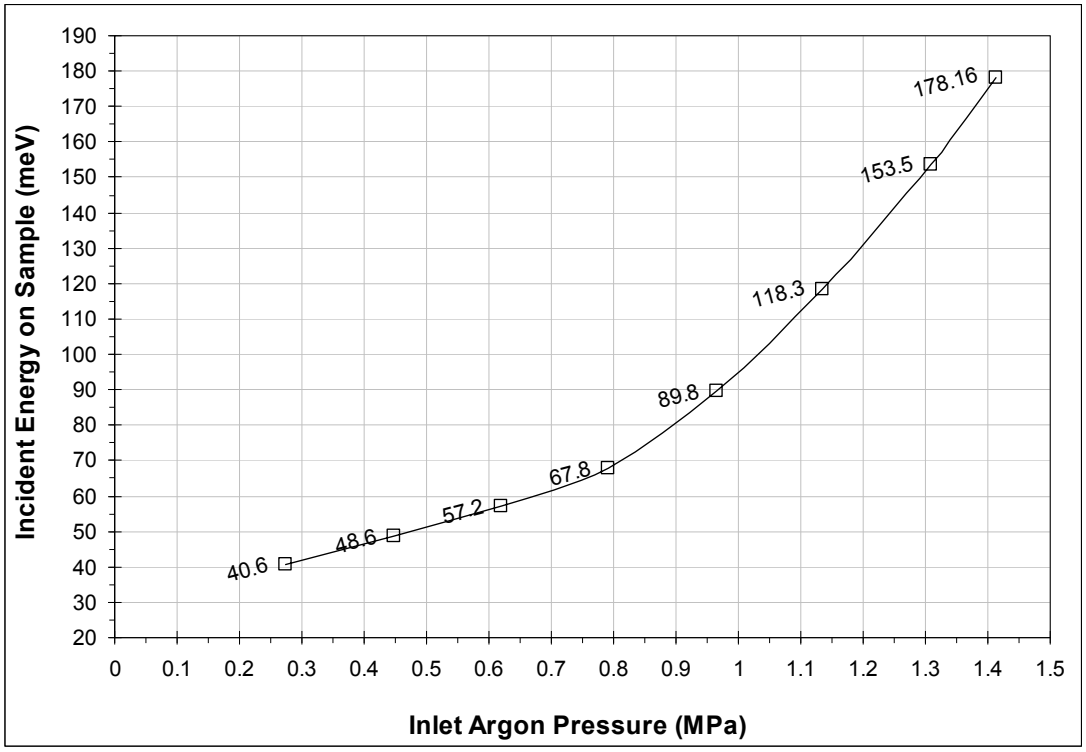

Figure 4.15: Argon incident energy characterization results using a 0.254 mm nozzle orifice diameter.

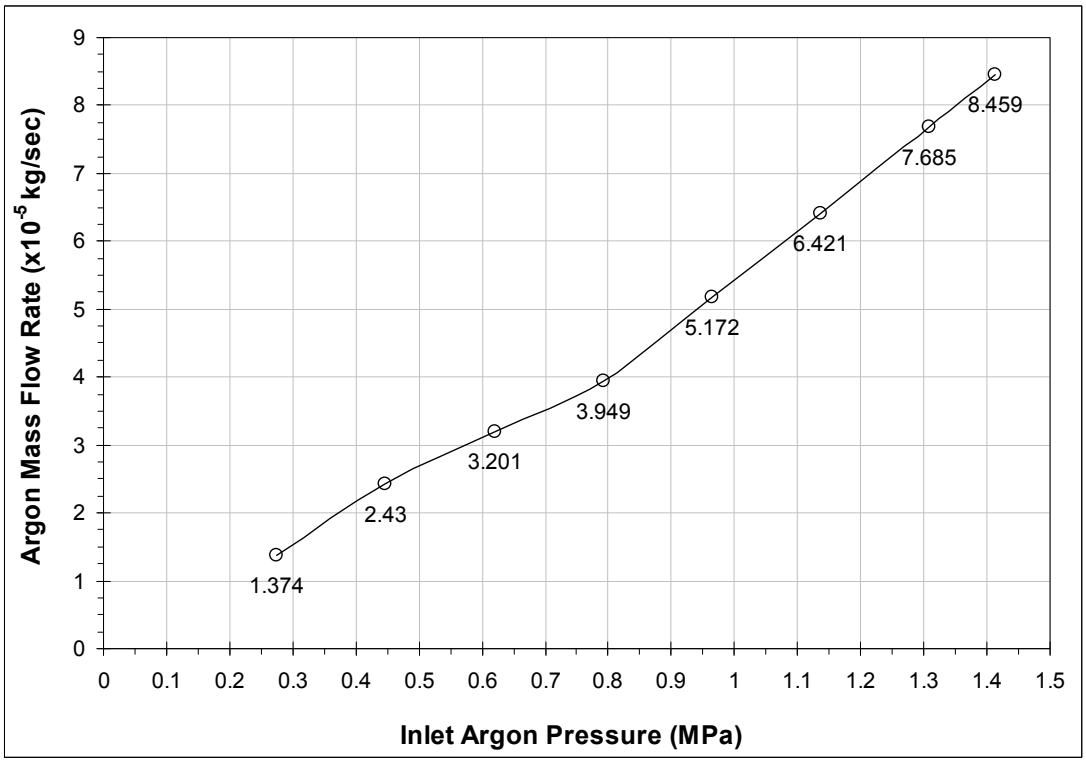

Figure 4.16: Argon mass flow rate results at 8 discrete inlet pressure steps.

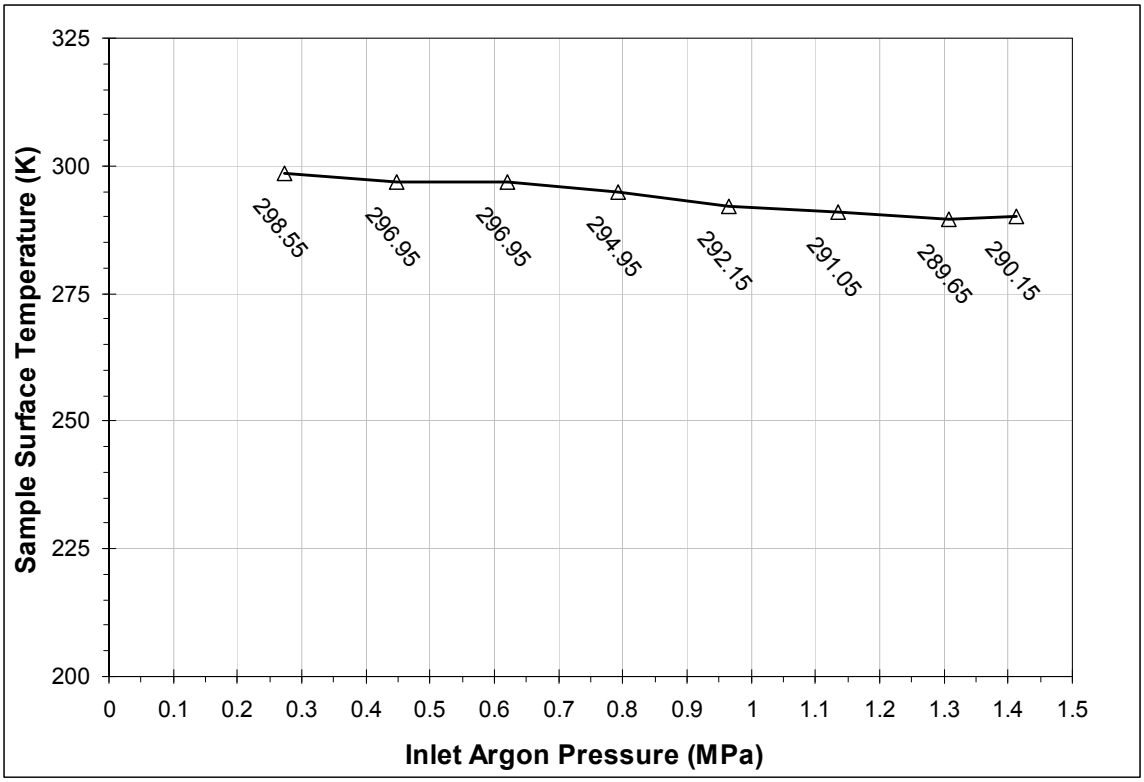

Figure 4.17: Sample surface temperature results at 8 discrete inlet pressure steps.

4.2.3 Experimental Apparatus for Collinear Four-Probe Resistivity Measurements

As part of the DES experimental validation methods outlined in Chapter 5, the standardized four-probe method was used to obtain comparative electrical resistivity measurements. An experimental apparatus was designed and built to accomplish stationary flow conditions under vacuum or pressure. Figure 4.18 shows the four-probe experimental setup which used "pogo stick" spring loaded point contacts that were appropriately tensioned to make good electrical contact when interfaced with the sample. Additionally, two type K thermocouples were secured at the sample mounting station for temperature measurement. Figure 4.19 displays the assembled four-probe experiment with enclosure and all leads in place.

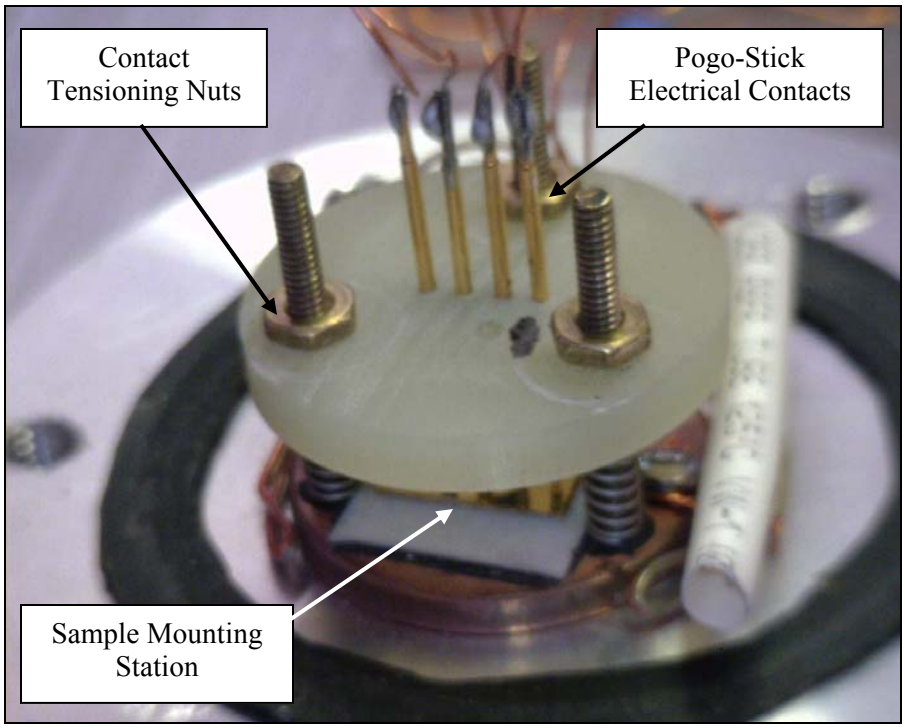

Figure 4.18: Four-probe resistivity experimental sample mounting station. Note the four gold pogo-stick style contacts that are appropriately tensioned to make good electrical contact with the sample.

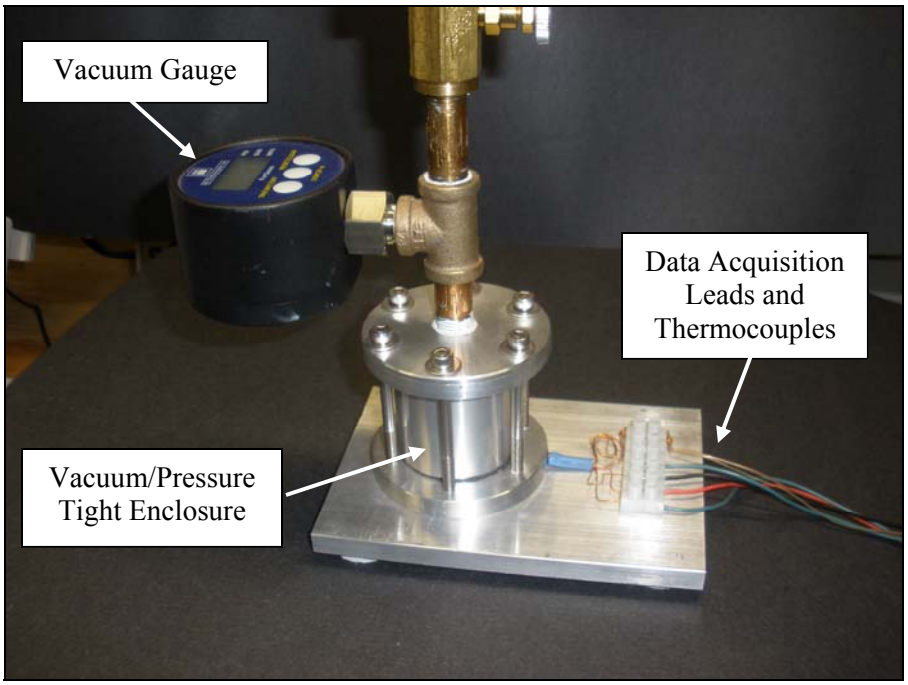

Figure 4.19: Assembled four-probe resistivity experiment with enclosure, leads and thermocouples in place. The sample mounting station detailed in Figure 4.18 is located inside of the vacuum/pressure enclosure.

All four-probe measurements followed the widely used standardized procedures.[113-114] A Keithley Model 6221 current source and Keithley Model 2182 nanovoltmeter were used to provide the required source current and voltage measurements needed to obtain the final four-probe resistivity data. Vacuum measurement was obtained by a Supco digital gauge with 0 – 0.101 kPa range, 0.01 Pa resolution and +/-0.5% accuracy.

4.2.4 Experimental Apparatus for Resistance Measurements

As part of the experimental investigation outlined in Chapter 5, accurate resistance measurements were required on various samples. The equipment used to accomplish this was a BK Precision 5491 5½ digit bench multimeter. With respect to resistance measurements, the meter was used on the 120 Ω range which equated to a 1 mΩ resolution with 0.1% accuracy.

4.3 Data Acquisition Equipment and Analysis Methods

4.3.1 Data Acquisition Equipment and Operating Parameters

In practice, the accurate repeatable acquisition of thermal noise data requires careful selection of experimental equipment. One of the principle difficulties is the presence of noise in the data acquisition equipment. Herein lies the primary objective of this section: to review the design, selection and implementation of the experimental equipment required to obtain DES measurements on low resistance samples. This research defines the term low resistance as any sample measuring less than 50 ohms. One of the key components to successful measurement of thermal noise of low resistance samples is the proper selection and usage of the first stage amplification. As shown in the experimental equipment diagram of Figure 4.20, this was

accomplished by the use of a Stanford Research SR554 transformer preamplifier. The transformer can be operated in the non-powered configuration which provides a gain of 100 and also eliminates any possibility of AC power line interference noise.[115] The rated input noise is $100\text{pV}/\sqrt{\text{Hz}}$ which shall be used in gain calculations later in this section. The experimental

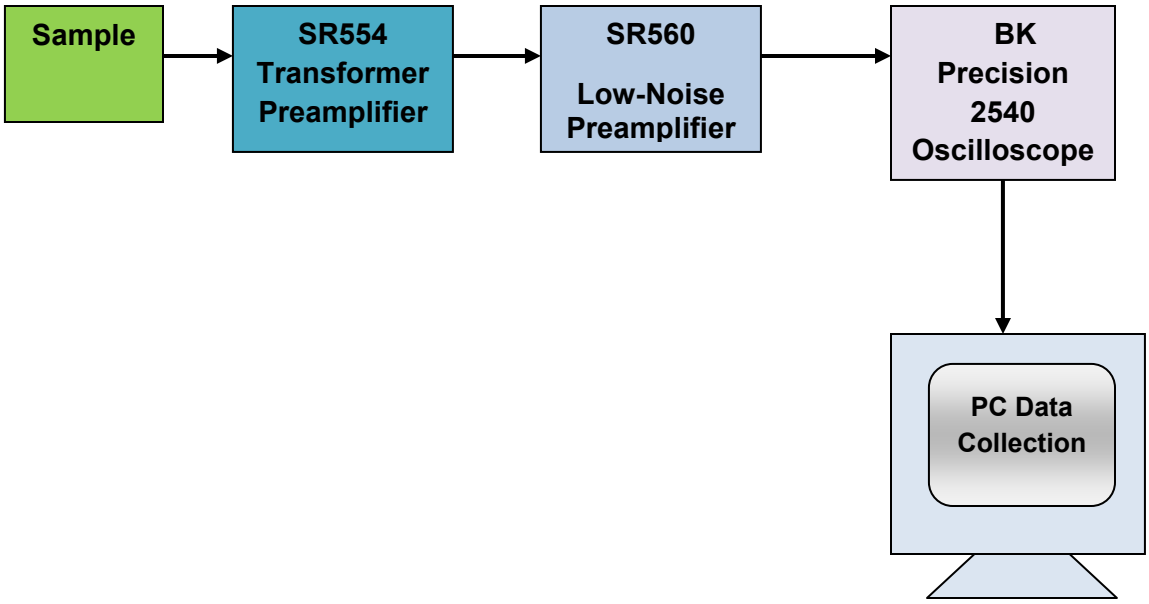

Figure 4.20: The DES experimental equipment diagram.

samples used in this investigation had resistance ranges from approximately 4 – 9.5 Ω and were measured in the 20 -30 kHz range. As indicated by the red hatched box in Figure 4.21, this resistance range allows the SR554 to operate under nearly optimum conditions. The SR554 amplitude response has also been verified to lie in the 40 dB range as shown in Figure 4.22. This ensures the transformer gain performance of no less than 100.[115] Following the first stage transformer amplifier is a Stanford Research SR560 low noise preamplifier as shown in Figure

4.20. This preamplifier is equipped with low-pass, high-pass and band-pass configurable filters.[116] The band-pass filter configuration was used in this work and set to 20 – 30 kHz as mentioned previously.

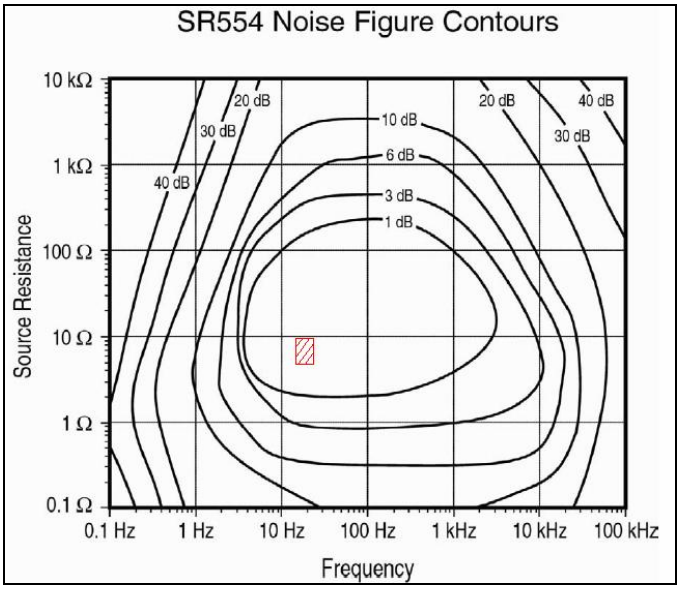

Figure 4.21: The Stanford Research SR554 transformer preamplifier noise figure contour plot. The red hatched box shows the operational range of the SR554 during the course of this research.

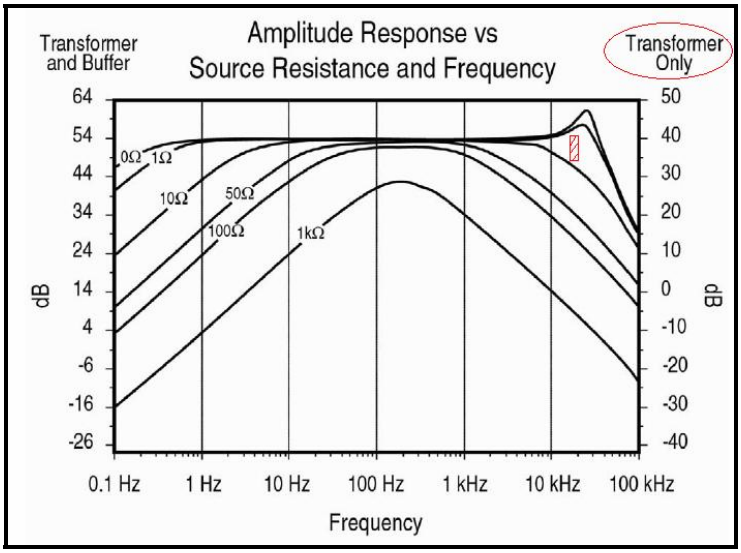

Figure 4.22: The Stanford Research SR554 transformer preamplifier amplitude response vs source resistance and frequency. The red hatched box shows the operational range of the SR554 during the course of this research.

The SR560 preamplifier was operated in the battery powered mode for complete isolation from AC line voltage interference and unwanted superfluous noise.[116] The SR560 gain setting was adjusted at 50,000 for all DES measurements reported in this work. The rated input noise is $4\text{nV}/\sqrt{\text{Hz}}$ which shall be used in gain calculations later in this section. As indicated by the red hatched box of Figure 4.23, the SR560 was operated under nearly optimum conditions to achieve accurate thermal noise data measurements. It should be noted that the input or source resistance to the SR560 is the SR554 transformer winding which is approximately 10,000 times the actual sample resistance.[115] Therefore, the impedance matching characteristics of the SR554 with the SR560 results in an effective DES measurement system when applied to low resistance materials. All electronic equipment used throughout this entire research endeavor was turned on and allowed to warm up a minimum of one hour before data acquisition began.

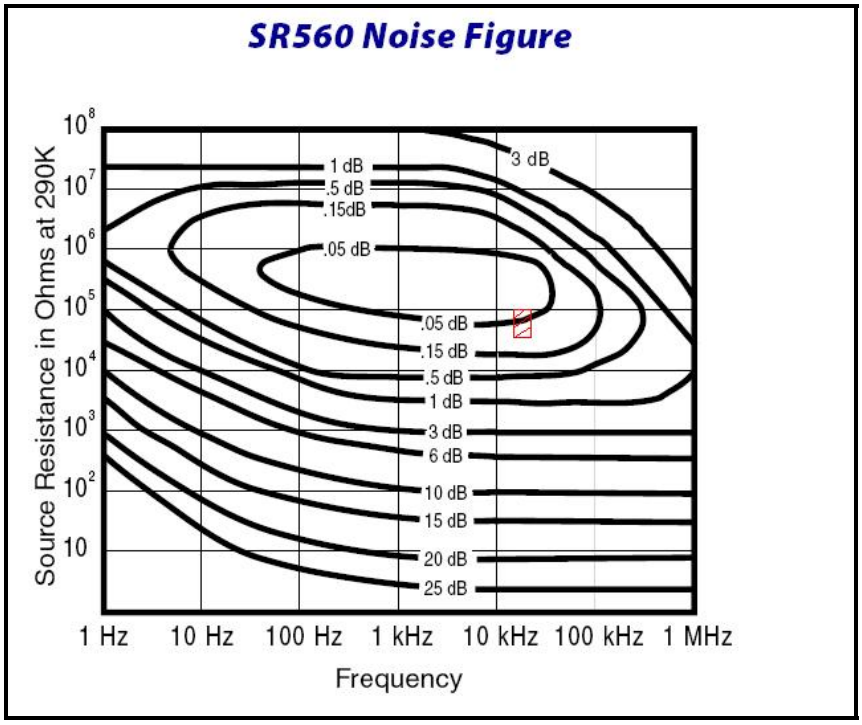

4.23: The Stanford Research SR560 low-noise preamplifier noise figure contour plot. The red hatched box shows the operational range of the SR554 during the course of this research.

To ensure that the fundamental Johnson/Nyquist voltage fluctuations are lifted above the inherent equipment noise, a sample calculation is presented which duplicates the calculations used on all materials in this work. Consider a 4 Ω sample material at 298 K temperature and measured at Δf = 20,000 Hz. The first stage gain by the SR554 transformer preamplifier is 100. Using the standard Johnson/Nyquist noise voltage formula (see equation (3.1), the expected root-mean-square voltage present at the SR560 low noise preamplifier input terminals is:

$$\sqrt{4 \cdot 1.38 \times 10^{-23}\,\text{J/K} \cdot 298\ \text{K} \cdot 4\ \Omega \cdot 20000\ \text{Hz}}\ \cdot\ 100\ \text{Gain}\ = 3.62\ \mu\text{V}\,. \tag{4.7}$$

The inherent noise of the SR554 transformer is calculated to be:

$$\frac{120 \times 10^{-12}\,\text{V}}{\sqrt{\text{Hz}}} \cdot \sqrt{20000\ \text{Hz}} \cdot 100\ \text{Gain}\ =\ 1.69\ \mu\text{V}\,, \tag{4.8}$$

which results in a DES signal to transformer noise ratio of 2.14. Proceeding to the next stage of amplification with a gain of 50,000 (SR560), the DES signal is approximated as:

$$3.62\ \mu\text{V}\ \cdot\ 50000\ \text{Gain} = 181\ \text{mV}\,. \tag{4.9}$$

The inherent noise of the SR560 low-noise preamplifier is calculated to be:

$$\frac{4 \times 10^{-9}\,\text{V}}{\sqrt{\text{Hz}}} \cdot \sqrt{20000\ \text{Hz}} \cdot 50000\ \text{Gain} = 28.28\ \text{mV}\,, \tag{4.10}$$

which results in a DES signal to amplifier noise ratio of 6.4. Clearly, one can see that the DES signal approximated in equation (4.9) will be the primary measurement at the oscilloscope input. All samples used in this investigation were checked by the above calculation procedure to ensure that the oscilloscope measurement was the sample noise only with no equipment noise interference.

4.3.2 Experimental DES Data Acquisition, Analysis and Calibration Details

The spectroscopic basis of the DES experiment requires a careful consideration of the measurement and analysis of the random voltage fluctuations. Given a record of continuous voltage fluctuations of temporal length T, the fluctuations can be converted to a sequence of N equally spaced values with no significant loss of information if $N \geq 2\Delta fT$.[96] The time T is defined as $T = n\Delta t$, where n is a sequence of sample values spaced equally in time by Δt. The experimental procedure used in this work acquired 120 oscilloscope screen shots of data where each screenshot consisted of 4000 data points. The oscilloscope time base setting was 2.5 μs with a sampling rate of 100 MSa/s which equates to discrete data points taken every 10 ns. Inherent in the numerical analysis of the data, one must consider the discrete fast Fourier transform requirement of 2^n data points per transform operation. Subsequently, each DES data field contained $N = 479{,}232$ data sample values and $2\Delta fT = 191.69$. The inequality $N \geq 2\Delta fT$ is unequivocally satisfied. Next, the Nyquist cutoff or folding frequency f_c is expressed as:[96]

$$f_c = \frac{1}{2\Delta t}, \tag{4.11}$$

where Δt is the time resolution interval of 1/100MSa/s or 10 ns. The DES spectroscopic settings produce an f_c = 50 MHz which is required to be well above the voltage mean square value at the measurement frequency range. Due to the band-pass filter setting of 20 -30 kHz, this is not an issue experimentally. The minimum frequency resolution bandwidth f_m available from the data field is:[96]

$$f_m = \frac{1}{N\Delta t}, \tag{4.12}$$

which equates to 208.67 Hz for the experimental investigation reported in this document.
As mentioned in Section 3.2.1, the experimental data record of voltage fluctuations is equivalent to the appropriate PSD (voltage or thermal). Therefore, the inverse discrete Fourier transform is numerically calculated to obtain the relevant ACF. During the numerical inverse Fourier transform process however, the result is subject to a bias error due to a circular effect in the calculation procedure.[96] The typical method used to alleviate this numerical anomaly is to create a new data record of *zeros* with length equal to $1/2(2^n)$ where n is the number of data points to be numerically calculated by the Fourier transform algorithm. For example, consider an inverse Fourier transform algorithm that can accommodate 4096 data points. Numerically, the analysis uses 2048 data points of actual voltage PSD data while zeros are inserted into the remaining 2048 data points. Upon algorithm completion, one discards the results for $t > 1/2(2^n)$ and keeps the valid data occupying the temporal range $0 \le t \le 1/2(2^n)$.[96] Moreover, a further correction factor is required to remove the ramp bias error over the range $0 \le t \le 1/2(2^n)$ which is given by:[96]

$$\Gamma_V(t) = \frac{T}{T-t}\hat{\Gamma}_V(t), \tag{4.13}$$

where $\hat{\Gamma}_V(t)$ is the ACF result that was "padded" with zeros before inverse transformed. It should be made perfectly clear that although the voltage PSD is used in the above example and equation (4.13), the numerical process applies to the thermal PSD as well.

As part of the experimental setup and calibration, the measurement of the equipment gain and impedance factor $Z(f_0)\Delta f$ defined in equations (3.6) – (3.8) must be determined.[94] To measure $Z(f_0)\Delta f$, the experimental material typically located at the sample mounting location is replaced with an oscillating source. This work used a BK Precision Model 4010A function generator set to sine wave output. The function generator sine wave output must be attenuated due to the large gain of the SR554 transformer and SR560 amplifier combination. A voltage divider circuit was used which had an attenuation α of 0.00065. The BK precision oscilloscope was then used to alternatively record the input and output voltages V_{in} and V_{out}, respectively. The function generator was then incrementally stepped from 0 to 50 kHz in 1 kHz steps. The oscilloscope was used to confirm the exact 1 kHz frequency output at each incremental setting. The amplifier system response expressed as $\left(V_{out}/\alpha V_{in}\right)^2$ defines the equipment gain/impedance factor through the expression:[94]

$$Z(f_0)\Delta f = \int_0^\infty \left(V_{out}/\alpha V_{in}\right)^2 df\ . \tag{4.14}$$

As indicated by equation (4.14), numerical integration of the measured $\left(V_{out}/\alpha V_{in}\right)^2$ over the encompassing band pass filter settings results in the impedance/gain factor $Z(f_0)\Delta f$ specific to the

experimental setup. A typical calibration plot is shown below in Figure 4.24. Using the results of five separate calibration runs, $Z(f_0)\Delta f$ was found to be 6.312×10^{13} Hz.

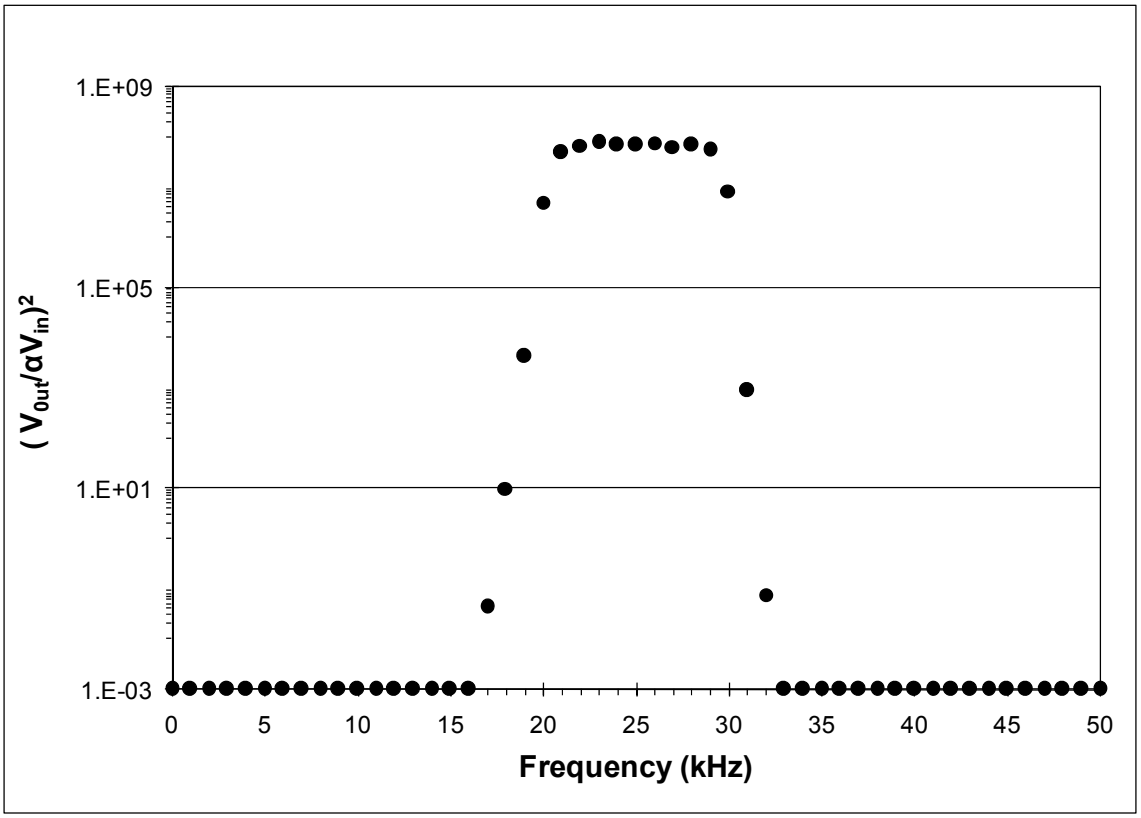

4.24: Typical experimental equipment impedance/gain factor plot representing $Z(f_0)\Delta f$. Five separate calibration runs were performed followed by numerical integration on each impedance/gain factor plot. The result was $Z(f_0)\Delta f$ equivalent to 6.312×10^{13} Hz.

Chapter 5

Experimental Validation and Results of Dynamic Electron Scattering Measurements on Metals with Gaseous Boundaries

5.1 Experimental Scope of Objectives

The primary objective of this chapter is twofold. Of foremost importance, a validation of the DES experiment, methodology and data analysis techniques has been formulated and executed. This fundamental requirement lends credibility to the experimental data on any material. Second, the effects of a gaseous boundary on conductors quantified through experimental results constitutes one of the key components of the central problem detailed in Chapter 1. In accordance with this objective, this chapter shall report the complete experimental results for the electronic transport properties of several metals. The experimental validation method and results are conveyed in Section 5.2. Section 5.3 reports the results of thin metal films, primarily Au and Cu under stationary Ar and He boundary conditions. Section 5.4 reports the results of the Au and Cu thin films placed under non-stationary Ar and He flow conditions. The various gaseous boundaries are selected in an attempt to experimentally answer the central problem of this research: does nanoscale material scattering effects due to gaseous boundaries alter the material transport properties? The experimental results are summarized with a discussion in Section 5.5 which provides an overview of the DES measurement results.

5.2 Dynamic Electron Scattering Experimental Validation by Double Verification Technique

The process used to validate the DES experimental method incorporated a redundant methodology based upon both standard reference materials and a standardized measurement procedure. In summary, Boltzmann's constant was initially obtained by DES measurements on a copper sample through well established techniques.[94,117] This was followed by DES data collection on a US National Bureau of Standards (NBS) standard reference material stainless steel 1461 sample, which allowed comparison to the NBS published values of resistivity. See Appendix E for the NBS Certification sheet and relevant values of electrical resistivity and thermal conductivity. Subsequent measurements were then performed on the NBS 1461 sample using the collinear four-probe resistivity method. This allowed a second data correlation point in conjunction with NBS published values to help validate the experimental results. Finally, the Seebeck coefficient was obtained by DES measurements on a Pb sample which is a recognized standard reference material amongst the transport property experimental community.[30,118] The Seebeck coefficient results then allowed comparison to the widely accepted published values by Roberts.[118] Unfortunately, there is no standard measurement technique comparable to the four-probe method to validate the electronic thermal conductivity. Hence, the validation of the resistivity will serve to also validate the electronic thermal conductivity measurements with the contention that the rigorous Green-Kubo technique will stand to cross-validate the experimental method.

All experimental data and results reported in this paper were obtained between 10 kHz and 30 kHz or equivalently, 20 kHz Δf. The data collection procedure consisted of acquiring 120 oscilloscope screen captures of the sample voltage fluctuations. To elaborate on the opening

summary of this section, Boltzmann's constant was determined by the use of a 0.079 mm (40 gauge) diameter deoxidized annealed copper wire of 99.999% purity obtained from Alfa Aesar Co. Due to the sample holder contact pads constructed of copper, a similar material was chosen to eliminate the possibility of thermoelectric affects during heating. Overnight vacuum was executed before each data acquisition period and measurements were taken at approximately 15 mTorr. Voltage fluctuation data was collected at three temperatures; 298 K, 355 K and 383 K. The experimental values of $k_B T$ are plotted in Figure 5.1 versus temperature T. A least-squares fit results in $k_B = 1.357 \times 10^{-23}$ and extrapolation of the line indicates an abscissa intercept of 90 mK. These results are in good agreement with the accepted values of 1.3807×10^{-23} J/K and 0 K intercept. Moreover, the successful measurement of Boltzmann's constant indicates that the fluctuation spectra is that from the copper sample only simply because the resistive heating changed the sample material temperature only. Therefore, the DES data response to the increased sample temperature indicates the specific noise measurement of the sample only. Stated in other words, we contend that the data represents that of the Cu wire sample only. This conclusion is important with respect to experimentally verifying the general experimental setup such as equipment, data leads, coaxial cables, etc.

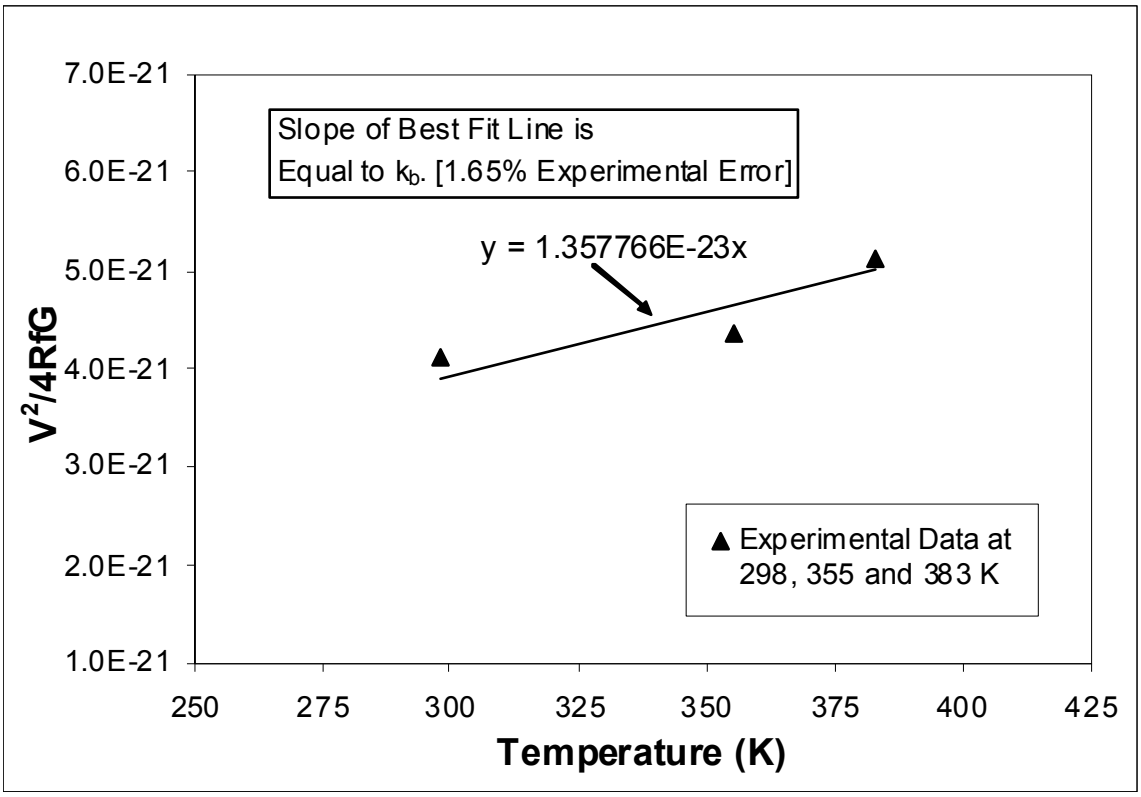

Figure 5.1: Plot of $k_B T$ vs T for the macroscale deoxidized annealed copper sample. Good agreement with the accepted value of $1.3807 \times 10^{-23}\ J/K$ was found which helps to validate the experimental setup and data acquisition system.

To continue the validation methodology outlined in the opening of this section, fluctuation data was collected at 298 K on NBS 1461 stainless steel. A 1 mm thick slice was cut from the round NBS 1461 rod material which measured 12.67 mm in diameter. The 1 mm slice was then carefully machined down to a fine wire measuring 1.3 ohms resistance. The experimental data analysis steps summarized in Section 3.3 were used to obtain all DES results and transport property measurements. Figure 5.2 provides a typical set of both DES squared voltage fluctuations and the corresponding ACF numerically calculated from equation (3.15) and (4.13). Equation (3.56) was used on the inverse Fourier transformed data to obtain the

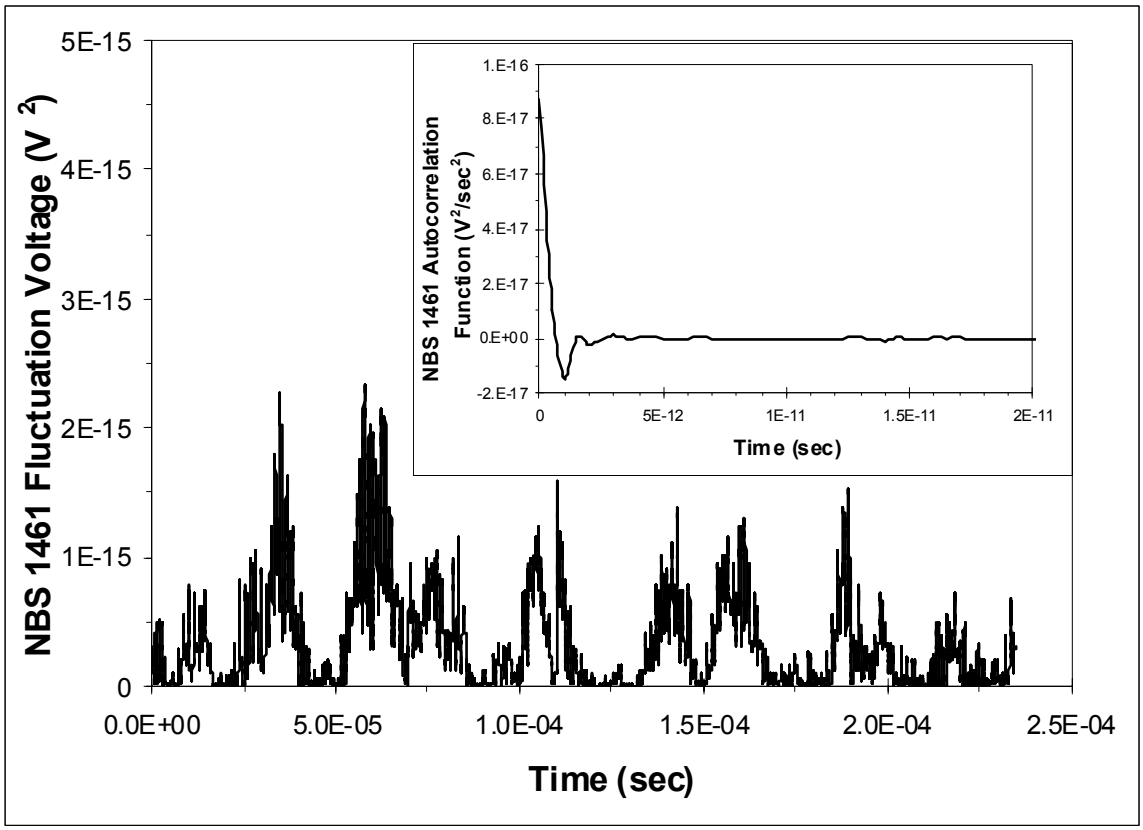

Figure 5.2: Standard reference material NBS 1461 sample voltage fluctuation squared and corresponding ACF. Note the initial ACF exponential decay followed by oscillatory behavior, which dampens at approximately 4 ps.

experimental electronic relaxation time. The electrical resistivity was then obtained through the Green-Kubo equation (3.36). The electronic thermal conductivity was also measured by using equation (3.46) and compared to NBS published thermal conductivity (see Appendix E for NBS Certificate of data) for a qualitative assessment. Obviously, the NBS value encompasses both electronic and lattice contributions and should be higher than the DES results. In addition to validating the DES methodology and theory through the use of a standard reference material, additional resistivity measurements were taken by the widely accepted four-point collinear probe technique. The rationale behind the additional measurement lies in the goal of obtaining comparative fluctuation measurements to a standard experimental method, i.e. the four-probe

technique. Section 4.2.3 of Chapter 4 gives the experimental details and setup of the four-probe measurement station. A second slice of NBS 1461 measuring 12.67 mm in diameter and 1.11 mm thick was cut from the master sample and used for the four-probe experiment.

Table 5.1 gives relative results of resistivity, thermal conductivity and the Lorenz number for both the Cu and NBS 1461 reference materials. The agreement between NBS published values and fluctuation and four-probe resistivity is within 1.1% and 3.9% respectively. Additionally, the DES resistivity is within 5% of the four-probe measurement. The experimental results of resistivity compared to the NBS values are considered excellent and multiple DES runs showed stable repeatability of the data. Resistivity measurements of the Cu sample were higher than the published value,[120] which is attributed to the inevitable variability in deoxidized annealed copper wire properties due to manufacturing methods. Experimentally however, the DES resistivity was within 9.9% of the four-probe value thus lending confidence to the DES Cu resistivity data. The DES electronic thermal conductivity is noted to be approximately 65% of the NBS value, which makes qualitative sense considering the lack of phonon contribution to the data. Regarding the Cu electronic thermal conductivity measurement, the decreased value compared to the reference value[121] is expected due to the reference material being pure soft copper instead of deoxidized annealed wire. A thorough literature search has revealed no published values of the Lorenz number for NBS 1461 and it appears that Table 5.1 contains the first reported measurement. Furthermore, the Lorenz number for pure copper[121] shown in Table 5.1 was used due to the same unavailability of published values for a deoxidized annealed material. It should be noted that the DES Lorenz number of 2.49E-8 $W \cdot \Omega/K^2$ for NBS 1461 is surprisingly close to the theoretical value of 2.45E-8 $W \cdot \Omega/K^2$.[121] The experimental value of the Lorenz number for Cu is found to be approximately 25% higher than the theoretical value.

Deviations of the theoretical value of the Lorenz number are not uncommon however and are attributed to different average relaxation times exhibited by the thermal and electrical currents.[42]

Table 5.1: Comparison of published data values and experimental results of NBS 1461 and deoxidized annealed copper

	ρ_{Ref} $(\Omega \cdot m)$	ρ_{DES} $(\Omega \cdot m)$	$\rho_{4-\text{Probe}}$ $(\Omega \cdot m)$	k_{Ref} $(W/m \cdot K)$	k_{DES} $(W/m \cdot K)$	L_{Ref} $\left(W\Omega/K^2\right)$	L_{DES} $\left(W\Omega/K^2\right)$
NBS 1461	[a]8.1E-7	8.01E-7	8.42E-7	[a]14.32	9.28	N/A	2.49E-8
Cu	[b]2.03E-8	2.803E-8	2.525E-8	[c]385	325.5	[c]2.2E-8	3.06E-8

[a]NBS Certificate data, see Appendix E, [b]Deoxidized annealed Cu, see Ref. 120, [c]Pure Cu value, see Ref. 121

Tables 5.2 and 5.3 provide additional experimental DES data from the NBS 1461 and Cu samples with good agreement found between the experimental and theoretical power spectral densities and Johnson/Nyquist noise. The higher measured mobility of Cu relative to NBS 1461 agrees with the corresponding larger diffusion coefficient. The diffusion coefficient however, is noted to differ by an order of magnitude between the two materials and this brings forth a noteworthy finding. During the course of this research, it was found that the use of the ACF method to determine electrical and thermal conductivities produced much higher experimental accuracy and repeatability than the use of the relaxation time method. This is attributed to the intrinsic physics encompassed by each physical value. The ACF naturally and clearly reveals energy and momentum exchange coupled with relaxation processes albeit hidden in the subtle differences in the integrated value of this sensitive function. All data to date indicates that the ACF contains a certain fine structure that reveals these energy and momentum processes. In

contrast, the relaxation time reflects an *average* time between electron collisions and is incapable of encompassing the temporal energy and momentum exchange processes so elegantly captured by the ACF.

Table 5.2: Experimental and theoretical voltage and thermal power spectral densities and Johnson/Nyquist noise values for the standard reference material NBS 1461 and deoxidized annealed copper

	S_{Q-DES} (W/Hz)	$S_{Q-Theory}$ (W/Hz)	S_{V-DES} (V^2/Hz)	$S_{V-Theory}$ (V^2/Hz)	$\sqrt{V^2}_{DES}$ (V)	$\sqrt{V^2}_{Theory}$ (V)
NBS 1461	4.54E-21	4.11E-21	2.39E-20	2.14E-20	21.88E-9	20.69E-9
Cu	4.62E-21	4.09E-21	1.01E-19	9.05E-20	44.73E-9	42.56E-9

Table 5.3: DES electron velocity diffusion coefficient, relaxation time and mobility for the standard reference material NBS 1461 and deoxidized annealed copper

	D_e (m^2/sec)	τ (sec)	μ $(m^2/V\cdot\text{sec})$
NBS 1461	1.78E-29	2.351E-13	0.0413
Cu	1.15E-28	3.751E-13	0.0458

The method formulated to validate the Seebeck coefficient entailed DES measurements on the thermoelectric standard material Pb. The Pb sample consisted of a 0.5 mm diameter Pb wire of 99.999% purity obtained from the Alfa Aesar Co. The sample was carefully wound to fit properly into the sample holder and measured 3.24 ohms at 298 K. DES data collection was

executed at a sample temperature of 298 K. The experimental data analysis steps summarized in Section 3.3 were used to obtain all DES results and transport property measurements. Of specific note for this validation run is the use of the cross-correlation function given by equation (3.24). The DES experimental results produced an absolute Seebeck coefficient of 1.19 $\mu V/K$ which is within 13% agreement with the published value of -1.05 $\mu V/K$. This result requires some further explanation. The existence of negative Seebeck coefficients is not uncommon in metals and is usually attributed to the Fermi surface extending past the Brillouin zone.[122] Traditional thermoelectric experiments determine the sign of the Seebeck coefficient by noting the measured voltage slope (positive or negative) during the application of a thermal gradient.[30] DES experiments however, are run under thermal equilibrium conditions and directly measure the *absolute* Seebeck coefficient in lieu of the *relative* Seebeck coefficient of traditional experiments. Therefore, the determination of the Seebeck coefficient sign is a subject of further work. Additional results from the Pb sample are electronic thermal conductivity of 27.12 W/m-K and Lorenz number of 1.56E-8 $W \cdot \Omega/K^2$. The published values of Pb thermal conductivity (including both electronic and lattice contributions) is 35.08 W/m-K and Lorenz number equal to 2.49E-8 $W \cdot \Omega/K^2$.[123] The DES thermal electronic conductivity is approximately 77% of the total thermal conductivity which makes quantitative sense with respect to the electronic contribution only. The DES results are considered excellent with respect to the thermoelectric Seebeck coefficient.

A concluding overview of the above validation method and comparative results indicates that the theoretical foundation and corresponding DES experiment are producing repeatable and valid experimental data.

5.3 Dynamic Electron Scattering Experimental Results on Au and Cu Thin Films Subject to Stationary Pressurized Gaseous Boundaries

5.3.1 Experimental Motivation Behind Using Au and Cu Thin Films Interfaced with Noble Gases

The experimental investigation of Au and Cu thin films was motivated by the central research problem components detailed in Chapter 1. To reiterate one of the primary motivations of this research, the large surface area to volume ratio raises the possibility of gaseous surface scattering effects that may perturb the material transport properties. Therefore, the fundamental objective of this entire work enjoys a concentrated existence in the remainder of this chapter. Each experimental design and intent is focused on attempting to measure a conductors electronic transport properties and any perturbations that may exist under various gaseous boundary conditions. In conjunction with the conducting material objectives, noble gases were chosen as the bounding scatterer. Thus, the possibility of chemical reactions or bonding between the subject gas and conductor is minimized due to the inert character of the gas. Theoretically, this should allow material effects to be centered primarily around pure scattering between the gas particle and material surface. Stated in other words, the scattering effects due to inelastic and/or elastic interactions alone is experimentally desired. The gas adsorption process is of course present and unavoidable however, the experimental results have shown a fairly clear distinction between the two effects. Helium was selected to allow measurements of a light particle with large collision density while Argon was selected to obtain data on a heavy particle with a somewhat smaller collision density. From a scattering standpoint of a *flowing* gaseous medium, the gas particle mass and collision density are not the only factor at play here. The wave vectors of He and Ar are correspondingly different which has a direct impact on the electron jellium with

respect to electrical and thermal transport.[124] Additionally, the gas wave vectors change as a function of bulk gas velocity which applies to the non-stationary flow experiments performed during this research effort. Specifically, the gas wave vectors increase due to the decreasing DeBroglie wavelength as bulk gas velocity increases. This effect is due to the gas wave vector q_g expression:

$$q_g = \frac{2\pi}{\lambda_{DB}}, \tag{5.1}$$

$$\lambda_{DB} = \frac{h}{p} = \frac{h}{\left[m_g\left(v_g + U\right)\right]}, \tag{5.2}$$

where λ_{DB} is the gas DeBroglie wavelength, m_g is the gas particle mass, v_g is the mean gas particle velocity and U is the bulk gas flow velocity. The Ar and He wave vectors and DeBroglie wavelength characteristics were analyzed at the bulk flow velocities used experimentally during this work (see Section 4.2.2). The gas wave vector/wavelength analysis is shown in Figure 5.3 below. The Ar wave vector is larger than the He wave vector whether stationary or flowing. We find that as the gas incident energy E_i increases, the Ar wave vector increases much faster than the He wave vector. It is important to note that the gas wave vector is a function of the bulk gas velocity, therefore, the stationary gas experimentation detailed in Section 5.3.4 does not undergo the transient wave vector behavior just described.

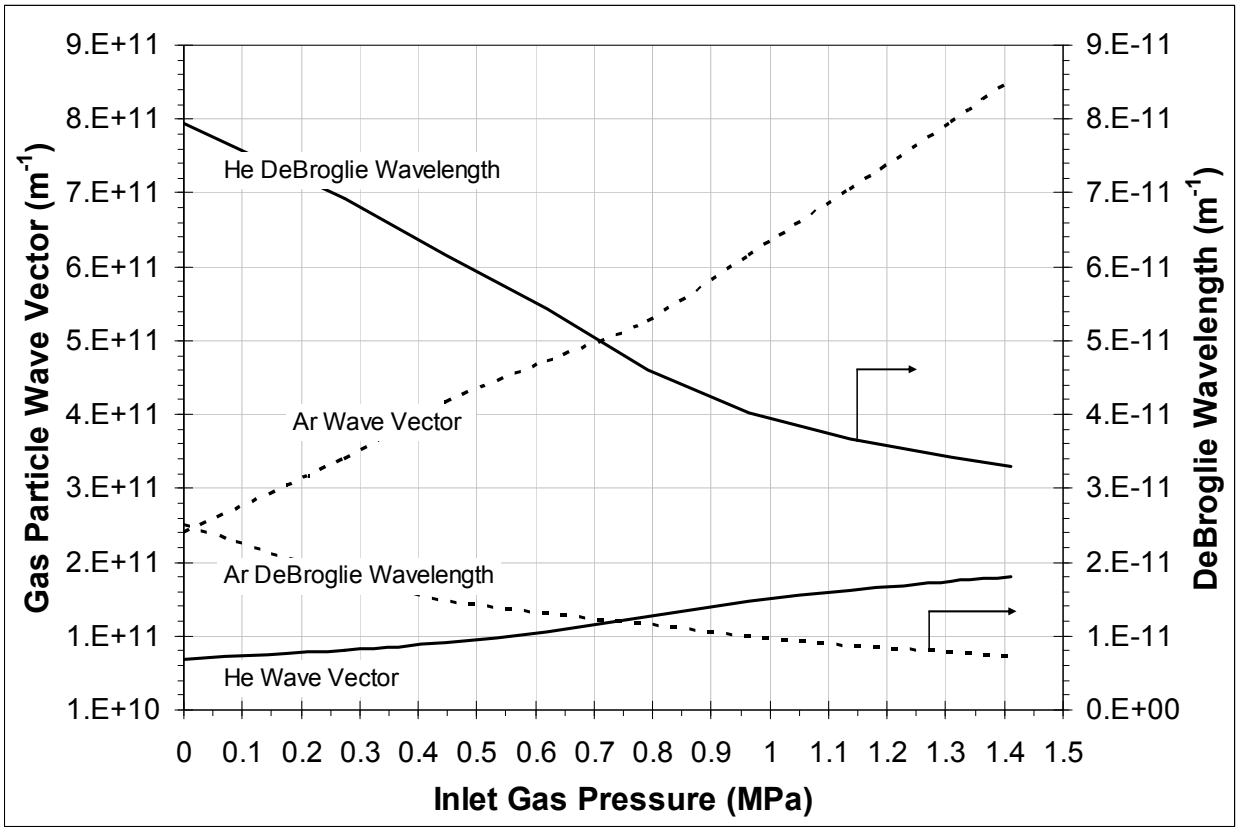

Figure 5.3: Ar and He gas particle wave vectors and corresponding DeBroglie wavelengths corresponding to the inlet gas pressure used during the experimental non-stationary runs of Section 5.4.

As a final observation, the impact energy E_i range of both gases allowed a great deal of experimental ground to be covered, especially with respect to encompassing elastic and inelastic phonon scattering.[36]

In addition to the above objectives, electronic noise is of fundamental importance in nanoscale materials,[125] especially with regards to electronic devices. Fundamental transport properties such as electron diffusion and drift velocity can be affected by low dimensional confinement,[85,126] which can ultimately affect device operation. Therefore, the measurement of the velocity diffusion coefficient D_e, electron relaxation time τ and mobility μ in high application materials such as Au and Cu is pertinent, especially in the nanoscale regime.

Furthermore, the electrical resistivity and thermal conductivity are known to deviate in thin films due to electron confinement and the corresponding surface scattering effects.[127-128] Clearly, this points to a possible change in the Lorenz number and associated Wiedemann-Franz law,[42,129-130] which can now be measured directly by the DES method.

In order to investigate the above parameters, especially with respect to a large surface area to volume ratio, 30 nm thick Au and Cu samples were chosen to provide dimensional confinement in one direction to the average electron mean free path of approximately 39 nm.

5.3.2 Au and Cu Thin Films Material Characterization

The Au and Cu samples consisted of 30 nm thin films deposited by electron beam evaporation on glass slides and supplied by Lebow Co. of California. The Cu samples were left in their unannealed state. One set of Au samples was annealed to gather comparative data to unannealed Au. The annealing procedure included a four hour linear ramp up from room temperature to 525 K. The Au samples were then held at 525 K for 1 hour followed by a six hour linear ramp down to room temperature. Both Cu and Au samples were stored under a N_2 environment for the duration of this research in order to help eliminate any oxidation effects (primarily to the Cu samples). Surface characterization of the Cu samples only was performed through Atomic Force Microscopy (AFM). The primary objectives of the AFM study was to obtain information on the grain size, RMS surface roughness and the presence (or not) of any material voids. The primary results of the AFM study are shown below in Figures 5.4 – 5.10. At the 1 μm AFM scan setting, the grain size was approximately 13.538 nm and the RMS roughness was approximately 7.564 nm. The surface morphology shown in Figure 5.7 and 5.8 indicate that

no voids or island formations appear to be present. At the 1 nm AFM scan setting, the grain height is approximately 3.629 nm and the RMS roughness is approximately 1.086 nm.

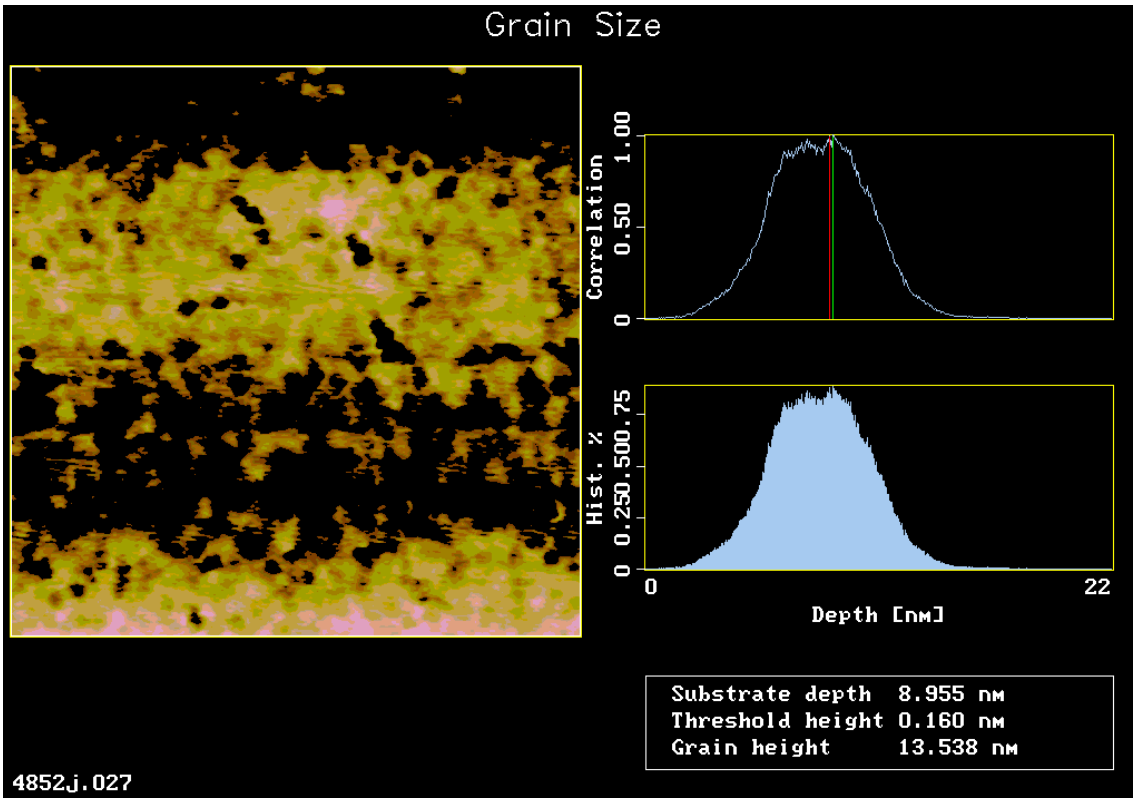

Figure 5.4: AFM grain size results at a scan setting of 1 μm. The grain height is approximately 13.538 nm.

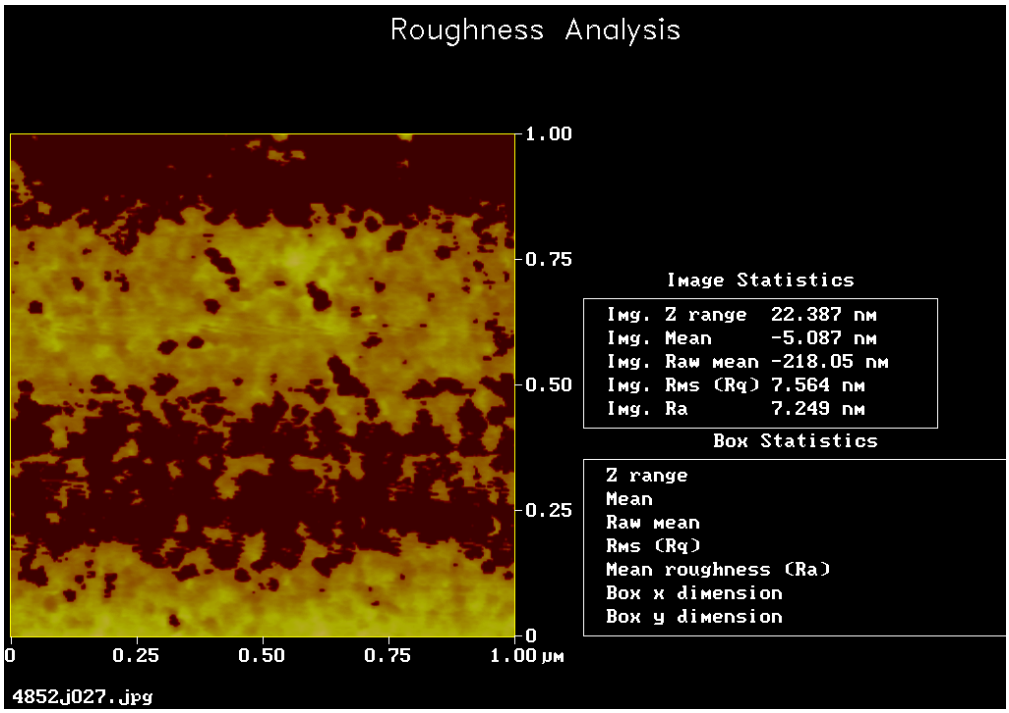

Figure 5.5: AFM roughness results at a scan setting of 1 μm. The RMS roughness is approximately 7.564 nm.

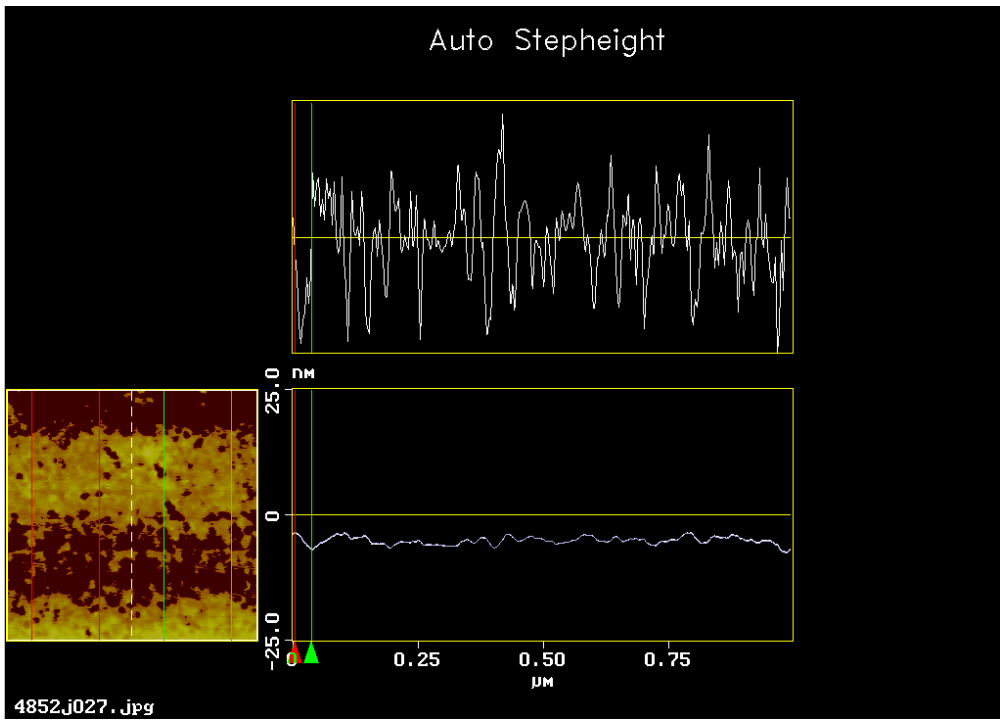

Figure 5.6: AFM auto step height results at a scan setting of 1 μm.

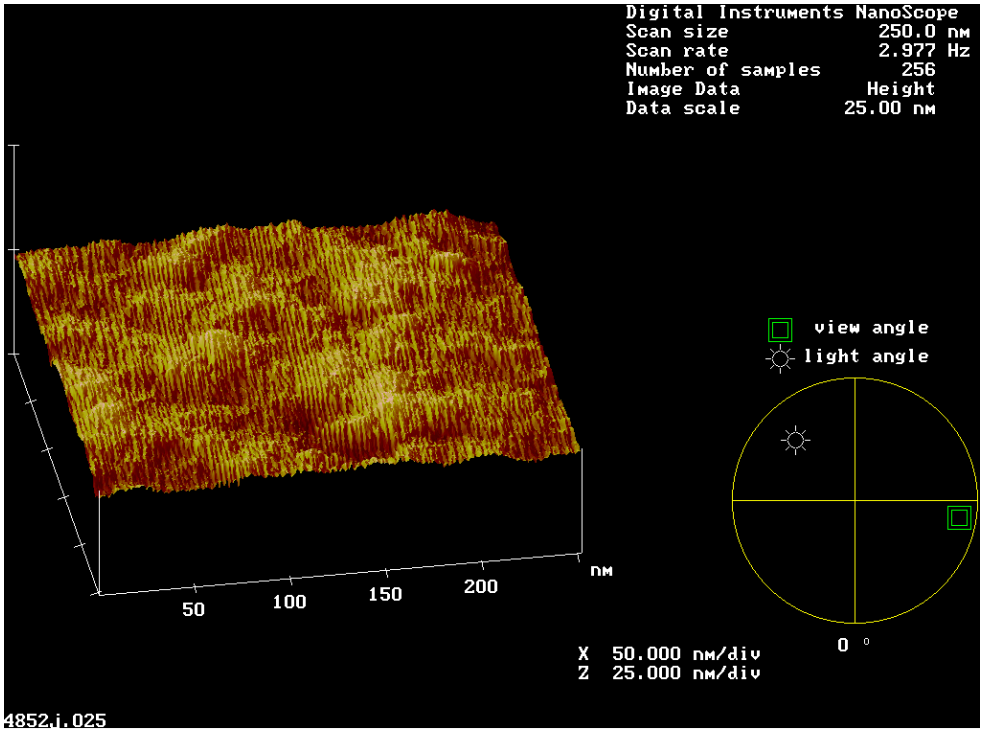

Figure 5.7: AFM surface morphology at a scan setting of 250 nm. There are no indications of material voids or island formations.

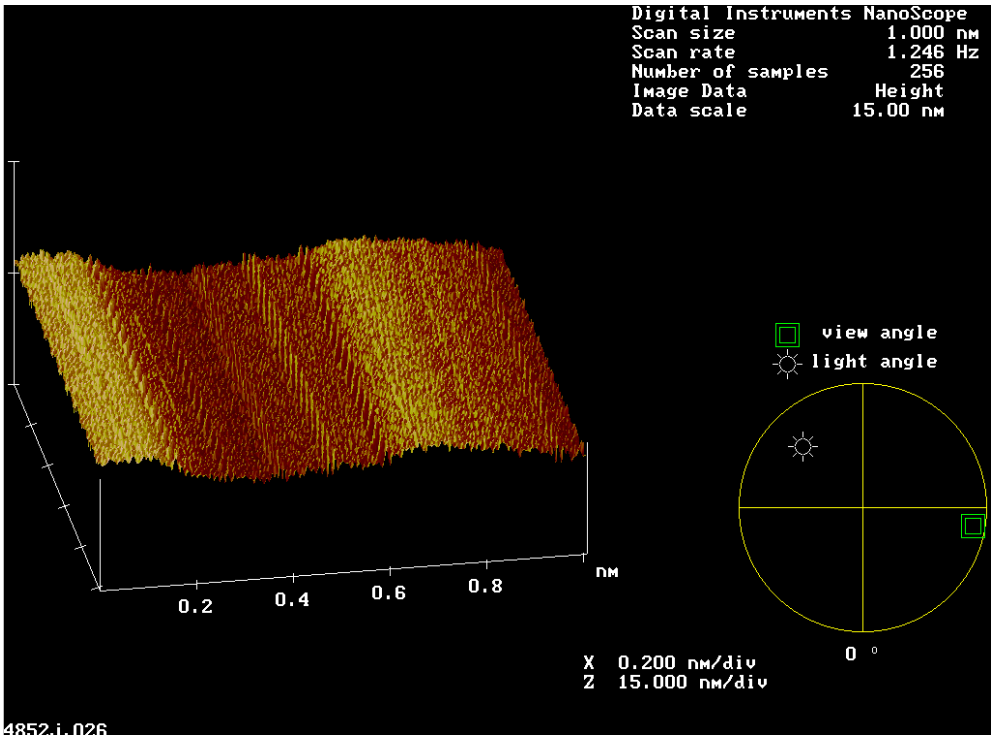

Figure 5.8: AFM surface morphology at a scan setting of 1 nm.

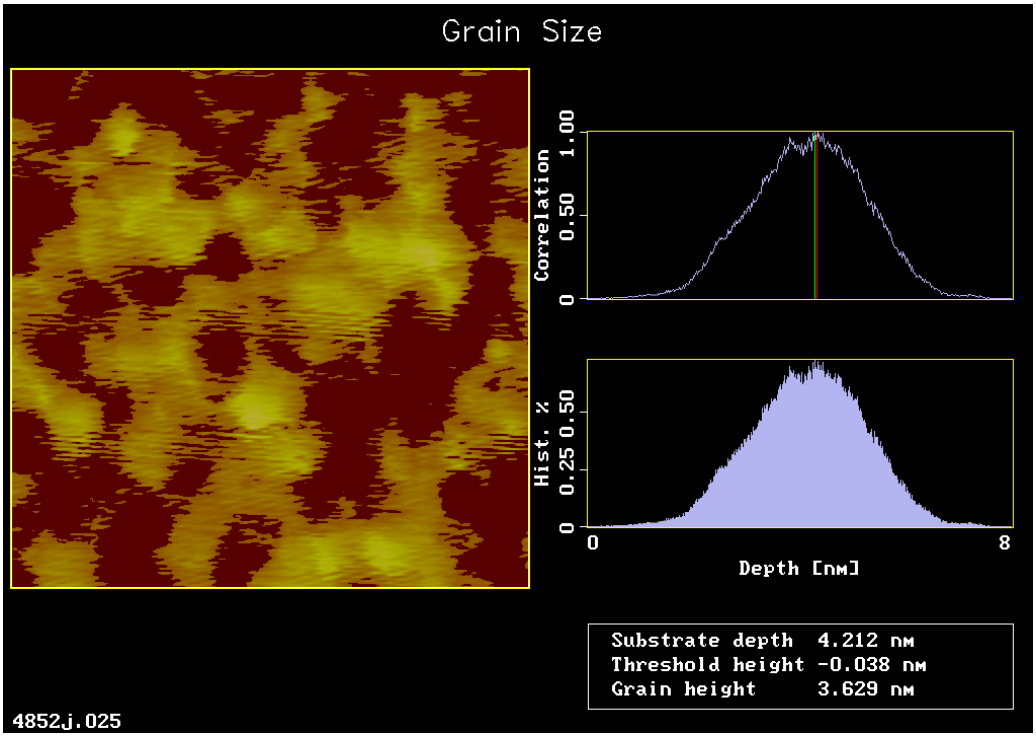

Figure 5.9: AFM grain size results at a scan setting of 250 nm. The grain height is approximately 3.629 nm.

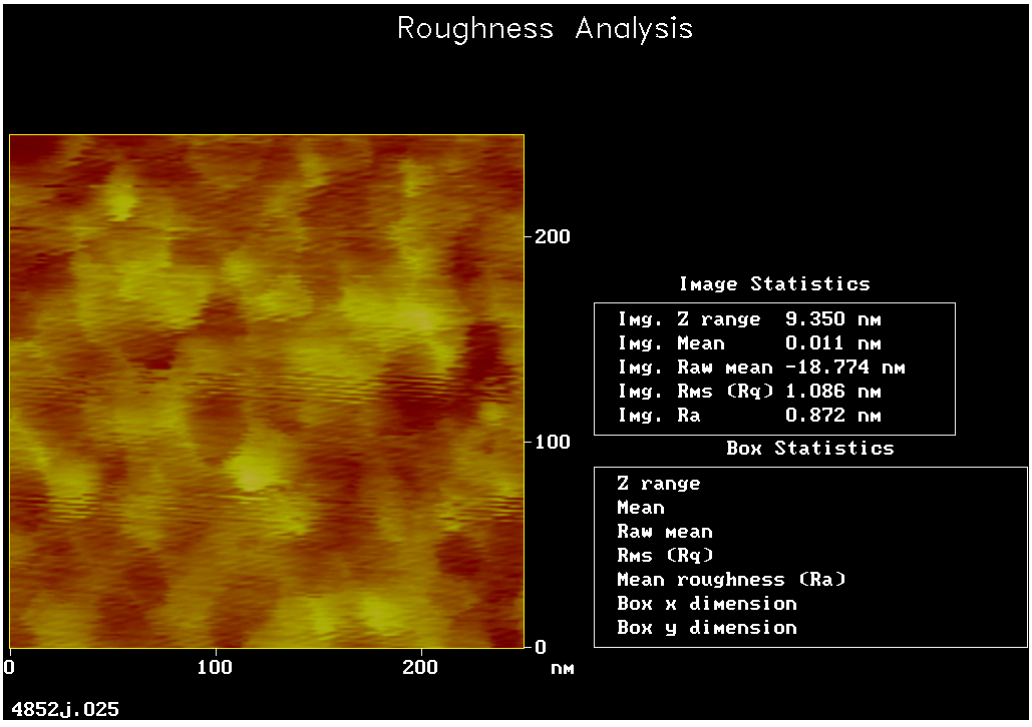

Figure 5.10: AFM roughness results at a scan setting of 250 nm. The RMS roughness is approximately 1.086 nm.

Each experimental sample was cut to approximately 2 mm x 7 mm to accommodate the vacuum/pressure apparatus sample holder and all measurements were taken at 298 ± 1 K. Helium Grade 4.9 rated at 99.997% purity was used throughout this investigation.

5.3.3 Additional Validation of the DES Experiment Through Four-Probe Resistivity Comparative Measurements on Au and Cu Thin Films

Before progressing straight in to the He pressure experimental results, and in order to further confirm the DES results, four-probe resistivity measurements were taken on both 30 nm Au and Cu unannealed samples. The same four-probe experimental apparatus and method was used on the Au and Cu as that of Section 5.2. A comparison to transport properties reported in the literature was also desired to render completion to the data analysis. Table 5.4 gives comparative results of the resistivity, electronic thermal conductivity and the associated Lorenz number. The DES resistivity measurement agreed within 13.6% and 4.8% of the four-probe data for the Au and Cu samples respectively. The corresponding reference resistivity[131-132] was lower however it is well established that thin film fabrication methods can result in large resistivity variations due to grain boundaries and impurities, especially for unannealed materials.[127] Consequently, higher credibility is given to the DES comparison to four-probe data in lieu of the reference data. The DES results of the electronic thermal conductivity show a larger thermal conductivity for Cu than Au, which agrees with macroscopic values. The generally lower thermal conductivity compared to bulk samples is attributed to increased grain boundaries and surface scattering that is prevalent in thin metal films, especially in the unannealed state. The DES thermal conductivity for Au was found to be approximately 6% lower than the referenced

material[133] while the thermal conductivity for Cu measured approximately 22% lower than the reference data.[134] The lattice thermal conductivity is often quoted to be negligible in good electrical conductors[42] however based upon the data of Table 5.4, this consensus may not apply to nanoscale materials. In fact, the literature base shows no experimental data on electronic thermal conductivity measurements of thin metal films to support this claim. The results shown in Table 5.4 are direct experimental results, which imply that the electronic thermal conductivity for these particular samples is dominant, however it is accompanied by *non-negligible* lattice conductivity, 6% and 27% for Au and Cu respectively when compared to the references.[133-134] The resulting DES Lorenz number for both Au and Cu lies above the theoretical value. The large Cu Lorenz number is credited to the inclusion of inelastic scattering within the elastic landscape, which accompanies thin films and the known fabrication/annealing issues discussed earlier. The Lorenz number from the reference literature is included merely as an order of magnitude value as it is cross calculated from different experimental groups and samples.

Table 5.4: Comparison of DES measurements to 4-probe method and prior published results

	ρ_{Ref} $(\Omega \cdot m)$	ρ_{DES} $(\Omega \cdot m)$	$\rho_{4-\text{Probe}}$ $(\Omega \cdot m)$	k_{Ref} $(W/m \cdot K)$	k_{DES} $(W/m \cdot K)$	L_{Ref} $\left(W\Omega/K^2\right)$	L_{DES} $\left(W\Omega/K^2\right)$
30 nm Au	[a]5.1E-8	5.253E-8	6.081E-8	[c]200	188.6	[e]3.42E-8	3.32E-8
30 nm Cu	[b]6.0E-8	9.682E-8	1.017E-7	[d]326.6	256.5	[e]6.56E-8	8.33E-8

[a]See Ref. 131, [b]See Ref. 132, [c]Thermal conductivity includes both lattice and electronic contributions, see Ref. 133
[d]Thermal conductivity includes both lattice and electronic contributions, see Ref. 134
[e]Lorenz number cross-calculated from corresponding ρ_{Ref} and k_{Ref} data

Tables 5.5 and 5.6 provide additional DES data from the nanoscale samples with good agreement found between the experimental and theoretical power spectral densities and Johnson/Nyquist noise. The *thermal* power spectral density has particular relevance in the spectroscopic scope of DES. This value, although rarely used,[86] expresses fluctuations in energy modes that when considered within the fluctuation-dissipation theory, gives a lucid connection to the electronic thermal conductivity. Furthermore, the thermal PSD at time zero is a function of temperature only. Therefore, the real utility of the thermal power spectral density would be realized in temperature dependent studies coupled with ACF analysis.

The relaxation time of Cu measured slightly larger than the Au sample yet the Cu resistivity is noted to be higher than Au for these particular samples. This again illustrates the fine structure embodied in the ACF as the DES resistivity agrees quite well with the four-probe data yet the relaxation time is counterintuitive. As mentioned earlier, the relaxation time is an average value representing a spectrum of relaxation times within the material. The diffusion coefficient of Au is found to be approximately 54% lower than the Cu sample. This result again points to the possibility of excessive grain structure scattering. The corresponding Au mobility is higher than the Cu, which agrees with the resistivity results.

Table 5.5: Experimental and theoretical voltage and thermal power spectral densities and Johnson noise values for nanoscale Au and Cu thin films

	S_{Q-DES} (W/Hz)	$S_{Q-Theory}$ (W/Hz)	S_{V-DES} (V^2/Hz)	$S_{V-Theory}$ (V^2/Hz)	$\sqrt{V^2}_{DES}$ (V)	$\sqrt{V^2}_{Theory}$ (V)
30 nm Au	3.71E-21	4.12E-21	1.46E-19	1.633E-19	54.22E-9	57.13E-9
30 nmCu	3.77E-21	4.11E-21	3.06E-19	3.35E-19	78.33E-9	81.85E-9

Table 5.6: DES electron velocity diffusion coefficient, relaxation time and mobility for nanoscale Au and Cu thin films

	D_e (m^2/sec)	τ (sec)	μ $(m^2/V \cdot \text{sec})$
30 nm Au	2.16E-28	3.481E-12	0.0311
30 nmCu	3.99E-28	3.538E-12	0.00855

The breadth of spectroscopic information held within DES measurements is now exemplified through analysis of the Au and Cu thin film ACF's. The fact that the ACF contains a great deal of physics manifested by the underlying kinetic landscape of the material is a gross understatement. Qualitative information is observable by visual inspection alone in addition to the sensitive integrated values produced by this function. Figure 5.10 presents the 30 nm Au and Cu autocorrelation functions obtained by DES measurements of the power spectral density $S_V(f_0)$. The initial temporal decay was found to follow an exponential profile up to the first zero axis crossing only. Subsequent oscillatory behavior followed due to rapid energy and momentum transport with the lattice. Closer analysis of the oscillations reveals that multiple frequencies are present. This is attributed to electron confinement in the 30 nm direction and the subsequent increase in observable surface scattering effects. Fundamentally, the lower energy surface phonons or Raleigh waves[135] become a dominant contributor to lattice scattering mechanisms due to the large increase in surface area to volume ratio of nanostructures. This boundary induced phenomena is hypothesized to create an increase in off-diagonal matrix

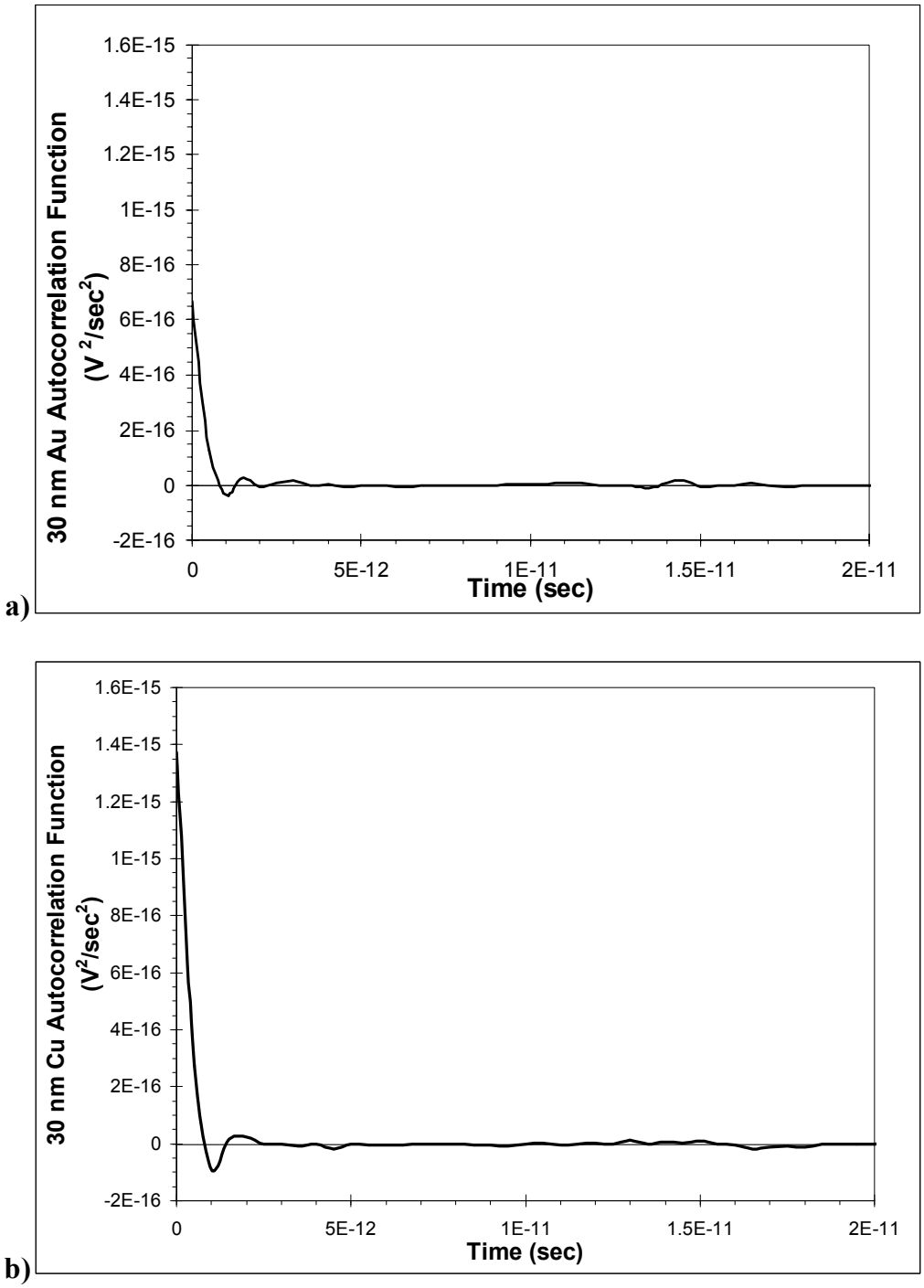

Figure 5.11: Typical autocorrelation function for the Au and Cu nanoscale samples. **a**) The oscillatory behavior of the Au sample following the initial exponential decay is due to energy and momentum exchange processes that are contained in off-diagonal correlation function terms. **b**) The Cu sample ACF shows notable differences in oscillation magnitudes and times. Additionally, the magnitude at time zero is larger than the Au sample due to the higher sample resistance.

contributions to the ACF with underlying energy and momentum terms.[84] The wavelike features evidenced in Figure 5.11 stems from the energy dependence of the various scattering mechanisms including the surface phonons that result in momentum randomizing fluctuations that show up as positive and negative oscillations. This phenomena has been demonstrated numerically through Monte Carlo simulations[80] however the experimental observation of these oscillations in nanostructures, through the DES methodology is indeed remarkable. A comparison of the ACF behavior for the bulk and nanoscale Cu sample is shown in Figure 5.12. The bulk Cu sample relaxation time was measured at 3.751×10^{-13} compared to 3.538×10^{-12} for the Cu thin film, which clarifies the difference in the initial decay slope. Moreover, the decaying oscillations of the nanoscale Cu sample are more pronounced than the bulk sample, which is credited to augmented surface scattering effects. Clearly, these oscillations contribute to the integrals of equations (3.36), (3.46) and (3.51) and reveal a probable deviation in transport properties. This unique observation of electron diffusion phenomena in macro and nanoscale Cu gives the experimentalist valuable data on the inherent change in electron scattering mechanisms due to low dimensional confinement. With regards to autocorrelation functions obtained from the thermal power spectral density $S_Q(f_0)$, identical features to $S_V(f_0)$ were observed.

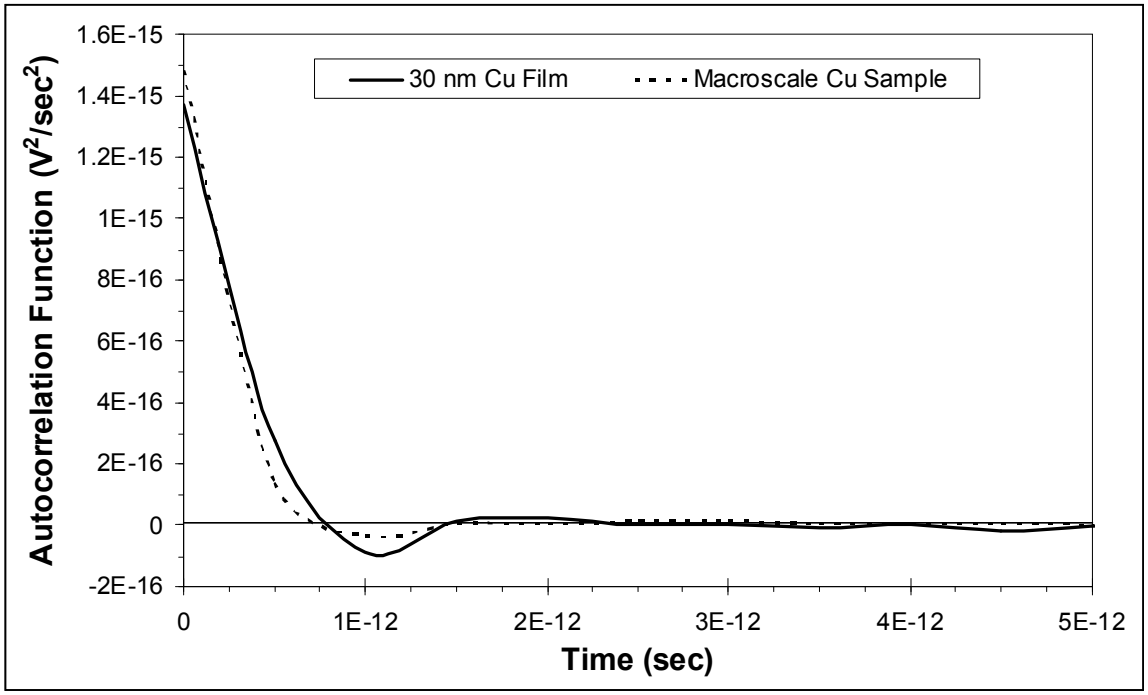

Figure 5.12: Comparison of Cu macroscale and nanoscale autocorrelation function behavior to 5 ps. The macroscale Cu relaxation time was found to be an order of magnitude shorter than the nanoscale Cu. Increased oscillations in nanoscale decay after the zero axis crossing are attributed to increased surface scattering effects. The macroscale decay is found to exhibit increased damping effects compared to the Cu thin film.

With additional validation of the DES experiment now in place, we proceed to the determination of the appropriate He pressures to submit the Au and Cu samples to. Procedurally speaking for both He and Ar, overnight vacuum at 15 mTorr was executed before each data acquisition period and measurements were taken under both 15 mTorr vacuum and 1 atm Ar and He pressure. No differences were noted in the data between vacuum and 1 atm pressure for the Ar/He environments which makes sense when reviewing the gaseous collision density at both of these pressures. Figure 5.13 below shows the He collision density on a 2 mm x 7 mm sample surface over a range of pressures. While it is true that the results of Figure 5.13 show approximately 5 orders of magnitude increase in He collision density at 1 atm over vacuum, the 15 mTorr vacuum calculations still predict approximately 6×10^{17} He gas particle *collisions per*

second. Furthermore, one is reminded that the gas particle impact energy E_i is unchanged at any pressure for stationary flow (approximately 26 meV E_i). Therefore, the conclusion is reached that the 15 mTorr vacuum collision density is not low enough to show a change in electronic

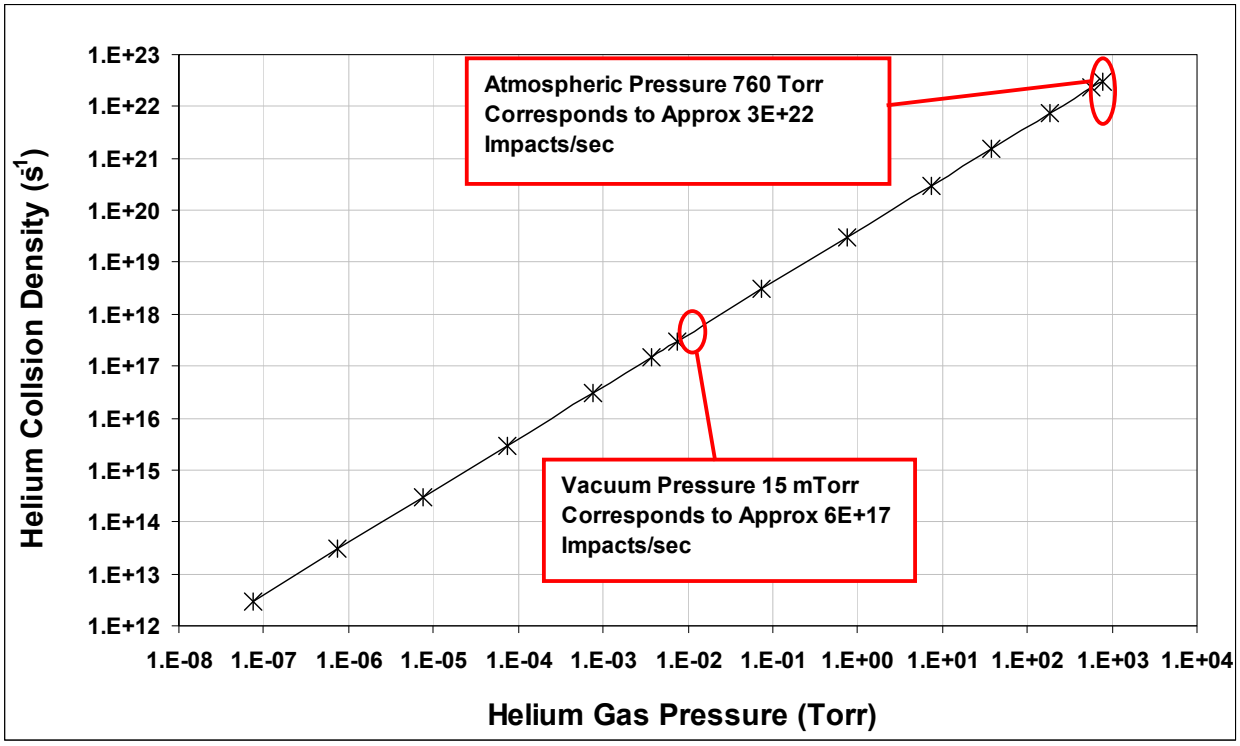

Figure 5.13: The Helium collision density on a 2 mm x 7 mm surface as a function of pressure. The vacuum pressure of 15 mTorr corresponds to the DES experimental vacuum level and 760 Torr corresponds to approximately 1 atm pressure.

transport properties. With this preliminary experimental conclusion in place, the remaining experimental runs under stationary He and Ar (Section 5.3.4) were made at pressures of 118.589 kPa (1.17 atm) and 1418.25 kPa (14 atm). A thorough literature search confirmed the 1418.25 kPa pressure as being well below that required to induce Fermi surface distortion and subsequent resistivity perturbations.[136-137]

Before proceeding to the Au and Cu transport property measurements, the voltage spectral distribution requires analysis. This result is rarely reported experimentally,[86,138] yet is an important parameter to check when determining whether a material exhibits stationary or non-stationary fluctuations. This statement is especially important with regards to nanomaterials. The verification of stationary random variables eliminates *a priori* assumptions and is part of the foundation of thermal noise theory that ensures the experimentalist that the data averages are independent of time.[86] The normalized voltage spectral distribution for Au and Cu presented in Figure 5.14 is found to be Gaussian which agrees with long standing theory[86] and verifies the existence of stationary noise processes. An interesting observation of Figure 5.14b is the increase in fluctuation modes due to the higher resistance of the Cu sample.

a)

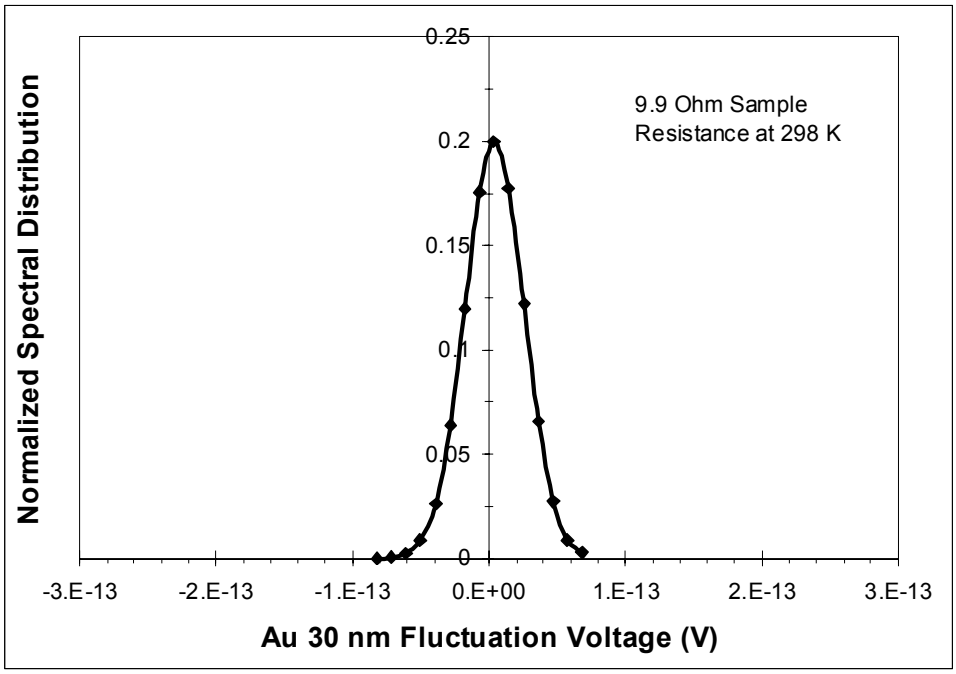

b)

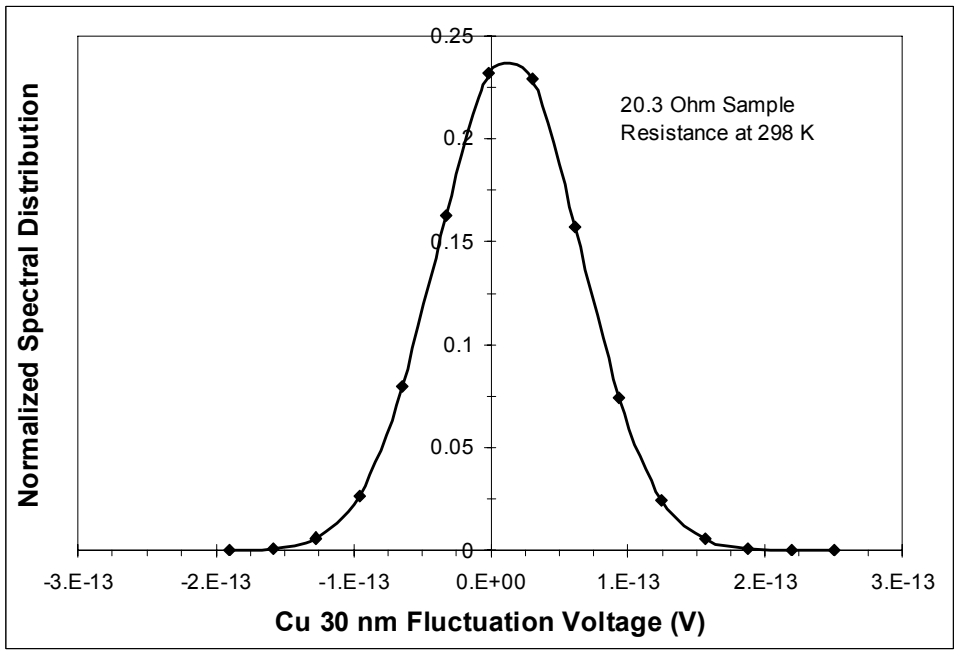

Figure 5.14: Normalized distribution of the experimental voltage fluctuations for the Au and Cu 30 nm samples. **a)** The Gaussian form of the Au voltage fluctuations verifies the existence of a stationary fluctuating process. **b)** The Cu sample also shows a Gaussian distribution with a clear increase in modes due to the larger sample resistance.

5.3.4 Au and Cu Thin Films Under Vacuum, Atmospheric and Pressurized Stationary Helium

The primary objective of subjecting thin metal films to a non-flowing inert gas pressurized environment is to experimentally assess the metal transport properties while increasing the gas collision density only. The use of He is motivated by the experimental goal of obtaining DES measurements with a very low mass gas particle. The gas particle impact energy E_i is unchanged by this process as verified by no change in sample or sample holder temperature during the pressurization process. The experiment was run in three steps with three corresponding data collection points. Experimental step 1 included the addition of He to the sample chamber (see sample chamber Figures 4.1 – 4.4 for details) to raise the pressure from 15 mTorr (overnight vacuum) to 118.589 kPa as determined by the supporting results of Figure 5.13. Data collection was then taken at 118.589 kPa. Step 2 included the pressurization of the sample chamber to 1418.25 kPa which represented the high pressure portion of the experiment. Data collection was then taken at 1418.25 kPa. Step 3 followed by releasing the He pressure and returning to 118.589 kPa with a final data collection session. The experimental motivation behind returning the high pressure environment back to the starting pressure of 118.589 kPa and collecting data was to determine whether any perturbed transport properties followed the return of He pressure back to the starting point.

As mentioned earlier, the Au and Cu samples consisted of approximately 2 mm x 7 mm by 30 nm thin film samples. The Au samples consisted of annealed and unannealed samples while the Cu samples remained unannealed for all experiments in this investigation. The primary experimental results are presented in plot format due to the multiple pressure regimes involved. Furthermore, the Lorenz number results are combined with the gas particle collision density to allow an assessment of any differences in the electric and thermal relaxation times

induced by a distinct change in surface scattering events. Experimentally, the transport coefficient ratio expressed by the Lorenz number (see equation (3.54) is found to provide useful quantitative information through controlled gaseous boundary condition changes.

Figures 5.15 and 5.16 below shows the results of Au and Cu voltage and thermal PSD's at each He pressure cycle regime. The Au voltage PSD of Figure 5.15 was found to decrease due to annealing of the sample which is expected, due to the drop in measured sample resistance after annealing. The thermal PSD however, is noted to be nearly identical for both unannealed and annealed samples. This is expected due to the thermal PSD dependence on temperature only. A minor decrease in both PSD's is also noted at high pressure. This decrease directly corresponds to a small decrease in the mean square fluctuating voltage. Upon return to the 118.589 kPa pressure, all PSD's closely return to their original values thus suggesting a correlation with He pressure.

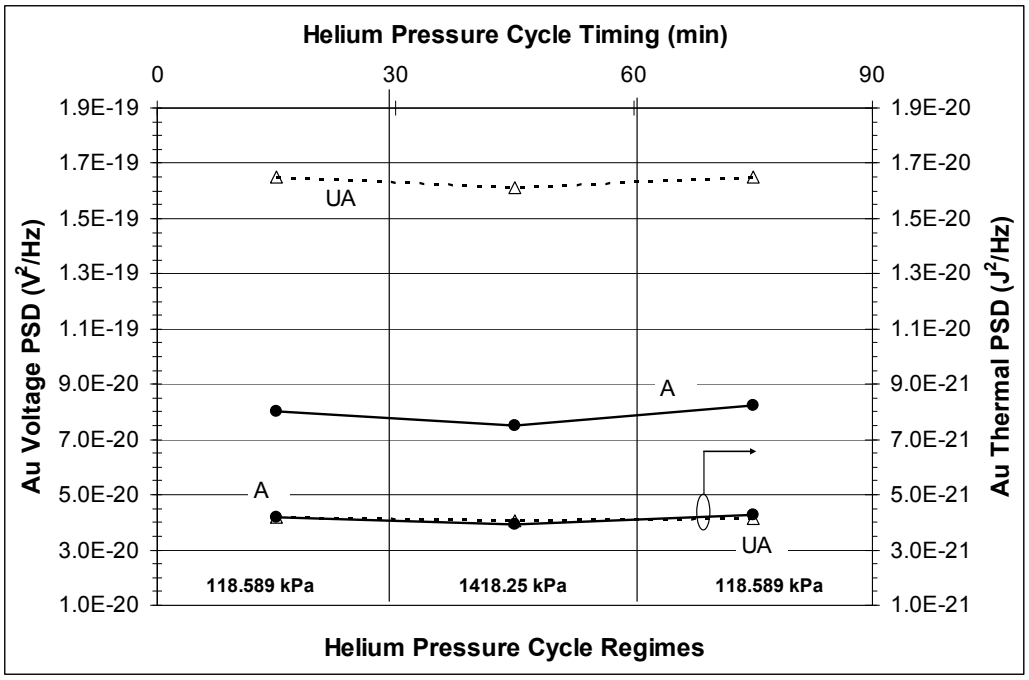

Figure 5.15: The Au voltage and thermal PSD results are shown for the three experimental He pressure cycles. Unannealed (UA) and annealed (A) Au samples were used as indicated by the open triangles (dashed line) and solid circle markers (solid line) respectively.

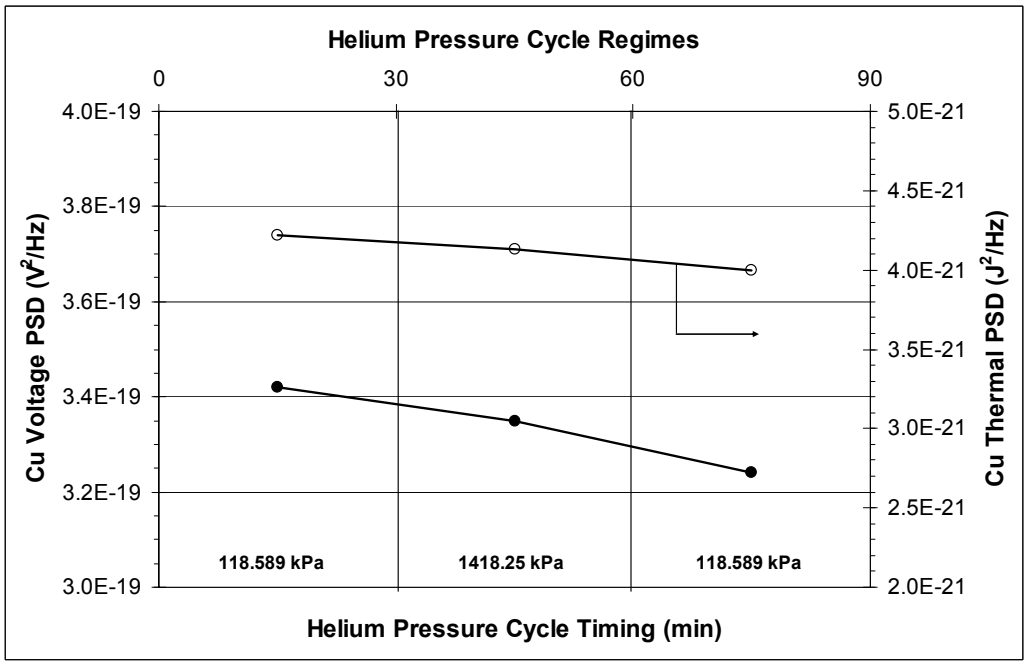

Figure 5.16: The Cu voltage and thermal PSD results are indicated by the solid circle markers and open circles respectively for the three experimental He pressure cycles. Unannealed Cu samples were used throughout this investigation.

Figures 5.17 and 5.18 below show the results of Au and Cu electronic thermal conductivity and electrical resistivity at each He pressure cycle regime. The unannealed Au shows a clear change in both thermal conductivity and resistivity at the high pressure regime. The annealed Au sample indicates similar thermal conductivity behavior however differs in resistivity. There is a slight resistivity increase for the annealed sample throughout each pressure stage. This behavior is probably due to different electric scattering relaxation times than the thermal current. The Cu sample of Figure 5.18 reveals a distinct change in both thermal conductivity and resistivity due to high pressure and returns closely to the original value at the final experimental pressure regime.

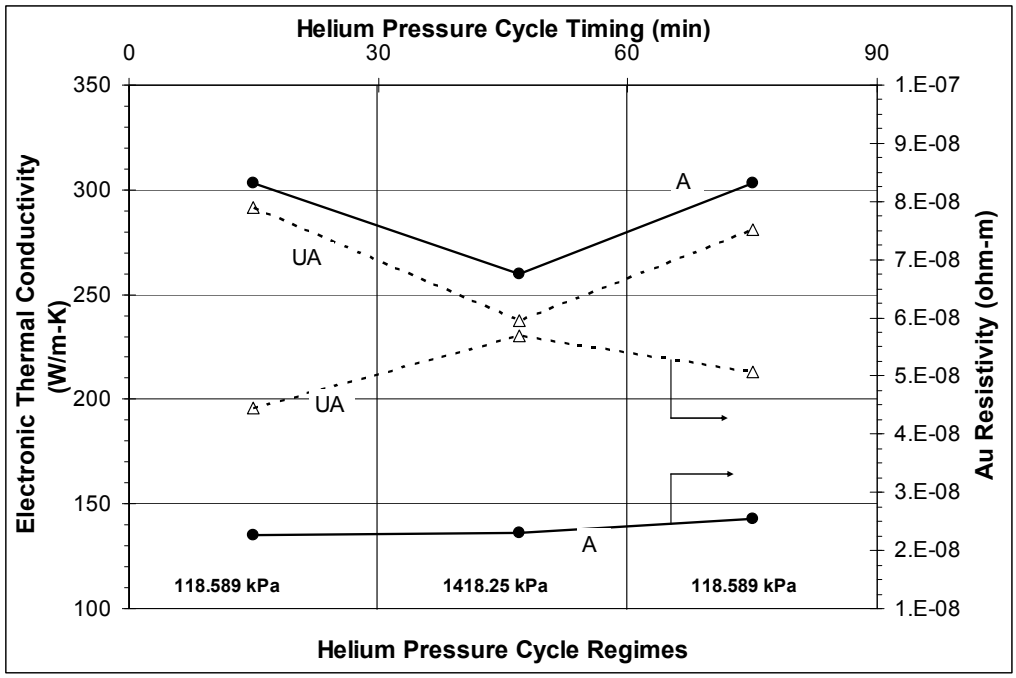

Figure 5.17: The Au electronic thermal conductivity and electrical resistance results are shown for the three experimental He pressure cycles. Unannealed (UA) and annealed (A) Au samples were used as indicated by the open triangles (dashed line) and solid circle markers (solid line) respectively.

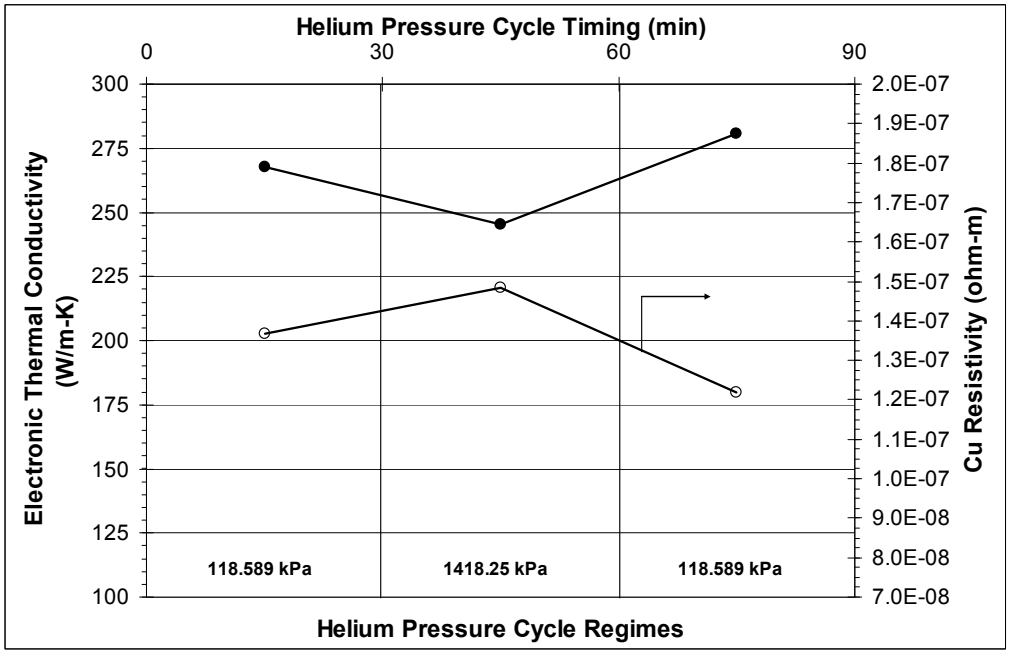

Figure 5.18: The Cu electronic thermal conductivity and electrical resistivity results are indicated by the solid circle markers and open circles respectively for the three experimental He pressure cycles. Unannealed Cu samples were used throughout this investigation.

In order to gain a comparative assessment of the gaseous boundary on both nanostructures and bulk materials, the bulk Cu sample used in Section 5.2 was also placed under the same pressure regimes as the Au and Cu thin films. The motivation behind this experiment was to compare the results with the arguments put forth in Chapter 1; that gas particle scattering on nanosurfaces could possibly perturb material transport properties. The results for the bulk Cu electronic thermal conductivity and resistivity are shown in Figure 5.19. Compared to the results of the 30 nm Cu sample, there is basically no response to the high pressure He.

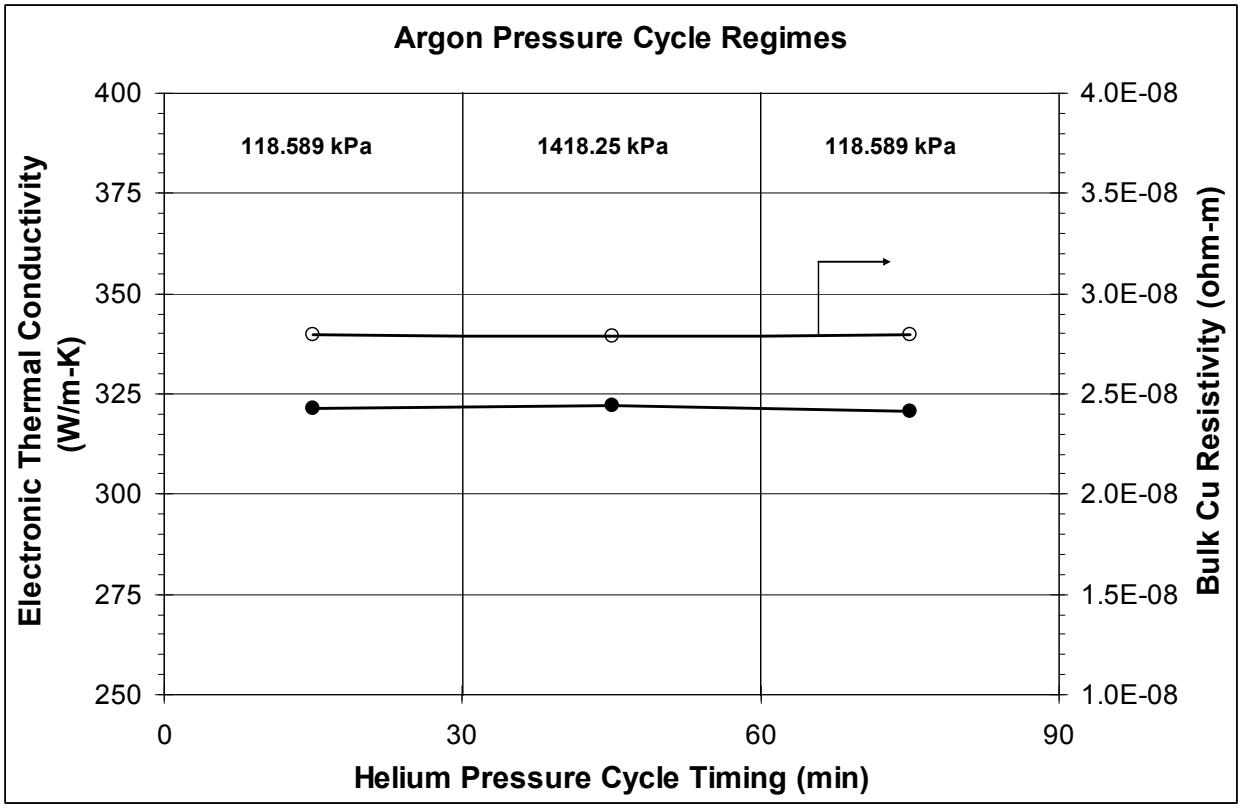

Figure 5.19: The bulk Cu electronic thermal conductivity and electrical resistivity results are indicated by the solid circle markers and open circles respectively for the three experimental He pressure cycles. The DES measurements show almost no change to either transport coefficient during each pressure stage.

Figures 5.20 and 5.21 below show the results of Au and Cu Lorenz number and collision density at each He pressure cycle regime. The annealed Au sample changes very little through the three pressure regimes and is within 8% of the theoretical value of $2.45\times10^{-8}\ \mathrm{W\Omega K^{-2}}$. Compared to the unannealed Au, this result in itself is surprisingly close to that predicted by theory and is obviously a result of the annealing process. This experimental observation is in agreement with previous thin film transport property reports which find that thin film fabrication anomalies are common and are often improved upon during the annealing process.[127] The Lorenz number for the unannealed Au decreases slightly at 1418.25 kPa and subsequently returns to nearly the same value at the final pressure stage. The Lorenz number for the Cu sample increases at 1418.25 kPa followed by a decrease to a lower value than the initial measurement. The Cu Lorenz number is also noted to be approximately higher than theoretical value which coincides with thin film fabrication anomalies of unannealed samples.

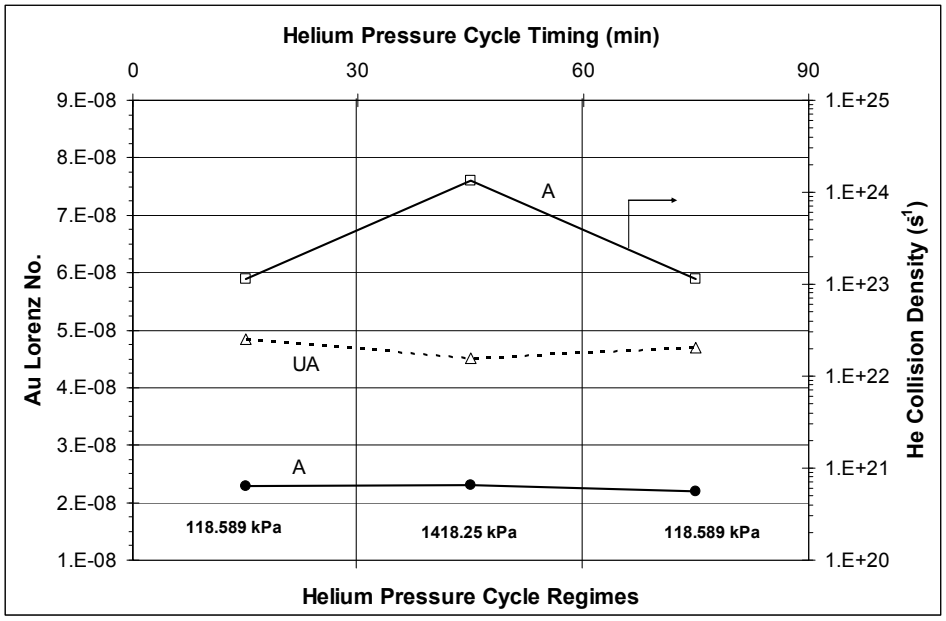

Figure 5.20: The Au Lorenz number results are shown for the three experimental He pressure cycles. Unannealed (UA) and annealed (A) Au samples were used as indicated by the open triangles (dashed line) and solid circle markers (solid line) respectively. The He collision density (open squares and solid line) is calculated to increase by an order of magnitude during the high pressure stage of the experiment.

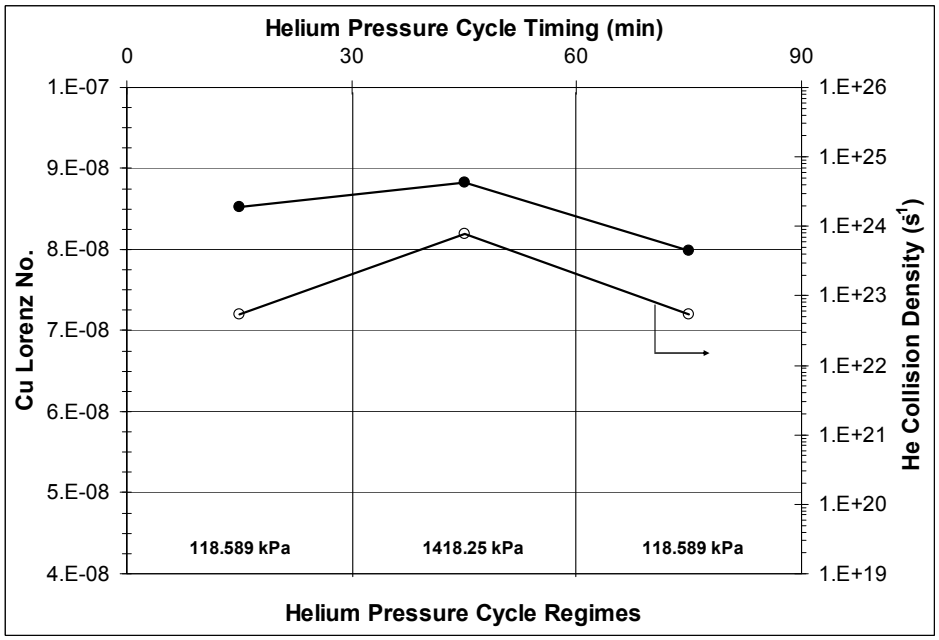

Figure 5.21: The Cu Lorenz number result is shown by the solid circle markers for the three experimental He pressure cycles. Unannealed Cu samples were used throughput this investigation. The He collision density (open circles) is calculated to increase by an order of magnitude during the high pressure stage of the experiment.

Figures 5.22 and 5.23 below show the results of Au and Cu Seebeck coefficient at each He pressure cycle regime. The unannealed Au sample shows a noticeable decrease at 1418.25 kPa which coincides with the thermal conductivity and resistivity behavior shown in Figure 5.17. The drop from 1.92 μVK^{-1} to 1.57 μVK^{-1} represents an approximate 18% decrease yet the Seebeck returns to 2 μVK^{-1} at the final pressure stage of the experiment. The annealed Au was measured at a lower initial value of 1.5 μVK^{-1} and decreased to approximately 1.43 μVK^{-1} at the high pressure stage. This corresponds to approximately 5% decrease compared to the 28% decrease of the unannealed Au. The final pressure regime resulted in an almost identical return to the initial Seebeck coefficient value for the annealed Au. The Cu sample showed a Seebeck coefficient that decreased slightly at each He pressure regime. Initially at 1.33 μVK^{-1}, the Seebeck coefficient decreased to 1.28 μVK^{-1} at 1418.25 kPa followed by approximately 1.27 μVK^{-1} at the final pressure stage. The published value for the Au and Cu Seebeck coefficients are 1.94 μVK^{-1} and 1.83 μVK^{-1} respectively at 300 K which agrees closely[30] with the stage 1 pressure regime of Figures 5.22 and 5.23.

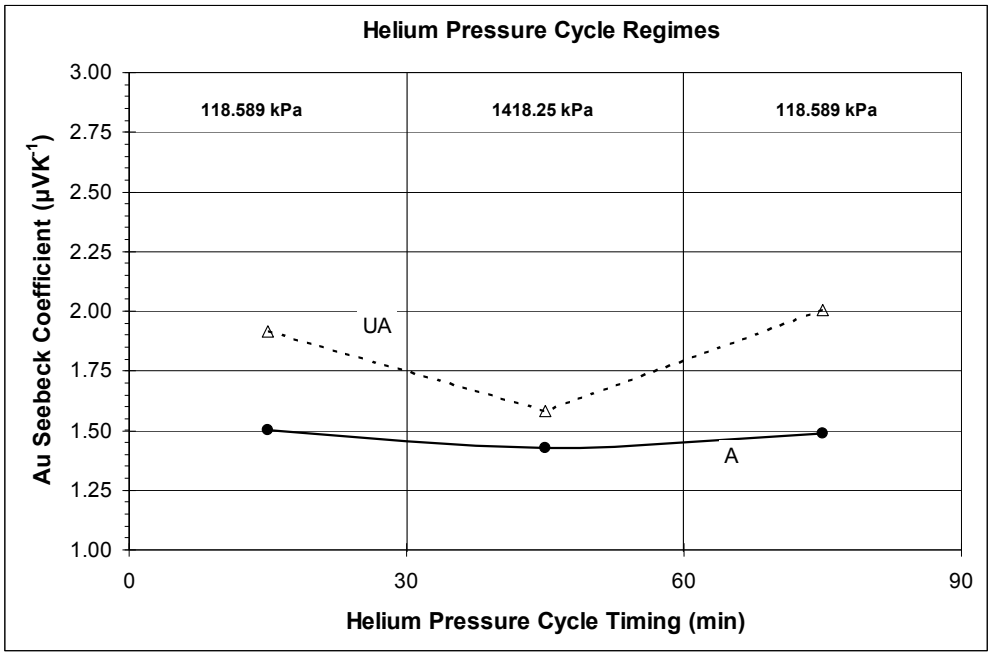

Figure 5.22: The Au Seebeck coefficient results are shown for the three experimental He pressure cycles. Unannealed (UA) and annealed (A) Au samples were used as indicated by the open triangles (dashed line) and solid circle markers (solid line) respectively.

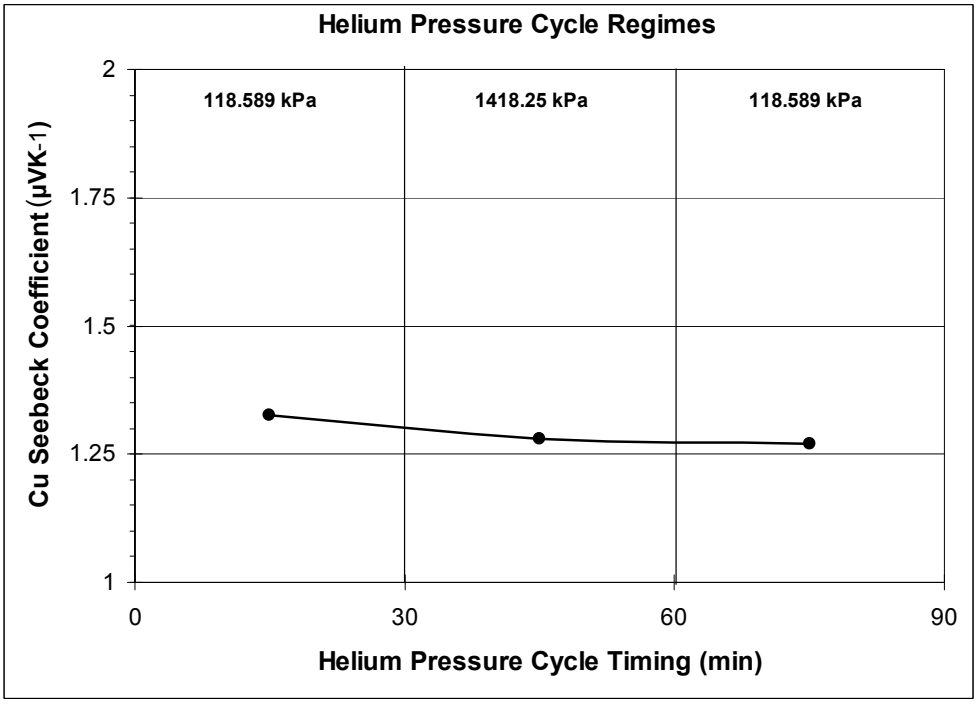

Figure 5.23: The Cu Seebeck coefficient results are indicated by the solid circle markers for the three experimental He pressure cycles. Unannealed Cu samples were used throughout this investigation.

The perturbations of the transport coefficients just reviewed are indicative of subtle changes to the ACF which surface analytically during numerical integration. The fine structure displayed by the ACF's resulted in clear and distinct changes to the relevant transport coefficients through the Green-Kubo formalism outline in Chapter 3. Therefore, a comparative analysis of the structure and behavior of the Au and Cu ACF's during the low and high pressure regimes was both experimentally and theoretically important. Figures 5.24 and 5.25 give a comparative ACF for both Au and Cu at low and high pressure. The main plot extends out to 20 ps while the inset show early temporal behavior up to 3 ps. The differences in the low and high pressure decay are noted to begin at or very near the first zero axis crossing. The initial exponential decrease from $t = 0$ is fairly similar for each ACF. During the first dip however, oscillatory behavior clearly differs under high pressure He. This phenomena is again hypothesized to be induced by the increased He surface collision density which dynamically changes the energy and momentum relaxation behavior of the electron ensemble. Through the rigorous Green-Kubo theory, the numerical integration of these functions results in the measurements reported in the beginning of this section. The experimental observation and measurement of the surface perturbations due to a He boundary through the voltage fluctuation spectra ACF is significant and has not been reported by any other group.

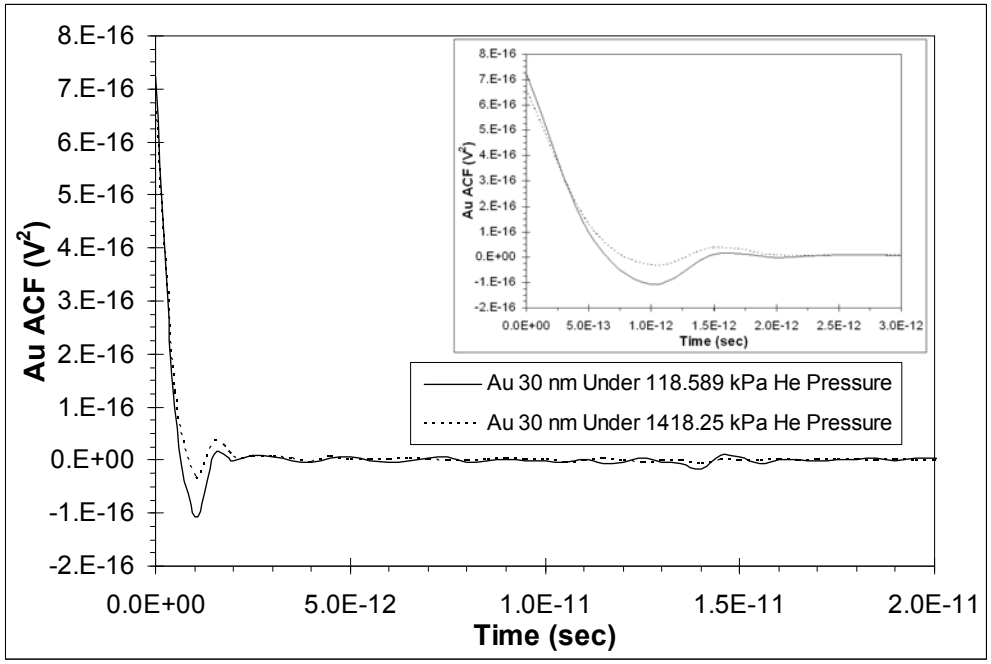

Figure 5.24: Comparative results of the Au ACF at He pressures of 118.589 kPa and 1418.25 kPa. The ACF oscillatory behavior at high pressure is attributed to increased surface scattering effects due to the large He collision density. The main plot extends temporally to 20 ps while the inset shows short-time behavior out to 3 ps.

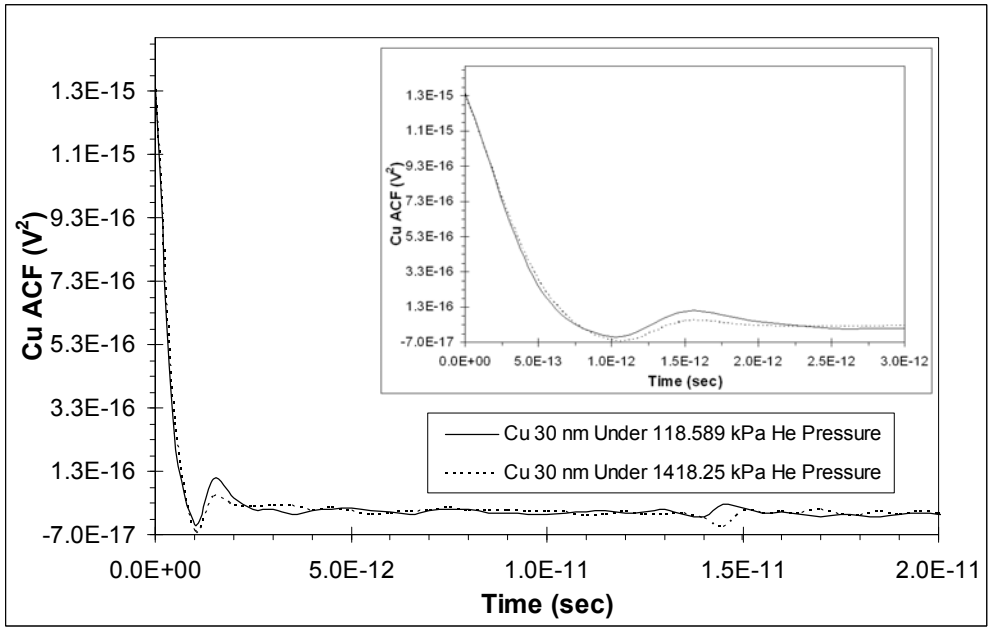

Figure 5.25: Comparative results of the Cu ACF at He pressures of 118.589 kPa and 1418.25 kPa. The ACF oscillatory behavior at high pressure is attributed to increased surface scattering effects due to the large He collision density. The main plot extends temporally to 20 ps while the inset shows short-time behavior out to 3 ps.

In summary, the measurement of Au and Cu thin films under He stationary pressure environments has been accomplished through the DES experimental method. There is clear evidence of transport property deviations for both materials due to an increase in the He collision density at the nanostructure surface. Evidence of this phenomenon is provided by the final stage of the experiment where many material properties return to values close to their initial magnitude. Further evidence of the increased gas energetic perturbations are clearly found in the ACF fine structure at each experimental pressure. Some deviations during the final pressure are to be expected due to an increased He physical adsorption rate under increased pressures.[34] Subsequently, the thin film surface should contain an increased percentage of He atoms at or near the surface which acts as additional scattering sites to the electron ensemble. In general, the annealed Au sample shows a lower response to pressure increases than the unannealed Au. This effect is hypothesized to occur due to the improvement of grain boundaries, surface steps, etc. during the annealing process. Hence, the general crystal lattice relaxation due to annealing is hypothesized to produce a transition to greater elastic scattering events by the electron ensemble as evidenced by the Lorenz number. The bulk Cu sample used to obtain comparative results showed no real transport property changes during DES measurements. An unexpected result is the close agreement of the thermal PSD among all samples. Theoretically, the thermal PSD at time zero is a function of temperature only with no dependence on a materials resistance.[86] Yet, the thin films of this study have undergone large He collision density increases. Consequently, the evidence thus far suggests that the thermal PSD remains a function of temperature only regardless of the scattering landscape that may exist (at $t = 0$). The thermal PSD decay away from time zero is found to contain the same fine structure as the voltage PSD. This is evidenced by the changes to the thermal conductivity and Seebeck coefficients under He pressure.

5.3.5 Au and Cu Thin Films Under Vacuum, Atmospheric and Pressurized Stationary Argon

The DES experimental objectives given in Section 5.3.4 shall apply to this section as well. The gaseous interface will be Ar with the intent of experimentally measuring the effects of increased gas particle collision density due to the high pressure regime, with a heavy gas particle (compared to He) and a lower collision density. The experimental setup and execution is also identical to Section 5.3.4 in order to maintain a comparative data base between the two experiments.

Figures 5.26 and 5.27 below shows the results of Au and Cu voltage and thermal PSD's at each Ar pressure cycle regime. Compared to He, similar thermal PSD behavior and magnitude is noted and again found to be nearly identical for both unannealed and annealed samples. Very little deviation of the Au thermal PSD occurs during the high pressure Ar stage which is similar to the He high pressure measurements. The annealed Au voltage PSD decreases in the high pressure regime and returns closely to the initial value during the final experimental pressure stage. The unannealed Au however, increases slightly at each data measurement point indicating an increasing Johnson/Nyquist noise voltage. The Cu sample behaves similarly by increasing slightly at each pressure stage.

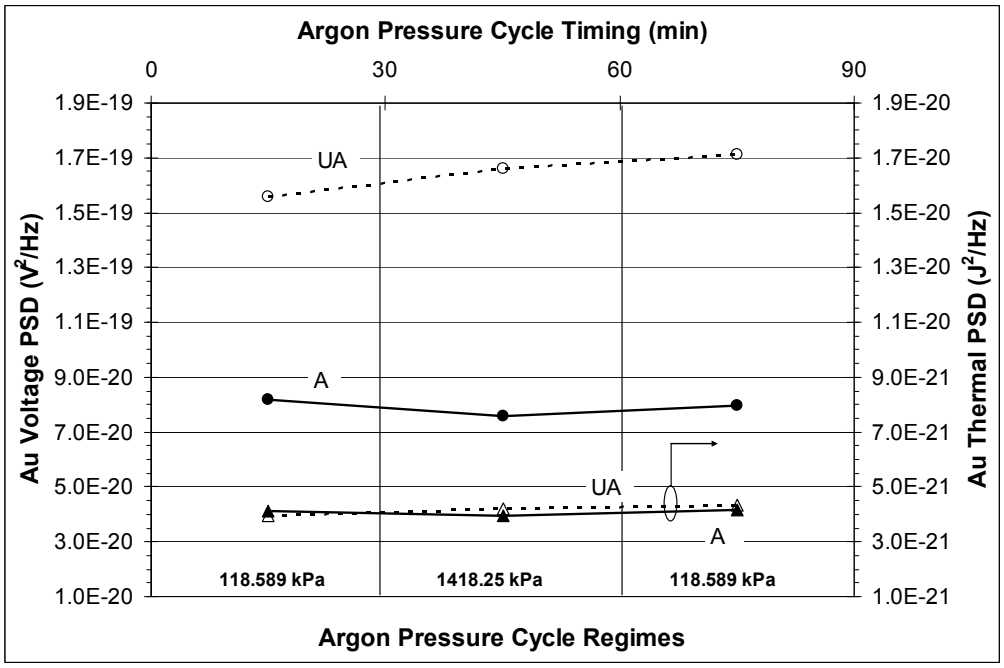

Figure 5.26: The Au voltage and thermal PSD results are shown for the three experimental Ar pressure cycles. Unannealed (UA) and annealed (A) Au samples were used as indicated by the open markers (dashed line) and solid markers (solid line) respectively.

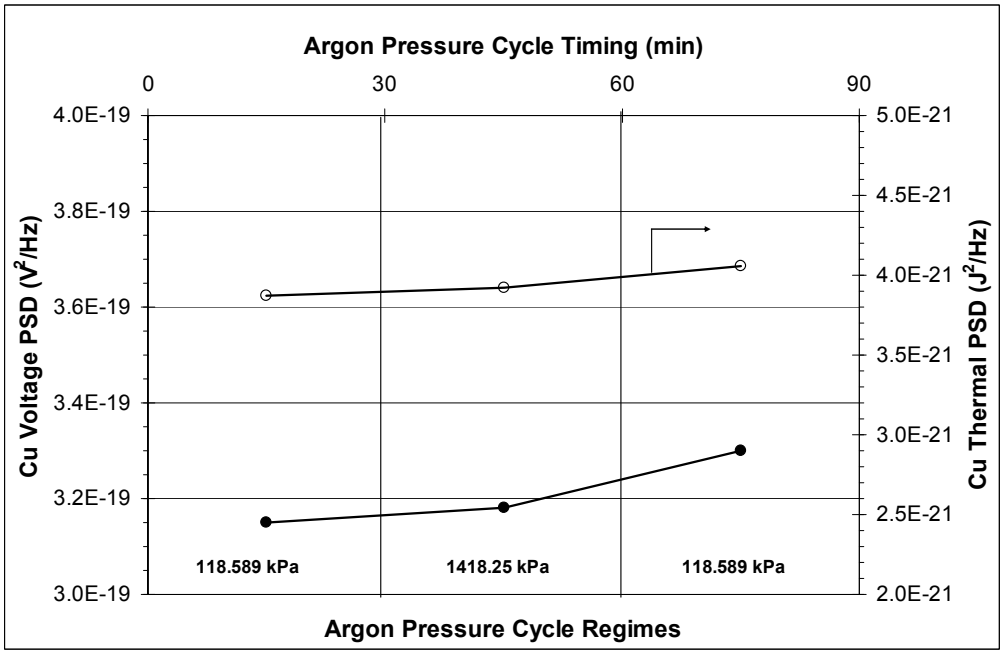

Figure 5.27: The Cu voltage and thermal PSD results are indicated by the solid circle markers and open circles respectively for the three experimental Ar pressure cycles. Unannealed Cu samples were used throughout this investigation.

Figures 5.28 and 5.29 below show the results of Au and Cu electronic thermal conductivity and electrical resistivity at each Ar pressure cycle regime. The unannealed Au shows a distinct variation in both thermal conductivity and resistivity at the high pressure regime. The annealed Au sample thermal conductivity decreases at high pressure which is not followed by the resistivity. There is a slight resistivity decrease for the annealed sample at the high pressure stage which remains basically unchanged in the last pressure regime. This behavior is similar to the annealed Au under He and is probably due to different electric scattering relaxation times than the thermal current. The Cu sample of Figure 5.29 reveals a distinct change in both thermal conductivity and resistivity due to high pressure and returns closely to the original value at the final experimental pressure regime. The Cu resistivity and thermal conductivity increases at 1418.25 kPa followed by a return to nearly the same values during the final pressure stage.

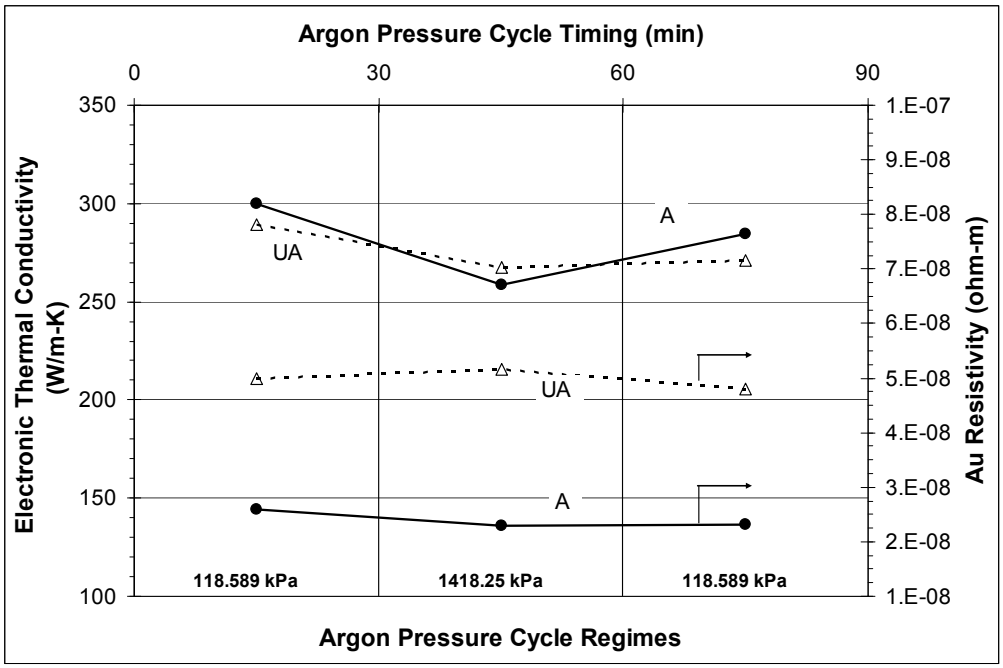

Figure 5.28: The Au electronic thermal conductivity and electrical resistance results are shown for the three experimental Ar pressure cycles. Unannealed (UA) and annealed (A) Au samples were used as indicated by the open triangles (dashed line) and solid circle markers (solid line) respectively.

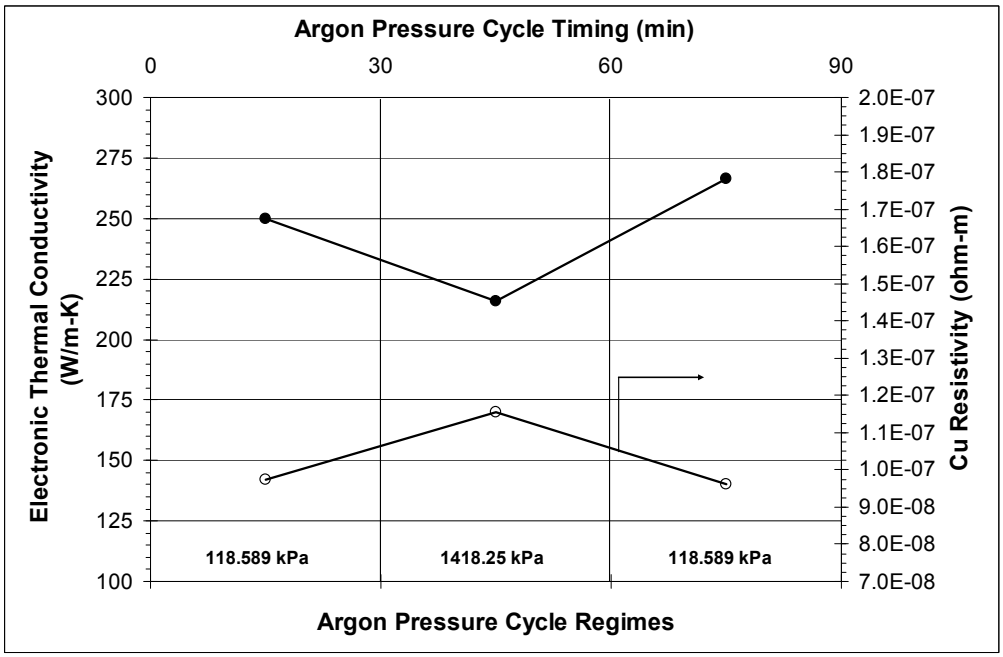

Figure 5.29: The Cu electronic thermal conductivity and electrical resistivity results are indicated by the solid circle markers and open circles respectively for the three experimental Ar pressure cycles. Unannealed Cu samples were used throughput this investigation.

The comparative measurement of the bulk Cu sample submitted to an Ar boundary is displayed in Figure 5.30. There was no real response to Ar at low and high pressures which is similar to the He interface. Compared to the responsive 30 nm Cu thin film, the macroscopic bulk sample appears to be driven by volume based scattering mechanisms instead of surface dominant scattering displayed by the thin film.

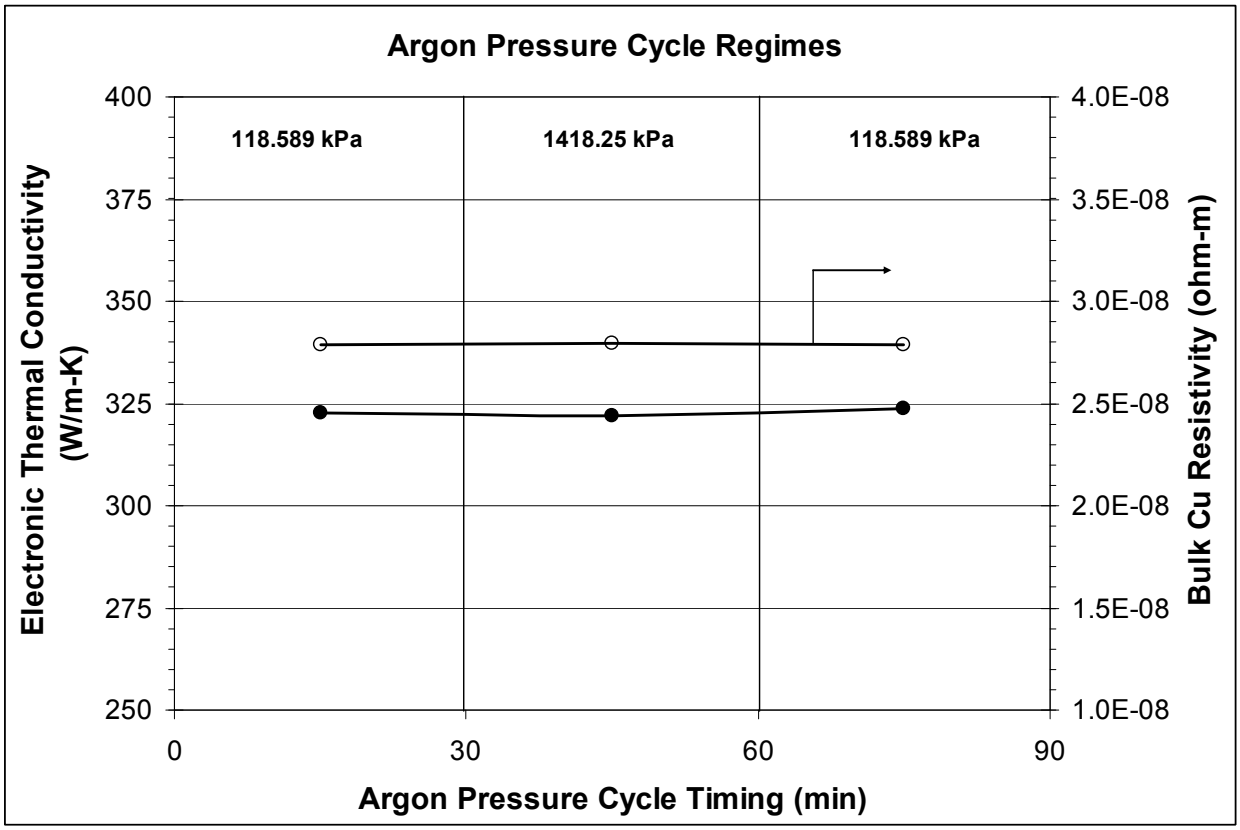

Figure 5.30: The bulk Cu electronic thermal conductivity and electrical resistivity results are indicated by the solid circle markers and open circles respectively for the three experimental Ar pressure cycles. The DES measurements show almost no change to either transport coefficient during each pressure stage.

Figures 5.31 and 5.32 below show the results of Au and Cu Lorenz number and collision density at each Ar pressure cycle regime. The annealed Au sample changes very little through the three pressure regimes which is similar to the He environment. The annealed Au Lorenz

number is amazingly close to the He stationary flow runs and is within 8.2% of the theoretical value of 2.45×10^{-8} $W\Omega K^{-2}$. The Lorenz number for the unannealed Au decreases slightly at both the 1418.25 kPa and 118.589 pressures stages. The Lorenz number for the Cu sample increases at 1418.25 kPa followed by another increase at the final pressure stage. The Cu Lorenz number measurement is also noted to be fairly close to the He runs.

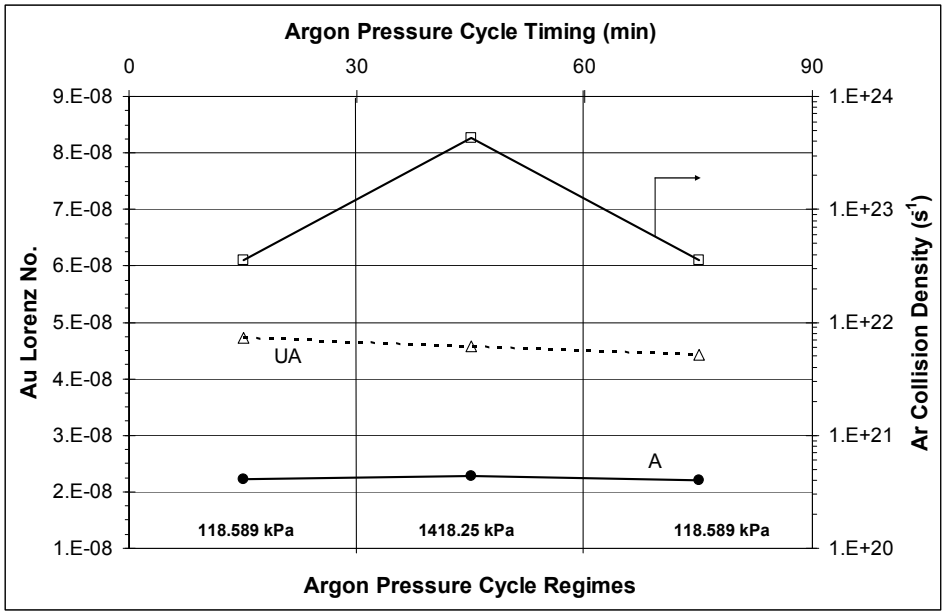

Figure 5.31: The Au Lorenz number results are shown for the three experimental Ar pressure cycles. Unannealed (UA) and annealed (A) Au samples were used as indicated by the open triangles (dashed line) and solid circle markers (solid line) respectively. The Ar collision density (open squares and solid line) is calculated to increase by an order of magnitude during the high pressure stage of the experiment.

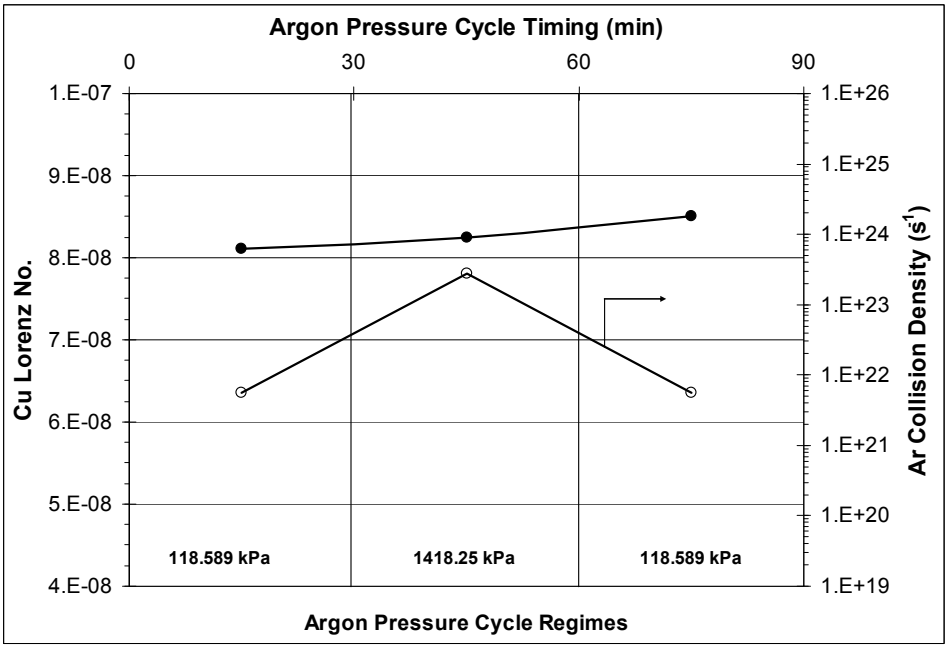

Figure 5.32: The Cu Lorenz number result is shown by the solid circle markers for the three experimental Ar pressure cycles. Unannealed Cu samples were used throughput this investigation. The Ar collision density (open circles) is calculated to increase by an order of magnitude during the high pressure stage of the experiment.

Figures 5.33 and 5.34 below show the results of Au and Cu Seebeck coefficient at each Ar pressure cycle regime. The unannealed Au sample shows a noticeable decrease at 1418.25 kPa which coincides with the thermal conductivity and resistivity behavior shown in Figure 5.28. The drop from 2.04 μVK^{-1} to 1.78 μVK^{-1} represents an approximate 13% decrease and returns to approximately 1.9 μVK^{-1} at the final pressure stage of the experiment. The annealed Au was measured at a lower initial value of 1.29 μVK^{-1} and increased to approximately 1.56 μVK^{-1} at the high pressure stage. This corresponds to approximately 21% increase compared to the 13% decrease of the unannealed Au. The final pressure regime resulted in a value of 1.68 μVK^{-1} Seebeck coefficient value for the annealed Au. The Cu sample showed a Seebeck coefficient that remained close to the initial value even at the 1418.25 kPa pressure. Initially at 1.21 μVK^{-1}, the Seebeck coefficient increased to 1.34 μVK^{-1} at the final Ar pressure stage.

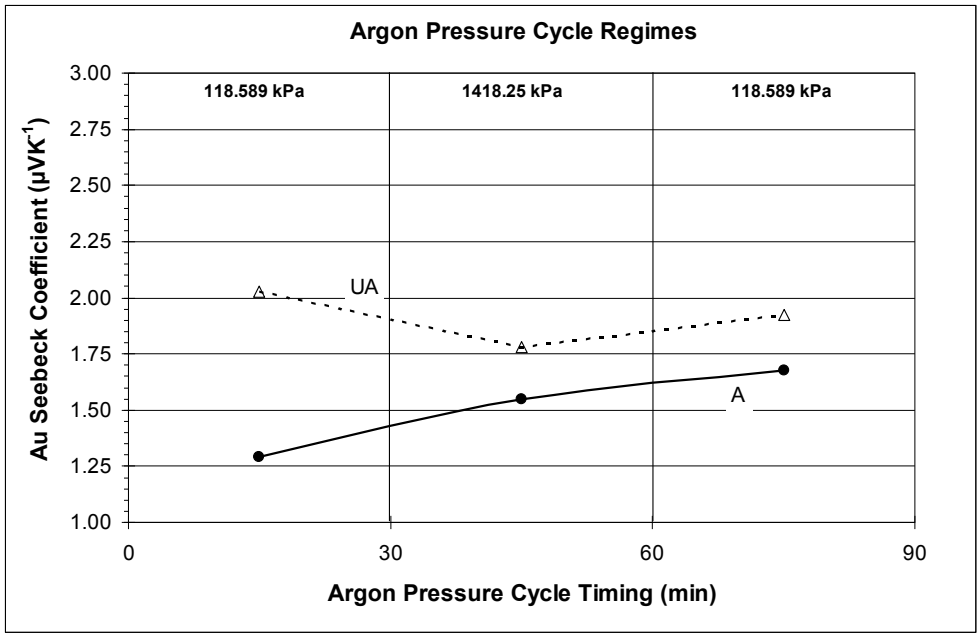

Figure 5.33: The Au Seebeck coefficient results are shown for the three experimental Ar pressure cycles. Unannealed (UA) and annealed (A) Au samples were used as indicated by the open triangles (dashed line) and solid circle markers (solid line) respectively.

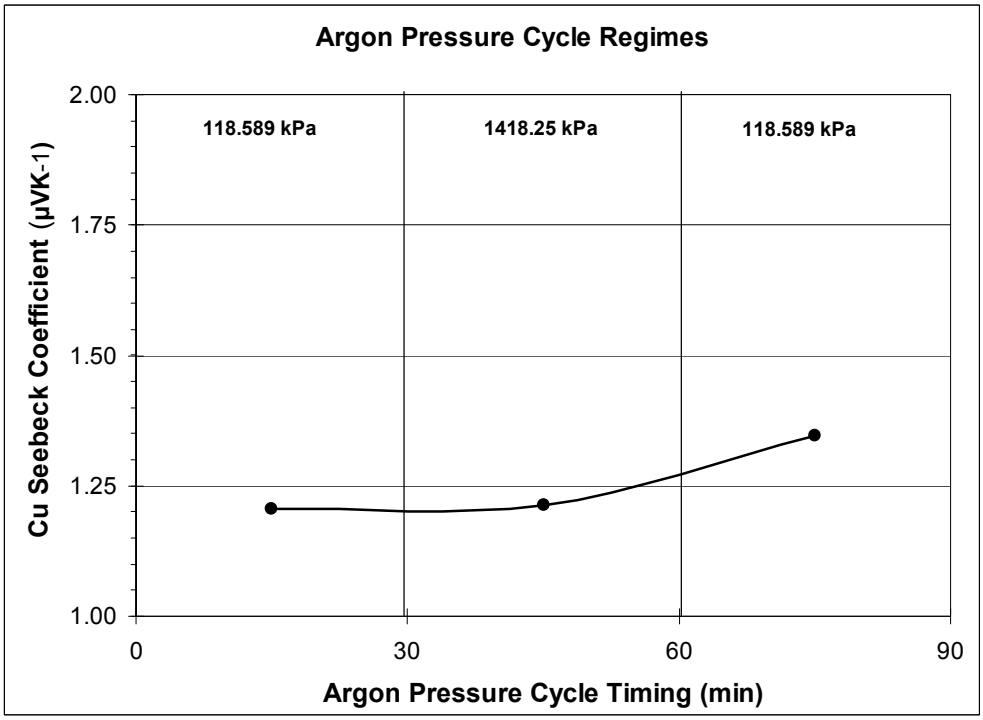

Figure 5.34: The Cu Seebeck coefficient results are indicated by the solid circle markers for the three experimental Ar pressure cycles. Unannealed Cu samples were used throughput this investigation.

The Au and Cu ACF comparative plots at low and high Ar pressure are shown in Figures 5.35 and 5.36. The primary differences are again found in the oscillatory region around 1 – 10 ps. This behavior is similar to the He ACF results of the previous section thus suggesting the general increase in gas collision density to produce similar results, despite the difference in gas atomic masses.

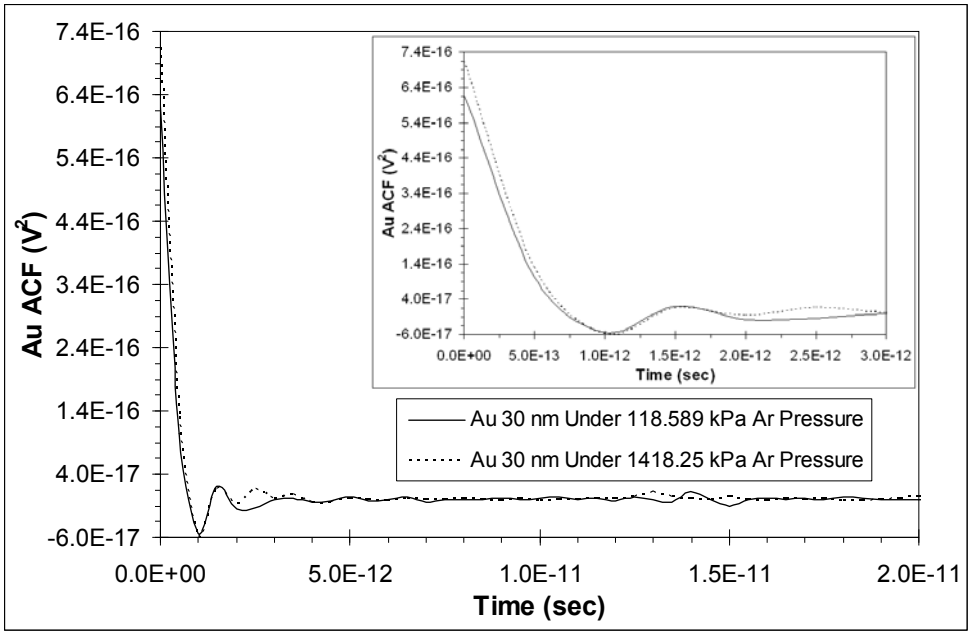

Figure 5.35: Comparative results of the Au ACF at Ar pressures of 118.589 kPa and 1418.25 kPa. The ACF oscillatory behavior at high pressure is attributed to increased surface scattering effects due to the increased Ar collision density. The main plot extends temporally to 20 ps while the inset shows short-time behavior out to 3 ps.

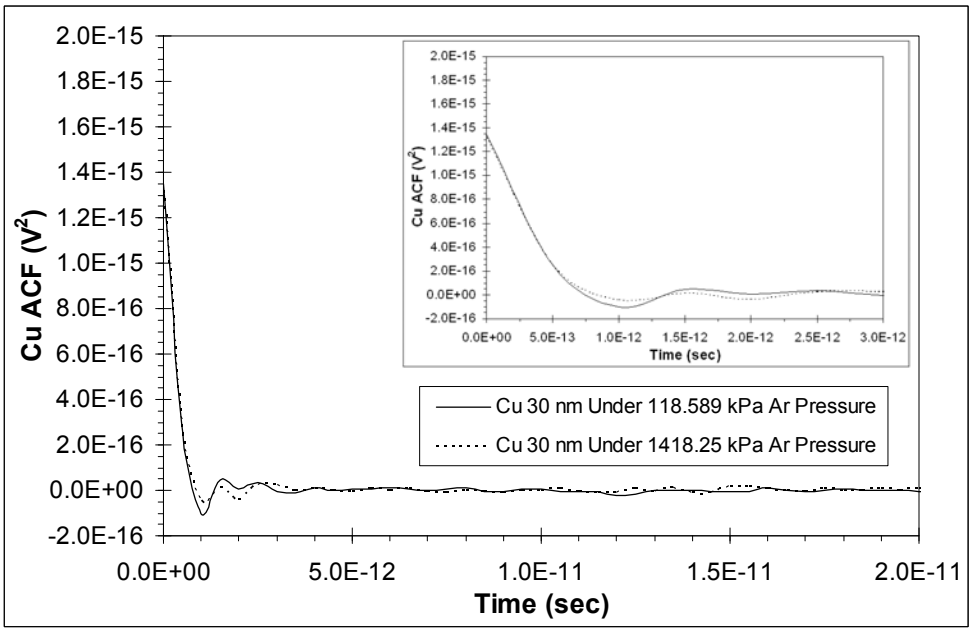

Figure 5.36: Comparative results of the Cu ACF at Ar pressures of 118.589 kPa and 1418.25 kPa. The ACF oscillatory behavior at high pressure is attributed to increased surface scattering effects due to the increased Ar collision density. The main plot extends temporally to 20 ps while the inset shows short-time behavior out to 3 ps.

In summary, the measurement of Au and Cu thin films under Ar stationary pressure environments has been accomplished through the DES experimental method. Similar to the He environment, there is clear evidence of transport property deviations for both materials due to an increase in the Ar collision density at the nanostructure surface. Further evidence of this phenomenon is provided by the final stage of the experiment where some Cu material properties return to values close to their initial magnitude. Deviations during the final pressure stage are found to be more prevalent than the He results which points toward the likelihood of different Ar adsorption effects during the high pressure stage. In general, the annealed Au sample again shows a lower response to pressure increases than the unannealed Au. The close agreement of the thermal PSD at time zero among all samples is repeated in the Ar DES measurements. Finally, the ACF analysis at low and high Ar pressures shows clear differences in oscillatory behavior which is similar to the He results.

5.4 Dynamic Electron Scattering Experimental Results on Au and Cu Thin Films Subject to Non-Stationary Flowing Gaseous Boundaries

5.4.1 Au and Cu Thin Films Subject to Non-Stationary Helium Flow

The objective of this section is to experimentally quantify the electronic transport property effects on Au and Cu thin films subjected to a non-stationary flowing He boundary. The principal difference between a stationary and non-stationary gaseous boundary is the change in gas particle impact energy E_i and wave vector q_g. Due to the construction of the flow chamber (see Section 4.2.4), a vacuum could not be performed before each experimental run. This flow chamber design feature was intentional in order to allow normal ambient surroundings such as

air and humidity to reach equilibrium conditions with each sample. This design feature is based upon foresight of the possible development of gas sensors as a result of this research. Quite simply, a gas sensor will not be put under vacuum before usage and will probably be in some imperfect ambient prior to operation. Therefore, the perturbation effects of a flowing gas boundary on a nanoscale material that is not in pristine condition, but may have some ambient adsorption (air, water vapor, etc.) already in place, was a part of the primary objectives. The DES experimental steps taken for each non-stationary flow experiment proceeded as follows. Voltage fluctuation data was taken initially at no-flow conditions. The inlet gas pressure to the nozzle was then incremented in discrete steps of 172.369 kPa, 344.738 kPa, 689.476 kPa, 1034.21 kPa and 1310.00 kPa with data again taken at each pressure step after a five minute wait period to ensure steady state thermal conditions. As detailed in Section 4.2.4, the gas temperature decreased slightly due to Joule-Thomson cooling effects of the nozzle thus inducing a corresponding sample temperature decrease through convective cooling. The mock samples approach to steady state took approximately two minutes. Therefore, a conservative wait period of five minutes was chosen to ensure steady state thermal conditions of the sample. This data collection process continued until a maximum gas inlet pressure of 1.412 MPa was reached. For the He runs, the corresponding discrete sample impact energies E_i were 32.4 meV, 38.8 meV, 49.2 meV, 68.6 meV, and 83.5 meV respectively. The 30 nm samples were cut to approximately 2 mm x 7 mm for both Au and Cu. Unannealed samples were used exclusively for this phase of experimentation. The primary experimental results are presented in plot format due to the multiple gas impact energy range. Furthermore, the Lorenz number results are combined with the gas particle collision density to allow an assessment of any differences in the electric and thermal relaxation times induced by a distinct change in surface scattering events.

Experimentally, the transport coefficient ratio expressed by the Lorenz number (see equation (3.54) is found to provide useful quantitative information through controlled gaseous boundary condition changes.

The DES experimental PSD results for Au and Cu under He flow are shown in Figures 5.37 – 5.38. The Au voltage PSD was found to increase steadily at each stage of increasing E_i. The Au thermal PSD remained fairly stable through each flow regime. The Cu voltage also increased at each stage of increasing E_i but with increased oscillatory behavior. As expected, the Cu thermal PSD remained fairly stable throughout the experiment.

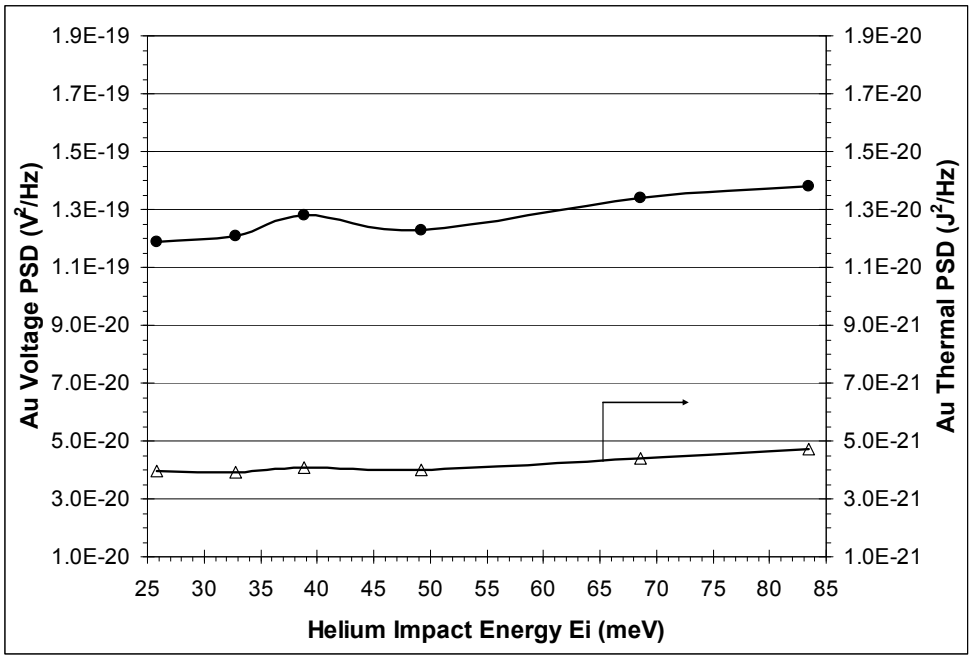

Figure 5.37: Au 30 nm sample voltage and thermal PSD response from stationary (25.8 meV) to 83.5 meV He impact energy. The solid circles (solid line) and open triangles (solid line) represent the voltage and thermal PSD's respectively.

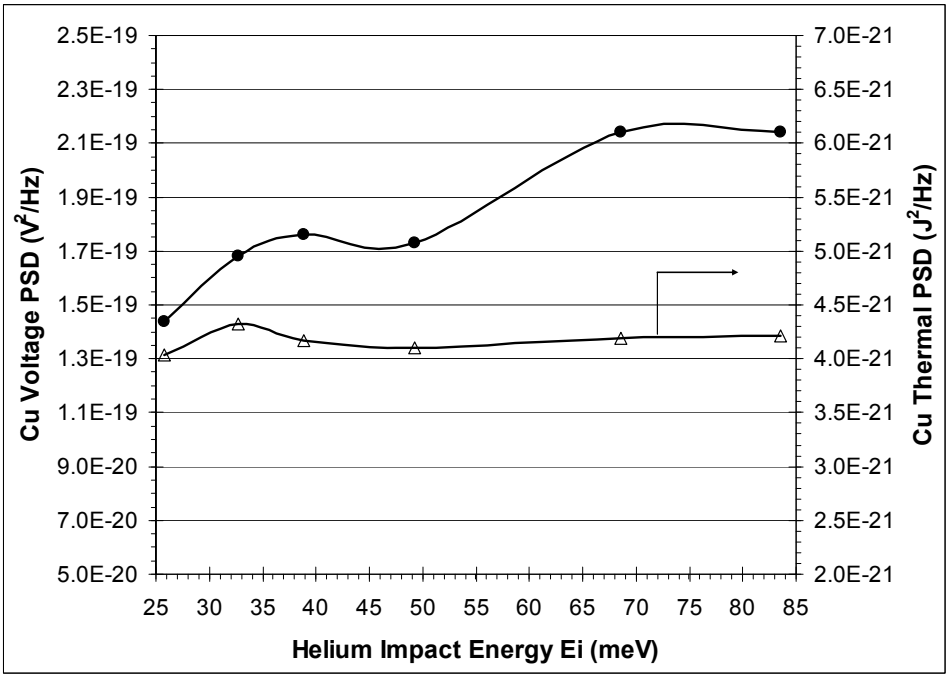

Figure 5.38: Cu 30 nm sample voltage and thermal PSD response from stationary (25.8 meV) to 83.5 meV He impact energy. The solid circles (solid line) and open triangles (solid line) represent the voltage and thermal PSD's respectively.

The electronic thermal conductivity and resistivity response to He flow is shown in Figures 5.39 – 5.40. The Au thermal conductivity shows an increase at 32.4 meV followed by a steady decrease at each corresponding impact energy. Beginning at approximately 290 W/m-K, the Au thermal conductivity measured 234 W/m-K at 83.5 meV which is a 19% drop. The corresponding Au resistivity measured approximately 4.63E-8 Ω-m at stationary flow and increased to 5.19E-8 Ω-m at 83.5 meV which is a 12% increase. Beginning at approximately 182 W/m-K, the Cu thermal conductivity measured 145 W/m-K at 83.5 meV which is a 20% drop and comparable to the Au response. The Cu resistivity however increased steadily at each flow step. The Cu resistivity measured 5.68E-8 Ω-m at stationary flow and increased to 6.51E-8 Ω-m at 83.5 meV which is a 14.6% increase.

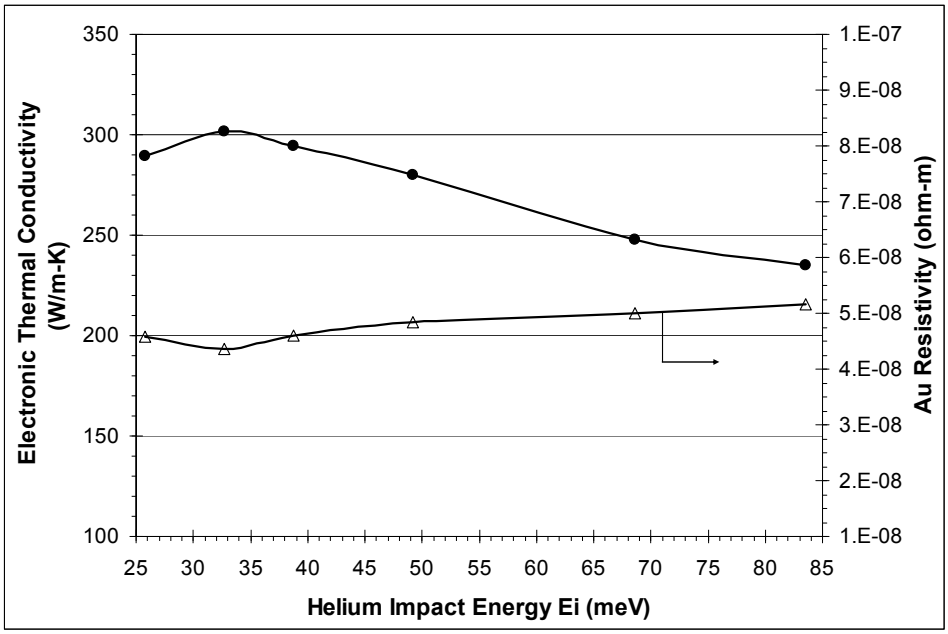

Figure 5.39: Au 30 nm sample electronic thermal conductivity and resistivity response from stationary (25.8 meV) to 83.5 meV He impact energy. The solid circles (solid line) and open triangles (solid line) represent the electronic thermal conductivity and resistivity respectively.

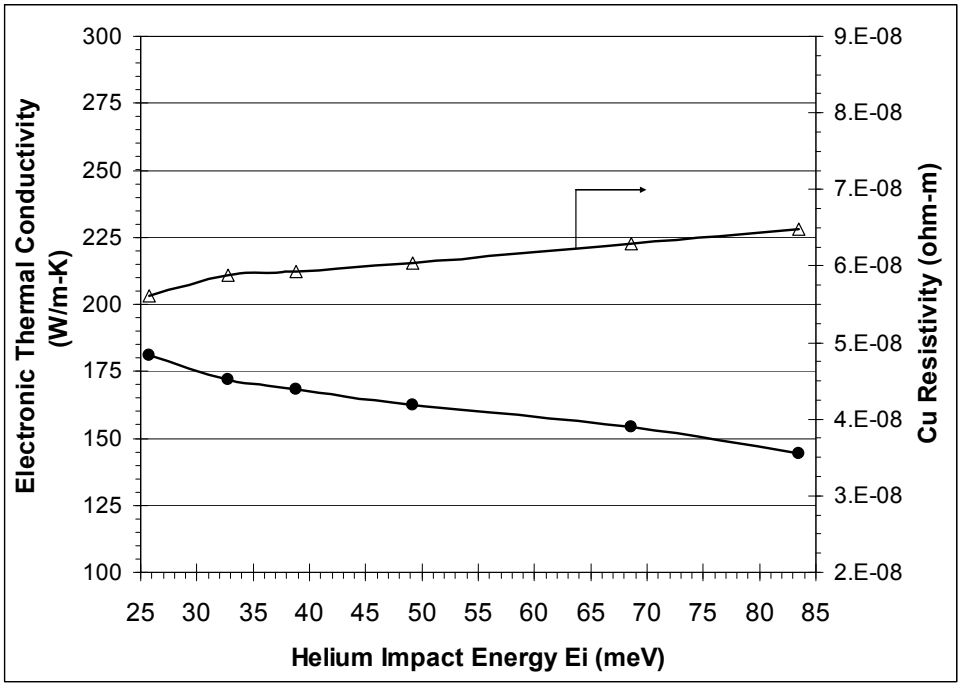

Figure 5.40: Cu 30 nm sample electronic thermal conductivity and resistivity response from stationary (25.8 meV) to 83.5 meV He impact energy. The solid circles (solid line) and open triangles (solid line) represent the electronic thermal conductivity and resistivity respectively.

In order to gain a comparative assessment of the gaseous boundary on both nanostructures and bulk materials, the bulk Cu sample used in Section 5.2 was also placed under the same impact energy E_i regimes as the Au and Cu thin films. The motivation behind this experiment was to compare the results with the arguments put forth in Chapter 1; that gas particle scattering on nanosurfaces could possibly perturb material transport properties. The results for the bulk Cu electronic thermal conductivity and resistivity are shown in Figure 5.41. Compared to the results of the 30 nm Cu sample, there is basically no response to the increasing He impact energy.

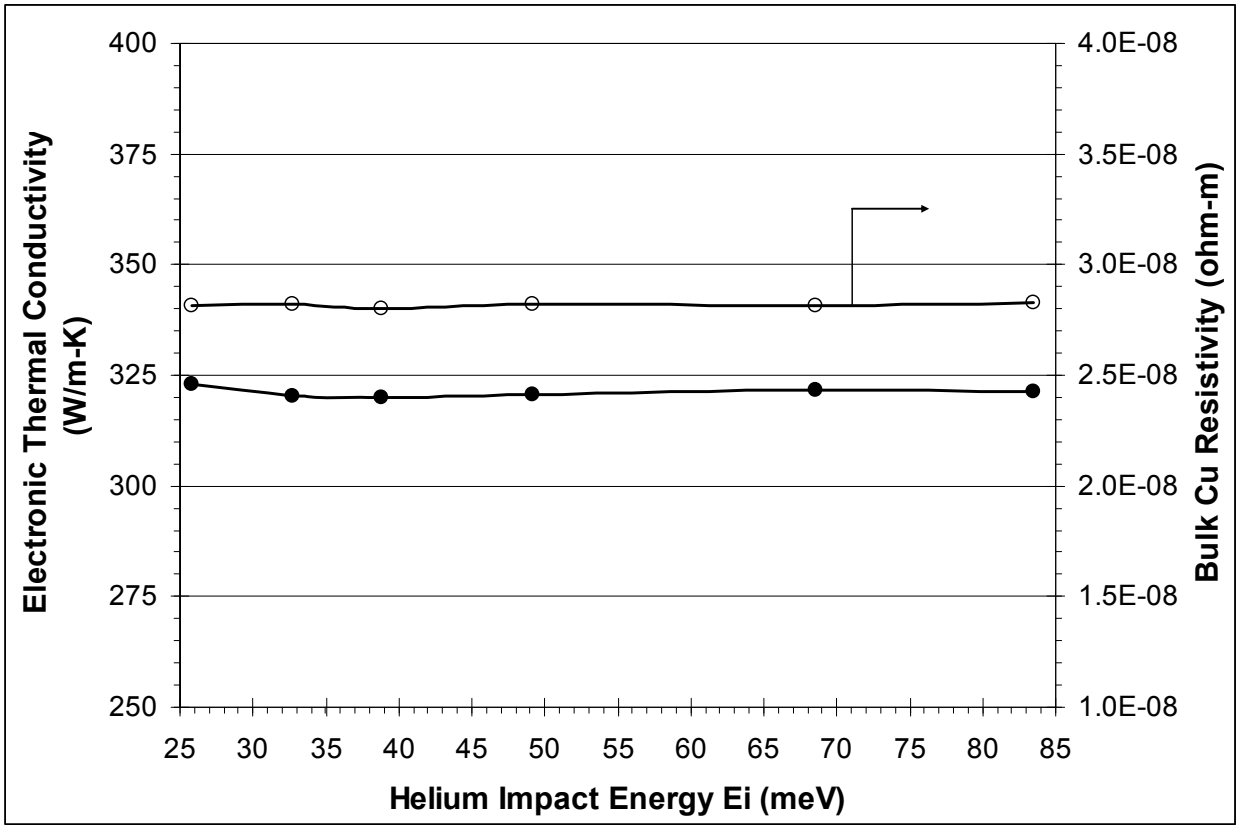

Figure 5.41: The bulk Cu electronic thermal conductivity and electrical resistivity results are indicated by the solid circle markers and open circles respectively for the six impact energy flow regimes. The DES measurements show almost no change to either transport coefficient during each E_i step.

The Lorenz number and corresponding He collision density at each He energetic impact energy E_i for both Au and Cu are shown in Figures 5.42 and 5.43. The DES measurements on the Au sample resulted in an immediate Lorenz number drop at the first flow regime of 32.4 meV. The Au Lorenz number then deviated little through the remaining stages of flow energy. The Cu sample also showed an initial drop at 32.4 meV however not as pronounced as the Au sample. The Cu Lorenz number measured approximately 3.7 $W\Omega K^{-2}$ which is similar to the approximate Au Lorenz number of 3.6 $W\Omega K^{-2}$.

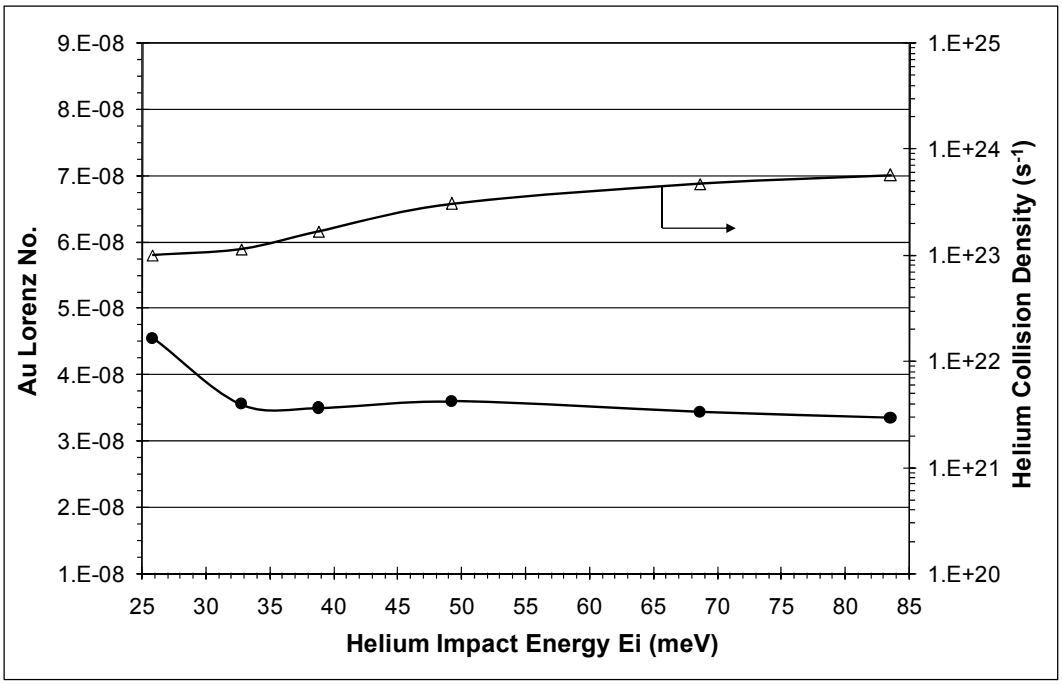

Figure 5.42: The Au Lorenz number results are shown for the six impact energy flow regimes as solid circles (solid line). The He collision density (open triangles and solid line) increases with each corresponding He impact energy increase.

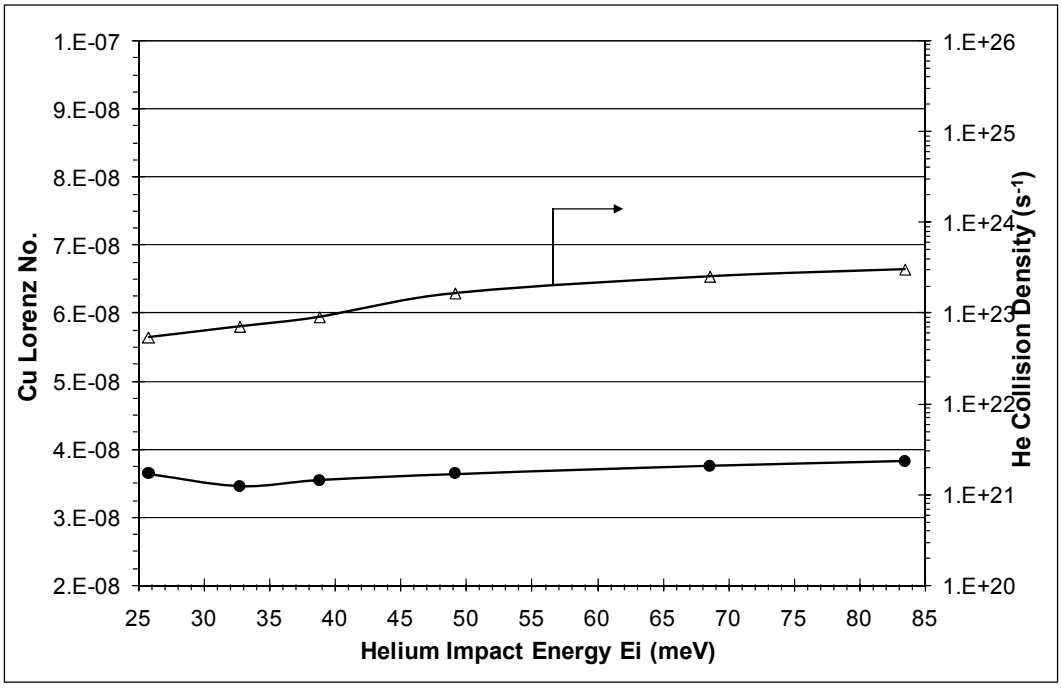

Figure 5.43: The Cu Lorenz number results are shown for the six impact energy flow regimes as solid circles (solid line). The He collision density (open triangles and solid line) increases with each corresponding He impact energy increase.

The Au and Cu Seebeck coefficient response to He impact energy is shown in Figures 5.44 and 5.45. The Au Seebeck shows an immediate drop at the 32.4 meV stage with a slow increase at subsequent He impact energies. The initial Au Seebeck value of 2.03 μVK^{-1} dropped to 1.56 μVK^{-1} at 32.4 meV which is approximately 23% decrease. The Cu sample measured 1.57 μVK^{-1} at stationary flow and increased to 2.31 μVK^{-1} at 32.4 meV. The Cu Seebeck then varied slightly followed by an increase to 2.86 μVK^{-1} at 68.6 meV. The Au sample showed similar behavior at the 68.6 meV step.

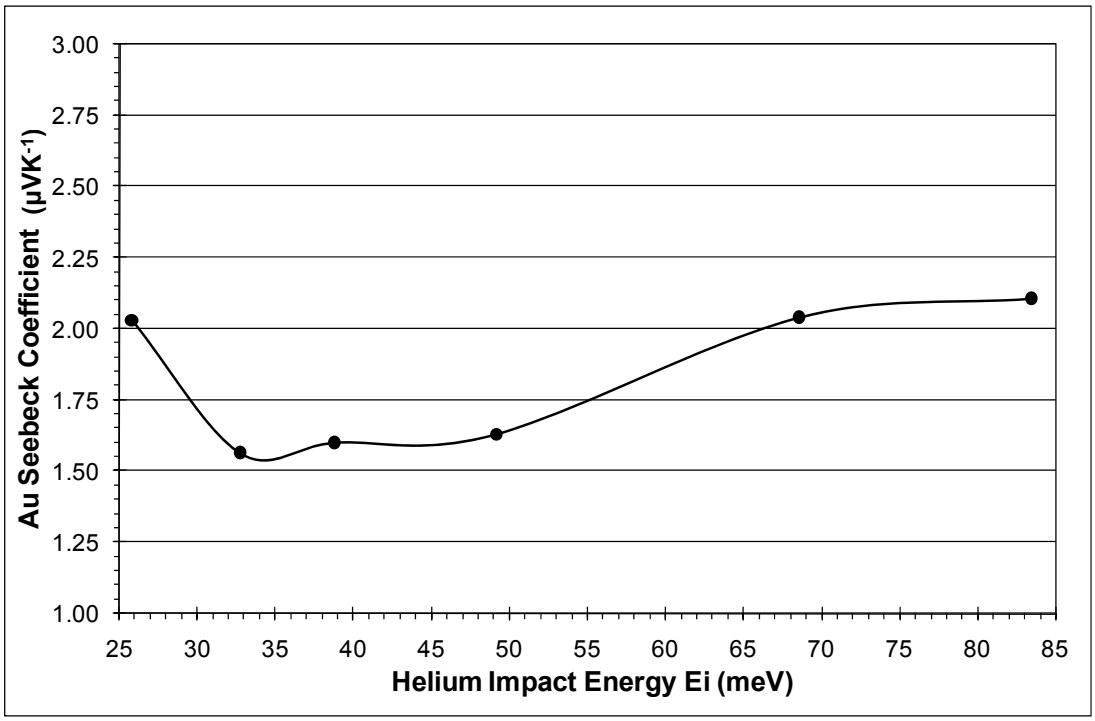

Figure 5.44: The Au Seebeck coefficient results are shown for the six impact energy flow regimes.

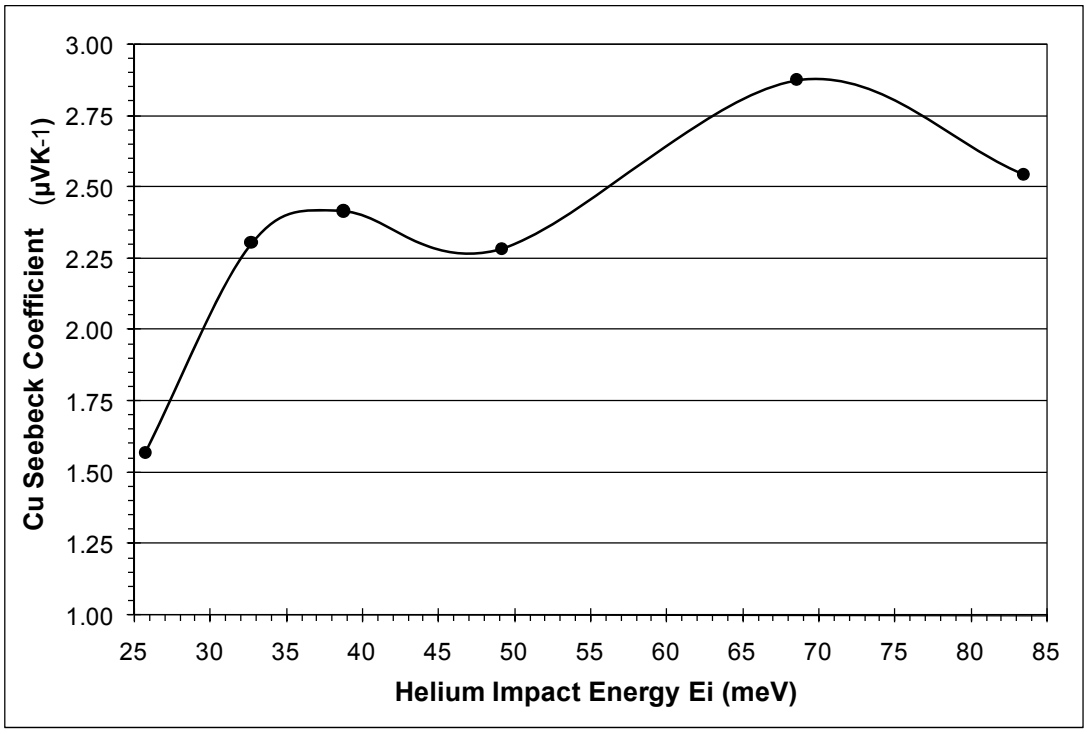

Figure 5.45: The Au Seebeck coefficient results are shown for the six impact energy flow regimes.

The perturbations of the transport coefficients just reviewed once again point to subtle changes to the ACF which surface analytically during numerical integration. The fine structure displayed by the ACF's for a non-stationary flow field again resulted in clear and distinct changes to the relevant transport coefficients through the Green-Kubo formalism outline in Chapter 3. Therefore, a comparative analysis of the structure and behavior of the Au and Cu ACF's at discrete impact energy regimes was deemed both experimentally and theoretically important. Figures 5.46 and 5.47 give a comparative ACF for both Au and Cu at the 25.8 meV (no-flow condition) and the 83.5 meV E_i. The main plot extends out to 20 ps while the inset show early temporal behavior up to 3 ps. The differences in the low and high E_i decay are noted to begin at or very near the first zero axis crossing which is identical to the low and high He pressure ACF behavior. The initial exponential decrease from $t = 0$ is fairly similar for each ACF. During the first dip however, oscillatory behavior clearly differs under 83.5 meV He. The oscillatory behavior also appears to slightly more pronounced further out in time than the stationary pressure results shown in Figure 5.24 and 5.25. This phenomenon is hypothesized to be induced by the increased He surface collision density and impact energy coupled with He gas wave vector q_g increases, which dynamically changes the energy and momentum relaxation behavior of the electron ensemble. The experimental observation and measurement of the surface perturbations due to a *flowing* He boundary through the voltage fluctuation spectra ACF is experimentally significant and has not been reported by any other group.

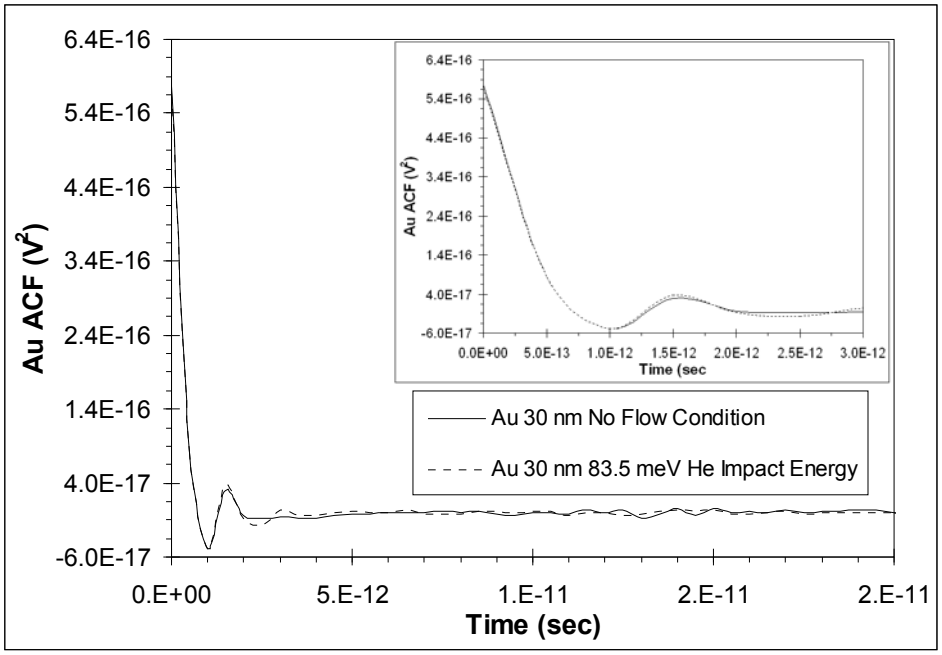

Figure 5.46: Comparative results of the Au ACF at 25.8 meV (no-flow) and 83.5 meV He E_i. The ACF oscillatory behavior at 83.5 meV is attributed to increased surface scattering effects due to a combined increase in He scattering effects such as collision density, E_i and q_g. The main plot extends temporally to 20 ps while the inset shows short-time behavior out to 3 ps.

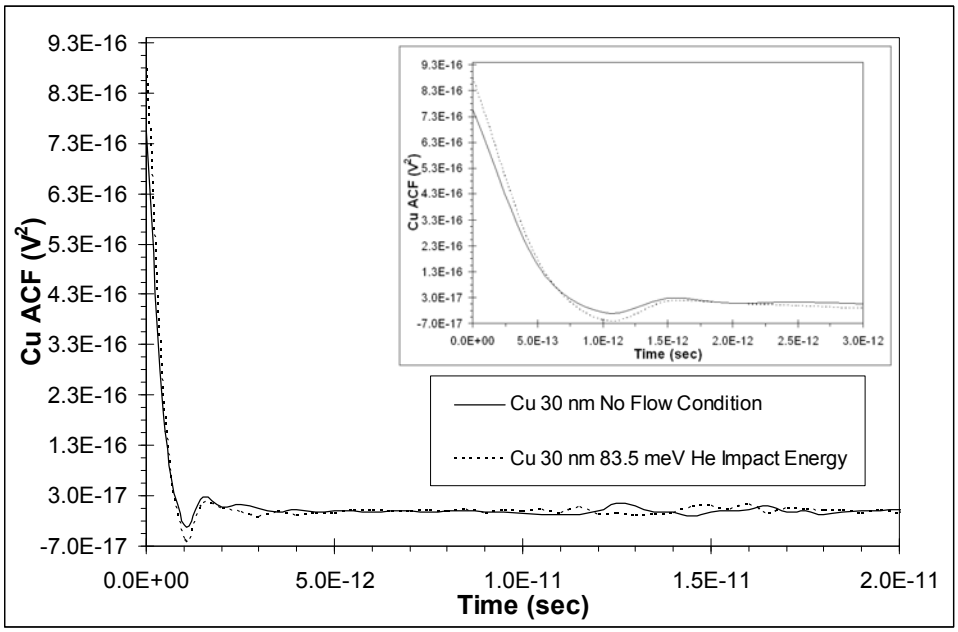

Figure 5.47: Comparative results of the Cu ACF at 25.8 meV (no-flow) and 83.5 meV He E_i. The ACF oscillatory behavior at 83.5 meV is attributed to increased surface scattering effects due to a combined increase in He scattering effects such as collision density, E_i and q_g. The main plot extends temporally to 20 ps while the inset shows short-time behavior out to 3 ps.

The overwhelming experimental evidence of gaseous scattering effects perturbing the Au and Cu thin film transport properties led this investigation to consider another measurement technique to again validate the DES results. The DES data so far has been consistent and repeatable despite the unique boundary conditions and environments that each nanoscale material has been subjected to. Indeed, the experimental methodology and application regime is on new ground yet is holding up rigorously despite the analytical pounding that is underway. Therefore, the experimental implementation of direct resistance measurements was executed with two primary objectives. First, the direct measurement of Au and Cu resistance during He flow would help validate the DES electrical resistivity results. Second, the known cooling effect of the flow chamber nozzle was expected to induce a *decrease* in sample resistance due to the negative temperature coefficient of resistivity of both Au and Cu. Subsequently, the question arose whether He scattering effects would offset or overcome the normal physical behavior of decreasing resistance due to a drop in sample temperature. Therefore, the resistance measurements were also desired as an aid in interpreting the DES data. The resistance measurements were executed using the equipment detailed in Section 4.2.4. The data sampling rate was set to one sample per second. Helium impact energies were identical to all other non-stationary flow experiments in order to maintain a comparative data base. The same Au and Cu samples used in the DES experiments were used for the resistance measurements. Moreover, the same flow chamber and sample holder apparatus was used which greatly simplified this additional experimental validation effort.

Figure 5.48 and 5.49 below show the Au and Cu 30 nm resistance behavior at He no-flow conditions and at He flow conditions. The step increase in resistance is clearly evident upon initiation of He flow. The Au sample resistance increased approximately 2.2% from 7.599 Ω to

7.768 Ω when He flow was started. There is a slight decrease in resistance during the flow period which is probably due to sample temperature decrease and He adsorption effects which may change the overall surface scattering dynamics. The abrupt decrease in resistance when He flow was stopped is clearly visible. The Cu sample resistance increased approximately 0.04% from 9.583 Ω to 9.579 Ω when He flow was started. A slight decrease in Cu resistance is again noted during the flow period similar to the Au results. The distinct decrease in Cu resistance when He flow is stopped is again evident.

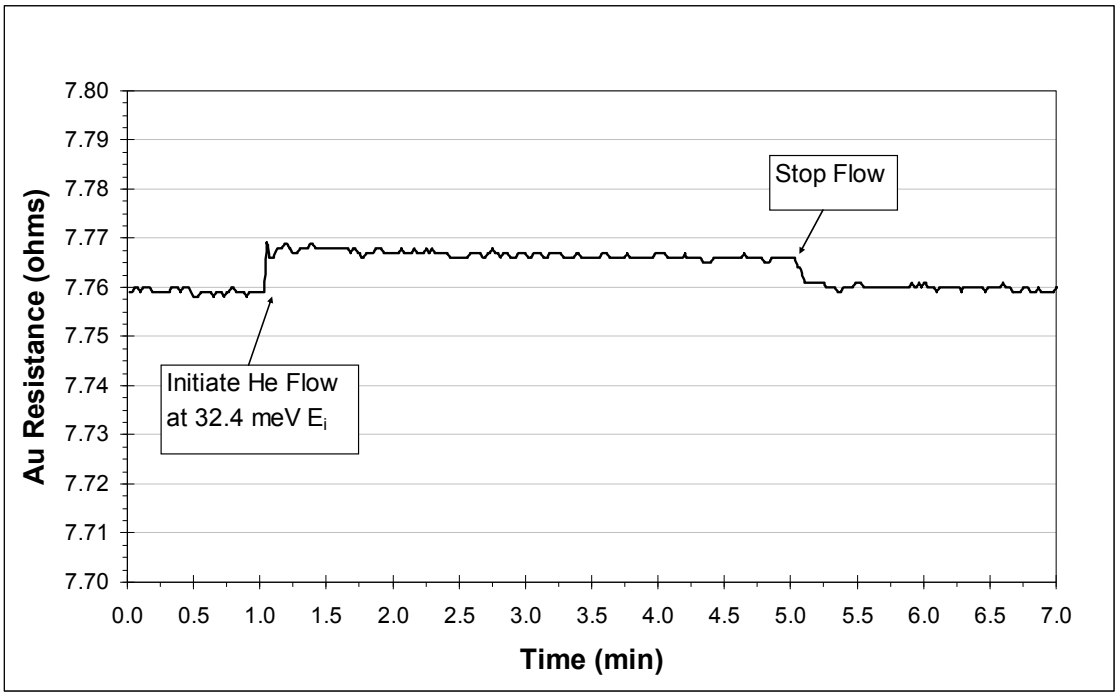

Figure 5.48: Au 30 nm sample resistance under 25.8 meV (no-flow) and 32.4 meV He E_i. The distinct drop in Au resistance is clearly evident when He flow ceased.

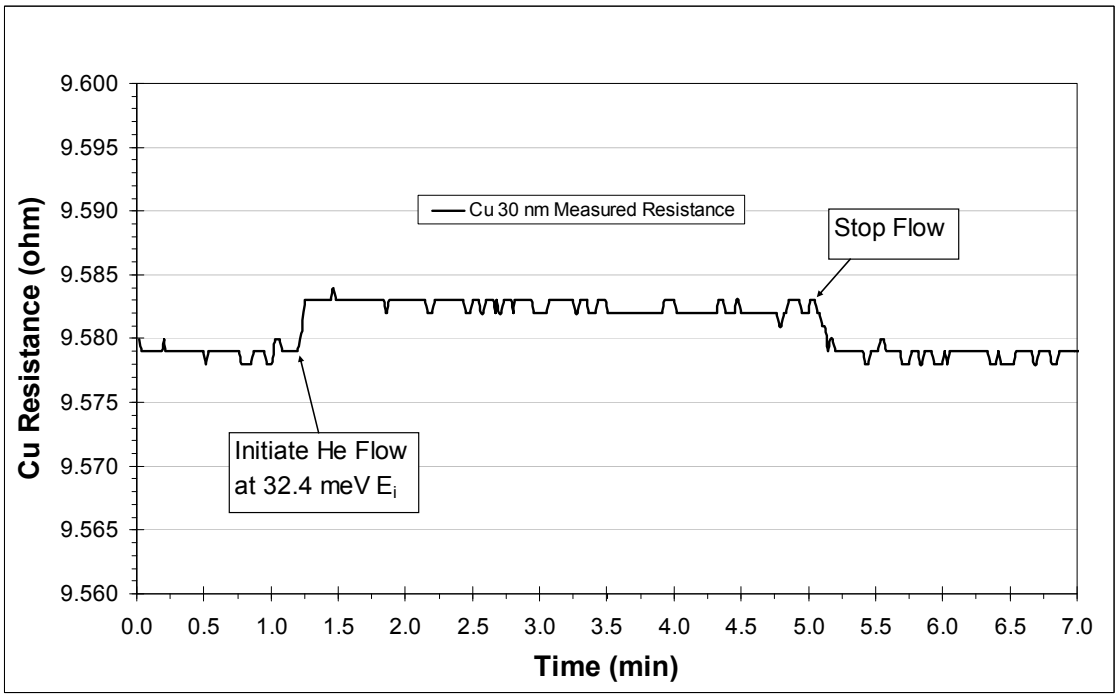

Figure 5.49: Cu 30 nm sample resistance under 25.8 meV (no-flow) and 32.4 meV He E_i. The distinct drop in Cu resistance is clearly evident when He flow ceased.

In order to obtain resistance data at each He E_i, the experiment was run at the relevant impact energies consecutively. Beginning with the no-flow condition, each relevant He E_i was initiated for two minutes followed by the next impact energy in stepwise fashion. Upon completing the 83.5 meV regime, flow was stopped for three minutes followed by another set of discrete He flow steps. This process was executed three times to assess the repeatability of the He scattering process on each nanostructure. Figures 5.50 and 5.51 below show the results for the subject Au and Cu 30 nm samples. The Au sample shows a clear stepwise response to each He E_i. It is important to note that *the resistance is increasing despite a predicted decrease in resistance due to the cooling of the sample*. This is a major result with respect to the central research problem of this work and the DES experimental method. Specifically, the double verification method of both DES and resistance measurements is strongly indicating that gaseous surface scattering can perturb nanoscale transport properties. The first stop-flow condition at 11 minutes shows a large negative spike. These spikes were found to be common at the start and stop flow points and were all very short in duration. In fact, during the experimental work, the instrumentation clearly showed the spikes at nearly every start/stop flow point however they were not always captured by the data collection system due to the sampling rate of 1 Hz. The spikes were found to *always* show increased resistance on start-flow and *always* show decreased resistance on stop-flow. Further discussion of this phenomena shall ensue later in this chapter. The Cu sample also showed clear stepwise response to each He energy regime. However, as the experimental staging continued, some decay in the distinct steps are evident. This is also noted in the Au sample although not as pronounced. This behavior is attributed to overall temperature decreases and accumulated He adsorption effects.

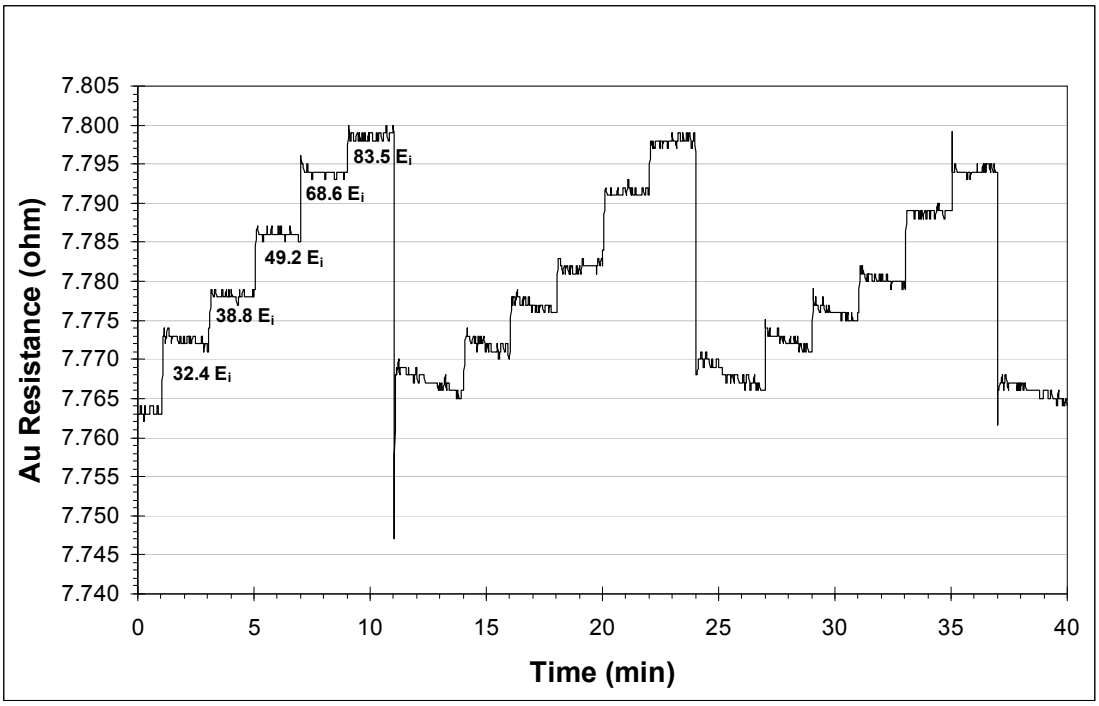

Figure 5.50: Au 30 nm sample placed under consecutive stepwise He impact energy E_i. The process was repeated three times while continuously collecting data.

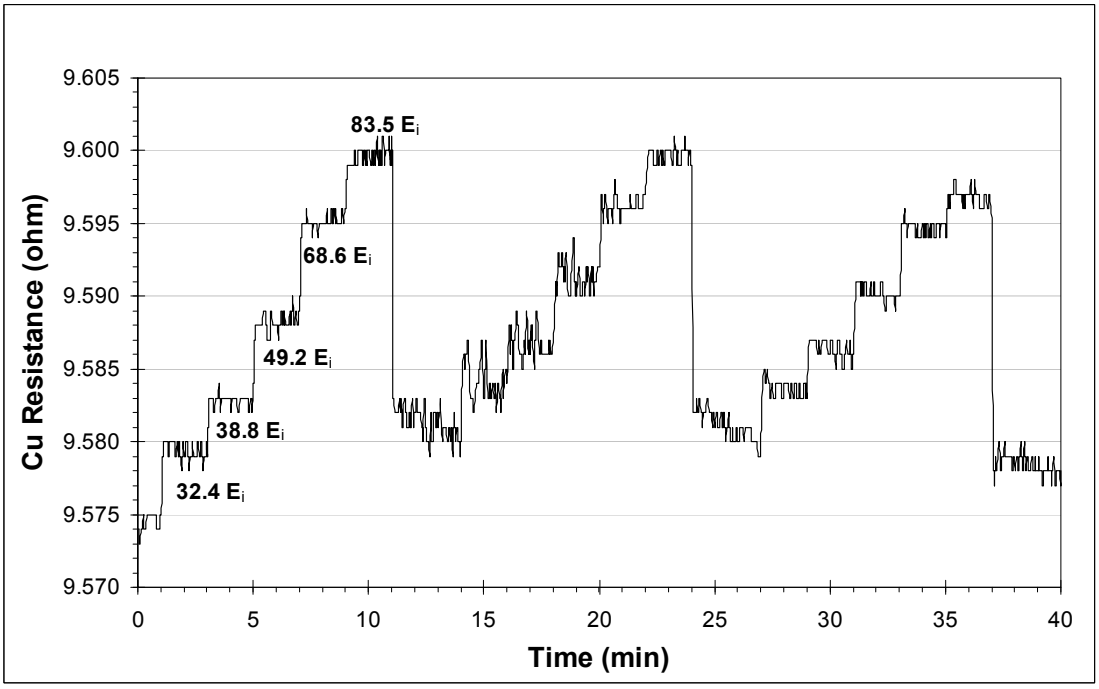

Figure 5.51: Cu 30 nm sample placed under consecutive stepwise He impact energy E_i. The process was repeated three times while continuously collecting data.

To gather comparative data of the theoretical response of the Au and Cu resistance due to sample cooling and the actual resistance, each sample was run at E_i = 83.5 meV for four minutes. Resistance data was collected and then compared to the *predicted* resistance drop due to the decreased sample temperature. The predicted resistance drop was calculated via the relevant temperature coefficient of resistance.[139] The calculated resistance used actual experiment calibration temperature data from the instrumented mock sample detailed in Section 4.2.2, Figure 4.11. The motivation behind this experiment was to assess how the sample resistance is predicted to behave versus the actual thin film response. Figures 5.52 and 5.53 show the Au and Cu results respectively. At 83.5 meV, the sample temperature decreases by approximately 4.6 K due to Joule-Thomson cooling. This corresponds to a predicted drop in Au resistance of 0.071 Ω as shown in Figure 5.52. As expected from previous experimental results however, the Au resistance increased immediately from 7.746 Ω to approximately 7.85 Ω or an increase of 0.104 Ω. The slight decay immediately after flow initialization matches up almost identically with the sample predicted resistance drop due to decreased temperatures. Therefore, we argue that the thin films response during the flow experiments are due to coupled effects. Namely, 1) dominant gaseous surface scattering that perturb transport properties and 2) material transport properties that deviate slightly due to temperature effects. However, the most important observation is that the gaseous surface scattering appears to be dominant, which is in overwhelming support of the central research problem. It is important to also note the Au resistance dip upon He stop-flow. This experiment, in conjunction with all other experimental evidence is indicating that the negative spikes are due to the immediate disappearance of He surface scattering followed by the material resistance quickly decaying to the value associated with the lower sample temperature, yet captured by the quick warming of this small sample due to He stop-flow. The positive spikes

noted to be present at every start-flow point, are hypothesized to be due to the immediate onset of He surface scattering that momentarily disrupts the equilibrium electron ensemble thus causing an increase in resistance. The electron ensemble quickly dissipates the new dynamic He (or Ar) energetic gas field to other scattering sites within the lattice domain thus settling into equilibrium at the newly perturbed resistivity value. From this point, resistance dips or rises are probably induced by slow temperature changes and physical adsorption effects of the incident gas. The Cu sample shown in Figure 5.53 showed nearly identical behavior as the Au sample. The Cu temperature coefficient predicted a resistance drop of 0.188 Ω while the sample actually increased in resistance by 0.025 Ω.

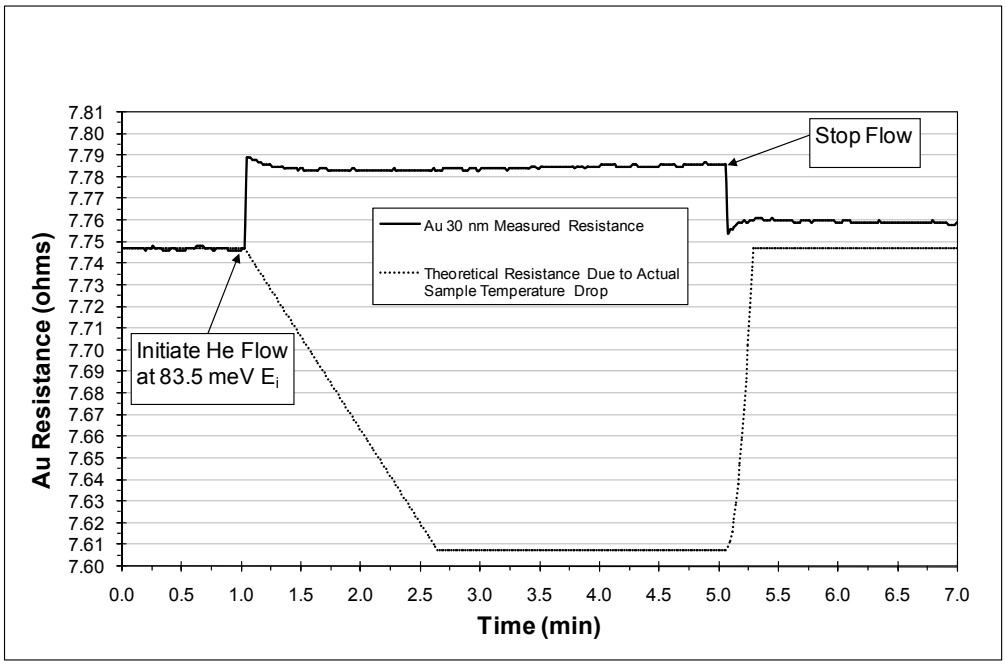

Figure 5.52: Au 30 nm sample under He impact energy of 83.5 meV. The predicted sample resistance due the actual sample temperature drop is plotted as a comparative analysis to help assess the nanostructure behavior under gaseous scattering effects.

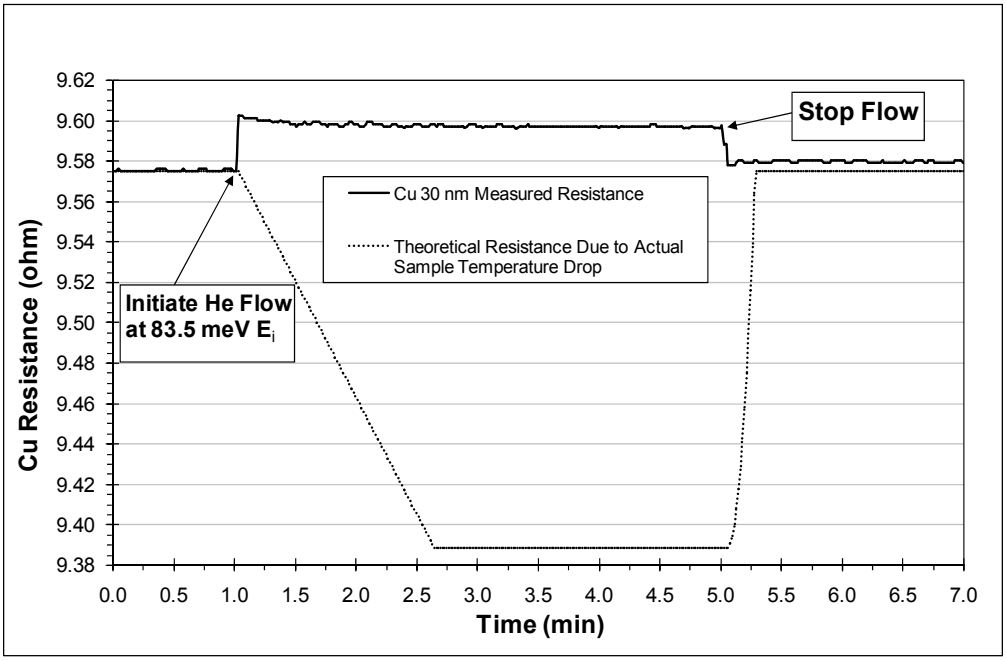

Figure 5.53: Cu 30 nm sample under He impact energy of 83.5 meV. The predicted sample resistance due the actual sample temperature drop is plotted as a comparative analysis to help assess the nanostructure behavior under gaseous scattering effects.

The Au and Cu 30 nm sample resistance as a function of He gas impact angle is shown in Figures 5.54 and 5.55. The Au shows a clear increase in resistance at 0 theta compared to 10 and 20 theta. Additionally, the start/stop flow spikes are captured very well during this experiment. The Cu sample also shows a resistance increase at each angle with the 0 theta resistance slightly less than the 10 and 20 theta values. The objective of this experiment was simply to assess the presence of He surface scattering at angles other than 0 theta. This objective was met as the resistance undergoes clear perturbations at 10 and 20 theta.

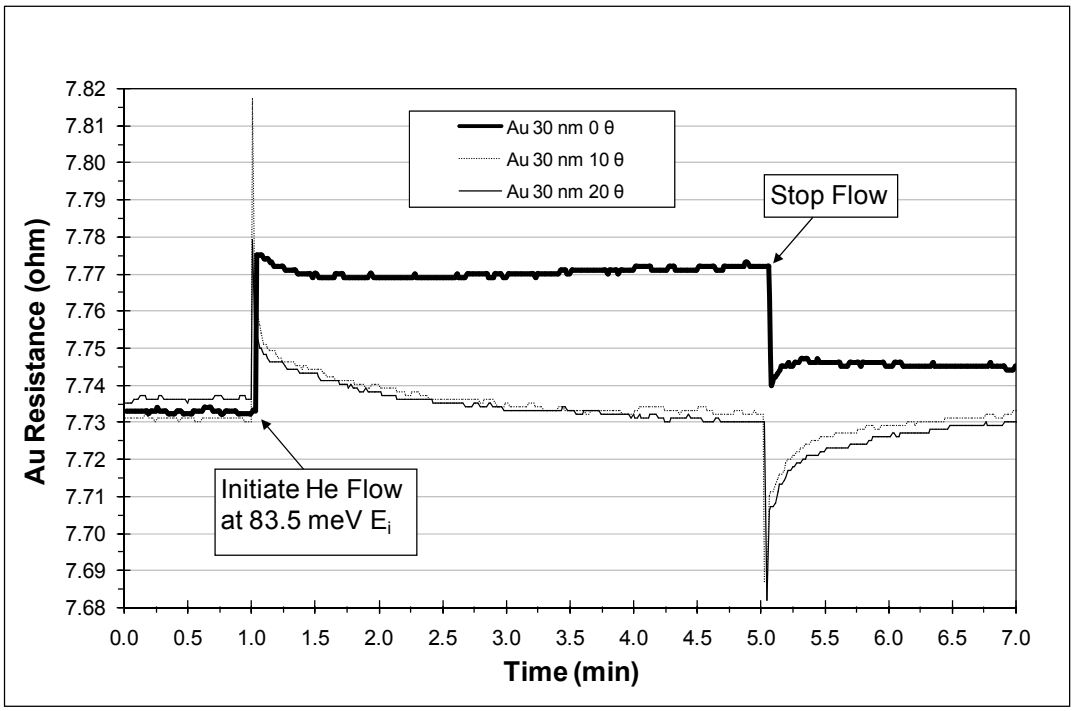

Figure 5.54: Au 30 nm sample under 83.5 meV He at sample impact angles of 0, 10 and 20 degrees theta.

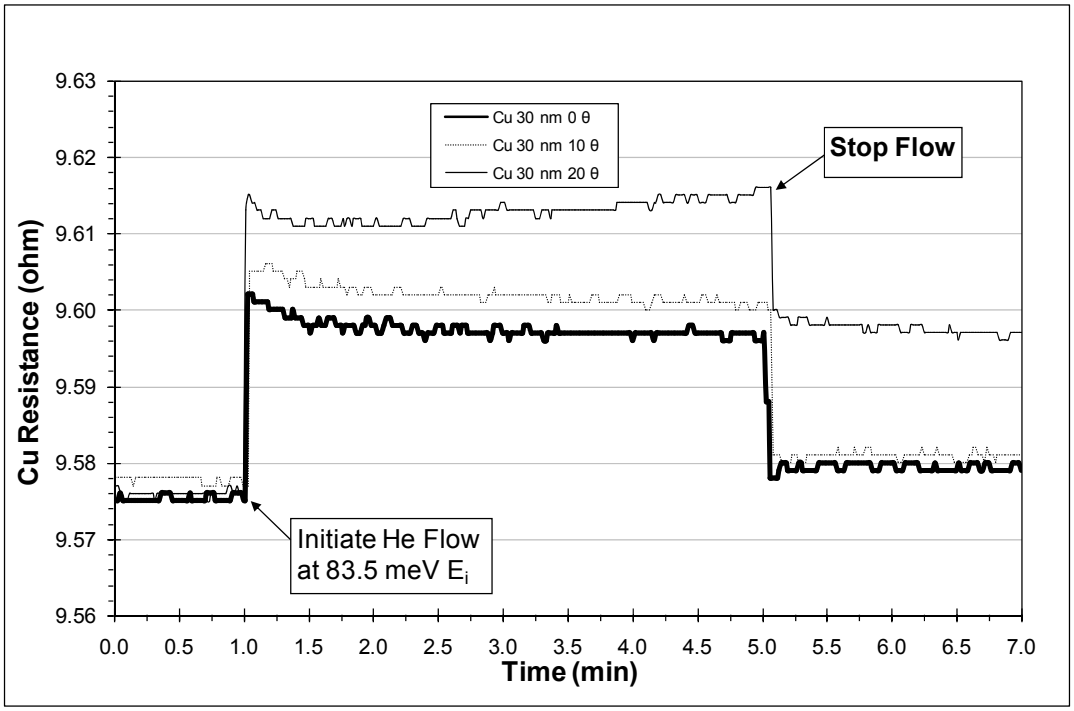

Figure 5.55: Cu 30 nm sample under 83.5 meV He at sample impact angles of 0, 10 and 20 degrees theta.

As mentioned previously, the non-stationary gaseous flow has increasing E_i, q_g and collision density as input gas pressure is increased. The experimental design however, encompassed a single point impact energy E_i that was nearly identical between He and Ar. This single point E_i occurred at the He input pressure of 1034.21 kPa, E_i = 68.6 meV and at the Ar input pressure of 689.47 kPa, E_i = 67.8 meV. Therefore, a data comparison is possible between He and Ar at the same E_i. Figures 5.56 and 5.57 display the resistance measurements resulting from this proportional impact energy. The Au sample showed a larger increase in resistance for the He flow rising 0.033 Ω above the initial resistance of 7.756 Ω. The same Au sample under Ar flow increased 0.007 Ω above the initial resistance of 7.760 Ω. An interesting feature of the He and Ar response on the same plot is the larger decay rate of Au resistance after Ar flow is initiated. The Au decay rate under He flow is not as pronounced. This characteristic is attributed to the lower sample temperature under Ar flow compared to He flow (3.6 K drop versus 3.1 K drop) as well as the decreased collision density of the Ar flow field. The theoretical results of Chapter 2 also predicted increased perturbation effects due to larger collision densities for the crystal lattice (phonon scattering). The Cu sample showed similar behavior with a larger resistance increase for the He flow field than the Ar flow field. The Cu resistance increased 0.021 Ω over the initial 9.874 Ω value during He flow while the Ar flow induced an initial spike followed by enough sample cooling and adsorption effects to overcome the surface scattering perturbations. The start/stop flow spikes are also noted to be fairly well captured for both gas species.

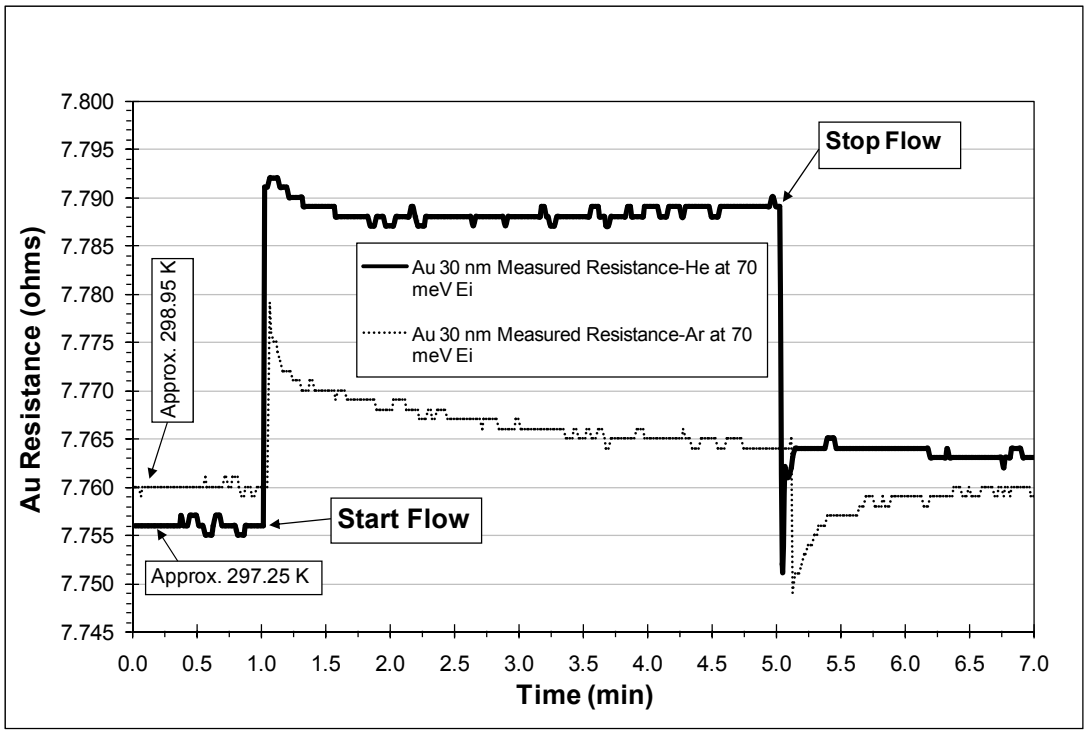

Figure 5.56: Au 30 nm sample run under both He and Ar at nearly identical impact energies.

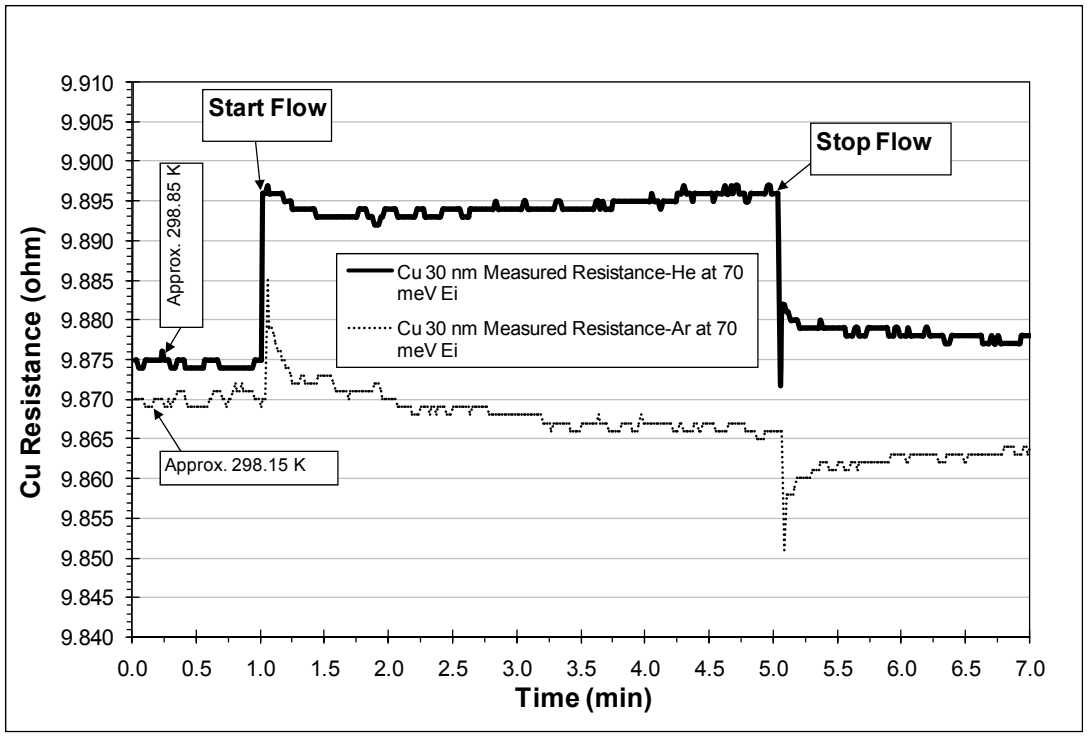

Figure 5.57: Cu 30 nm sample run under both He and Ar at nearly identical impact energies.

5.4.2 Au and Cu Thin Films Subject to Non-Stationary Argon Flow

The objective of this section is to experimentally quantify the electronic transport property effects on Au and Cu thin films subjected to a non-stationary flowing Ar boundary. The experimental parameters remain identical to the previous section except for the use of Ar as the interfacial flowing medium.

The DES experimental PSD results for Au and Cu under Ar flow are shown in Figures 5.58 – 5.59. The Au voltage PSD was found to decrease slightly at the first Ar flow step but then remain fairly stable at each subsequent E_i. The Au thermal PSD remained fairly stable through each flow regime. The Cu voltage PSD also oscillated slightly at the first two flow steps however smoothed out for the remaining E_i. As expected, the Cu thermal PSD remained fairly stable throughout the experiment.

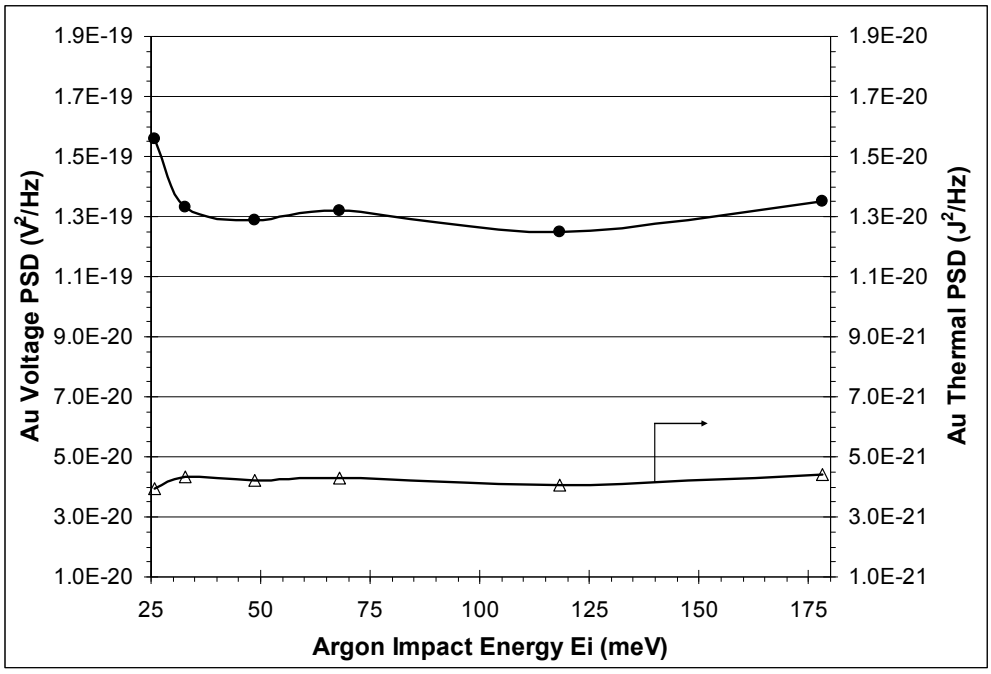

Figure 5.58: Au 30 nm sample voltage and thermal PSD response from stationary (25.8 meV) to 178.16 meV Ar impact energy. The solid circles (solid line) and open triangles (solid line) represent the voltage and thermal PSD's respectively.

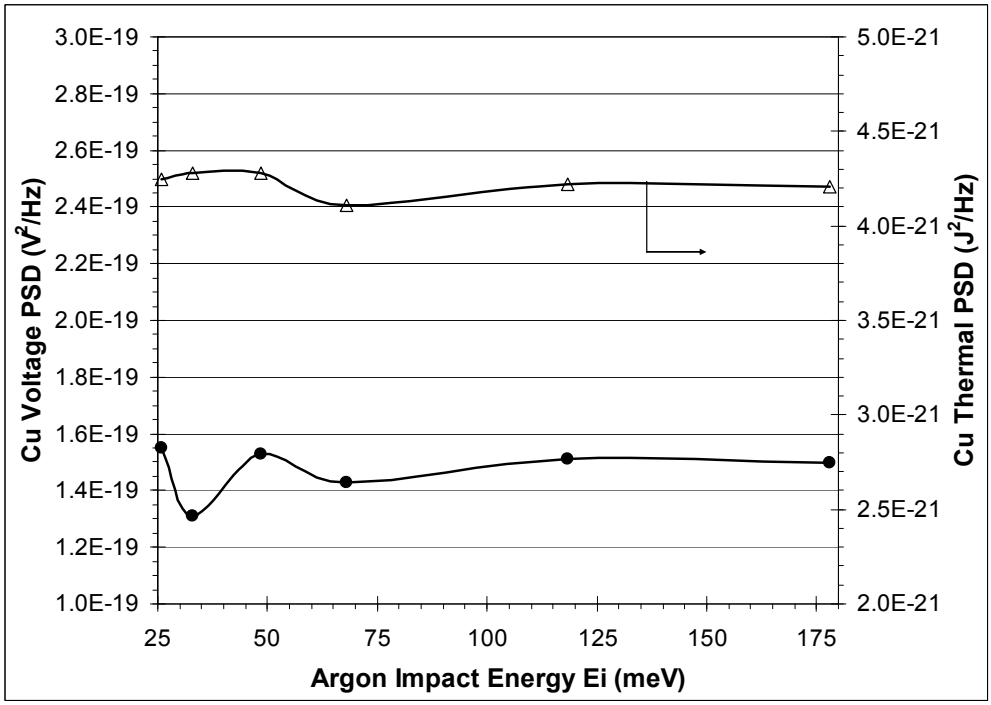

Figure 5.59: Cu 30 nm sample voltage and thermal PSD response from stationary (25.8 meV) to 178.16 meV Ar impact energy. The solid circles (solid line) and open triangles (solid line) represent the voltage and thermal PSD's respectively.

The electronic thermal conductivity and resistivity response to Ar flow is shown in Figures 5.60 – 5.61. The Au thermal conductivity shows an increase at 32.4 meV followed by a steady decrease at each corresponding impact energy. Beginning at approximately 290 W/m-K, the Au thermal conductivity measured 248 W/m-K at 178.16 meV which is a 15% drop. The corresponding Au resistivity measured approximately 4.61E-8 Ω-m at stationary flow and increased to 5.27E-8 Ω-m at 178.16 meV which is a 14% increase. Beginning at approximately 181 W/m-K, the Cu thermal conductivity measured 142 W/m-K at 178.16 meV which is a 22% drop. The Cu resistivity however increased initially followed by a minor dip then rise again. The Cu resistivity measured 3.81E-8 Ω-m at stationary flow and increased to 4.48E-8 Ω-m at 178.16 meV which is a 17% increase.

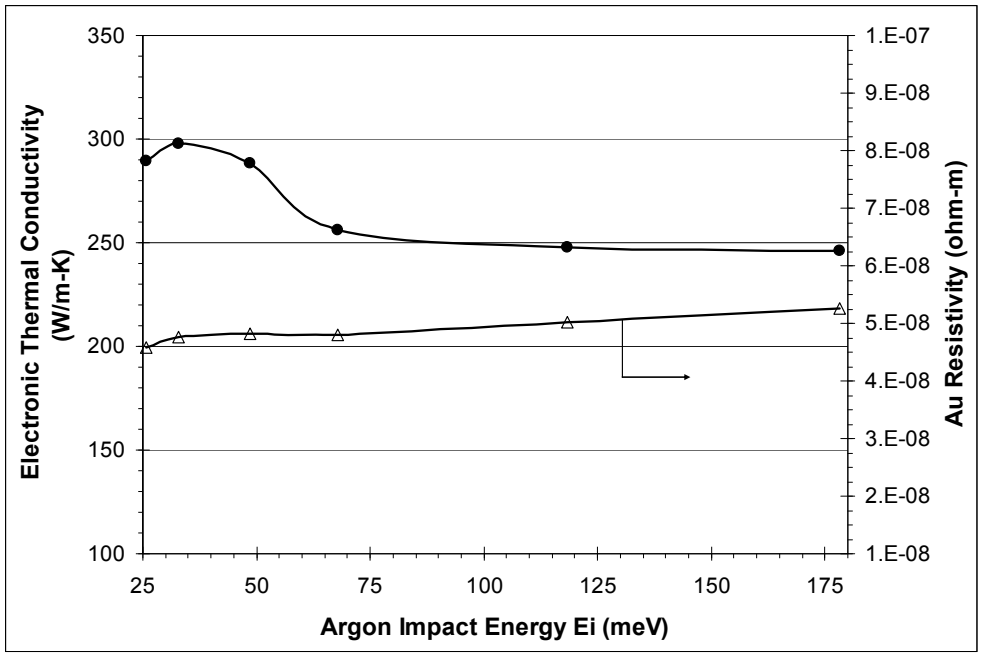

Figure 5.60: Au 30 nm sample electronic thermal conductivity and resistivity response from stationary (25.8 meV) to 178.16 meV Ar impact energy. The solid circles (solid line) and open triangles (solid line) represent the electronic thermal conductivity and resistivity respectively.

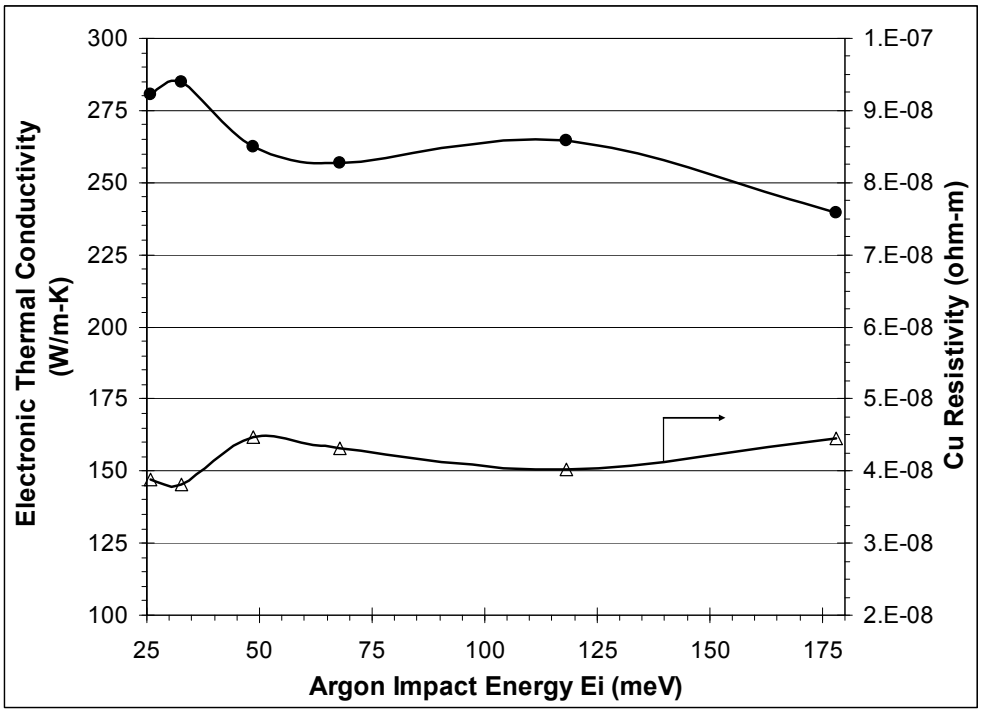

Figure 5.61: Cu 30 nm sample electronic thermal conductivity and resistivity response from stationary (25.8 meV) to 178.16 meV Ar impact energy. The solid circles (solid line) and open triangles (solid line) represent the electronic thermal conductivity and resistivity respectively.

In order to continue the comparative assessment of the gaseous boundary on both nanostructures and bulk materials, the bulk Cu sample used in Section 5.2 was also placed under the same Ar impact energy E_i regimes as the Au and Cu thin films. The motivation behind this experiment was to compare the results with the arguments put forth in Chapter 1: that gas particle scattering on nanosurfaces could possibly perturb material transport properties. The results for the bulk Cu electronic thermal conductivity and resistivity are shown in Figure 5.62. Compared to the results of the 30 nm Cu sample, there is basically no response to the increasing Ar impact energy.

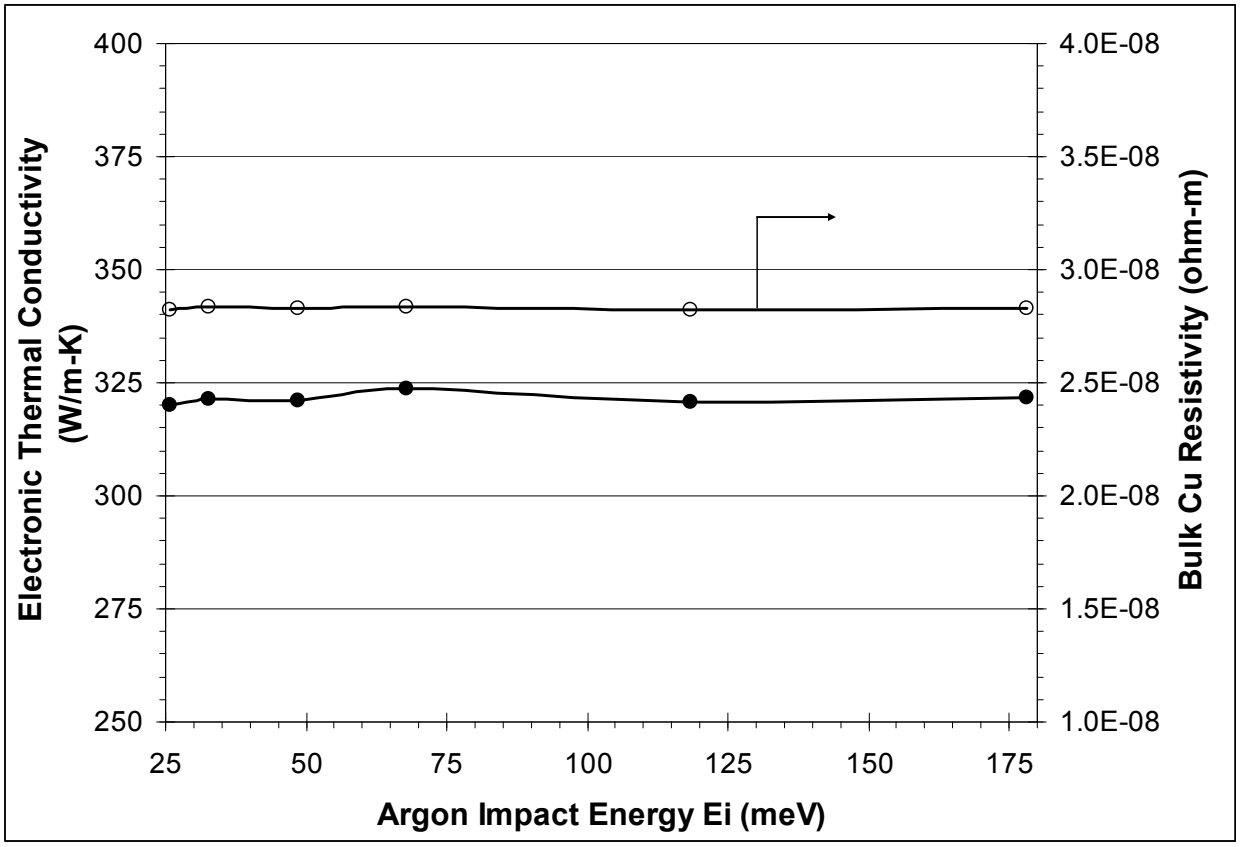

Figure 5.62: Bulk Cu electronic thermal conductivity and electrical resistivity results are indicated by the solid circle markers and open circles respectively for the six impact energy flow regimes. The DES measurements show almost no change to either transport coefficient during each E_i step.

The Lorenz number and corresponding Ar collision density at each Ar energetic impact energy E_i for both Au and Cu are shown in Figures 5.63 and 5.64. The DES measurements on the Au sample resulted in an immediate Lorenz number drop at the first flow regime of 32.4 meV. The Au Lorenz number then slowly decreased through the remaining stages of flow energy. The Cu sample also showed an initial bump at 32.4 meV followed by a fairly consistent value for the remaining flow stages. The Cu Lorenz number measured approximately 3.7 $W\Omega K^{-2}$ which is similar to the approximate Au average Lorenz number of approximately 3.45 $W\Omega K^{-2}$.

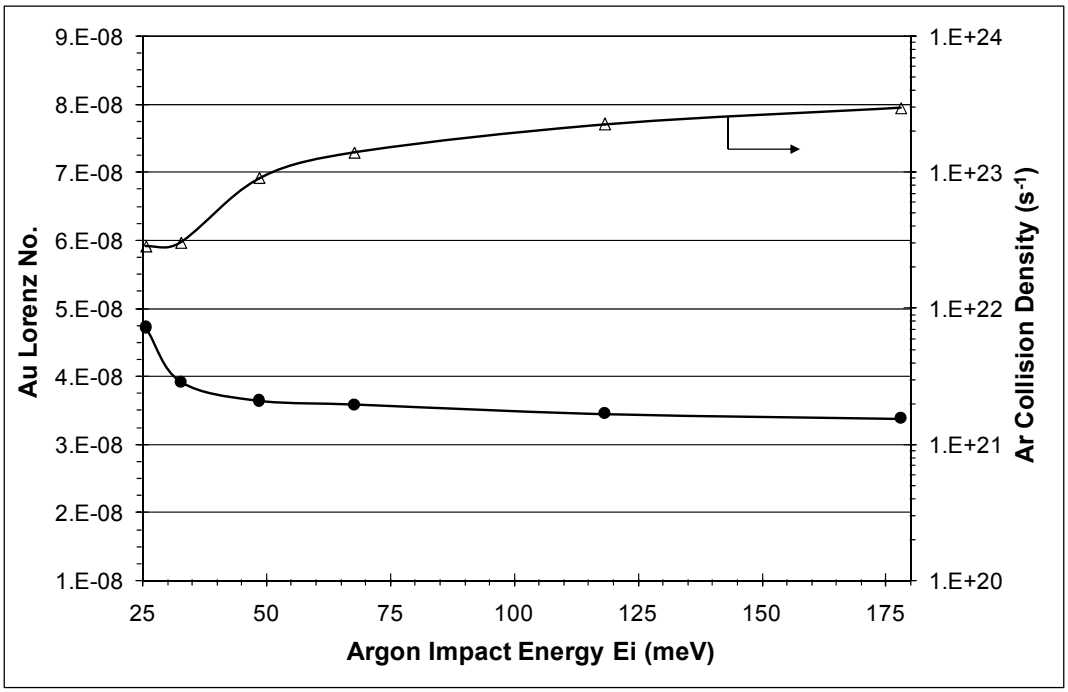

Figure 5.63: The Au Lorenz number results are shown for the six impact energy flow regimes as solid circles (solid line). The Ar collision density (open triangles and solid line) increases with each corresponding Ar impact energy increase.

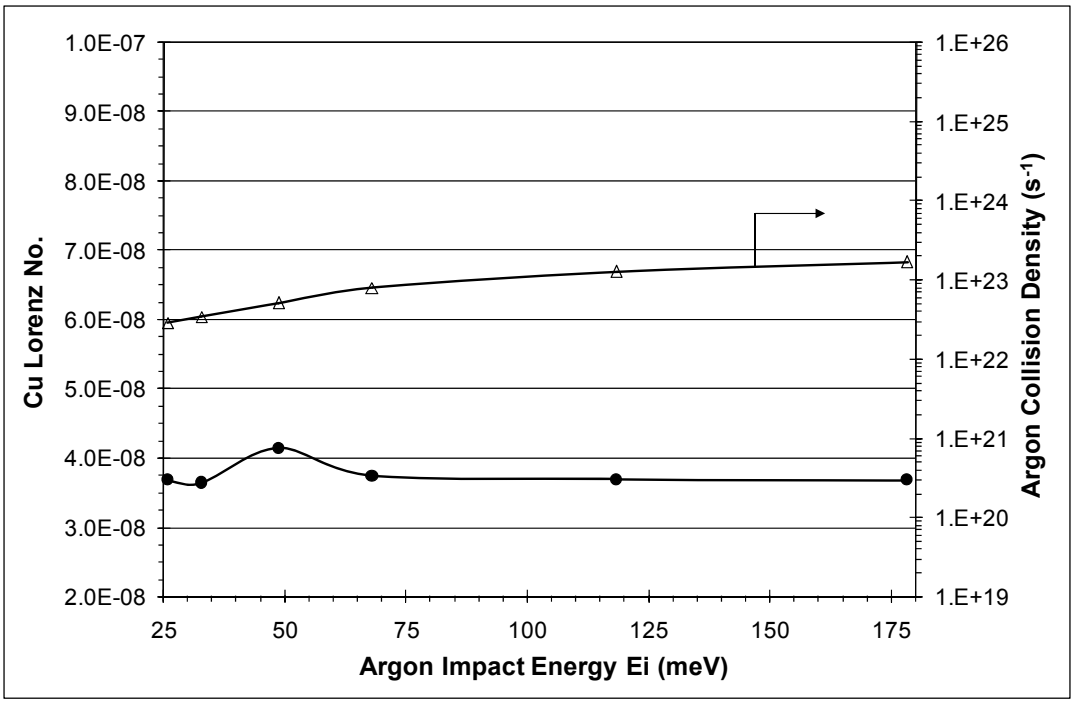

Figure 5.64: The Cu Lorenz number results are shown for the six impact energy flow regimes as solid circles (solid line). The Ar collision density (open triangles and solid line) increases with each corresponding Ar impact energy increase.

The Au and Cu Seebeck coefficient response to Ar impact energy is shown in Figures 5.65 and 5.66. The DES measurements show an immediate drop at the 32.4 meV stage with a slow increase at the next two Ar impact energies. The Au Seebeck value then stabilizes at the last two flow stages. The initial Au Seebeck value of 2.04 μVK^{-1} dropped to 1.84 μVK^{-1} at 32.4 meV which is approximately 10% decrease. The Cu sample measured 1.20 μVK^{-1} at stationary flow and increased to 1.66 μVK^{-1} at 32.4 meV. The Cu Seebeck then increased slowly ending up at 2.23 μVK^{-1} at 178.16 meV.

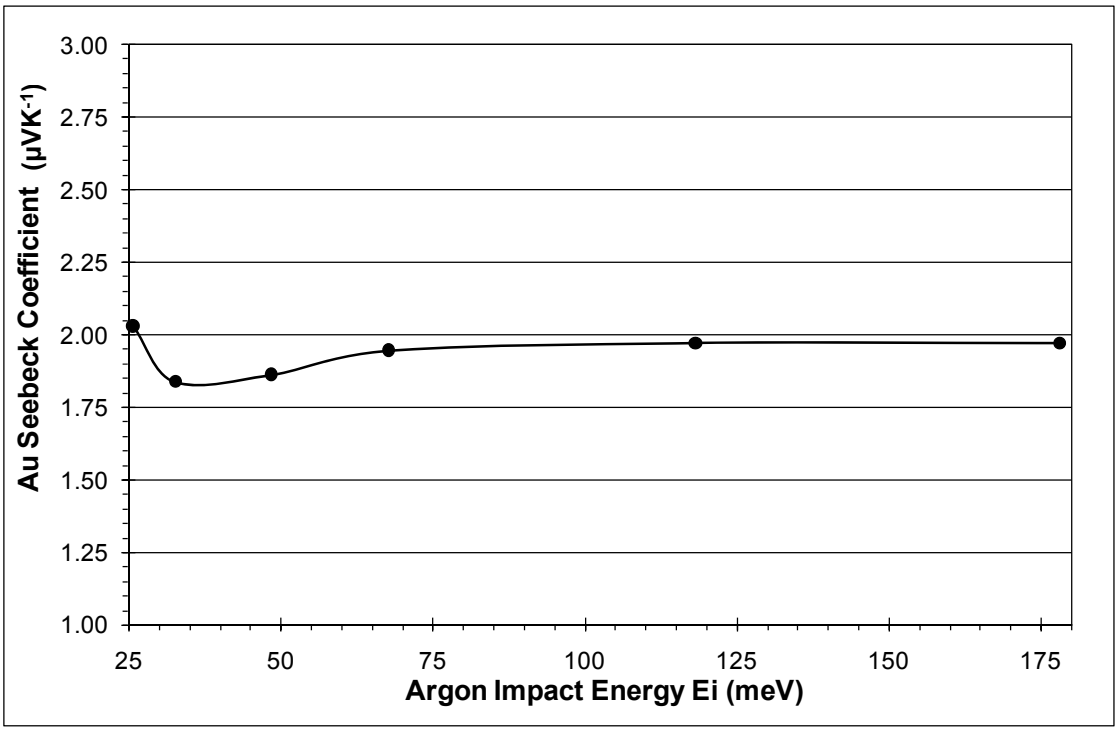

Figure 5.65: The Au Seebeck coefficient results are shown for the six impact energy flow regimes.

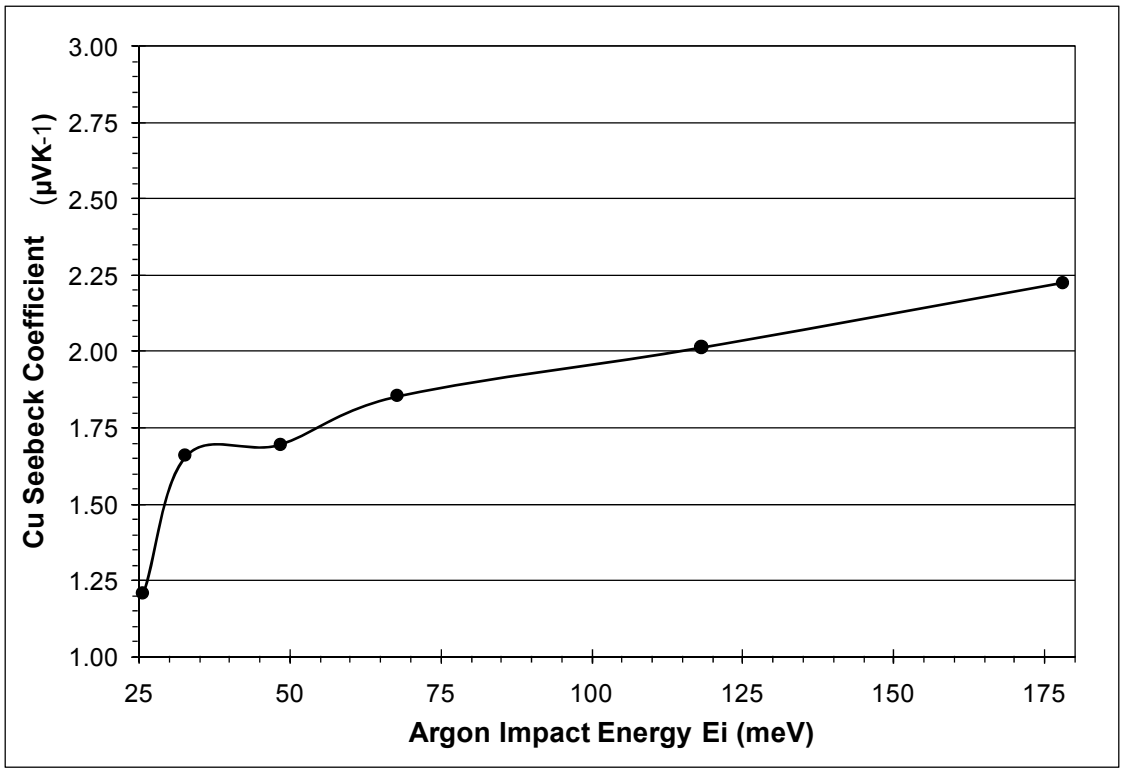

Figure 5.66: The Cu Seebeck coefficient results are shown for the six impact energy flow regimes.

The analysis of the Au and Cu ACF's behavior in the flowing Ar gas field continues in this section. Clearly, a comparative analysis of the structure and behavior of the Au and Cu ACF's at discrete impact energy regimes is both experimentally and theoretically important. Figures 5.67 and 5.68 give a comparative ACF for both Au and Cu at the 25.8 meV (no-flow condition) and the 178.16 meV E_i. The main plot extends out to 20 ps while the inset show early temporal behavior up to 3 ps. The differences in the 25.8 meV (no-flow) and 178.16 meV E_i decay are noted to be at or very near the first zero axis crossing which is identical to the previous Ar and He ACF behavior. For example, the initial exponential decrease from $t = 0$ is fairly similar for each ACF. During the first dip however, oscillatory behavior clearly differs under 178.16 meV Ar. The oscillatory behavior also appears to slightly more pronounced further out in time than the stationary pressure results shown in Figure 5.35 and 5.36. This phenomenon is hypothesized to be induced by the increased impact energy coupled with larger Ar gas wave vector q_g, which dynamically changes the energy and momentum relaxation behavior of the electron ensemble. The experimental observation and measurement of the surface perturbations due to a *flowing* Ar boundary through the voltage fluctuation spectra ACF is experimentally significant and has not been reported by any other group.

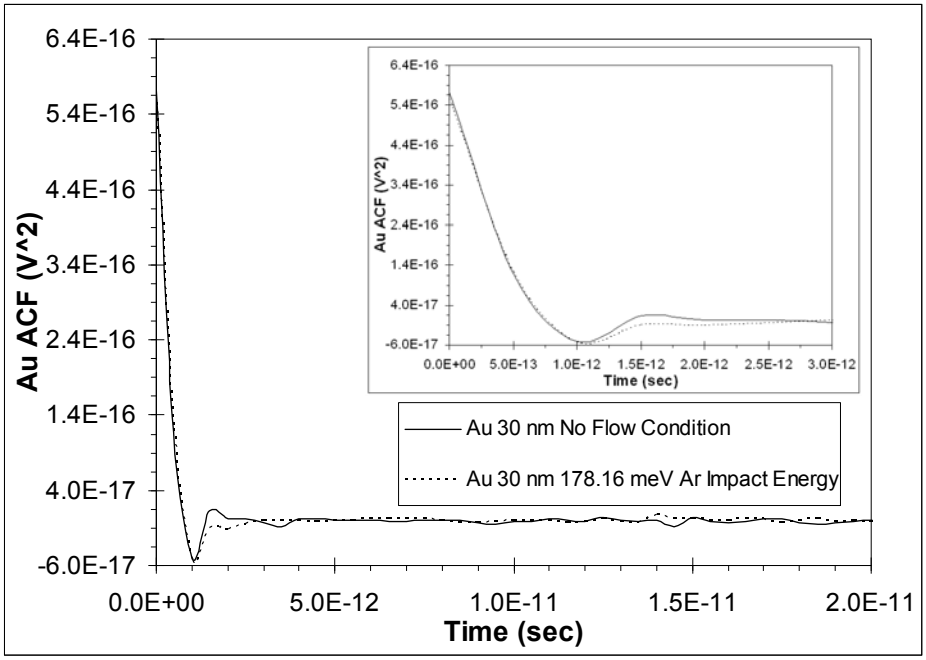

Figure 5.67: Comparative results of the Au ACF at 25.8 meV (no-flow) and 178.16 meV Ar E_i. The ACF oscillatory behavior at 178.16 meV is attributed to increased surface scattering effects due to a combined increase in Ar scattering effects such as collision density, E_i and q_g. The main plot extends temporally to 20 ps while the inset shows short-time behavior out to 3 ps.

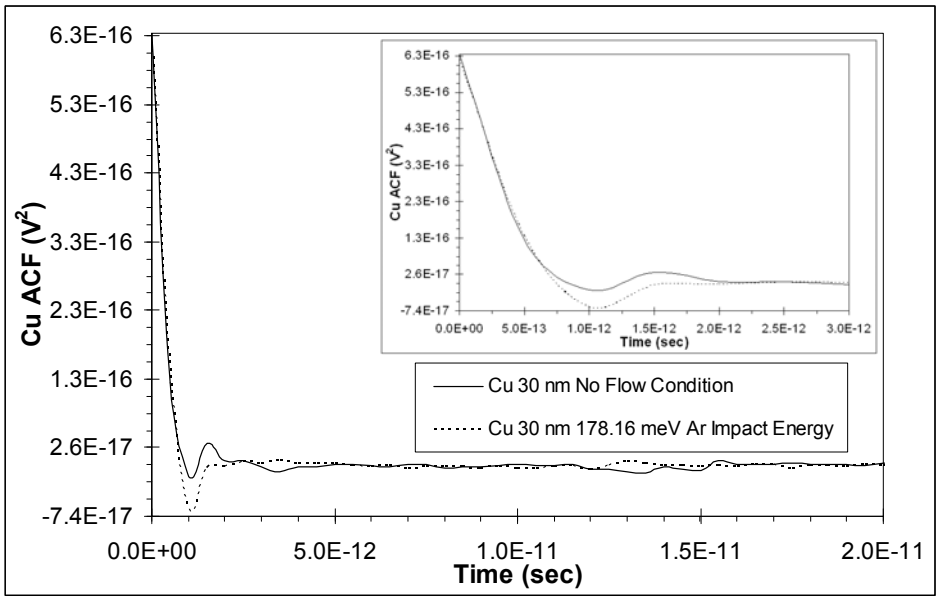

Figure 5.68: Comparative results of the Cu ACF at 25.8 meV (no-flow) and 178.16 meV Ar E_i. The ACF oscillatory behavior at 178.16 meV is attributed to increased surface scattering effects due to a combined increase in Ar scattering effects such as collision density, E_i and q_g. The main plot extends temporally to 20 ps while the inset shows short-time behavior out to 3 ps.

The motivation of obtaining resistance data on the Au and Cu 30 nm thin films remains the same as the previous section. Fundamentally, the resistance measurements are desired as an aid in interpreting the DES data. The resistance measurements were executed using the equipment detailed in Section 4.2.4. The data sampling rate was set to one sample per second. Argon impact energies were identical to all other non-stationary flow experiments in order to maintain a comparative data base. The same Au and Cu samples used in the DES experiments were used for the resistance measurements. Moreover, the same flow chamber and sample holder apparatus was used which greatly simplified this additional experimental validation effort.

Figure 5.69 and 5.70 below show the Au and Cu 30 nm resistance behavior at Ar no-flow conditions and at Ar flow conditions. The step increase in resistance is clearly evident upon initiation of Ar flow yet less pronounced than the He flow results of Figures 5.48 and 5.49. The Au sample resistance increased approximately 0.06% from 7.76 Ω to 7.765 Ω when Ar flow was started. There is a slight decrease in resistance during the flow period which is probably due to sample temperature decrease and Ar physical adsorption effects which may change the overall surface scattering dynamics. The abrupt decrease in resistance when Ar flow was stopped is clearly visible. The Cu sample resistance increased approximately 0.02% from 9.865 Ω to 9.867 Ω when Ar flow was started. The distinct decrease in Cu resistance when He flow is stopped is again evident.

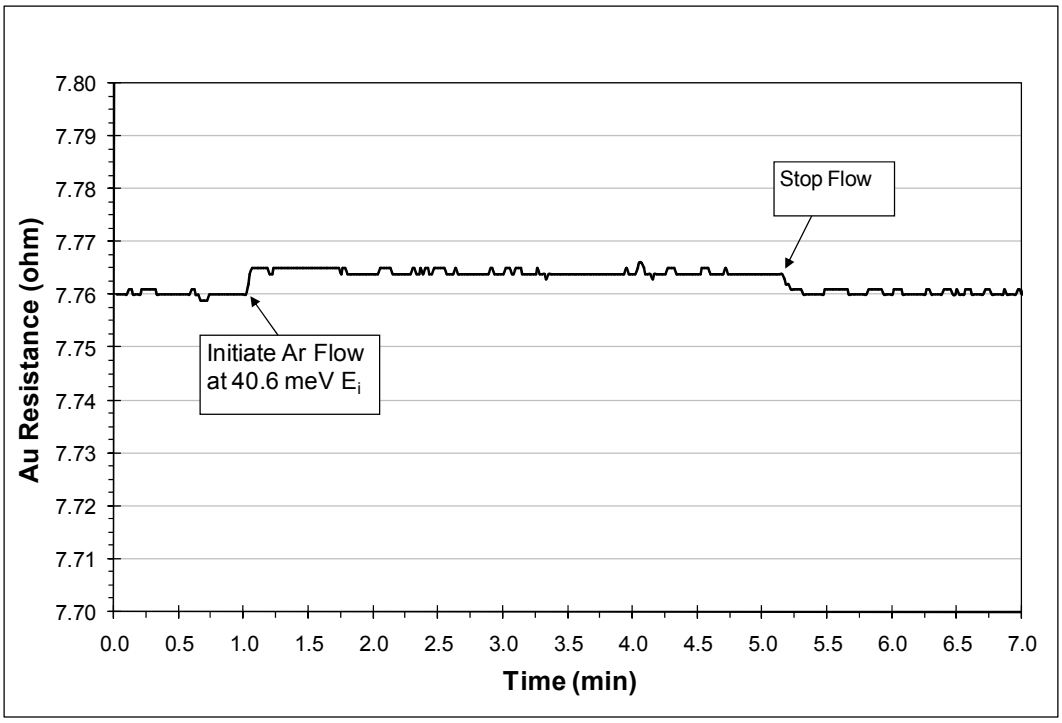

Figure 5.69: Au 30 nm sample resistance under 25.8 meV (no-flow) and 40.6 meV Ar E_i. The distinct drop in Au resistance is clearly evident when Ar flow ceased.

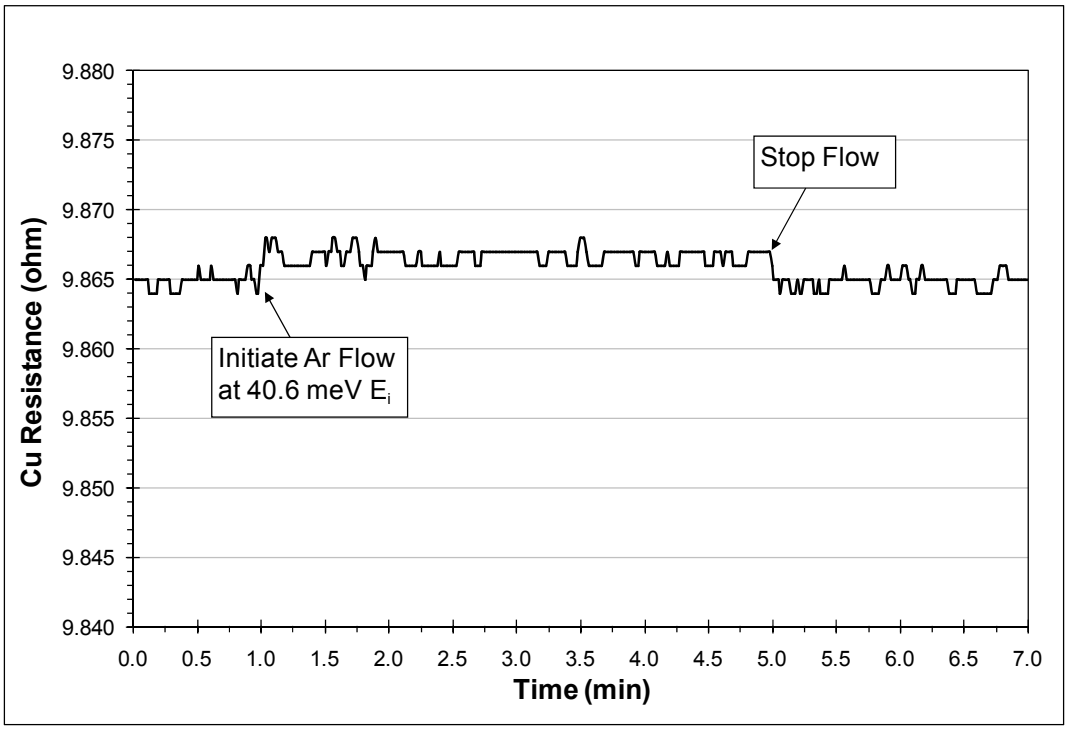

Figure 5.70: Cu 30 nm sample resistance under 25.8 meV (no-flow) and 40.6 meV Ar E_i. The distinct drop in Cu resistance is clearly evident when Ar flow ceased.

In order to obtain resistance data at each Ar E_i, the experiment was run at the relevant impact energies consecutively. Beginning with the no-flow condition, each relevant Ar E_i was initiated for two minutes followed by the next impact energy in stepwise fashion. Upon completing the 178.16 meV regime, flow was stopped for three minutes followed by another set of discrete Ar flow steps. This process was executed three times to assess the repeatability of the Ar scattering process on each nanostructure and to gather comparative stepwise resistance data for reference to the He runs of the previous section. Figures 5.71 and 5.72 below show the results for the subject Au and Cu 30 nm samples. The Au sample shows a stepwise response to each Ar E_i however considerable decay of the resistance step profiles are noted. This behavior is clearly the result of sample cooling at higher Ar impact energies which overcome the surface scattering effects. The presence of the now characteristic positive and negative spikes at each start/stop flow point is evident in Figure 5.71. The deep prolonged negative spikes at each Ar stop-flow point indicate that the sample temperature drop is the driving force which is inducing stepwise resistance decay. The Cu sample also showed a stepwise response to each Ar energy regime however with even less distinction than the Au sample. There appeared to be a Cu resistance rise at the 178.16 meV stage for the last two repeating profiles.

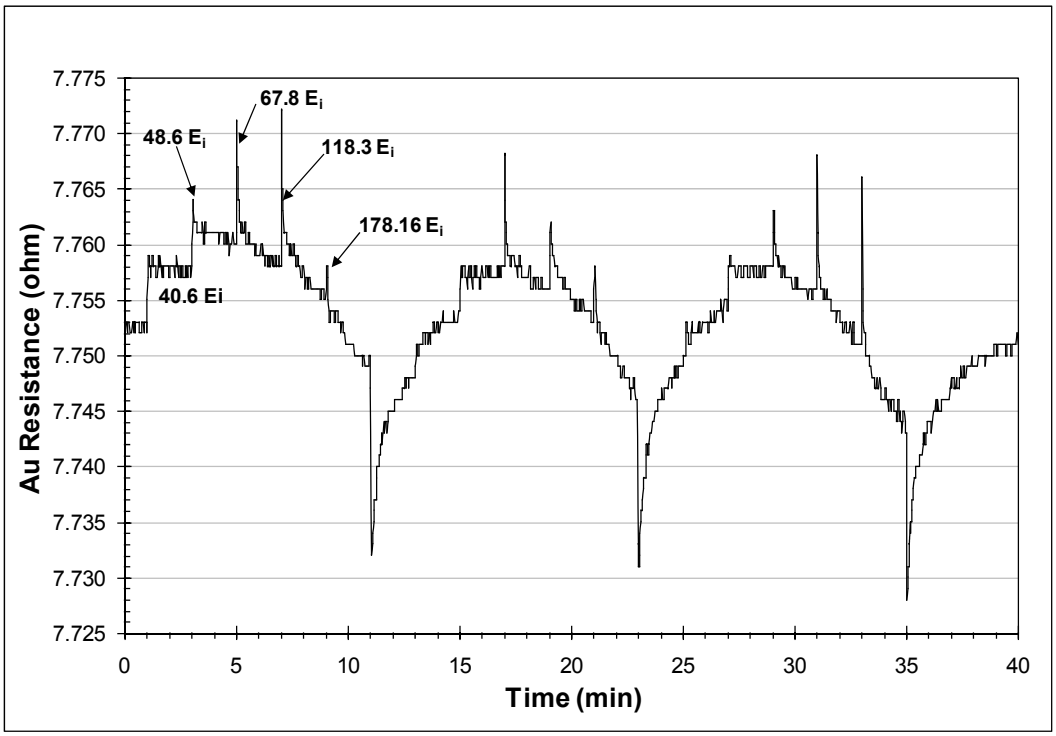

Figure 5.71: Au 30 nm sample placed under consecutive stepwise Ar impact energy E_i. The process was repeated three times while continuously collecting data.

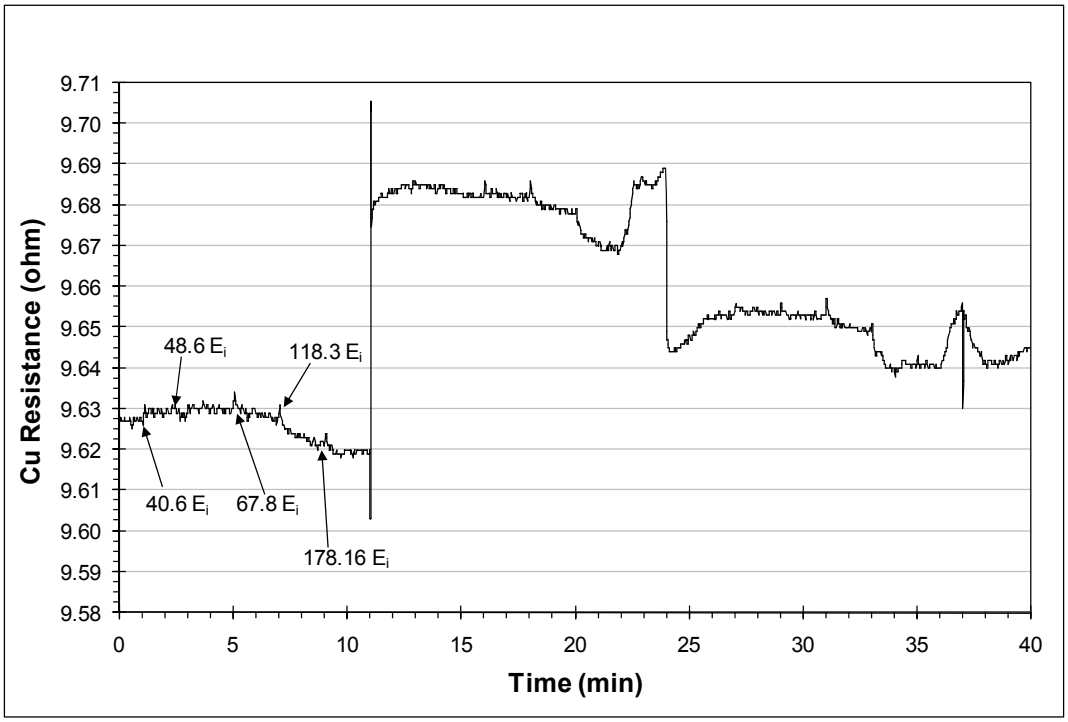

Figure 5.72: Cu 30 nm sample placed under consecutive stepwise Ar impact energy E_i. The process was repeated three times while continuously collecting data.

To gather comparative data of the theoretical response of the Au and Cu resistance due to sample cooling and the actual resistance, each sample was run at E_i = 178.16 meV for four minutes. Resistance data was collected and then compared to the predicted resistance drop due to the decreased sample temperature. The predicted resistance drop was calculated via the relevant temperature coefficient of resistance.[139] The calculated resistance used actual experiment calibration temperature data from the instrumented mock sample detailed in Section 4.2.2, Figure 4.11. The motivation behind this experiment was to assess how the sample resistance is predicted to behave versus the actual thin film response and to obtain comparative data to the results of Figures 5.52 and 5.53. Figures 5.73 and 5.74 show the Au and Cu results respectively. At 178.16 meV, the sample temperature decreases by approximately 8.4 K due to Joule-Thomson cooling. This corresponds to a predicted drop in Au resistance of 0.23 Ω as shown in Figure 5.73. As expected from previous experimental results however, the Au resistance increased immediately from 7.755 Ω to approximately 7.77 Ω or an increase of 0.015 Ω. The resistance decay begins immediately after flow initialization and continues through nearly all of the four minute experimental flow period. Subsequently, the argument is maintained that the thin films response during the flow experiments are due to coupled effects. Namely, dominant gaseous surface scattering that perturb transport properties and material transport properties that deviate slightly due to temperature effects. In conjunction with all of the results thus far, the most important observation is that the gaseous surface scattering appears to be present which is in overwhelming support of the central research problem. The Cu sample shown in Figure 5.74 showed similar initial behavior as the Au sample. The resistance decay however stabilized around midway through the flow period. The Cu temperature coefficient

predicted a resistance drop of 0.301 Ω while the sample actually increased in resistance by 0.025Ω.

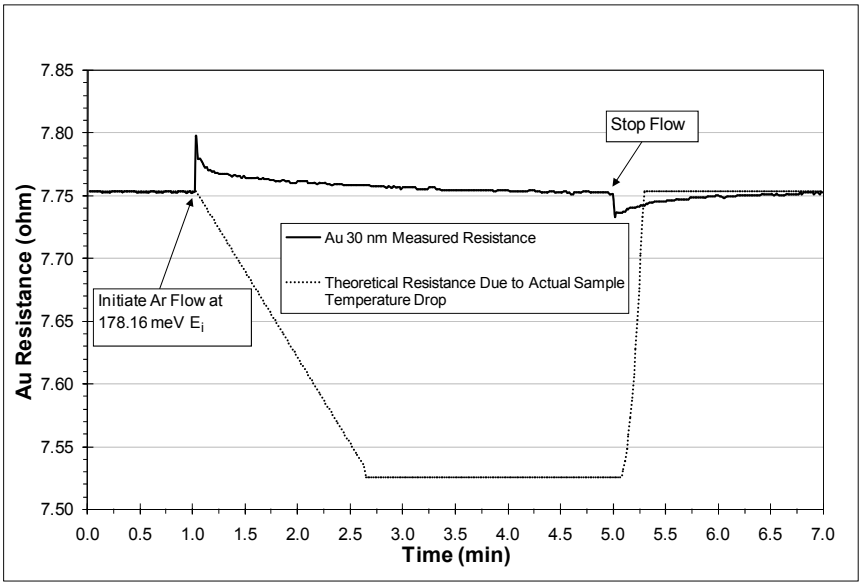

Figure 5.73: Au 30 nm sample under Ar impact energy of 178.16 meV. The predicted sample resistance due the actual sample temperature drop is plotted as a comparative analysis to help assess the nanostructure behavior under gaseous scattering effects.

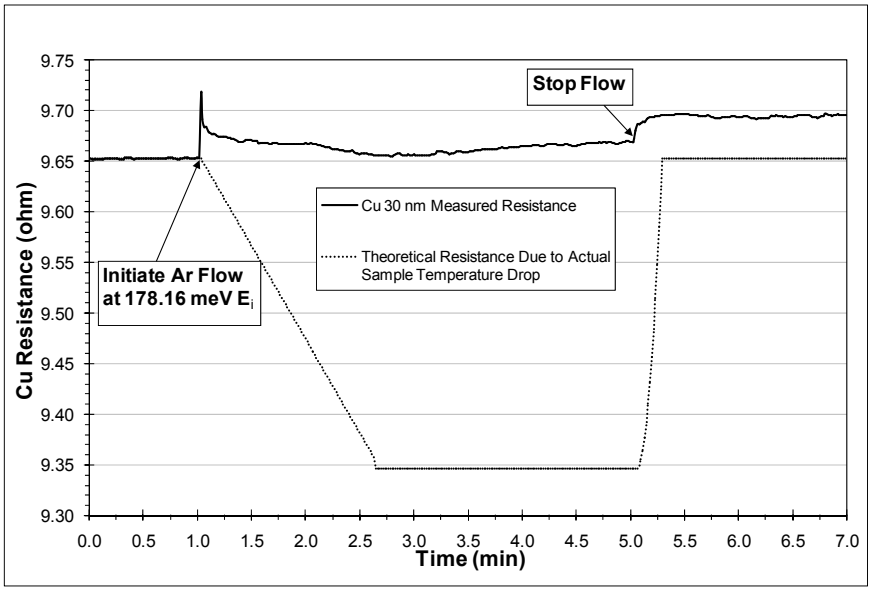

Figure 5.74: Cu 30 nm sample under Ar impact energy of 178.16 meV. The predicted sample resistance due the actual sample temperature drop is plotted as a comparative analysis to help assess the nanostructure behavior under gaseous scattering effects.

The Au and Cu 30 nm sample resistance as a function of Ar gas impact angle is shown in Figures 5.75 and 5.76. The Au shows a slight increase in resistance at 0 theta compared to 10 and 20 theta. Additionally, the start/stop flow spikes are captured very well during this experiment. The Cu sample also shows a resistance increase at each angle with the 0 theta resistance approximately comparable to the 10 and 20 theta values. The objective of this experiment was simply to assess the presence of He surface scattering at angles other than 0 theta. This objective was met as the resistance undergoes clear perturbations at 10 and 20 theta.

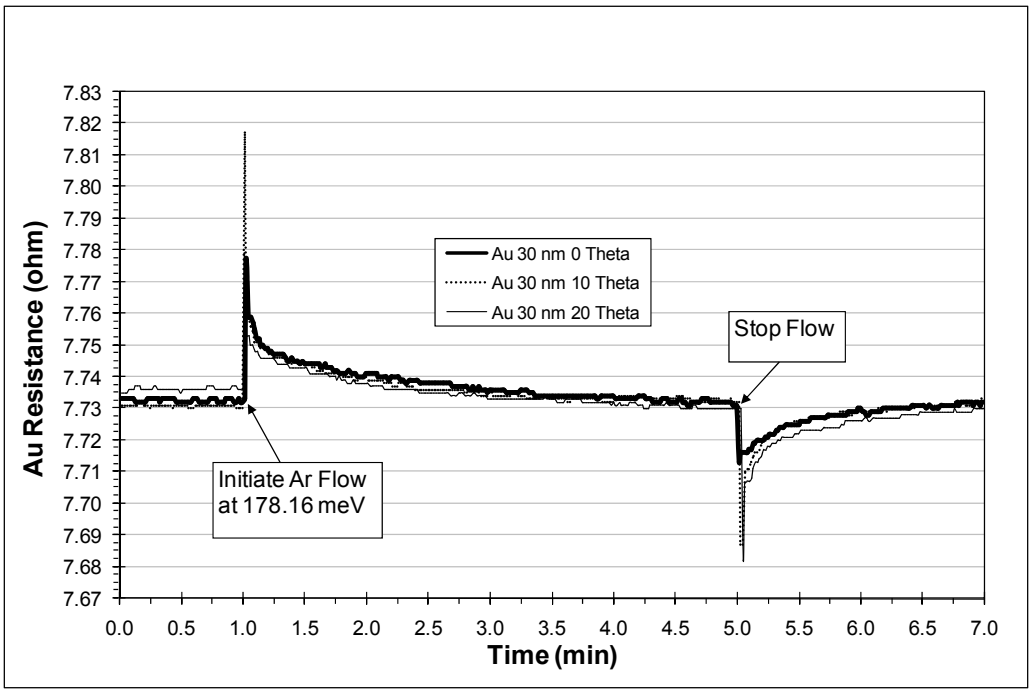

Figure 5.75: Au 30 nm sample under 178.16 meV Ar at sample impact angles of 0, 10 and 20 degrees theta.

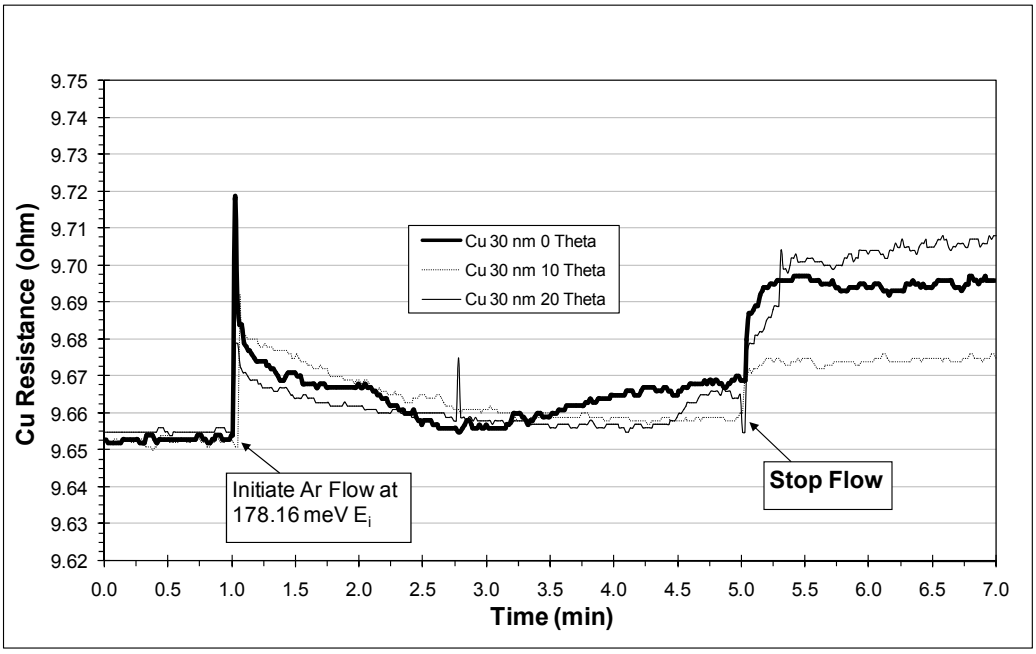

Figure 5.76: Cu 30 nm sample under 178.16 meV Ar at sample impact angles of 0, 10 and 20 degrees theta.

5.5 DES Experimental Summary

The experimental investigation conveyed in this chapter addressed the two primary objectives outlined in Section 5.1; 1) DES experimental validation and verification and 2) experimental transport property measurements of metal conductors interfaced with various gaseous boundary conditions. The first objective was met through excellent DES experimental agreement with a standardized material (NBS 1461), a standard resistivity experimental technique (collinear four-probe method) and verification against straight-forward resistance measurements. The second objective was met with successful DES measurements of thin film Au and Cu placed under Ar and He gas pressure and flow environments in order to quantify the relevant scattering effects. The results of these measurements are summarized below.

- The voltage PSD was perturbed under both Ar and He boundaries for both the pressure and flow runs. This result indicates a change to the mean square voltage which *must* be induced by a perturbed electrical resistivity through the Johnson/Nyquist relation.
- The thermal PSD remained fairly stable with little change during the Ar and He pressure and flow regimes. This result agrees with theory which predicts the thermal PSD to be temperature dependent only.
- The 30 nm Au and Cu electronic thermal conductivity and electrical resistivity were perturbed for both Ar and He pressure as well as flow cases. This result helps to validate the perturbed voltage PSD which is a result of a change in material resistance. In general, the Au sample showed a greater perturbation to conductivity and resistivity throughout all of the runs.
- The bulk Cu sample showed no change in electronic thermal conductivity or electrical resistivity under any boundary condition applied during this research. This indicates

overwhelming evidence that the gas-surface scattering effects begin to contribute appreciably to the overall scattering landscape for low-dimensional conductors.

- The Lorenz number for both Au and Cu samples changed accordingly during the pressure and flow runs in response to the perturbed conductivity and resistivity. The Lorenz numbers plotted with gas collision density gave useful insight into the Lorenz number response and the increased gaseous scattering sites.
- The Au and Cu Seebeck coefficient showed perturbed values under the various gaseous boundaries however with less correspondence to each gaseous regime than the conductivity or resistivity.
- The distinct results of straight-forward resistance measurements on the 30 nm Au and Cu thin films gave overwhelming evidence of the transport property perturbations as surface scattering increased. In agreement with the DES results, the Au sample showed an increased resistance response to both He and Ar flows than the Cu response.
- An interesting result of this work is that the electron jellium has responded through measurable perturbations to each gas *in both the elastic and inelastic* phonon scattering regime as loosely defined by the helium atom scattering community.

The final bullet above is considered an important result in this work. The measurement of material resistance under various gaseous boundaries is nothing spectacular or new. However the validating results of the resistance measurements, provided by comparative DES data is considered to be a major result of this work. This reasoning is due to the multi-transport property measurement capability of DES. The validation of the resistivity measurements validates the electronic thermal conductivity and Seebeck data through the rigorous formalism of the Green-Kubo theory. Hence, the experimental method

to measure the thermal and thermoelectric material properties of a material under various boundary conditions is considered viable and robust through the methods described in this report.

The perturbed transport properties of the 30 nm Au and Cu thin films reported in this chapter appear to be induced by traditional well understood kinetic scattering mechanisms.[1,32,33] Basically, an incoming gas particle approaches the electron jellium at the material surface resulting in quantum wave function overlap. The resulting elastic or inelastic collision then perturbs both the gas particle and electron trajectories. The helium atom scattering spectroscopic community gathers data from their He detection sensors while this work analyzes the sensitive electronic autocorrelation function which holds a great deal of kinetic and dynamic scattering information. Chemical adsorption effects between the Ar/He and the Au/Cu thin films are ruled out due to the inert gases used and the chemical inactivity prevalent at the experimental conditions imposed by this work. Some physical adsorption of each gas has occurred during the experimental runs, especially during the pressure work of Section 5.3. It is well known that increased pressure accelerates the physical adsorption process.[34] However, the results of this investigation show that physical adsorption is not the primary scattering component for the subject materials and gases used. Physical adsorption is a transient process that takes a finite period of time to occur.[34] The immediate transport property response, as exemplified by the resistance measurements of Section 5.4 clearly show that the scattering is not due to physical adsorption, but is due to kinetic interactions. The immediate step-like drop in resistance shown in Section 5.4 is overwhelming proof of the kinetic scattering mechanism between the gas field and metal surface that has become a dominant perturbation mechanism. Moreover, the ability to

perturb metal transport properties through a gaseous interface is attributed to the surface area to volume increase as proved by the comparative measurements on bulk copper also reported in this chapter.

Chapter 6

The Generalized Application of Fluctuation Spectroscopy to Other Energetic Transport Mediums

6.1 Introduction to Dynamic Fluctuation Spectroscopy

Throughout this report, the primary theoretical and experimental tool used to attack the central research problem has been *Dynamic Electron Scattering* or DES. The validation of this new experimental method as well as the results of the various other experimental techniques surrounding the DES methodology has shown overwhelming evidence of a robust repeatable spectroscopic method with the capability of producing extremely low error results. Throughout this research effort, it has been repeatedly found that the utility of this experimental method goes far beyond the scope of this investigation. For example, the electronic specific heat C_V may be calculated through the thermal PSD by simply rearranging equation (3.21) to obtain:

$$C_V = \frac{S_q^2(f_0)}{k_B T^2}. \tag{6.1}$$

By taking DES data of a conductor or semiconductor over a wide temperature range, the electronic specific heat could easily be obtained along with a multitude of additional electronic transport properties. Quite simply, we argue that the expansion of the DES method to other applications is limited only by the applicability of irreversible thermodynamics to the subject system. If one can establish a relation between the *impedance* in a general linear dissipative system and the *fluctuations* of appropriate generalized *forces*, then the fluctuation spectra may be measured experimentally and used to obtain transport property information. *The primary difference between the method developed in this work and other existing spectroscopic methods is the elimination of an externally applied probe to gather dynamic experimental data.* Neutron scattering, light scattering, helium atom scattering and electron scattering (i.e. low energy electron diffraction) are just a few examples[1,2,62,140-141] of the ever-present external probe currently used in spectroscopic work. Instead of external bombardment, the approach of this research is to simply "listen" to the material. By the term listen, we mean to measure the inherent fluctuations of the subject forces. The Johnson/Nyquist noise voltage happened to be the fluctuating force in this investigation. Through this technique, one is able to eliminate the need for applying external gradients, potentials and probes. This condition, once an experimental necessity, now allows the powerful characterization of certain materials such as nanostructures to be submitted to specific boundary conditions and engineered from the "bottom up" to respond in ways previously unknown. Obviously, the spectroscopic technique developed in this work goes far beyond the electron ensemble. Therefore, the term *Dynamic Fluctuation Spectroscopy* or DFS is used to encompass the many different spectroscopic applications that are applicable to the initial work developed here. Figure 6.1 below shows the general architecture of the DFS method. The dark solid lines of DES represent theoretical and experimental development mainly

embodied in this report. The gray dashed lines show immediate applications that are as of yet undeveloped.

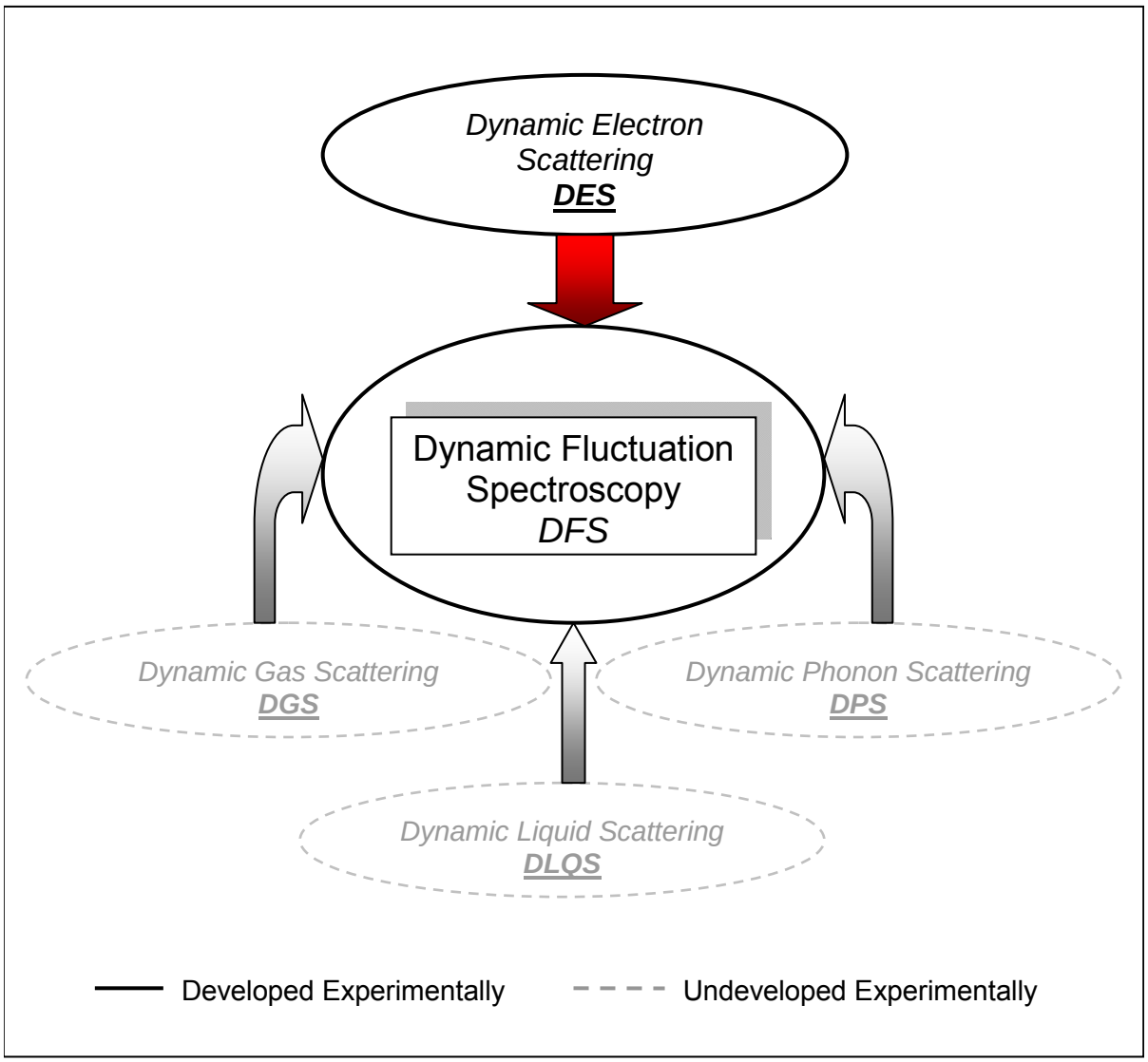

Figure 6.1: Dynamic Fluctuation Spectroscopy or DFS encompasses all sub-spectroscopic components such as DES. The DFS method uses no external probe but instead "listens" to a materials inherent fluctuations thus allowing the use of irreversible thermodynamics to measure transport properties through linearized transport theory. Three immediate undeveloped applications would be gases, liquids and phonons.

To expand on Figure 6.1, pressure fluctuations in a gas or liquid could be measured thus resulting in fluctuation spectra that would be treated theoretically similar to that developed in Chapter 3. Furthermore, acoustic thermal fluctuations could be measured on a solid (dielectric, conductor, semiconductor, etc.) thereby obtaining lattice fluctuation spectra that would again be treated similar to that developed in Chapter 3. These statements are not expressed without firm theoretical grounding. The realization of the applicability of the DFS method led this research to ascertain the feasibility of the spectroscopic information suggested in Figure 6.1. The results of the feasibility study of DGS, DPS and DLQS resulted in an unexpected derivation of a general form of the Nyquist/Johnson noise equation $\overline{V^2} = 4k_B TR\Delta f$. Section 6.2 gives details of the derivation and final results of the generalized fluctuation spectra relation for gases, liquids and crystal lattices.

6.2 Derivation of the Fluctuation Spectra Relation for Gases, Liquids and Phonons

The objective of this section is to derive the mean-square pressure fluctuation expression for gases and liquids as well as the acoustic thermal fluctuations of the solid crystal lattice or equivalently, phonons. The derivation follows closely the same derivation by Callen and Welton[142] which was a critical theoretical component that set the stage for the development of Green-Kubo linear response theory used heavily in this work. Despite an intensive literature search, the derivation of this section has not been found in the literature base. The reason for this is the probable lack of any need to describe the fluctuations in any formal manner. With the intended development of DFS however, this research is uniquely interested in the closed form analytic expression of pressure and acoustic thermal fluctuation spectra. Furthermore, this

derivation is somewhat appended and the reader is encouraged to review the benchmark paper by Callen and Welton for additional details.[142]

If a system is dissipative, an impedance may be defined. Additionally, the proportionality constant between the square of a perturbation amplitude and the power is related to the impedance. Comment is offered immediately that despite the electrical system analogy, the theory and result is indeed a generalized one capable of encompassing all systems that fall under the categories previously set forth. The unperturbed Hamiltonian H_0, is subsequently perturbed and expressed as:

$$H = H_0\left(q_k \ldots p_k \ldots\right) + PQ\left(q_k \ldots p_k \ldots\right), \tag{6.2}$$

where H is the perturbed Hamiltonian, q_k and p_k are coordinates and momenta of the system respectively, Q is a function of the coordinates and momenta and P is a time dependent function that measures the instantaneous magnitude of the perturbation. The function Q in this derivation differs from the example given by Callen and Welton[142] as their intent was to derive the Nyqist/Johnson expression with the mean-square voltage as a primary result. In the present derivation, Q is expressed as:

$$Q = \sum_{i=1} m_i v_i x_i / L\,, \tag{6.3}$$

where m_i is the mass of the ith gas, liquid or crystal ion particle, v_i is the velocity of the gas, liquid or crystal ion particle, x_i is the distance from one end of the system boundary and L is the

total length of the system boundary. The component of equation (6.3) $m_i v_i$, is merely the momentum of the *i*th particle p_i. This clarification is important and shall be explained further in due course. Next, consider the perturbation to take on sinusoidal form:

$$P = P_0 \sin \omega t , \tag{6.4}$$

where the subject derivation identifies P as the impressed force. Standard time dependent perturbation theory is now engaged to compute the power dissipation. The set of eigenfunctions is represented by $\psi_1, \psi_2 ... \psi_n$ which are associated with the unperturbed Hamiltonian H_0 which gives:

$$H_0 \psi_n = E_n \psi_n . \tag{6.5}$$

Furthermore, the actual wavefunction shall be ψ. The expansion of ψ in terms of the eigenfunctions ψ_n results in:

$$\psi = \sum_n a_n(t) \psi_n . \tag{6.6}$$

Equation (6.6) now allows substitution of ψ into the Schroedinger equation which takes the form:

$$H_0 \psi + P_0 \sin \omega t Q \psi = \frac{i\hbar \partial \psi}{\partial t} . \tag{6.7}$$

Equation (6.7) produces a set of first order equations for the coefficients $a_n(t)$ which can be integrated. Through the analysis of transition probabilities and Boltzmann factor weighting followed by integration over energy, the derivation arrives at the power expression:

$$\text{Power} = \frac{P_0^2 \pi\omega}{2} \int_0^\infty \rho(E) f(E) \left\{ \left| \langle E + \hbar\omega | Q | E \rangle \right|^2 \rho\left(E + \hbar\omega\right) - \left| \langle E - \hbar\omega | Q | E \rangle \right|^2 \rho\left(E - \hbar\omega\right) \right\} dE \,. \tag{6.8}$$

The primary result of equation (6.8) is that when a small periodic perturbation is applied to a system which is characterized by eigenstates densely distributed in energy, then the power dissipation is quadratic in the perturbation. Continuing in the linear response regime, one may define an impedance $Z(\omega)$ where both real and complex quantities are implied. Therefore, the following relation of the force P to the response $\dot{Q}$ is arrived at:

$$P = Z(\omega)\dot{Q} \,, \tag{6.9}$$

where,

$$\dot{Q} = \frac{dQ}{dt} = \frac{d\left(m_i v_i\right)}{dt} = \frac{dp_i}{dt} \,. \tag{6.10}$$

Equation (6.10) has been expanded to clearly show that the time rate of change of the linear gas, liquid or crystal lattice ion momentum is equal to the resultant force P acting upon the particle, scaled by the impedance $Z(\omega)$. Furthermore, for the derivation underway, the impedance is defined as:

$$Z(\omega) = Z_A(\omega), \tag{6.11}$$

where the *acoustic* impedance is represented by $Z_A(\omega)$. Pause is taken to fully analyze equations (6.9) – (6.11). These results are considered a major contribution to this work and have not appeared in the literature base. This observation is offered with the fullest confidence that the author has not reviewed every single relevant publication yet has also not missed many. The acoustic impedance is a common material property for gases, liquids and solids and is defined as an acoustic wave loss mechanism prevalent to gases, liquids or solids.[143] Hence, the acoustic impedance is the counterpart to electrical impedance in the Johnson/Nyquist theory and is the so-called generalized impedance used rigorously in linear transport theory.[101] To continue this derivation, let Z_A represent the real part of $Z_A(\omega)$ thus allowing the average power to be given:

$$\text{Power} = \frac{P_0^2 Z_A}{2\left|Z_A(\omega)\right|^2}. \tag{6.12}$$

Thus far, this derivation has considered a system to which an applied force P has induced a response $\dot{Q}$. In conjunction with the DFS philosophy, the system is to be analyzed in thermal equilibrium with no applied force P. Despite the absence of the applied force, it is well known that this system will exhibit a fluctuating $\dot{Q}$, which may be coupled with a fluctuating force.[97] Let $\left\langle P^2 \right\rangle$ be the mean-square value of the force fluctuation spectra and let $\left\langle \dot{Q}^2 \right\rangle$ be the mean-square value of the fluctuating $\dot{Q}$. Next, let the system be known to be in the nth eigenstate. The hermitian property of H_0 causes the expectation value of $\dot{Q}$ to vanish. Through introduction

of a frequency ω, multiplication by the weighting factor $f(E_n)$ and again introducing the energy density factor $\rho(E)$, the mean-square $\dot{Q}$ is obtained:

$$\left\langle \dot{Q}^2 \right\rangle = \int_0^\infty \hbar\omega^2 \left[\int_0^\infty \rho(E) f(E) \left\{ \left| \left\langle E+\hbar\omega \middle| Q \middle| E \right\rangle \right|^2 \rho(E+\hbar\omega) \right.\right.$$

$$\left.\left. + \left| \left\langle E-\hbar\omega \middle| Q \middle| E \right\rangle \right|^2 \rho(E-\hbar\omega) \right\} dE \right] d\omega . \tag{6.13}$$

Straightforward rearrangement of equation (6.13) yields the mean-square force fluctuations:

$$\left\langle P^2 \right\rangle = \int_0^\infty |Z_A|^2 \hbar\omega^2 \left[\int_0^\infty \rho(E) f(E) \left\{ \left| \left\langle E+\hbar\omega \middle| Q \middle| E \right\rangle \right|^2 \rho(E+\hbar\omega) \right.\right.$$

$$\left.\left. + \left| \left\langle E-\hbar\omega \middle| Q \middle| E \right\rangle \right|^2 \rho(E-\hbar\omega) \right\} dE \right] d\omega . \tag{6.14}$$

Progressing straight to the general relation expressed by:

$$\left\langle P^2 \right\rangle = \frac{2}{\pi} \int_0^\infty Z_A E(\omega, T) d\omega , \tag{6.15}$$

where

$$E(\omega, T) = \frac{1}{2}\hbar\omega + \frac{\hbar\omega}{\exp(\hbar\omega / k_B T) - 1}, \tag{6.16}$$

where T is the temperature and equation (6.16) is the average energy at temperature T of an oscillator of natural frequency ω. Specific note should be taken of the analytical correlation of equation (6.16) and the derivation currently underway. Oscillatory pressure behavior, especially

in the acoustic sense, is well described by this periodic function. At temperatures where $k_B T \gg \hbar\omega$, the equipartition of energy is utilized to express the energy as:

$$E(\omega, T) \approx k_B T . \tag{6.17}$$

The general force fluctuation spectra now assumes the form:

$$\left\langle P^2 \right\rangle = \left(\frac{2}{\pi}\right) k_B T \int_{\omega_1}^{\omega_2} Z_A d\omega . \tag{6.18}$$

Incorporating mean-square force fluctuations *per unit area A* (which is simply mean-square pressure) and recognizing that $\omega = 2\pi f$, results in the final expression of mean-square pressure fluctuations applicable to gases, liquids and crystal lattices:

$$\frac{\left\langle P^2 \right\rangle}{A} = 4 k_B T Z_A \Delta f . \tag{6.19}$$

Equation (6.19) is obviously of the same form as the Johnson/Nyquist equation for voltage fluctuations. The primary differences are that mean-square pressure fluctuations are determined by the acoustic impedance instead of mean-square voltage fluctuations that are determined by electrical resistance. Therefore, this section has derived the mean-square pressure fluctuations of gases, liquids and solid crystal lattices (acoustic thermal phonons). Through Green-Kubo linear response transport theory, the measurement of pressure fluctuations will allow transport properties such as viscosity, speed of sound, thermal conductivity, specific heat, etc. to be

determined. The cross spectral density (used in DES to measure the Seebeck coefficient) would allow new experimental insight into gaseous diffusion phenomena which is another physical display of Onsager's reciprocity theory.[103-104]

This section is concluded by a brief statement of the experimental feasibility of measuring pressure fluctuations in gases, liquids and solids. Basically, the subject pressure measurements have been accomplished by various groups although their experimental objectives were far removed from the intentions held within DFS. Gas and liquid pressure fluctuations can be measured by acoustic microphones. A solid materials acoustic thermal fluctuations or equivalently, pressure fluctuations, can be measured by sensitive piezoelectric sensors. The methods and research are detailed in References 144-151.

Chapter 7

The Theoretical Connection Between Quantum Decoherence and the Emergence of Statistical Ensembles Exhibiting Fluctuation Spectra

7.1 The Quantum Decoherence Connection to Linear Response Theory

The objective of this brief chapter is to show the theoretical connection between quantum decoherence and the emergence of statistical ensembles, either quantum mechanical or classical mechanical. Stated in other words, the aim is to make the theoretical argument that the bridge from a closed quantum system to a statistical ensemble must occur through quantum decoherence.

The autocorrelation function $\Gamma(t + \Delta t)$ is conveniently expressed quantum mechanically in terms of Heisenberg operators of the fluctuating quantities. The ACF can be written in terms of the product of two Heisenberg operators taken at instants t and $t + \Delta t$, i.e., $\hat{\Gamma}(t)\hat{\Gamma}(t+\Delta t)$.[86] The hat designates an operator and the operator $\hat{\Gamma}(t)$ is associated with the fluctuation $\Gamma(t)$. The expectation of the fluctuation, the operator which is $\hat{\Gamma}(t)$, is:

$$\left\langle \hat{\Gamma}(t) \right\rangle = \mathrm{Tr}(\rho, \hat{\Gamma}(t)), \tag{7.1}$$

where ρ represents the quantum density matrix component. Then, the corresponding correlation function may be written as:

$$\Gamma(t,t+\Delta t)=\frac{1}{2}\left\langle\left[\hat{\Gamma}(t),\hat{\Gamma}(t+\Delta t)\right]\right\rangle, \tag{7.2}$$

$$=\frac{1}{2}\left[\mathrm{Tr}\left(\rho\hat{\Gamma}(t,t+\Delta t)\right)\right]. \tag{7.3}$$

Equation (7.3) is identical to that expressed in Green-Kubo theory.[101] Furthermore, equation (7.3) is also identical to that describing the correlations of a system and an environment that are under quantum entanglement.[152] The diagonalized quantum density matrix appeared due to energetic correlations with the environment.[153-154] The ACF *cannot be defined until decoherence has occurred*. Therefore, we discuss the phenomena in terms of causality. In temporal progression, a closed quantum system is introduced to an external environment through Hamiltonian interactions. The closed quantum systems density matrix off-diagonal terms vanish thus leaving robust diagonal eigenstates only. At this point the correlations to the environment can now be defined through temperature, energy or mass interactions. The birth of a statistical ensemble has just occurred and can be appropriately named microcanonical, canonical or grand canonical ensemble. The temperature, energy or mass interactions necessarily fluctuate as the equations of motion take the energy carriers through phase space slightly perturbing their Hamiltonian with each energetic encounter.[155] An example of this phenomena with direct relevance to the current research was provided by Garrity.[156] One may now use the partition

function on this ensemble to obtain thermodynamic functions or one may use linear transport theory to obtain transport properties from the relevant fluctuation spectra.

This chapter is concluded by three statements that are presented without detailed proof but are easily derivable through the remarks and equations put forth in the beginning of this chapter.

Statement 1: *The energetic perturbation of an isolated Hamiltonian cannot persist in a system previously in a closed quantum state, without the onset of quantum decoherence due to environmental interactions. The resulting system plus environment defines a statistical ensemble that can be described by quantum or classical statistical mechanics.*

Statement 2: *In order to maintain energetic equilibrium, Hamiltonian fluctuations must remain a causal effect with respect to quantum decoherence. Spontaneous energetic fluctuations are present only in the decohered regime and manifested by quantum correlations between a system and the environment. The quantum correlations result in transport properties that are appropriately termed pointer observables.*

Statement 3: *The spontaneous transport of heat and/or charge in the form of energetic fluctuations is necessary in order to maximize the system entropy.*

Chapter 8

Conclusion and Discussion

8.1 Conclusive Summary of the Central Research Problem

8.1.1 The Central Research Problem

The central research problem introduced in Chapter 1 explicitly outlined three components that make up the central research problem covered by this investigation. Component 1 included theoretical concepts that support the scattering process of a solid surface interfaced with a gas particle field. This objective was addressed in Chapter 2 through a comprehensive derivation and analysis of phonon scattering due to gas particle interactions. The kinetic based derivation specifically fit the research objectives of this work and showed greater dependence on gas collision densities than gas particle mass. Additionally, the well known effects of physical adsorption were computationally analyzed in tandem with gas particle scattering. The results show non-negligible contributions to the total phonon relaxation time by the dynamic gaseous interface. Hence, these results suggest that the effects of physical adsorption are not a singular lone scattering process, but are accompanied by appreciable elastic/inelastic scattering by the gas particle field. The scattering of the electron jellium by adjacent gas particles was addressed by the use of an electron scattering probability that encompassed gas particle velocity components. The scattering probability however, does not completely satisfy the objectives of component 1. To assess the transport properties of a solid,

further numerical work is needed. The additional theoretical model was assembled and derived in the form of a finite element solution to the variational form of the Boltzmann transport equation. The solution technique uses the penalty function method and two triangular linear finite elements were used to obtain an example solution to electrical resistivity. The finite element discretization to a nanostructure resulting in discrete transport coefficient values at specific locations of the material specifically addresses the theoretical objective of component 1. Component 2 of this research effort holds the experimental aspects of nanostructure scattering due to a gaseous interface. Chapters 3 – 5 contain the experimental theory, design, characterization and results of a new method to obtain transport information from an electron ensemble. The development of Dynamic Electron Scattering or DES resulted from the experimental necessity to measure transport properties of a material that is under specific controlled boundary conditions. The formulation of the DES experiment resulted in theoretical coupling to the rigorous Green-Kubo formalism thereby generating multiple transport property measurements within one experimental data set. Moreover, the lack of any required thermal or potential gradients enables the method to be used on experimentally difficult materials such as nanostructures. This new experimental method was quickly recognized to be applicable to many other applications such as gases, liquids and phonons as outlined in Chapter 6. The successful validation of the DES experiment lended confidence to the results of thin metal films submitted to noble gas interfaces. The experimental results of Au and Cu thin films under both pressure and flow clearly show that gas particle scattering is measurable through transport property perturbations. In fact, the evidence was so clear that straightforward resistance measurements were initiated for both Ar and He flow fields. The resistance data showed clear discrete step-like response of the thin films which helped eliminate physical adsorption as a

leading contributor to the electron scattering. An experimental bonus of the resistance data was the minor deviations seen in the final experimental stages (after pressure or flow was removed) that were clearly attributable to adsorption. The direct measurement of the Lorenz number allowed deviations to electrical and thermal relaxation times to be assessed. Through well developed scattering theory, smaller wave vectors carried by the subject scatterer (a gas particle in this work) perturb the thermal current more so than the electrical current. As shown in Chapter 5, helium consistently showed smaller wave vectors thus providing a scattering background that may test wave vector deviations. The Lorenz number response agreed with wave vector scattering theory and is a subject of further work. Another major contribution to the objectives of component 2 is the *direct measurement of the absolute Seebeck coefficient*. Current experimental techniques measure the relative Seebeck coefficient and must use thermal gradients and at least two thermoelectric materials. The DES method however, allows a direct measurement of this thermoelectric coefficient without any applied thermal gradients which again enables powerful experimental capabilities. Finally, the comparative experimental results on a bulk Cu specimen indicate that surface scattering effects tend to dominate low dimensional materials. There were no deviations to the bulk Cu electronic thermal conductivity or electrical resistivity under pressure or flow for both Ar and He.

Component 3 held the relations of quantum decoherence to a solid surface scattering by a gas field. The primary result of this work with respect to this objective is the recognition of the theoretical link between decoherence and the energetic fluctuation spectra autocorrelation function. Chapter 7 briefly lays out the relation between the decohered diagonalized quantum density matrix and the autocorrelation function of fluctuations. The result is a theoretical bridge between a closed quantum system and the entry point into statistical mechanics.

8.1.2 Research Lessons Learned

The course of this research was filled with trials and tribulations that presented many challenges to the central problem. Many, many experiments had to be rerun due to errors and mistakes that had to be corrected. The theoretical work of this investigation took many paths as well, often leading to dead ends or circling back to a known trivial result. Therefore, this conclusive chapter would not be considered complete without some mention of the lessons learned.

- When measuring voltage noise fluctuations, never trust any extraneous source to be noise free. Turn off radios, unneeded equipment and any other electronic devices. For example, the temperature data acquisition device used to interface the thermocouples to the PC was found to introduce noise into the sample even without physical contact, and while turned off. The temperature data acquisition system had to be unplugged to eliminate the noise. Twelve experiments had to be rerun.
- Triple check the equipment used to interface and amplify the noise signal. Select the equipment that will operate in the optimum design region for the subject experiment. The purchase of a low noise amplifier that was operating outside of its optimum design parameters resulted in five sets of experimental data garbage.
- Check all numerical analysis routines on *small sets of data*. Then validate the routines several more times, again on small data sets. Dynamic Fluctuation Spectroscopy requires large amounts of data to reach the statistically stationary regime. Numerical subroutines such as Fourier transform algorithms take time to run over the entire data set. A numerical error in the beginning of this work resulted in a huge amount of lost time by requiring many data sets to be rerun.

- Keep a separate copy of the raw unprocessed experimental data. If there is a numerical error found sometime later, you can resurrect the raw data to reprocess without having to rerun the experiment. Always save data in three separate places. Several experiments had to be rerun during this investigation due to not archiving the raw data.
- Don't be afraid to beat on the data. A solid set of experimental data that is supported by rigorous theory becomes stronger and holds up solidly to numerical pounding. Carefully scrutinize all results, even when they don't make sense. The initial coupling of the Green-Kubo theory to the Johnson/Nyquist noise was expected to result in electrical conductivity in this work yet the results did not agree. The realization of the measurement being electrical resistivity only resulted after careful step-by-step understanding of Green-Kubo theory. Approximately twenty experiments were initially run using the experimentally calculated relaxation time to obtain resistivity before fully understanding that the theory predicted resistivity when measuring voltage fluctuations, not conductivity. Much time was spent reprocessing many experimental data sets to calculate the electrical resistivity.

8.2 Future Work

The future work of this research primarily involves two paths. First, the verification of Au and Cu nanostructure sensitivity to gaseous boundaries immediately suggest the development of gas nanosensors. Initially, these sensors may be resistance based only which differs from the extensive reports on $1/f$ noise of nanoscale gas sensors.[157-180] The study of sensor optimization would be the initial priority. Some immediate optimization possibilities resulting from this work would be surface area enhancement such as the addition of ridges or bumps in order to increase the effective electron jellium scattering due to the bounding gas. Material fabrication

optimization would include designing a material that maximizes the electron wave function decay into the gas field. This would provide enhanced wave function overlap and subsequent electron perturbation effects as the incoming gas particle approaches. A camera-type device using an array of thin film nanosensors could be placed in a flow field and interfaced to computer software that gives full visualization of the interfacial flow field. Thus, characterization of bounding gas flows could be accomplished that could be used for micro and nano applications. The gas nanosensor array would be similar to the microbolometer array used in infrared cameras.

The second path for future work involves the continued development of Dynamic Fluctuation Spectroscopy. Chapter 6 has initialized this path by recognizing the huge applicability range of this new experimental method. In fact, practically any system that can be described by irreversible thermodynamics is a candidate for the DFS method. Some initial paths may include the following:

- Materials placed in a magnetic field followed by DFS.
- Nanocomposites and superlattices characterization.
- Deformable surface conductors or semiconductors.
- Diffusion experiments on gases through DFS cross spectral density work.

This concludes the research effort addressing nanoscale thermal fluctuation spectroscopy.

References

[1]H. Luth, *Solid Surfaces, Interfaces and Thin Films*, 4th ed., Springer, New York, (2001)

[2]G. Benedek and U. Valbusa (ed.), *Dynamics of Gas-Surface Interaction*, Springer-Verlag, New York, (1982)

[3]H. Kaplan, *Effect of an Impurity Layer on Surface Waves*, Phys. Rev., **125**, 1271-1276, (1962)

[4]G. P. Brivio and T. B. Grimley, *Lifetimes of Electronically Adiabatic Vibrational States of a Chemisorbed Atom*, J. Phys. C: Solid State Phys., **10**, 2351-2363, (1977)

[5]T. C. Au Yeung, T. C. Chiam, C. Q. Sun, M. Gu, W. Z. Shangguan and C. H. Kam, *Effect of Surface Bond-Order Loss on the Electronic Thermal Conductivity of Metallic Polycrystalline Films*, J. Appl. Phys., **98**, 113 707-1 – 113 707-6, (2005)

[6]V. Bortolani, G. Santoro, U. Harten and J. P. Toennies, *Surface Phonon Calculations for Noble Metals: Comparison with He-Surface Scattering Experiments*, Surf. Science, **148**, 82-89, (1984)

[7]K. Lenarcic-Poljanec, M. Hodoscek, D. Lovric and B. Gumhalter, Surf. Science, **251/252**, 706-711, (1991)

[8]R. Brako and D. M. Newns, *Differential Cross Section for Atoms Inelastically Scattered from Surfaces*, Phys. Rev. Lett., **48**, 1859-1862, (1982)

[9]J. P. Toennies, *Helium Atom Scattering Studies of the Lattice Dynamics of Clean Metal Surfaces*, Physica Scripta, 39-46, **T19**, (1987)

[10]A. P. Graham, F. Hofmann, J. P. Toennies and J. R. Manson, *Helium Atom Scattering from Isolated CO Molecules on Copper(001)*, J. Chem. Phys., **105**, 2093-2098, (1996)

[11]B. Jackson, *Mean Field Approach to Molecule-Surface Scattering at Finite Temperature: One Phonon Theory*, J. Chem. Phys., **89**, 2473-2481, (1988)

[12]B. Gans, S. K. King, P. A. Knipp, D. D. Koleske and S. J. Sibener, *Structure and Dynamics of $Cu_3Au(001)$ Studied by Elastic and Inelastic Helium Atom Scattering*, J. Elec. Spectr. Related Phen., **54/55**, 333-341, (1990)

[13]D. J. Gaspar, A. T. Hanbicki and S. J. Sibener, *Inelastic Multiphonon Helium Scattering from a Stepped Ni(977) Surface*, J. Chem. Phys., **109**, 6947-6955, (1998)

[14]K. C. Janda, J. E. Hurst, C. A. Becker, J. P. Cowin, D. A. Auerbach and L. Wharton, *Direct Measurement of Velocity Distributions in Argon Beam-Tungsten Surface Scattering*, J. Chem. Phys., **72**, 2403-2410, (1980)

[15]L.D. Hicks, M. S. Dresselhaus, *Thermoelectric Figure of Merit of a One-Dimensional Conductor*, Phys. Rev. B, **47**, 16 631-16 634, (1993)

[16]S. M. Lee, D. G. Cahill, *Heat Transport in Thin Dielectric Films*, J. Appl. Phys., **81,** 2590-2595, (1997)

[17]P. K. Schelling, S. R. Phillpot, P. Keblinski, *Phonon Wave Packet Dynamics at Semiconductor Interfaces by Molecular Dynamics Simulation*, Appl. Phys. Lett., **80**, 2484-2486, (2002)

[18]S. Yu, K. W. Kim, M. A. Stroscio and G. J. Iafrate, *Electron-Acoustic Phonon Scattering Rates in Cylindrical Quantum Wires*, Phys. Rev. B, **51**, 4695-4698, (1995)

[19]Y. S. Ju, *Phonon Heat Transport in Silicon Nanostructures*, Appl. Phys. Lett., **87**, 153 106-1 -152 106-3, (2005)

[20]D. J. Griffiths, *Introduction to Quantum Mechanics*, Prentice Hall, Inc., New Jersey, (1995)

[21]L. I. Schiff, *Quantum Mechanics*, 3rd ed., McGraw-Hill, Inc., New York, (1968)

[22]G. D. Mahan, *Many-Particle Physics*, 3rd ed., Kluwer Academic/Plenum Publishers, New York, (2000)

[23]U. Fano, *Description of States in Quantum Mechanics by Density Matrix and Operator Techniques*, Rev. Mod. Phys., **29**, 74-93, (1957)

[24]E. Joos and H. D. Zeh, *The Emergence of Classical Properties Through Interaction with the Environment*, Z. Phys. B: Condensed Matter, **59**, 223-243, (1985)

[25]W. H. Zurek, *Environment-Induced Superselection Rules*, Phys. Rev. D, **26**, 1862-1880, (1982)

[26]S. Datta, *Electronic Transport in Mesoscopic Systems*, Cambridge University Press, New York, (1995)

[27]D. E. Engelescu, M. C. Cross and M. L. Roukes, *Heat Transport in Mesoscopic Systems*, Superlattices and Microstructures, **23**, 673-689, (1998)

[28]K. Schwab, E. A. Henriksen, J. M. Worlock and M. L. Roukes, *Measurement of the Quantum of Thermal Conductance*, Nature, **404**, 974-976, (2000)

[29]L. G. C. Rego and G. Kirczenow, *Quantized Thermal Conductance of Dielectric Quantum Wires*, Phys. Rev. Lett., **81**, 232-235, (1998)

[30]D.M Rowe (ed.), *CRC Handbook of Thermoelectrics*, CRC Press, New York, (1995)

[31]S. Volz (ed.), *Microscale and Nanoscale Heat Transfer*, Springer, New York, (2007)

[32]M. Lundstrom, *Fundamentals of Carrier Transport*, 2nd ed., Cambridge University Press, Cambridge, (2000)

[33]B. K. Ridley, *Quantum Processes in Semiconductors*, 4th ed., Oxford University Press, Oxford, (1999)

[34]G. D. Billing, *Molecule Surface Interactions*, John Wiley & Sons, New York, (2000)

[35]C. Kaden, P. Ruggerone, J. P. Toennies, G. Zhang and G. Benedek, *Electronic Pseudocharge Model for the Cu(111) Longitudinal Surface-Phonon Anomaly Observed by Helium Atom Scattering,* Phys. Rev. B, **46**, 13 509-13 525, (1992)

[36]N. S. Luo, P. Ruggerone and J. P. Toennies, *Electron-Phonon Coupling at Metal Surfaces Probed By Helium Atom Scattering*, Physica Scripta, **T49**, 584-592, (1993)

[37]G. U. Sumanasekera, C. K. W. Adu, S. Fang and P. C. Eklund, *Effects of Gas Adsorption and Collisions on Electrical Transport in Single-Walled Carbon Nanotubes*, Phys. Rev. Lett., **85**, 1096-1099, (2000)

[38]H. E. Romero, K. Bolton, A. Rosen and P. C. Eklund, *Atom Collision-Induced Resistivity of Carbon Nanotubes*, Science, **307**, 89-93, (2005)

[39]H. Y. Yu, B. H. Kang, U. H. Pi, C. W. Park and S. Y. Choi, *V_2O_5 Nanowire-Based Nanoelectronic Devices for Helium Detection*, Appl. Phys. Lett., **86**, 253102-1 – 253102-3, (2005)

[40]A. K. Sood and S. Ghosh, *Direct Generation of a Voltage and Current by Gas Flow Over Carbon Nanotubes and Semiconductors,* Phys. Rev. Lett., **93**, 086601-1 – 086601-4, (2004)

[41]S. Ghosh, Ak. Sood and N. Kumar, *Carbon Nanotube Flow Sensors*, Science, **299**, 1042-1044, (2003)

[42]T. M. Tritt (ed.), *Thermal Conductivity: Theory, Properties and Applications*, Kluwer Academic/Plenum Publishers, New York, (2004)

[43]J. B. Johnson, *Thermal Agitation of Electricity in Conductors*, Phys. Rev., **32**, 97, (1028)

[44]H. Nyquist, *Thermal Agitation of Electric Charge in Conductors*, Phys. Rev., **32**, 110-113, (1928)

[45]G. P. Zhigal'skii and B. K. Jones (ed.), *The Physical Properties of Thin Metal Films*, Taylor and Francis, New York, (2003)

[46]R. Kubo, *Thermal Statistical-Mechanical Theory of Irreversible Processes I*, J. Phys. Soc. Japan., **12**, 570-586, (1957)

[47]R. Kubo, M. Yokota and S. Nakajima, *Statistical-Mechanical Theory of Irreversible Processes II. Response to Thermal Disturbance*, J. Phys. Soc. Japan., **12**, 1203-1211, (1957)

[48]M. S. Green, *Markoff Random Processes and the Statistical Mechanics of Time-Dependent Phenomena*, J. Chem. Phys., **20**, 1281-1295, (1952)

[49]K. C. Janda, J. E. Hurst, C. A. Becker, J. P. Cowin, D. J. Auerbach and L. Wharton, *Direct Measurement of Velocity Distributions in Argon Beam-Tungsten Surface Scattering*, J. Chem. Phys., **72**, 2403-2410, (1980)

[50]R. E. Allen, G. P. Alldredge and F. W. deWette, *Studies of Vibrational Surface Modes II. Monatomic FCC Crystals*, Phys. Rev. B, **4**, 1661-1681, (1971)

[51] K. M. Leung, G. Schon, R. Rudolph and H. Metiu, *The Use of an Independent Boson Model to Study the Dynamic Effects of Electron Excitations by a Particle Colliding with a Metal Surface*, J. Chem. Phys., **81**, 3307-3321, (1984)

[52]Z. Kirson, R. B. Gerber and A. Nitzan, *Studies Excitation and Emission of Metal Electrons in Atom-Surface Collisions*, Surf. Science, **124**, 279-296, (1983)

[53]N. Esbjerg and J. K. Norskov, *Studies Dependence of the He-Scattering Potential at Surfaces on the Surface-Electron Density Profile*, Phys. Rev. Lett., **45**, 807-810, (1980)

[54]J. F. Annett and P. M. Echenique, *Long-Range Excitation of Electron-Hole Pairs in Atom-Surface Scattering*, Phys. Rev. B, **36**, 8986-8991, (1987)

[55]J. J. Wortman and K. S. Canady, *Influence of Oxygen on the Resistance of Gold Films*, Appl. Phys. Lett., **9**, 75-76, (1966)

[56]C. Yu, Q. Hao, S. Saha, L. Shi, X. Kong and Z. L. Wang, *Integration of Metal Oxide Nanobelts with Microsystems for Nerve Agent Detection*, Appl. Phys. Lett., **86**, 063101-1-063101-3, (2005)

[57]A. Amirav and M. J. Cardillo, *Electron-Hole Pair Creation by Atomic Scattering at Surfaces*, Phys. Rev. Lett., **57**, 2299-2302, (1986)

[58]A. Amirav, W. R. Lambert, M. J. Cardillo, P. L. Trevor, P. N. Luke and E. E. Haller, *Electron-Hole Pair Creation at a Ge(100) Surface by Ground-State Neutral Xe Atoms*, J. Appl. Phys., **59**, 2213-2215, (1986)

[59]K. L. Ekinci and M. L. Roukes, *Nanoelectromechanical Systems*, Rev. Sci. Instrum., **76**, 061101-1-061101-12, (2005)

[60]H. Helvajian and E. Y. Robinson, *Micro and Nanotechnology for Space Systems*, The Aerospace Press, Los Angeles, CA (1997)

[61]P. L. Garrity, *Dynamic Phonon Scattering Rates of Nanosurfaces with Gas Particles*, Nanotechnology, **18**, 365703-1 – 365703-7, (2007)

[62]B. J. Berne and R. Pecora, *Dynamic Light Scattering with Applications to Chemistry, Biology and Physics*, Dover Publications, New York, (1976)

[63]T. Yamane, N. Nagai, S. Katayama and M. Todoki, *Measurement of Thermal Conductivity of Silicon Dioxide Thin Films Using the 3ω Method*, J. Appl. Phys., **91**, 9772-9776, (2002)

[64]V. P. Shidlovskiy, *Introduction to Dynamics of Rarefied Gases*, Elsevier, New York, (1967)

[65]C. M. Chambers and E. T. Kinzer, *Higher Dimensional Crystal Models: A Theory of Thermal Accommodation Coefficients*, Surf. Science, **4**, 33-47, (1966)

[66]J. O. Hirschfelder and C. F. Curtiss, *Molecular Theory of Gases and Liquids*, Wiley, New York, (1964)

[67]S. D. Stoddard and J. Ford, *Numerical Experiments on the Stochastic Behavior of a Lennard-Jones Gas System*, Phys. Rev. A, **8**, 1504-1512, (1973)

[68]S. C. Saxena and R. K. Joshi, *Thermal Accommodation and Adsorption Coefficients of Gases*, Hemisphere Publishing, New York, (1989)

[69]R. A. Oman, *Numerical Calculations of Gas-Surface Calculations*, AIAA J., **5**, 1280-1287, (1967)

[70]K. Bolton and A. Rosen, *Computational Studies of Gas-Carbon Nanotube Collision Dynamics*, Phys. Chem. Chem. Phys., **4**, 4481-4488, (2002)

[71]R. G. Steg and P. G. Klemens, *Scattering of Rayleigh Waves by Surface Irregularities*, Phys. Rev. Lett., **24**, 381-383, (1970)

[72]G. U. Sumanasekera, C. K. W. Adu, S. Fang and P. C. Eklund, *Effects of Gas Adsorption and Collisions on Electrical Transport in Single-Walled Carbon Nanotubes*, Phys. Rev. Lett., **85**, 1096-1099, (2000)

[73]J. Zou and A. Balandin, *Phonon Heat Conduction in a Semiconductor Nanowire*, J. Appl. Phys., **89**, 2932-2938, (2001)

[74]J. W. Gadzuk and H. Metiu, *Theory of Electron-Hole Pair Excitation in Unimolecular Processes at Metal Surfaces I. X-Ray Edge Effects*, Phys. Rev. B, **22**, 2603, (1980)

[75]G. P. Brivio and T.B. Grimley, *Lifetimes of Electronically Adiabatic Vibrational States of a Chemisorbed Atom*, J. Phys. C, **10**, 2351, (1977)

[76]O. Gunnarsson and K. Schonhammer, *Inelastic Scattering of Rare-Gas Atoms from Metal Surfaces. Excitation of Electron-Hole Pairs*, Phys. Rev. B, **25**, 2514-2521, (1982)

[77]J. M. Ziman, *The General Variational Principle of Transport Theory*, Canadian. J. Phys., **34**, 1256-1273, (1956)

[78]R. Brunetti and C. Jacobini, *Diagonal and Off-Diagonal Contributions to Autocorrelation of Velocity Fluctuations in Semiconductors,* Phys. Rev. Lett., **50**, 1164-1167, (1983)

[79] R. Brunetti and C. Jacobini, *Analysis of the Stationary and Transient Autocorrelation Function in Semiconductors*, Phys. Rev. B, **29**, 5739-5748, (1984)

[80]D. K. Ferry and J. R. Barker, *Generalized Diffusion, Mobility and the Velocity Autocorrelation Function for High-Field Transport in Semiconductors*, J. Appl. Phys., **52**, 818-824, (1981)

[81]B. R. Nag, S. R. Ahmed and M. D. Roy, *High-Field Autocovariance Coefficient, Diffusion Coefficient and Noise in InGaAs at 300 K*, Solid State Elec., **30**, 235-239, (1987)

[82]G. Hill, P. N. Robson and W. Fawcett, *Diffusion and the Power Spectral Density of Velocity Fluctuations for Electrons in InP by Monte Carlo Methods*, J. Appl. Phys., **50**, 356-360, (1979)

[83]R. Fauquembergue, J. Zimmermann, A. Kaszynski, E. Constant and G. Microondes, *Diffusion and the Power Spectral Density and Correlation Function of Power Spectral Density for Electrons in Si and GaAs by Monte Carlo Methods*, J. Appl. Phys., **51**, 1065-1071, (1980)

[84]A. Svizhenko, S. Bandyopadhyay and M. A. Stroscio, *Velocity Fluctuations and Johnson Noise in Quantum Wires: the Effect of Phonon Confinement*, J. Phys.: Condens. Matter, **11**, 3697-3709, (1999)

[85]L. Reggiani, P. Lugli, S. Gantsevich, V. Gurevich and R. Katilius, *Diffusion and Fluctuations in a Nonequilibrium Electron Gas with Electron-Electron Collisions*, Phys. Rev. B, **40**, 12 209-12 214, (1989)

[86]Sh. Kogan, *Electronic Noise and Fluctuations in Solids*, Cambridge University Press, Cambridge, (1996)

[87]A. van der Ziel, *Noise*, Prentice Hall, New York, (1956)

[88]P. Refregier, *Noise Theory and Application to Physics: From Fluctuations to Information*, Springer, New York, (2004)

[89]A. van der Ziel, *Noise: Sources, Characterization, Measurement*, Prentice Hall, New Jersey, (1970)

[90]M. J. Buckingham, *Noise in Electronic Devices and Systems*, Halstead Press, New York, (1983)

[91]L. Reggiani, C. Pennetta, V. Akimov, E. Alfinito and M. Rosini (ed.), *Unsolved Problems of Noise and Fluctuations UPoN 2005: Fourth International Conference on Unsolved Problems of Noise and Fluctuations in Physics, Biology and High Technology*, AIP, New York, (2005)

[92]T. Gonzalez, J. Mateos and D. Pardo (ed.), *Noise and Fluctuations: 18th International Conference on Noise and Fluctuations-ICNF 2005*, AIP, New York, (2005)

[93]R. M. Mazo, *Brownian Motion Fluctuations, Dynamics and Applications*, Oxford University Press, New York, (2002)

[94]P. Kittel, W. R. Hackleman and R. J. Donnelly, *Undergraduate Experiment on Noise Thermometry*, Am. J. Phys., **46**, 94-100, (1978)

[95]T. J. Witt, *Diffusion Using the Autocorrelation Function to Characterize Time Series of Voltage Measurements*, Metrologia, **44**, 201-209, (2007)

[96]J. S. Bendat and A. G. Piersol, *Engineering Applications of Correlation and Spectral Analysis*, John Wiley & Sons, 2nd Ed., New York, (1993)

[97]D. A. McQuarrie, *Statistical Mechanics*, University Science Books, Sausalito, (2000)

[98]J. C. Gibbings, *Diffusion Using the Autocorrelation Function to Characterize Time Series of Voltage Measurements*, J. Phys. A: Math. Gen., **15**, 1991-2002, (1982)

[99]R. Zwanzig, *Time-Correlation Functions and Transport Coefficients in Statistical Mechanics*, Ann. Rev. Phys. Chem., **16**, 67-102, (1965)

[100]M. Toda, R. Kubo and N. Saito, *Statistical Physics I Equilibrium Statistical Mechanics*, Springer-Verlag, 2nd Ed., New York, (1991)

[101]R. Kubo, M. Toda and N. Hashitsume, *Statistical Physics II Nonequilibrium Statistical Mechanics*, Springer-Verlag, 2nd Ed., New York, (1991)

[102]E. Helfand, *Transport Coefficients from Dissipation in a Canonical Ensemble*, Phys. Rev., **119**, 1-9, (1960)

[103]L. Onsager, *Reciprocal Relations in Irreversible Processes I*, Phys. Rev., **37**, 405-426, (1931)

[104]L. Onsager, *Reciprocal Relations in Irreversible Processes II*, Phys. Rev., **37**, 2265-2279, (1931)

[105]V. I. A. Margulis, E. A. Gaiduk and N. A. Smolanov, *Size Effects in Thermal Noise Characteristics of Electrons in Polycrystalline Metallic Films*, Thin Solid Films, **382**, 297-305, (2001)

[106]V. I. A. Margulis, T. V. Piterimova and E. A. Gaiduk, *Effects of Surface Scattering on the Thermal Noise Properties and AC Conductance of Whiskers*, Physica B, **324**, 90-101, (2002)

[107]O. M. Bulashenko and V. A. Kochelap, *Johnson-Nyquist Noise for a 2D Electron Gas in a Narrow Channel*, J. Phys.: Condens. Matter, **5**, L469-L474, (1993)

[108]R. Morrison, *Grounding and Shielding Techniques in Instrumentation*, John Wiley & Sons, Sausalito, (1967)

[109]D. J. Griffiths, *Introduction to Electrodynamics*, 3rd Ed., Prentice Hall, New York, (1999)

[110]M. A. Saad, *Compressible Fluid Flow*, Prentice Hall, New York, (1985)

[111]F. Hofmann, J. P. Toennies and J. R. Manson, *The Transition from Single Phonon to Multiphonon Energy Transfer in Atom-Surface Collisions*, J. Chem. Phys., **106**, 1234-1247, (1997)

[112]J. R. Manson, *Inelastic Scattering From Surfaces*, Phys. Rev. B, **43**, 6924-6937, (1991)

[113]M. A. Tupta, *Instrumentation and Techniques for Measuring High Resistivity and Hall Voltage of Semiconducting Materials*, Keithley Instruments Technical Publications, 1-4, (2005)

[114]SEMI MF-84-02, *Test Method for Measuring Resistivity of Silicon Wafers with an In-Line Four Point Probe*, ASTM International F84-02, 1-14,

[115]*Model SR554 Transformer Preamplifier*, Stanford Research Systems Technical Publications, 1-13, (2004)

[116]*Model SR560 Low-Noise Preamplifier*, Stanford Research Systems Technical Publications, 1-21, (2006)

[117]Y. Kraftmakher, *Two student Experiments on Electrical Fluctuations*, Am. J. Phys., **63**, 932-935, (1995)

[118]R. B. Roberts, *The Absolute Scale of Thermoelectricity*, Phil. Mag., **36**, 91-107, (1977)

[119]R. B. Roberts, *The Absolute Scale of Thermoelectricity II*, Phil. Mag., **43**, 1125-1135, (1981)

[120]ASM Handbook, *Properties and selection: Nonferrous Alloys and Specialty Materials*, 10th Ed., Vol. 2 Publisher ASM, (1991)

[121]N. W. Ashcroft and N. D. Mermin, *Solid State Physics*, W.B. Saunders Co., New York, (1976)

[122]J. G. Gasser, *Understanding the Resistivity and Absolute Thermoelectric Power of Disordered Metals and Alloys*, J. Phys.: Condens. Matter, **20**, 1-14, (2008)

[123]C. Kittel, *Introduction to Solid State Physics*, 8th Ed., John Wiley & Sons, New York, (2005)

[124]H. Ibach and H. Luth, *Solid State Physics An Introduction to Theory and Experiment*, Springer-Verlag, New York, (1993)

[125]L. Reggiani, C. Penetta, G. Y. Trefan, J. C. Vassiere, L. Varani, V. Gruzhinskis, A. Reklaitis, P. Shiktorov, E. Starikov, T. Gonzales, J. Mateos, D. Pardo and O. M. Bulashenko, *Frontiers in Electronic Noise: From Submicron to Nanostructures*, Int. J. High Speed Electronics Sys., **10**, 111-117, (2000)

[126]O. M. Bulashenko and O. V. Kochelap, *Fluctuations of the Electron Drift Velocity in the Presence of the Fuchs Size Effect*, Sov. Phys. Solid State, **34**, 100-103, (1992)

[127]K. L. Chopra, *Thin Film Phenomena*, McGraw Hill, New York, (1969)

[128]C. Durkan and M. E. Welland, *Size Effects in the Electrical Resistivity of Polycrystalline Nanowires*, Phys. Rev. B, **61**, 14 215-14 218, (2000)

[129]Y. Zhang, N. P. Ong, Z. A. Xu, K. Krishana, R. Gagnon and L. Taillefer, *Determining the Wiedemann-Franz Ratio from the Thermal Hall Conductivity: Application to Cu and* $YBa_2Cu_30_{6.95}$, Phys. Rev. Lett., **84**, 2219-2222, (2000)

[130]X. Zhang, H. Xie, M. Fujii, H. Ago, K. Takahashi, T. Ikuto, H. Abe and T. Shimizu, *Thermal and Electrical Conductivity of a Suspended Platinum Nanofilm* Appl. Phys. Lett., **86**, 171912-1-171912-3, (2005)

[131]K. L. Chopra and L. C. Bobb, *Electrical Conduction in Thin Epitaxially Grown Gold Films*, J. Appl. Phys., **34**, 1699, (1963)

[132]R. Suri, A. P. Thakoor and K. L. Chopra, *Electron Transport Properties of Thin Copper Films I*, J. Appl. Phys., **46**, 2574-2582, (1975)

[133]Q. G. Zhang, B. Y. Cao, X. Zhang, M. Fujii and K. Takahashi, *Influence of Grain Boundary Scattering on the Electrical and Thermal Conductivities of Polycrystalline Gold Nanofilms*, Phys. Rev. B, **74**, 134109-1-134109-5, (2006)

[134]P. Nath and K. L. Chopra, *Thermal Conductivity of Copper Films*, Solid State Comm., **20**, 53-62, (1974)

[135]C. S. Jayanthi, H. Bilz, W. Kress and G. Benedek, *Nature of Surface-Phonon Anomalies in Noble Metals*, Phys. Rev. Lett., **59**, 795-798, (1987)

[136]R. Ahuja, A. K. Solanki and S. Auluck, *Effect of Pressure on the Fermi Surface of Noble Metals*, Phys. Rev. B, **39**, 9806-9808, (1989)

[137]C. Starr, *The Pressure Coefficient of Thermal Conductivity of Metals*, Phys. Rev., **54**, 210-216, (1938)

[138]D. A. Bell, *Distribution Function of Semiconductor Noise*, Proc. Phys. Soc. London, **B68**, 690-691, (1955)

[139]*CRC Handbook of Chemistry and Physics, 78th Ed.,* CRC Press, (1998)

[140]G. L. Squires, *Introduction to the Theory of Thermal Neutron Scattering*, Dover Publications, New York, (1978)

[141]C. S. Johnson, Jr. and D. A. Gabriel, *Laser Light Scattering*, Dover Publications, New York, (1981)

[142]H. B. Callen and T. A. Welton, *Irreversibility and Generalized Noise*, Phys. Rev., **83**, 34-40, (1951)

[143]R. A. Serway, *Physics for Scientists and Engineers with Modern Physics*, 4th Ed., Saunders College Publishing, Chicago, (1996)

[144]H. L. Chau and K. D. Wise, *Noise Due to Brownian Motion in Ultrasensitive Solid State Pressure Sensors*, IEEE Trans. Electron Dev., **ED-34**, 859-865, (1987)

[145]R. H. Mellen, *The Thermal-Noise Limit in the Detection of Underwater Acoustic Signals*, J. Acoust. Soc. Am., **24**, 478-480, (1952)

[146]H. F. Olson, *Microphone Thermal Agitation Noise*, J. Acoust. Soc. Am., **51**, 425-432, (1972)

[147]C. J. Van Burik and C. Th. J. Alkemade, *Spatial Correlation in Spontaneous Pressure Fluctuations of a Gas Inside an Acoustical Black Box*, J. Acoust. Soc. Am., **44**, 287-288, (1968)

[148]R. L. Weaver and O. I. Lobkis, *Ultrasonics Without a Source: Thermal Fluctuation Correlations at MHz Frequencies*, Phys. Rev. Lett., **87**, 134301-1-134301-4, (2001)

[149]O. I. Lobkis and R. L. Weaver, *On the Emergence of the Green's Function in the Correlations of a Diffuse Field*, J. Acoust. Soc. Am., **110**, 3011-3017, (2001)

[150]R. L. Weaver and O. I. Lobkis, *Elastic Wave Thermal Fluctuations, Ultrasonic Waveforms by Correlation of Thermal Phonons*, J. Acoust. Soc. Am., **113**, 2611-2621, (2003)

[151]R. Dieme, G. Bosman, T. Nishida and M. Sheplak, *Sources of Excess Noise in Silicon Piezoresistive Microphones*, J. Acoust. Soc. Am., **119**, 2710-2720, (2006)

[152]M. Schlosshauer, *Decoherence and the Quantum-To-Classical Transition*, Springer, New York, (2007)

[153]W. G. Unruh, *Reality and Measurement of the Wave Function*, Phys. Rev. A, **50**, 882-887, (1994)

[154]J. P. Paz, S. Habib and W. H. Zurek, *Reduction of the Wave Packet: Preferred Observable and Decoherence Time Scale*, Phys. Rev. D, **47**, 488-500, (1993)

[155]L. Stodolsky, *Sources Decoherence-Fluctuation Relation and Measurement Noise*, Phys. Reports, **320**, 51-58, (1999)

[156]P. L Garrity, *Quantum Decoherence of Nanodevices Under Convective and Radiative Boundary Conditions*, J. Appl. Phys., **100**, 104316-1-104316-9, (2006)

[157]A. Hoel, L. K. J. Vandamme, L. B. Kish and E. Olsson, *Current and Voltage Noise in WO_3 Nanoparticle Films*, J. Appl. Phys., **91**, 5221-5226, (2002)

[158]J. M. Smulko, J. Ederth, L. B. Gish, P. Heszler and C. G. Granqvist, *Higher Order Spectra in Nanoparticle Gas Sensors*, Fluctuations and Noise Lett., **4**, L597-L603, (2004)

[159]C. Kurdak, J. Kim, A. Kuo, J. J. Lucido, L. A. farina, X. Bai, M. P. Rowe and A. J. Matzger, *1/f Noise in Gold Nanoparticle Chemosensors*, Appl. Phys. Lett., **86**, 073506-1-073506-3, (2005)

[160]W. Kruppa, M. G. Ancona, R. W. Rendell, A. W. Snow, E. E. Foos and R. Bass, *Electrical Noise in Gold Nanocluster Sensors*, Appl. Phys. Lett., **88**, 053120-1-053120-3, (2006)

[161]P. Bruschi, F. Cacialli, A. Nannini and B. Neri, *Gas and Vapour Effects on the Resistance Fluctuation Spectra of Conducting Polymer Thin-Film Sensors*, Sens. Actuators B, **18**, 421-425, (1994)

[162]J. L. Solis, L. B. Kish, R. Vajtai, C. G. Granqvist, J. Olsson, J. Schnurer and V. Lantto, *Identifying Natural and Artificial Odors Through Noise Analysis with a Sampling and Hold Electronic Nose*, Sens. Actuators B, **77**, 312-315, (2001)

[163]L. B. Kish, R. Vajtai and C. G. Granqvist, *Extracting Information From Noise Spectra of Chemical Sensors: Single Sensor Electronic Noses and Tongues*, Sens. Actuators B, **71**, 55-59, (2000)

[164]P. Bruschi, A. Nannini and B. Neri, *Vapour and Gas Sensing by Noise Measurements on Polymeric Balanced Bridge Microstructures*, Sens. Actuators B, **24**, 429-432, (1995)

[165]F. N. Hooge, T. G. M. Kleinpenning and L. K. J. Vandamme, *Experimental Studies on 1/f Noise*, Rep. Prog. Phys., **44**, 479-532, (1981)

[166]S. Hashiguchi, Y. Yamagishi, T. Fukuda, M. Ohki, J. Sikula and P. Vasina, *Generation of 1/f Spectrum by Relaxation Process in Thin Film Resistors*, Qual. Rel. Eng. Inter., **14**, 69-71, (1998)

[167]K. M. van Vliet, A. van der Ziel and R. R. Schmidt, *Temperature-Fluctuation Noise of Thin Films Supported by a Substrate*, J. Appl. Phys., **51**, 2947-2956, (1980)

[168]A. Yang, X. Tao, R. Wang, S. Lee and C. Surya, *Room Temperature Gas Sensing Properties of SnO_2/Multiwall Carbon Nanotube Composite Nanofibers*, Appl. Phys. Lett., **91**, 133110-1-133110-3, (2007)

[169]M. J. Martin, J. E. Velazquez and D. Pardo, *Analysis of Current Fluctuations in Silicon pn+ and p+n Homojunctions*, J. Appl. Phys., **79**, 6975-6981, (1996)

[170]L. Roschier, R. Tarkiainen, M. Ahlskog, M. Paalanen and P. Hakonen, *Multiwalled Carbon Nanotubes as Ultrasensitive Electrometers*, Appl. Phys. Lett., **78**, 3295-3297, (2001)

[171]H. Ouacha, M. Willander, H. Y. Yu, Y. W. Park, M. S. Kabir, S. H. M. Persson L. B. Kish and A. Ouacha, *Noise Properties of an Individual and Two Crossing Multiwalled Carbon Nanotubes*, Appl. Phys. Lett., **80**, 1055-1057, (2002)

[172]P. G. Collins, M. S. Fuhrer and A. Zettl, *1/f Noise in Carbon Nanotubes*, Appl. Phys. Lett., **76**, 894-896, (2000)

[173]C. K. W. Adu, G. U. Sumanasekera, B. K. Pradhan, H. E. Romero and P. C. Eklund, *Carbon Nanotubes: A Thermoelectric Noise*, Chem. Phys. Lett., **337**, 31-35, (2001)

[174]A. U. Mac Rae and H. Levenstein, *Surface Dependent 1/f Noise in Germanium*, Phys. Rev., **119**, 62-69, (1960)

[175]V. E. Noble and J. E. Thomas, Jr., *Effects of Gaseous Ambients Upon 1/f Noise in Germanium Filaments*, J. Appl. Phys., **32**, 1709-1714, (1961)

[176]A. Sadrzadeh, A. A. Farajian and B. I. Yakobson, *Electron Transport of Nanotube Based Gas Sensors: An ab initio Study*, Appl. Phys. Lett., **92**, 022103-1-022103-3, (2008)

[177]J. W. Eberhard and P. M. Horn, *Temperature Dependence of 1/f Noise in Silver and Copper*, Phys. Rev. Lett., **39**, 643-646, (1977)

[178]A. Singh, T. Phanindra and A. Ghosh, *Electrochemical Fabrication of Ultralow Noise Metallic Nanowires with hcp Crystalline Lattice*, Appl. Phys. Lett., **93**, 102107-1-102107-3, (2008)

[179]A. Bid, A. Bora and A. K. Raychaudhuri, *1/f Noise in Nanowires*, Nanotechnology, **17**, 152-156, (2006)

[180]J. Kong, N. R. Franklin, C. Zhou, M. G. Chapline, S. Peng, K. Cho and H. Dai, *Nanotube Molecular Wires as Chemical Sensors*, Science, **287**, 622-625, (2000)

[181]W. F. Leonard and T. L. Martin, Jr., *Electronic Structure and Transport Properties of Crystals*, Robert E. Krieger Publishing Co., Malabar, Fl, (1979)

[182]J. M. Ziman, *Electrons and Phonons*, Clarendon Press, Oxford, (1960)

[183]W. D. Jumper and W.E Lawrence, *Low Temperature Electrical and Thermal Resistivities of Potassium: Deviations from Matthiessen's Rule,* Phys. Rev. B **16**, 3314-3321 (1977)

[184]S. Pettersson, *Solving the Phonon Boltzmann Equation with the Variational Method,* Phys. Rev. B **43**, 9238-9246 (1991)

[185]H. L. Engquist, *Solution of the Linearized Boltzmann Equation for Electrical Transport in Metals,* Phys. Rev. B, **21**, 2067 (1980)

[186]L. Lefton and D. Wei, *Numerical Approximation of the First Eigenpair of the p-Laplacian using Finite Elements and the Penalty Method,* Numer. Funct. Anal. And Optimiz. **18**, 389 (1997)

[187]J. N. Reddy, *Applied Functional Analysis and Variational Methods in Engineering*, Robert E. Krieger Publishing Co., Malabar, Fl, (1986)

[188]P. K. Kythe and D. Wei, *An Introduction to Linear and Nonlinear Finite Element Analysis: A Computational Approach*, Birkhauser, Boston, (2004)

[189]W. Jones and N.H. March, *Theoretical Solid State Physics, Vol. 2: Non-Equilibrium and Disorder,* Wiley-Interscience, New York, (1973)

[190]K. J. Bathe, *Finite Element Procedures in Engineering Analysis,* Prentice-Hall, New Jersey, (1982)

[191]J. S. Bendat and A. G. Piersol, *Random Data Analysis and Measurement Procedures,* 3rd Ed., John Wiley & Sons, Inc., New York, (2000)

[192]J. Sikula and M. Levinshtein (ed.), *Advanced Experimental Methods for Noise Research in Nanoscale Electronic Devices,* Kluwer Academic Publishers, Boston, (2004)

[193]G. H. Wannier, *Statistical Physics,* Dover, New York, (1966)

[194]M. B. Weissman and G. D. Dollinger, *Noise from Equilibrium Enthalpy Fluctuations in Resistors,* J. Appl. Phys., **52**, 3095-3098 (1981)

[195]C. Kittel, *Thermal Physics,* John Wiley & Sons, New York, (1969)

[196]L. D. Landau and E. M. Lifshitz, *Statistical Physics Part 1,* 3rd Ed., Elsevier, New York, (1980)

[197]J. W. Gibbs, *Elementary Principles in Statistical Mechanics,* Yale University, New Haven, (1902)

[198]K. Huang, 2nd Ed., *Statistical Mechanics,* John Wiley & Sons, New York, (1987)

Appendix A: Numerical Program: Phonon Scattering Due to Gas Particles

The following program was written in the MathCAD® version 13 numerical software environment. The program may be used to calculate the phonon scattering relaxation time due to gas particle interactions as outlined in Chapter 2, Section 2.2. The program also calculates many additional material parameters such as phonon scattering relaxation time due to adsorbed gas particles, phonon perturbation amplitudes due to gas particle interaction, deBroglie wavelengths, gas particle interaction energy and gas particle impacts per second. The first page of the program allows gas and solid material physical parameters to be input. The corresponding calculation results are clearly labeled with comments through the remainder of the program.

GAS PARAMETER INPUTS

Label Gas Type: Argon

$kb := 1.38065810^{-23}$

$U := 0$ Bulk Fluid Velocity, m/s

$Cp := 521.745$ Specific Ht, J/kg

$\gamma := 1.669$ Specific Ht Ratio

$Rgas := 208.1$ Gas Constant, J/kg-K

$Ti := 299.37$ Incident Gas Temp, K

$\rho gas := 1.62422$ Gas Density in kg/m^3

$mgaskg := 6.633471 10^{-26}$ Gas Molec Mass in kg's

$mgas := 39.948$ Gas Molec Mass Molar Mass

$P := 118589$ Incident Gas Pressure, Pa

$\varepsilon gas := 1.711210^{-21}$ Lennard Jones Const, J

$\sigma gas := 3.41810^{-10}$ Lennard Jones Const, m

$d := 3.5810^{-10}$ Gas Molec Diam, m

$\alpha := 0.70$ Acomm Coeff

$$Ma := \frac{U}{\sqrt{1.0 \cdot \gamma \cdot Rgas \cdot Ti}} \qquad Ma = 0$$

$$Tg := Ti + \frac{U^2}{2 \cdot Cp} \qquad Tg = 299.370$$ Stagnation Gas Temp

$$\theta := \frac{\pi}{2}$$ Thin Film Angle of Attack

SOLID PARAMETER INPUTS

Label Solid Type: Gold

$h := 6.6260751 0^{-34}$ Plancks Const

$hbar := 1.05456572661 0^{-34}$ Reduced Planck Constant

$x := 5.5 \cdot 10^{-3}$ Thin Film x Dimension

$y := 2.27 \cdot 10^{-3}$ Thin Film y Dimension

$a := 30.0 \cdot 10^{-9}$ Thin Film z Dimension

$\rho solid := 19320.0$ Solid Density in kg/m^3

$\varepsilon solid := 1.21441 0^{-21}$ Lennard Jones Const, J

$\sigma solid := 3.541 \cdot 10^{-10}$ Lennard Jones Const, m

$msolid := 196.97$ Lattice Ion Mass in amu's

$msolidkg := 3.270741 0^{-25}$ Lattice ion mass in kg

$vsound := 3240$ Velocity of Sound in Solid, m/s

$\Theta D := 170$ Debye Temp, K

$Tlattice := 298.6$ Lattice Temp, K

$latticedim := 4. \cdot 10^{-10}$ Crystal Lattice Ion Spacing

$$vgas := \left(\frac{8 \cdot kb \cdot Ti}{\pi \cdot mgaskg}\right)^{0.5} \qquad vgas = 398.33$$

$$eV := \left[\frac{\left[mgaskg \cdot \frac{(vgas + U)^2}{2}\right]}{1.60217710^{-19}}\right] \qquad eV = 0.03285$$

$$\lambda db := \frac{h}{mgaskg \cdot vgas}$$

$$\lambda db = 2.507660331678128 \times 10^{-11}$$

Gas DeBroglie Wavelength

$$DW := e^{-2 \cdot \left[\frac{(24 \cdot mgaskg \cdot eV \cdot \cos(0) \cdot Tlattice)}{\left(msolidkg \cdot 8.617343 \cdot 10^{-5} \cdot \Theta D^2\right)}\right]}$$

$$DW = 0 \times 10^{0}$$

Debeye Waller Factor

$$Wi := Ma \cdot \sin(\theta) \cdot \sqrt{\frac{\gamma}{2}} \qquad Wi = 0.00000000000000000$$

$$nv := \frac{P}{kb \cdot Ti} \qquad nv = 2.87 \times 10^{25}$$

Number Gas Molecs/m^3

$$L := \frac{1}{nv^{0.33333}} \qquad L = 3.27 \times 10^{-9}$$

Avg Gas Molec Separation Dist

$$\mu := \frac{mgas}{msolid} \qquad \mu = 2.03 \times 10^{-1}$$

Reduced Mass

$$\sigma := \left(\frac{\sigma gas + \sigma solid}{2}\right) \qquad \sigma = 3.479500 \times 10^{-10}$$

$$\beta := \left(\frac{\varepsilon gas}{2 \cdot msolid}\right) \cdot \left(\frac{48 \cdot hbar}{kb \cdot \sigma \cdot \Theta D}\right)^2 \qquad \beta = 0.000000000000000$$

$$uprime := \left(\frac{hbar}{\Theta D}\right) \cdot \left(2 \frac{Tg}{mgaskg \cdot kb}\right)^{0.5}$$

Lattice ion movement parameter

$$uprime = 1.586099 \times 10^{-11}$$

$$\gamma solid := 2 - \left(\beta \cdot \frac{1 + \mu}{\mu}\right) \qquad \gamma solid = 2 \times 10^{0}$$

$$\alpha 0 := 1.0 \cdot 10^{-12}$$

$$\alpha 1 := 2 \cdot uprime \qquad \alpha 1 = 3.17 \times 10^{-11}$$

$$\alpha 2 := \gamma solid \cdot \alpha 0 \qquad \alpha 2 = 2 \times 10^{-12}$$

$$\alpha 3 := (1 + \gamma solid) \cdot \alpha 1 \qquad \alpha 3 = 9.52 \times 10^{-11}$$

$$\omega L := \frac{0.5 \cdot kb \cdot \Theta D}{hbar} \qquad \omega L = 1.11 \times 10^{13}$$

Lattice Frequency Debye Approx. (1/sec)

$$\frac{1}{\omega L} = 8.99 \times 10^{-14}$$

Lattice Period (sec)

$$\left[\frac{vsound}{(\omega L)}\right] = 2.91 \times 10^{-10}$$

Phonon mfp

$$wavelngth := \frac{vsound}{\omega L} \qquad wavelngth = 2.91 \times 10^{-10}$$

Phonon Wavelength, m

$$\tau(t) := 2 \cdot \omega L \cdot t$$

Reduced Time

$\frac{latticedim}{L} = 0.1224$ This is the Lattice Spacing Ratio to Gas Interaction Distance

$\lambda dbphon := \frac{2 \cdot h \cdot \omega L}{kb \cdot Tlattice}$ $\lambda dbphon = 3.577188 \times 10^{0}$

$mfp := \frac{1}{nv \cdot d^2 \cdot \pi \cdot \sqrt{2}}$ $mfp = 6.12 \times 10^{-8}$

$\lambda dbelectron := \frac{hbar}{\left(4 \cdot 9.10938 \cdot 10^{-31} \cdot kb \cdot Tlattice\right)^{0.5}}$

$kn := \frac{mfp}{x}$ $kn = 1.113 \times 10^{-5}$ $\lambda dbelectron = 8.6 \times 10^{-10}$

$GarrityNo := \frac{x}{L}$ $GarrityNo = 1.68 \times 10^{6}$ Scattering Number Characterizing the Magnitude of Nanosurface-Gas Scattering Effects

$(x + mfp) \cdot (y + mfp) \cdot mfp \cdot nv = 2.19 \times 10^{13}$ No. Molec Within a mfp of Thin Film

$\chi := \left(e^{-Wi^2}\right) + Wi \cdot (1 + erf(Wi)) \cdot \sqrt{\pi}$ $\chi = 1 \times 10^{0}$

$Ni := nv \cdot \sqrt{\frac{Rgas \cdot Ti}{2 \cdot \pi}} \cdot \chi$

$Ni = 2.86 \times 10^{27}$ Incident No. Molec's per sq. meter

$t := 0, 1.0 \cdot 10^{-15} .. 1.0 \cdot 10^{-12}$ Lattice Response Time for Plotting, sec

$Nfilm := Ni \cdot x \cdot y$ $Nfilm = 3.57 \times 10^{22}$ Incident No. Molec's on Thin Film per second

$\frac{1}{Nfilm} = 2.8035686362777037 \times 10^{-23}$ MFT Between Molec's Inpacts

$(\alpha 0 \cdot J0(\tau(t))) =$	$(\alpha 1 \cdot J1(\tau(t))) \cdot 1 =$	$(\alpha 2 \cdot Jn(2, \tau(t))) \cdot 1 =$	$(\alpha 3 \cdot Jn(3, \tau(t))) \cdot 1 =$
$1 \cdot 10^{-12}$	$0.000 \cdot 10^{0}$	$0 \cdot 10^{0}$	$0 \cdot 10^{0}$
$10 \cdot 10^{-13}$	$3.530 \cdot 10^{-13}$	$0 \cdot 10^{0}$	$0 \cdot 10^{0}$
$10 \cdot 10^{-13}$	$7.059 \cdot 10^{-13}$	$0 \cdot 10^{0}$	$0 \cdot 10^{0}$
$9.99 \cdot 10^{-13}$	$1.058 \cdot 10^{-12}$	$1.11 \cdot 10^{-15}$	$0 \cdot 10^{0}$
$9.98 \cdot 10^{-13}$	$1.411 \cdot 10^{-12}$	$1.98 \cdot 10^{-15}$	$1.4 \cdot 10^{-15}$
$9.97 \cdot 10^{-13}$	$1.762 \cdot 10^{-12}$	$3.09 \cdot 10^{-15}$	$2.73 \cdot 10^{-15}$
$9.96 \cdot 10^{-13}$	$2.113 \cdot 10^{-12}$	$4.45 \cdot 10^{-15}$	$4.72 \cdot 10^{-15}$
$9.94 \cdot 10^{-13}$	$2.464 \cdot 10^{-12}$	$6.06 \cdot 10^{-15}$	$7.49 \cdot 10^{-15}$
$9.92 \cdot 10^{-13}$	$2.813 \cdot 10^{-12}$	$7.9 \cdot 10^{-15}$	$1.12 \cdot 10^{-14}$
$9.9 \cdot 10^{-13}$	$3.161 \cdot 10^{-12}$	$10 \cdot 10^{-15}$	$1.59 \cdot 10^{-14}$
$9.88 \cdot 10^{-13}$	$3.508 \cdot 10^{-12}$	$1.23 \cdot 10^{-14}$	$2.18 \cdot 10^{-14}$
$9.85 \cdot 10^{-13}$	$3.854 \cdot 10^{-12}$	$1.49 \cdot 10^{-14}$	$2.9 \cdot 10^{-14}$
$9.82 \cdot 10^{-13}$	$4.199 \cdot 10^{-12}$	$1.77 \cdot 10^{-14}$	$3.76 \cdot 10^{-14}$
$9.79 \cdot 10^{-13}$	$4.541 \cdot 10^{-12}$	$2.08 \cdot 10^{-14}$	$4.78 \cdot 10^{-14}$
$9.76 \cdot 10^{-13}$	$4.882 \cdot 10^{-12}$	$2.41 \cdot 10^{-14}$	$5.96 \cdot 10^{-14}$
...	...	...	...

$(\alpha 0 \cdot J0(\tau(t))) + (\alpha 1 \cdot J1(\tau(t))) + (\alpha 2 \cdot Jn(2, \tau(t))) + (\alpha 3 \cdot Jn(3, \tau(t))) =$

$1 \cdot 10^{-12}$
$1.35 \cdot 10^{-12}$
$1.71 \cdot 10^{-12}$
$2.06 \cdot 10^{-12}$
$2.41 \cdot 10^{-12}$
$2.77 \cdot 10^{-12}$
$3.12 \cdot 10^{-12}$
$3.47 \cdot 10^{-12}$
$3.82 \cdot 10^{-12}$
$4.18 \cdot 10^{-12}$
$4.53 \cdot 10^{-12}$
$4.88 \cdot 10^{-12}$
$5.24 \cdot 10^{-12}$
$5.59 \cdot 10^{-12}$
$5.94 \cdot 10^{-12}$
...

Lattice Ion Response to Gas Molecule Collision. The Periodic Motion Begins From the Potential Energy Forcing Function with Lattice Relaxation Occuring After the Collision.

$$\int_{.2001 \cdot 10^{-10}}^{\infty} \left(\frac{\sigma gas^{12}}{\sigma gas^{10}} \right) - \left(\frac{\sigma gas^{6}}{\sigma gas^{4}} \right) d\sigma gas = -2.232785162398896 \times 10^{-13}$$

Potential Energy Integral Assuming 0.5 Angstrom Closest Approach By Gas Molecule to Lattice Ion

$\Delta := uprime$ RMS Amplitude of Lattice Ion Deflection

$LJonesInteg := .23 \cdot 10^{-17}$

Relaxation Time Integral
Manual Entry
NOT SQUARED YET!

$vgas = 398.334$ Avg Gas Velocity, m/s

$p := mgaskg \cdot \frac{vgas^2}{2}$ $p = 0$ Gas Kinetic Energy

$\gamma relax := \left[L^2 \cdot \left(\frac{p}{hbar} \right)^2 \right]$ $\gamma relax = 2.66 \times 10^{10}$ Relaxation Time Parameter

$$\tau gas := \left(\frac{hbar^3}{32 \cdot \pi^2 \cdot \varepsilon solid^2 \cdot \Delta^2 \cdot L^2 \cdot \alpha \cdot Nfilm} \right) \cdot \left(\frac{1}{LJonesInteg^2} \right) \cdot \left[\frac{1}{\left(\frac{2}{\gamma relax} \right) - \frac{\ln(2 \cdot \gamma relax + 1)}{\gamma relax^2}} \right] \cdot p^{0.5}$$

$\tau gas = 6.845076700843762 \times 10^{-12}$

This Relaxation Time Represents The Relaxation Time Incurred During Gas Molecules Collisions With The NanoFilm Lattice Surface

Calculation of the Relaxation Time of the Lattice Surface with Adsorbed Gas Molecules now Follows:

$StickingProb := 0.5$

$Pstick := StickingProb \cdot e^{-(Ma)}$ Assume that the sticking probablility of an incoming gas molecule follows an exponential profile that is a function of the Mach No.

$\xi := 0.5$ $\xi = 0.5$ Fraction of Covered Nanofilm surface by adsorbed gas molecules

$rgas := \frac{d}{2}$ Gas molecule radius, m

$cads := \frac{\xi}{\pi \cdot rgas^2}$ $cads = 4.97 \times 10^{18}$ Concentration of adsorbed gas molecules per unit surface area

$\Delta m := mgaskg - msolidkg$ $\Delta m = 0 \times 10^{0}$ Difference in gas and solid masses, kg

$\nu := vsound$ Surface Rayleigh phonon velocity

$B := 3.1$ Varies from 3.2 when material Poisson ratio is 0.25 to 3.44 when Poisson ratio is 0.25 to 3.44 when Poisson ratio is 0.29 to 5.04 when Poisson ratio is 0.5

$kwavevector := \left(2 \cdot \pi \cdot \frac{\omega L}{vsound}\right)$ $kwavevector = 2.16 \times 10^{10}$ Phonon wave vector

$z := 0.01 \cdot 10^{-10}$ Depth from surface (z=0) of adsorbed gas molecule

$C1 := 140.0$

$wavelngth = 2.91 \times 10^{-10}$ For impurity depth vs phonon wavelength check

$C2 := 100.25$

$C3 := 100.25$ These constants describe scattering into surface and bulk waves. They decrease rapidly for adsorbed gas molecule depths z.

$$\tau ads := \frac{1}{\left(\frac{cads \cdot \Delta m^2}{8 \cdot \rho solid^2 \cdot B^2 \cdot \nu^4}\right) \cdot \left(\omega L^5\right) \cdot [[C1 \cdot (kwavevector \cdot z)] + [C2 \cdot (kwavevector \cdot z)] + [C3 \cdot (kwavevector \cdot z)]]}$$

$\tau ads = 7.46689947389365800E-012$ This relaxation time represents the relaxation time incurred during solid surface ions scattering with adsorbed gas molecules

Program End

Appendix B: Variational Solution to the Boltzmann Transport Equation Using the Finite Element Penalty Method

When materials are subjected to a thermal gradient or electrical potential, the subsequent flow of heat or electrical currents can be calculated with equations based upon linear response theory. Essentially, these partial differential equations utilize transport coefficients such as thermal conductivity or electrical resistivity that are highly dependent on material parameters, temperatures and boundary conditions.[42] The engineering community has typically relied on experimental results to determine the transport coefficients however the physicist is interested in the fundamental processes that determine their magnitudes. The fundamental theory that has become a mature well understood field is based upon scattering processes of electrons and phonons.[181] These quantized particles are the primary carriers of energy and charge in the transport processes of solids and their interactions determine the charge and heat current magnitudes. The fundamental transport equation that describes scattering events is the Boltzmann transport equation (BTE), which is a non-linear integro-differential equation in its basic form.[32,181] Solving this equation always begins by linearization followed by certain assumptions that are system and material dependent. A variational form of the BTE was derived by Ziman[182] with specific applicability to the transport coefficients. Subsequent numerical results were published by several groups[183-185] who used a trial function method that compared very well with experiment. All published results however, assumed consistent energy exchange processes throughout the crystal lattice thus producing a uniform transport property value throughout the material. This is not to say that anisotropic or energy dependent scattering in different crystallographic directions was not encompassed. The literature base does include

work that recognized complex scattering mechanisms, which typically resulted in closer agreement with experimental values. The assumption was however, that these anisotropic properties or complex scattering mechanisms were identical for each and every crystal within the lattice. With the advent of nanoscale materials, boundary conditions such as surface scattering, interfacial bonds and many others, now introduce scattering mechanisms that can perturb the normal transport coefficients, unlike their macroscopic counterparts. This perturbation can be a localized effect such as near an interface or within a few atomic layers of the surface. The utilization of this effect, through bottom-up material engineering can result in transport specific design that can enhance a devices operation. Therefore, the former solution method of the variational BTE of using a trial function under the assumption of material-wide applicability cannot give the detail required for transport specific nanoscale devices. Herein lies the main objective of this appendix. Specifically, a finite element solution of the variational BTE shall be derived and solved using a constrained penalty function method. The primary advantage to this procedure lies in the capability to discretize a nanomaterial thus allowing nodal solutions at appropriate locations within a material. This procedure then provides discrete transport property results at specific material locations, which enables powerful nanomaterial design capabilities.

The following derivations and results shall focus on the finite element formulation of the variational BTE describing the electrical resistivity of a material. All results apply to other variational BTE forms[182] that describe the thermal conductivity, thermoelectric effects, etc. Under steady state conditions, an electron distribution exists in a material that is described by the Fermi-Dirac distribution function $f_{\mathbf{k}}(\mathbf{r})$.[181] This distribution function measures the number of electrons in the $\mathbf{k}^{th}$ state in the neighborhood of the position vector $\mathbf{r}$. The $\mathbf{k}$ state is quite simply a wave vector, which reflects the quantum energy level of the electron. The distribution function

in the neighborhood of **r** can change through electron scattering events with the crystal lattice (phonons), impurity ions, other electrons, etc. During a scattering event, energy may be exchanged and an electron's wave vector or **k**-state may increase or decrease into another available **k**-state, which shall be called $\mathbf{k}'$. Clearly, this process can result in a distribution function $f_{\mathbf{k}}(\mathbf{r})$ that is out of equilibrium, which is precisely what happens under the application of an electric field. Figure B.1 shows the electron Fermi sphere that encompasses all available **k** states. Consider electrons that just prior to a collision, were in the differential volume element $d\mathbf{k}'$ about $\mathbf{k}'$. Of these, a fraction will be scattered into a different energy state $d\mathbf{k}$ about **k**. Therefore, under an applied electric field, there will be some flux of electrons per unit volume arriving *into* the volume element $d\mathbf{k}$ about **k** *from* the volume element $d\mathbf{k}'$ about $\mathbf{k}'$. This process induces a change to the distribution function, which is also shown in Figure B.1. The measure of the deviation of the distribution function from equilibrium conditions is expressed as:[182]

$$f_{\mathbf{k}} = f_{\mathbf{k}}^{0} - \varphi_{\mathbf{k}} \frac{\partial f_{\mathbf{k}}}{\partial E_{\mathbf{k}}}, \tag{B.1}$$

where $f_{\mathbf{k}}^{0}$ is the equilibrium distribution function and $\varphi_{\mathbf{k}}$ is just a function that measures the deviation from equilibrium of the distribution. In fact, it is the average extra energy that the electrons have because of the transport process. Referring back to Figure B.1, $\varphi_{\mathbf{k}}$ can be considered a modulating function to the distribution function gradient $\partial f_{\mathbf{k}} / \partial E_{\mathbf{k}}$. The function

$\varphi_{\mathbf{k}}$ lies in the same functional k-space as the electron distribution and can take on different values for $\varphi(\mathbf{k})$ and $\varphi(\mathbf{k}')$. In fact, if $\varphi(\mathbf{k}) = \varphi(\mathbf{k}')$, then the system is under equilibrium conditions and there can be no electric field perturbation present.

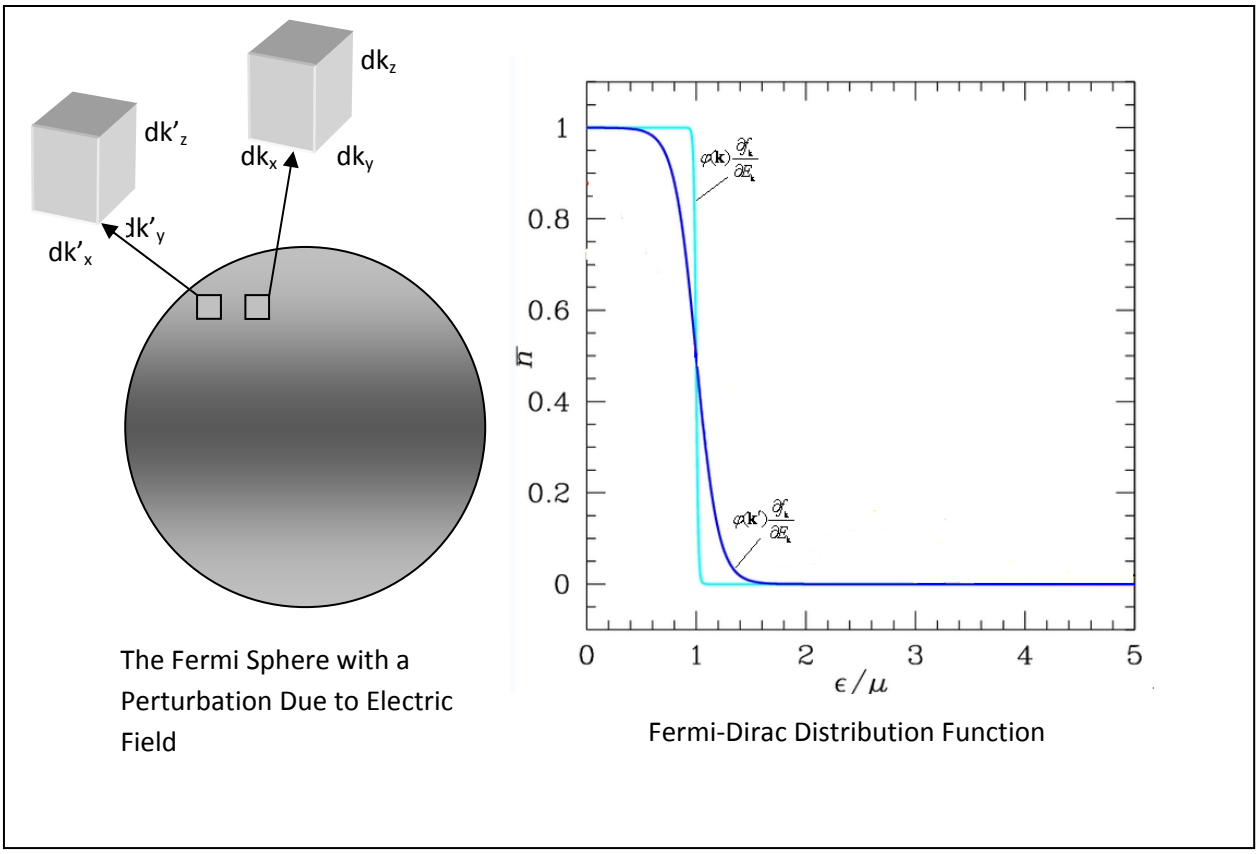

Figure B.1: The Fermi sphere encompassing **k**-states of the electron distribution. Electrons scatter in to, and out of differential elements at the Fermi surface. The resulting perturbation to the electron distribution function is modulated by the function $\phi(\mathbf{k}, \mathbf{k'})$.

Ziman[182] incorporated the function $\phi(\mathbf{k}, \mathbf{k'})$ into the variational formulation of the BTE in a unit electric field describing the resistivity of a solid as:

$$\rho = \frac{\dfrac{P_{\mathbf{k}}^{\mathbf{k}'}}{2k_B T}\iint \left[\phi(\mathbf{k}) - \phi(\mathbf{k}')\right]^2 d\mathbf{k} d\mathbf{k}'}{\left|\int e v_g \phi(\mathbf{k}) \dfrac{\partial f_{\mathbf{k}}}{\partial E_{\mathbf{k}}} d\mathbf{k}\right|^2}\ , \tag{B.2}$$

where k_B is Boltzmann's constant, T is the temperature of the solid, e is the fundamental electron charge, v_g is the electron wave packet group velocity, ρ is the material electrical resistivity and $P_{\mathbf{k}}^{\mathbf{k}'}$ is the wave vector transition probability. This probability is usually determined by a quantum mechanical solution to the particular scattering mechanism present. As a probability, it is always positive. For example, if the electron scattering probability with a gas particle is analyzed, then the quantum or classical transition probability $P_{\mathbf{k}}^{\mathbf{k}'}$ could be calculated from Chapter 2 equation (2.14) or (2.17) respectively. With regards to mathematical construct, the denominator of equation (B.2) is noted to be the microscopic expression for electrical conductivity σ. The minimization of equation (B.2) requires the knowledge of $\phi(\mathbf{k})$. If $\phi(\mathbf{k})$ can be found, then substitution into the above integrals yields the resistivity. Quite simply, the electrical resistivity is the extremal value of the variational function in unit electric field ($\mathbf{E} = 1$). This work incorporates the numerical approximation of equation (B.2) by using finite elements and the penalty method subject to a constraint similar to the method of Lefton and Wei.[186] Fundamentally, the constrained penalty method approximates a constrained optimization problem with an unconstrained one followed by standard search techniques to obtain solutions. Let $f(\mathbf{k})$ represent equation (B.2). Then consider:

$$\text{Minimize}\left\{ f(\mathbf{k}) : \mathbf{k} \in S \right\}, \tag{B.3}$$

where $f(\mathbf{k})$ is a continuous function through linear transformation on R^n and S is a constraint set in R^n.[187] The penalty function methodology is to replace equation (B.3) by an unconstrained approximation of the form:

$$\text{Minimize}\left\{ f(\mathbf{k}) + \frac{1}{2\varepsilon} K(\mathbf{k}) \right\}, \tag{B.4}$$

where ε is a positive constant known as the penalty parameter and $K(\mathbf{k})$ is a function on R^n satisfying (i) $K(\mathbf{k})$ is continuous , (ii) $K(\mathbf{k}) \geq 0$ for all $\mathbf{k} \in R^n$, and (iii) $K(\mathbf{k}) = 0$ iff $\mathbf{k} \in S$.[187] The linear transformation of **k**-space and real space R^n is implicit in the above conditions. During the numerical solution of equation (B.4), if ε is made suitably large, the minimum point of equation (B.2) will be in a region where $K(\mathbf{k})$ is small. Ideally then, as ε approaches infinity, the solution point of the penalty problem will converge to the solution of the constrained problem.[187-188]

Following the derivation of equation (B.2) by setting the electric field **E** to one, the constraint shall be imposed upon the current **J** to also be equal to one. Essentially, this means:

$\mathbf{J} = \sigma \cdot \mathbf{E}$, ($\mathbf{E}$ =1 by Ziman's Formulation[182]) giving:

$$\mathbf{J} = \sigma = \int e v_g \phi(\mathbf{k}) \frac{\partial f_{\mathbf{k}}}{\partial E_{\mathbf{k}}} d\mathbf{k} = 1 \text{ by the constraint formulation in this work} \tag{B.5}$$

Therefore, we setup the following penalty function problem:

$$\begin{aligned} &\text{Minimize } f(\mathbf{k}) = \frac{P_{\mathbf{k}}^{\mathbf{k}'}}{2k_B T} \iint \left[\phi(\mathbf{k}) - \phi(\mathbf{k}')\right]^2 d\mathbf{k} d\mathbf{k}' \\ &\text{Subject to } K(\mathbf{k}) = \left| \int e v_g \phi(\mathbf{k}) \frac{\partial f_{\mathbf{k}}}{\partial E_{\mathbf{k}}} d\mathbf{k} \right|^2 = 1 \end{aligned} \tag{B.6}$$

The finite element formulation of equation (B.6) was accomplished using two dimensional bi-linear triangle elements. Furthermore, the assumption of $\phi(\boldsymbol{\kappa}) = \phi(\mathbf{k}') = \phi(\mathbf{k} - \mathbf{k}')$ is made. This commonly used technique[189] allows the penalty function solution to consist of two results; $\phi(\mathbf{k})$ and $\phi(\boldsymbol{\kappa})$. Essentially, $\phi(\boldsymbol{\kappa})$ is the scattering energy function difference $\left(\phi(\mathbf{k}) - \phi(\mathbf{k}')\right)$. Let the constant $C_1 = P_{\mathbf{k}}^{\mathbf{k}'} / 2k_B T$ and recognizing the linear transformation of **k**-space and real space R^n, the objective function $f(\mathbf{k})$ is:

$$f(\mathbf{k}) = C_1 \iint \left[\phi(\mathbf{k}) - \phi(\boldsymbol{\kappa})\right]^2 d\mathbf{k} d\boldsymbol{\kappa} = C_1 \iint \phi^2(k_x, k_y) - 2\phi(k_x, k_y)\phi(k_x', k_y') + \phi^2(k_x', k_y') dk_x dk_y \tag{B.7}$$

where the primes indicate relation to $\phi(\boldsymbol{\kappa})$. Incorporating the bi-linear triangle shape functions $S_{ijk}^{(e)}$ into $f(\mathbf{k})$ from equation (B.7) yields:

$$f(\mathbf{k}) = C_1 \left[\iint_{\Omega^{(e)},\Omega^{'(e)}} \left[\phi_1^{(e)} \;\; \phi_2^{(e)} \;\; \phi_3^{(e)} \right] \begin{Bmatrix} S_1^{(e)} \\ S_2^{(e)} \\ S_3^{(e)} \end{Bmatrix} \left[S_1^{(e)} \;\; S_2^{(e)} \;\; S_3^{(e)} \right] \begin{Bmatrix} \phi_1^{(e)} \\ \phi_2^{(e)} \\ \phi_3^{(e)} \end{Bmatrix} dk_x' dk_y' dk_x dk_y - \right.$$

$$2 \iint_{\Omega^{(e)},\Omega^{'(e)}} \left[\phi_1^{(e)} \;\; \phi_2^{(e)} \;\; \phi_3^{(e)} \right] \begin{Bmatrix} S_1^{(e)} \\ S_2^{(e)} \\ S_3^{(e)} \end{Bmatrix} \left[S_1^{(e)} \;\; S_2^{(e)} \;\; S_3^{(e)} \right] \begin{Bmatrix} \phi_1^{'(e)} \\ \phi_2^{'(e)} \\ \phi_3^{'(e)} \end{Bmatrix} dk_x' dk_y' dk_x dk_y + \qquad \text{(B.8)}$$

$$\left. \iint_{\Omega^{(e)},\Omega^{'(e)}} \left[\phi_1^{'(e)} \;\; \phi_2^{'(e)} \;\; \phi_3^{'(e)} \right] \begin{Bmatrix} S_1^{(e)} \\ S_2^{(e)} \\ S_3^{(e)} \end{Bmatrix} \left[S_1^{(e)} \;\; S_2^{(e)} \;\; S_3^{(e)} \right] \begin{Bmatrix} \phi_1^{'(e)} \\ \phi_2^{'(e)} \\ \phi_3^{'(e)} \end{Bmatrix} dk_x' dk_y' dk_x dk_y \right]$$

Proceeding through integration in natural coordinates over the element area $\Omega^{(e)}$ and $\Omega^{'(e)}$ gives:

$$f(\mathbf{k}) = C_1 \left[\frac{\Omega^{(e)^2}}{12} \begin{bmatrix} \phi_1^{(e)} & \phi_2^{(e)} & \phi_3^{(e)} \end{bmatrix} \underbrace{\begin{bmatrix} 2 & 1 & 1 \\ 1 & 2 & 1 \\ 1 & 1 & 2 \end{bmatrix}}_{\underset{\sim}{K}^{(e)}} \begin{Bmatrix} \phi_1^{(e)} \\ \phi_2^{(e)} \\ \phi_3^{(e)} \end{Bmatrix} - \right.$$

$$\frac{\Omega^{(e)^2}}{12} \begin{bmatrix} \phi_1^{(e)} & \phi_2^{(e)} & \phi_3^{(e)} \end{bmatrix} \underbrace{\begin{bmatrix} 1/2 & 5/12 & 5/12 \\ 5/12 & 1/2 & 5/12 \\ 5/12 & 5/12 & 1/2 \end{bmatrix}}_{\underset{\sim}{K}^{'(e)}} \begin{Bmatrix} \phi_1^{'(e)} \\ \phi_2^{'(e)} \\ \phi_3^{'(e)} \end{Bmatrix} + \tag{B.9}$$

$$\left. \frac{\Omega^{(e)^2}}{12} \begin{bmatrix} \phi_1^{'(e)} & \phi_2^{'(e)} & \phi_3^{'(e)} \end{bmatrix} \underbrace{\begin{bmatrix} 2 & 1 & 1 \\ 1 & 2 & 1 \\ 1 & 1 & 2 \end{bmatrix}}_{\underset{\sim}{K}^{(e)}} \begin{Bmatrix} \phi_1^{'(e)} \\ \phi_2^{'(e)} \\ \phi_3^{'(e)} \end{Bmatrix} \right]$$

Gathering equation (B.9) into local element form results in:

$$\frac{C_1 \Omega^{(e)^2}}{12} \left(\underset{\sim}{\phi}^T \underset{\sim}{K}^{(e)} \underset{\sim}{\phi} - \underset{\sim}{\phi}^T \underset{\sim}{K}^{'(e)} \underset{\sim}{\phi}' + \underset{\sim}{\phi}^{'T} \underset{\sim}{K}^{(e)} \underset{\sim}{\phi}' \right). \tag{B.10}$$

As mentioned previously, the constraint equation $K(\mathbf{k})$ physically represents the electrical current. Therefore, the finite element integral formulation necessarily proceeds along the

element boundary. Let $C_2 = ev_g \, \partial f_{\mathbf{k}} / \partial E_{\mathbf{k}}$ and again utilizing a linear transformation to natural coordinates, the resulting constraint equation formulation is:

$$\left| C_2 \left[\phi_1^{(e)} \;\; \phi_2^{(e)} \;\; \phi_3^{(e)} \right] \int_0^1 \begin{Bmatrix} 1-\xi \\ \xi \\ 0 \end{Bmatrix} l_{ij}^{(e)} d\xi \right|^2 = 1$$

$$\left| C_2 \left[\phi_1^{(e)} \;\; \phi_2^{(e)} \;\; \phi_3^{(e)} \right] \int_0^1 \begin{Bmatrix} 0 \\ \xi \\ 1-\xi \end{Bmatrix} l_{jk}^{(e)} d\xi \right|^2 = 1 \qquad \text{(B.11)}$$

$$\left| C_2 \left[\phi_1^{(e)} \;\; \phi_2^{(e)} \;\; \phi_3^{(e)} \right] \int_0^1 \begin{Bmatrix} 1-\eta \\ 0 \\ \eta \end{Bmatrix} l_{ki}^{(e)} d\eta \right|^2 = 1$$

Which gives:

$$
\begin{Bmatrix}
\left\| \underbrace{\frac{C_2 l_{ij}^{(e)}}{2}\begin{Bmatrix}1\\1\\0\end{Bmatrix}}_{\underset{\sim}{F}_{ij}^{(e)}} \begin{bmatrix}\phi_1^{(e)} & \phi_2^{(e)} & \phi_3^{(e)}\end{bmatrix} \right\|^2 - 1
\end{Bmatrix} = 0
$$

$$
\begin{Bmatrix}
\left\| \underbrace{\frac{C_2 l_{jk}^{(e)}}{2}\begin{Bmatrix}0\\1\\1\end{Bmatrix}}_{\underset{\sim}{F}_{jk}^{(e)}} \begin{bmatrix}\phi_1^{(e)} & \phi_2^{(e)} & \phi_3^{(e)}\end{bmatrix} \right\|^2 - 1
\end{Bmatrix} = 0
$$

$$
\begin{Bmatrix}
\left\| \underbrace{\frac{C_2 l_{ki}^{(e)}}{2}\begin{Bmatrix}1\\0\\1\end{Bmatrix}}_{\underset{\sim}{F}_{ki}^{(e)}} \begin{bmatrix}\phi_1^{(e)} & \phi_2^{(e)} & \phi_3^{(e)}\end{bmatrix} \right\|^2 - 1
\end{Bmatrix} = 0 \qquad \text{(B.12)}
$$

Where compact notation in local element form results in:

$$
\left[\left(\underset{\sim}{F}^{(e)^T} \underset{\sim}{\phi} \right)^2 - 1 \right]. \qquad \text{(B.13)}
$$

The augmented objective function can now be assembled in full penalty method form specific to local elements:

$$f_\varepsilon(\mathbf{k}) = \left(\underset{\sim}{\phi}^T \underset{\sim}{K}^{(e)} \underset{\sim}{\phi} - \underset{\sim}{\phi}^T \underset{\sim}{K}^{'(e)} \underset{\sim}{\phi}' + \underset{\sim}{\phi}'^T \underset{\sim}{K}^{(e)} \underset{\sim}{\phi}'\right) + \frac{1}{2\varepsilon}\left[\left(\underset{\sim}{F}^{(e)^T} \underset{\sim}{\phi}\right)^2 - 1\right]^2 . \tag{B.14}$$

It should be noted that the constants C_1 and C_2 have been absorbed in to the appropriate matrices. The solution of ϕ and ϕ' are required which necessitates the gradient of $f_\varepsilon(\mathbf{k})$:[187]

$$\begin{aligned} \nabla_\phi f_\varepsilon(\mathbf{k}) &= 2\underset{\sim}{K}^{(e)} \underset{\sim}{\phi} - \underset{\sim}{K}^{'(e)} \underset{\sim}{\phi}' + \frac{2}{\varepsilon} \underset{\sim}{F}^{(e)^T} \underset{\sim}{\phi}\left[\left(\underset{\sim}{F}^{(e)^T} \underset{\sim}{\phi}\right)^2 - 1\right] = 0 \\ \nabla_{\phi'} f_\varepsilon(\mathbf{k}) &= 2\underset{\sim}{K}^{(e)} \underset{\sim}{\phi}' - \underset{\sim}{K}^{'(e)} \underset{\sim}{\phi} = 0 \end{aligned} . \tag{B.15}$$

Setting the element equations to zero as shown in equation (B.15) and solving by consistent iteration of the penalty parameter ε yields the stationary point of $\phi(\mathbf{k})$ and $\phi(\boldsymbol{\kappa})$. Additionally, for any positive value of ε, $f_\varepsilon(\mathbf{k})$ is a strictly convex function, so $\phi(\mathbf{k})$ and $\phi(\boldsymbol{\kappa})$ determine a global minimum.[187-188]

The primary motivation of the initial solution of equation (B.15) was to check numerical convergence performance as well as comparative results to a material of known resistivity. Moreover, the application to a nanoscale material would provide preliminary results specific to the discretized solution as mentioned in the opening section of this appendix. These objectives directed the numerical application to a Au thin film material. Two triangle bi-linear elements of dimension 1 x 1 were assembled using the pre/postprocessor Femap® as shown in Figure B.2. The elements are intended to model a section of the Au thin film near the surface of the material.

The global nodes 2 and 3 represent the surface while the lower nodes 1 and 4 represent the inner volume of the crystal lattice. Boundary conditions include a gaseous interface at the surface only, which equates to gas molecules bombarding the electron cloud inelastically thus increasing the probability of energy exchange, which is manifested through the functions $\phi(\mathbf{k})$ and $\phi(\boldsymbol{\kappa})$. The analysis used a temperature of 298 K and Fermi group velocity of 1.6E6 m/s. Surface scattering of electrons with phonons *and* a gaseous interface yielded a transition probability $P_{\mathbf{k}}^{\mathbf{k}'}$ of 0.9 at global nodes 2 and 3. Electron scattering with phonons only produced a transition probability of 0.7 at the interior global nodes 1 and 4.

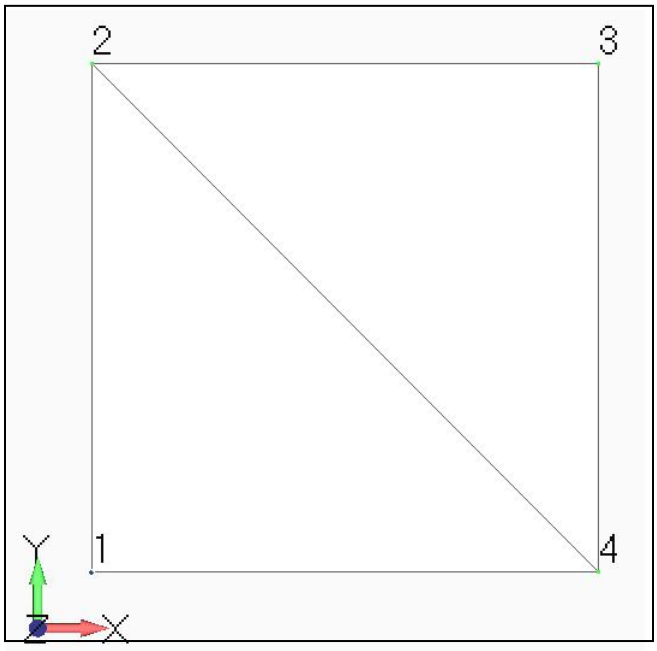

Figure B.2: Two triangle bi-linear elements were assembled to approximate the solution to equation (B.15). The global node numbers are shown as well as the global coordinate system

The coordinates of each element were obtained and a solution algorithm was implemented on MathCAD®. The relatively large value of 1 was chosen for the initial value of

ε. The value was then iteratively lowered until convergence of $\phi(\mathbf{k})$ and $\phi(\boldsymbol{\kappa})$ was found. The penalty parameter was approximately 1.0E-06 upon convergence as shown in Figure B.3. Smaller values of ε did not change the solution and no numerical oscillations or anomalies were noted.

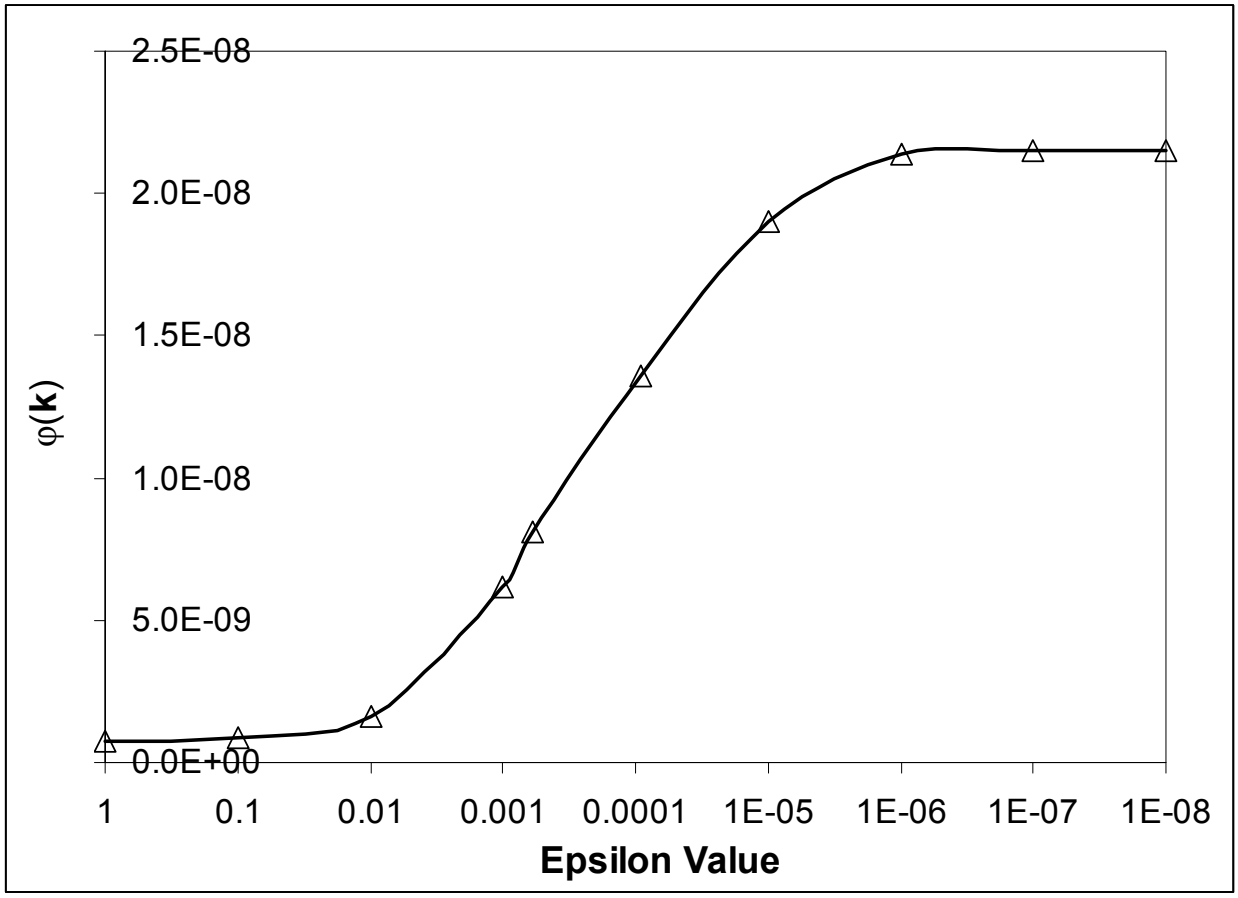

Figure B.3: Plot of the penalty parameter ε iterations and the resulting convergence of the perturbation function $\phi(\mathbf{k})$. Convergence was obtained at approximately ε = 1.0E-06.

An interesting finding of this work involves the physical meaning of the penalty parameter. Quite often, ε represents a physical parameter in a system[190] and this work has found similar character displayed by ε. The constraint on the integral representing electrical

conductivity obviously is forcing this integral to be equal to one. From equation (B.14) however, it can be seen that the penalty parameter naturally becomes equal to σ as ε decreases. Stated in other words, the constraint requires the BTE current $\int ev_g \phi(\mathbf{k}) \partial f_{\mathbf{k}} / \partial E_{\mathbf{k}} d\mathbf{k} = 1$ while the derivation of the variational BTE requires the electric field to also be equal to one. Revisiting equation (B.14) shows by inspection that the penalty parameter takes the form of electrical conductivity.

Upon convergence of the system of equations, the nodal value of resistivity was obtained and assigned to the corresponding node. Figure B.4 below provides the resistivity for the Au thin film. As expected, the increased electron scattering at the surface resulted in a larger resistivity than the inner nodes. The nodal values at the surface were also found to be identical which coincides with the applied boundary conditions. Experimental results of 30 nm Au thin films from Chapter 5 of this work showed resistivity values of approximately 5.4E-8 Ω-m. This result compares very well with the finite element average value of 5.32E-8 Ω-m. The discrete numerical results however, offer the advantage of locating specific areas of a material that experience deviations from the average value.

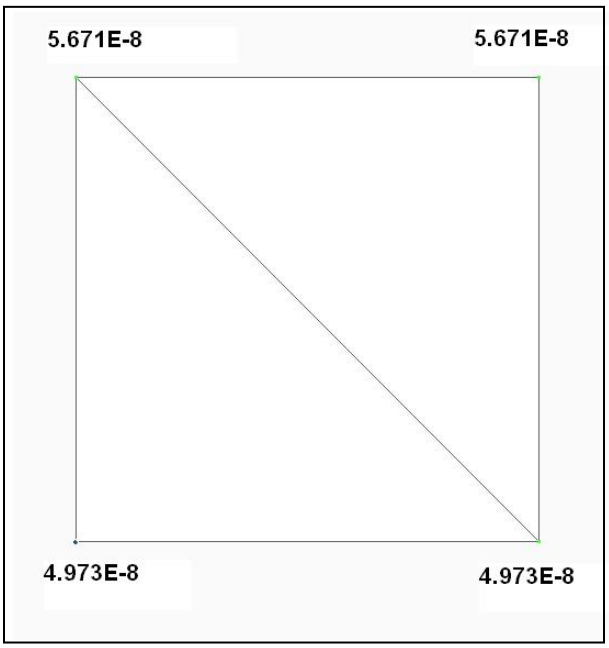

Figure B.4: Final results of the resistivity for the Gold thin film. The increased surface scattering resulted in a larger surface resistivity upon numerical convergence.

In conclusion, a numerical approximation of the variational BTE using finite elements and the penalty function method has been presented in this appendix. Previously, the BTE was solved through the use of trial functions with the assumption of identical scattering mechanisms throughout the crystal lattice. The discretization of a material volume, especially under low dimensional scale and various boundary conditions, has been shown to allow discrete spatial solutions to be determined. A two-element solution was obtained for a Au thin film and compared to the experimentally measured value with good agreement. The extension of this method to larger meshes and multiple scattering probabilities is straightforward through relevant computer code. Furthermore, the finite element formulation of other transport properties encompassed by the variational BTE such as the thermal conductivity or thermopower, is identical to the methodology presented here.

Appendix C: Proof of Experimental Power Spectral Density Measurement Due to Analog Filtering

Consider the experimental measurement of the fluctuating thermal voltage or noise of a metal or semiconductor. Figure C.1 below illustrates the apparatus for measuring the fluctuating voltage signal which is identical to that used in this research.

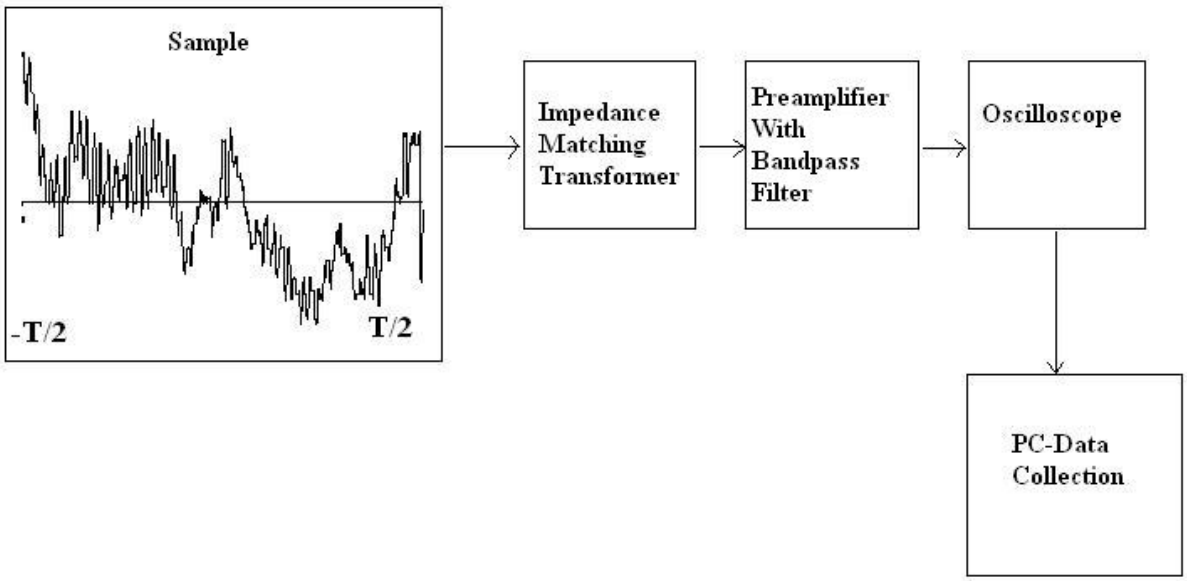

Figure C.1: Experimental apparatus used to measure thermal voltage fluctuations

The band pass filter used in the preamplifier results in an experimental measurement of the power spectral density $S_V(\omega)$ at the relevant band pass filter setting.[62,96,191-193] The objective of this appendix is to provide the proof of this statement. The experimental setup shown in Figure C.1 is common to other spectroscopic experimental techniques that use analog filtering

during the data acquisition process. Therefore, the proof that follows parallels the general mathematical format derived in other sources.[62,96,191-193] The voltage signal $V(t)$ obtained from the sample, measured for a time T, is first passed through an impedance matching transformer which serves to match low impedance samples to the preamplifier. The time T is defined as $T = n\Delta t$, where n is a sequence of equally spaced sample values spaced equally in time by Δt. The use of the transformer provided an input impedance to the preamplifier that resulted in amplifier operation within the very low noise region of the equipment noise figure contours (See Chapter 4, Section 4.3.1). An adjustable band pass filter is included in the SR560 preamplifier which was set at 10 kHz – 30 kHz. The filtered signal was then displayed by the oscilloscope which incorporated PC-based software to enable data acquisition of the waveform. Subsequently, the experimental data was numerically processed within Excel.

Returning to Figure C.1 and focusing on the sample voltage fluctuations, the function $V(t)$ measured over a time interval (-T/2 to T/2) can always be expressed in terms of its Fourier components:

$$V(t) = \frac{1}{\sqrt{T}} \sum_n A_n \exp(i\omega_n t), \tag{C.1}$$

where $\omega_n = \frac{2\pi}{T} n$ and A_n are Fourier coefficients. When passing through the band pass filter, some of the frequency components of $V(t)$ are filtered out. Therefore, the action of the band pass filter can be described by a set of numbers F_n which takes on the value of zero if the frequency

ω_n is not allowed through, and one otherwise. Therefore, the voltage signal $V(t)$ is transformed by the filter to an output voltage signal $V_{out}(t)$:

$$V_{out}(t) = \frac{1}{\sqrt{T}} \sum_n F_n A_n(t) \exp(i\omega_n t) . \tag{C.2}$$

Numerically, the fluctuating output voltage $V_{out}(t)$ is squared which equates to the square of equation (C.2):

$$\left|V_{out}(t)\right|^2 = \frac{1}{T} \sum_n \sum_{n'} F_{n'} F_n A_{n'} A_n \exp i(\omega_n - \omega_{n'})t . \tag{C.3}$$

The time average of the statistically stationary data is then taken numerically on 120 oscilloscope screen shots as shown in Figure C.2.

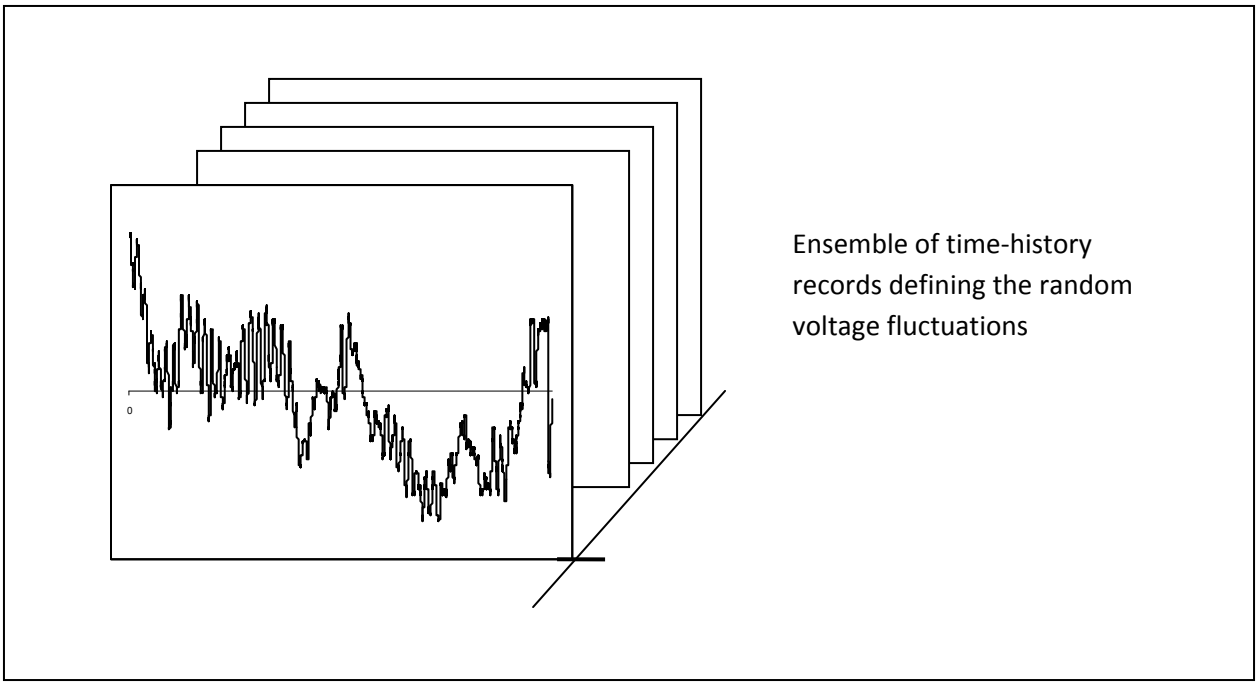

Figure C.2: The experimental data collection process which obtains a statistical ensemble of thermal voltage fluctuations through 120 oscilloscope screen shots.

It should be noted that the stationarity of the thermal noise of the sample, which is in thermal equilibrium, is unaffected by shifts in the time axis resulting in a power spectral density at a particular time entirely equivalent to the power spectral density at some later point in time. The ensemble time is approximated by the finite time average for ergodic signals. The averaged value of the collected data is then expressed as:

$$\left\langle \left| {V_{out}}^2 \right| \right\rangle = \frac{1}{T}\int_{-T/2}^{T/2} dt \left| V_{out} \right|^2 = \frac{1}{T}\int_{-T/2}^{T/2} \frac{dt}{T} \sum_n \sum_{n'} F_{n'} F_n A_{n'} A_n \exp i(\omega_n - \omega_{n'})t \,, \qquad \text{(C.4)}$$

where equation (C.3) has been substituted into equation (C.4). Evaluation of this integration over time yields:

$$\left\langle \left|V_{out}\right|^2 \right\rangle = \frac{1}{T}\sum_n F_n^2 \left|A_n\right|^2 . \tag{C.5}$$

Equation (C.5) can now be related to the autocorrelation function of the voltage fluctuations:

$$\left\langle \Gamma_V(t)\Gamma_V(t+\Delta t)\right\rangle = \frac{1}{T}\int_{-T/2}^{T/2} dt\left[\Gamma_{V_{out}}(t)\Gamma_{V_{out}}(t+\Delta t)\right], \tag{C.6}$$

where the notation of Chapter 3 has been used in equation (C.6). When the Fourier series expression of equation (C.1) is substituted into equation (C.6), the following expression is obtained:

$$\left\langle \Gamma_V(t)\Gamma_V(t+\Delta t)\right\rangle = \sum_n \sum_{n'} \frac{A_{n'}A_n}{T}\int_{-T/2}^{T/2}\frac{dt}{T}\exp i(\omega_n - \omega_{n'})t \exp(i\omega_n t) . \tag{C.7}$$

Which is directly equal to:

$$\left\langle \Gamma_V(t)\Gamma_V(t+\Delta t)\right\rangle = \sum_n \frac{\left|A_n\right|^2}{T}\exp(i\omega_n t) . \tag{C.8}$$

Multiplication of equation (C.8) by $\exp-(i\omega_n t)$ and integration over t from $-T/2$ to $T/2$ then results in:

$$|V_n|^2 \equiv \int_{-T/2}^{T/2} dt \left\langle \Gamma_V(t)\Gamma_V(t+\Delta t)\right\rangle \exp(-i\omega_n t) = 2\pi S_V(\omega_n), \tag{C.9}$$

where $S_V(\omega_n)$ is by definition the power spectral density of the time correlation function shown in equation (C.6). Substituting equation (C.9) into equation (C.5) gives:

$$\left\langle |V_{out}|^2 \right\rangle = \frac{2\pi}{T} \sum_n S_V(\omega_n) F_n^2 . \tag{C.10}$$

Equation (C.10) can be expressed in another form relevant to the thermal noise experiment. Due to the use of the band pass filter, the separation between adjacent frequencies $\Delta\omega_n = \omega_{n+1} - \omega_n = 2\pi/T$, so that

$$\left\langle |V_{out}|^2 \right\rangle = \sum_n \Delta\omega_n S_V(\omega_n) F_n^2 . \tag{C.11}$$

Now consider $T \to \infty, \Delta\omega_n \to 0$, then the sum in equation (C.11) can be written as an integral:

$$\lim_{T\to\infty} \left\langle \left|V_{out}\right|^2 \right\rangle = \int_{-\infty}^{\infty} d\omega S_V(\omega) \left|F(\omega)\right|^2 , \tag{C.12}$$

where the power spectral density $S_V(\omega)$ of V is determined by an average over an infinite time. Now returning to the fact that the thermal noise experiment utilizes a band pass filter, the filter function is expressed as:

$$\left|F(\omega)\right|^2 = \begin{cases} 1 & \omega_0 \le \omega \le \omega_0 + \Delta\omega \\ 0 & \text{otherwise} \end{cases} . \tag{C.13}$$

Resulting in:

$$\lim_{T\to\infty} \left\langle \left|V_{out}\right|^2 \right\rangle = S_V(\omega_0)\Delta\omega . \tag{C.14}$$

Therefore, the primary motivation of proving that the time average of $\left\langle \left|V_{out}\right|^2 \right\rangle$ is equivalent to the power spectral density $S_V(\omega)$ is accomplished through the above derivation. In fact, by

tuning the band pass filter through different bands and collecting data at each Δf, one can determine the spectrum of the fluctuating voltage. From an DES experimental view point, the power spectral density $S_V(\omega)$ at a single band pass filter setting is measured directly due to the use of analog filtering.

Appendix D: Alternative Proof of the Thermal Power Spectral Density Equivalence to Energetic Thermal Transport Spectra

The objective of the following derivation is to provide a second proof of the thermal PSD equivalence to the electron canonical ensemble thermal energy fluctuations. The first proof was given as Theorem 1 in Chapter 2, Section 3.2.1 which is repeated below followed by the alternate proof.

Theorem 1. *The thermal PSD* $S_Q(f_0)$ *is exactly equal to the electron canonical ensemble root-mean-square energy fluctuations,* $\sigma_H \equiv S_Q(f_0)$.

Proof 2: Energy fluctuations are expressed by the Johnson/Nyquist relation by the expression:

$$\frac{\bar{V}^2}{4R\Delta f} = k_B T \,. \tag{D.1}$$

The temperature fluctuations indicated by the right side of equation (D.1) are known as the noise temperature and are prevalent in all conductors and semiconductors.[86] The equilibrium temperature fluctuations correspond to enthalpy fluctuations as shown by equation (D.2):[194-196]

$$k_B \delta T = \delta h \,, \tag{D.2}$$

where the δ symbol indicates a spontaneous fluctuation. Next consider a small differential control volume in the corresponding conductor or semiconductor as show in Figure D.1 below. With respect to the x direction only (the y or z direction results are identical), an enthalpy heat current fluctuation is given by:

$$h_{x+dx} = h_x + \frac{\partial h_x}{\partial x} dx \,. \tag{D.3}$$

However, due to equilibrium conditions of the material, there is no steady uniform enthalpy current present which means $h_x = 0$. Therefore, the energy fluctuation is expressed by the second term only on the right side of equation (D.3). Utilizing the thermodynamic relation between the

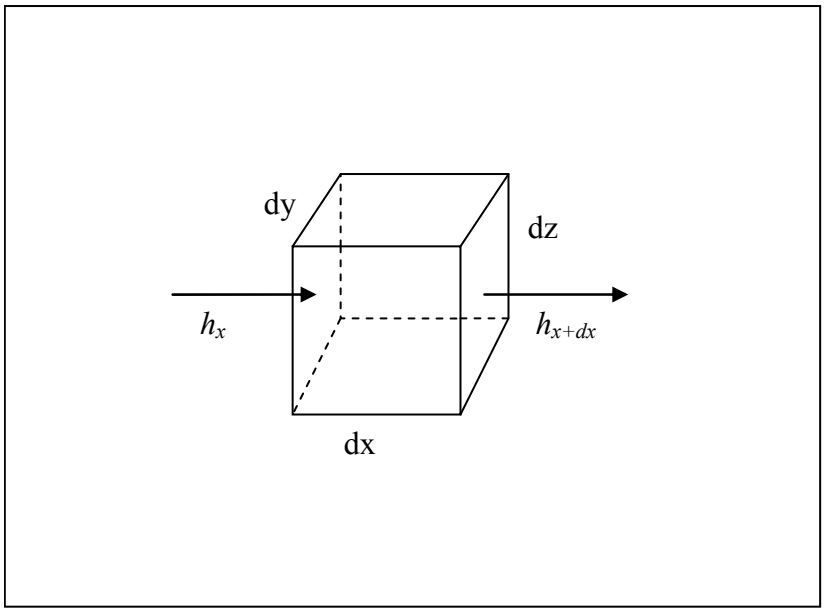

Figure D.1: The conductor or semiconductor differential control volume. The enthalpy current fluctuation is analyzed in the x direction.

differential increase in heat and the relation between the internal energy and particle number:[32]

$$dH = dQ = dU - \mu_n dN \,, \tag{D.4}$$

where the enthalpy is equivalent to the heat as shown by $dH = \mathrm{d}Q$ and capital letters are used to coincide with conventional thermodynamic nomenclature. On the right side of equation (D.4), U is the internal energy, μ_n is the chemical potential of particle n and N is the number of carriers. The spontaneous temperature and corresponding enthalpy fluctuation is now equated to the differential control volume expression:

$$k_B \delta T = \delta h = \frac{\partial h_x}{\partial x} dx = dH \,. \tag{D.5}$$

Equation (D.5) clearly shows that the temperature fluctuations expressed by the Johnson/Nyquist relation and noise temperature of equations (D.1) and (D.2) are equivalent to a spontaneous enthalpy perturbation. Consequently, this is related to an associated heat *current* perturbation:

$$dJ_Q = dJ_U - \mu_n dJ_N \,, \tag{D.6}$$

where the heat current, internal energy current and particle number current are represented by J_Q, J_U and J_N respectively. Furthermore, the heat current J_Q is identical to the Green-Kubo heat current of equation (3.46). This proof is briefly halted to examine the derivations and theory put forth so far. Equation (D.6) is theoretically important because it formulates a direct path to the

Green-Kubo correlation function integral of equation (3.46). This theoretical path is a generalized result that applies for example, to the work of Chapter 6. The inherent problems associated with a non-mechanical force such as temperature have been attacked by an alternative procedure in this appendix which is more direct than the method of Chapter 3, Section 3.2.2. Focusing again on the differential volume of Figure D.1, we recognize the volumetric expression as *dxdydz*. Equilibrium statistical mechanics has previously derived the mean enthalpy fluctuations in a differential volume which is given by:[197]

$$\langle \delta h \rangle = \frac{\sqrt{k_B T^2 C_V}}{dxdydz}. \tag{D.7}$$

The results of equation (D.7) are exactly equal to the electron canonical ensemble energy fluctuations.[97,198] The full equivalence to all relevant parameters are given in equation (D.8):

$$\sigma_E = \sigma_Q = \sqrt{k_B T^2 C_V} = \langle \delta h \rangle = k_B \langle \delta T \rangle = S_Q(f_0) = \Gamma_Q(0). \tag{D.8}$$

The results of equation (D.8) show the exact equivalence of mean square temperature fluctuations to the thermal fluctuation spectra and thermodynamic quantities. The importance of equation (D.8) is the specific application to Green-Kubo linear transport theory as described in Chapter 3.

This concludes Proof 2 of Theorem 1.

Appendix E: National Bureau of Standards Certificate for the Resistivity and Thermal Conductivity of NBS 1461 Austenitic Stainless Steel

The National Bureau of Standards certified documentation of NBS 1461 stainless steel properties used as a reference material in Chapter 5 to validate the DES experiment is shown below in Figure E.1

U. S. Department of Commerce
Malcolm Baldrige
Secretary

National Bureau of Standards
Ernest Ambler, Director

National Bureau of Standards

Certificate

Standard Reference Materials 1460, 1461, and 1462

Austenitic Stainless Steel Thermal Conductivity (λ) and Electrical Resistivity (ρ) as a Function of Temperature from 2 to 1200 K

J. G. Hust and A. B. Lankford

These Standard Reference Materials (SRM's) are to be used in calibrating methods for measuring thermal conductivity and electrical resistivity. They are available in rod form. SRM 1460 is 0.64 cm in diameter; SRM 1461 is 1.27 cm in diameter; and 1462 is 3.4 cm in diameter. All rods are 5.0 cm in length.

T(K)	λ (W·m^{-1}·K^{-1})	ρ (nΩ·m)	T (K)	λ (W·m^{-1}·K^{-1})	ρ (nΩ·m)
			50	6.08	599
2	0.152	593	60	6.98	606
3	.249	593	70	7.72	613
4	.352	593	80	8.34	622
5	.462	594	90	8.85	630
6	.575	594	100	9.30	639
7	.693	594	150	10.94	683
8	.814	594	200	12.20	724
9	.938	594	250	13.31	767
10	1.064	594	300	14.32	810
12	1.323	594	400	16.16	885
14	1.588	594	500	17.78	944
16	1.858	593	600	19.23	997
18	2.132	593	700	20.54	1045
20	2.407	593	800	21.75	1088
25	3.092	592	900	22.86	1127
30	3.763	592	1000	23.90	1162
35	4.404	593	1100	24.86	1197
40	5.01	595	1200	25.77	1234
45	5.57	597			

Figure E.1: National Bureau of Standards certificate of thermal conductivity and electrical resistivity for NBS 1461 austenitic stainless steel

Vita

Patrick Garrity was born in New Orleans, Louisiana and received his B. S. in Mechanical Engineering from the University of New Orleans in April of 2002 and his M. S. in Physics in December of 2003. He currently resides in Covington, Louisiana.